Crystallisation in Diesel and Biodiesel Fuel in Relation to their Solution Composition

Diana Milena Camacho Corzo

Submitted in accordance with the requirements for the degree of

DOCTOR OF PHILOSOPHY

(Chemical Engineering)

UNIVERSITY OF LEEDS

Institute of Particle Science and Engineering

School of Chemical and Process Engineering

September 2015

The candidate confirms that the work submitted is her own, except where work which has formed part of jointly authored publications has been included. The contribution of the candidate and the other authors to this work has been explicitly indicated below. The candidate confirms that appropriate credit has been given within the thesis where reference has been made to the work of others.

The work in Chapter 5 and some of the results in Chapter 7 of the thesis have appeared in publications as follows:
"Determination of the nucleation mechanism and kinetics from the analysis of polythermal crystallisation data: methyl stearate from kerosene solutions", CrystEngComm, January 2014, Diana M. Camacho Corzo, Antonia Borissova, Robert B. Hammond, Dimo Kashchiev, Kevin J. Roberts, Ken Lewtas, Iain More.
I was the principal investigator on the research addressed by this publication which includes the development of an experimental methodology that was part of my research work. The contributions of the other authors were: Dimo Kashchiev, Antonia Borissova, Robert B. Hammond, and Kevin J. Roberts are the developers of the (KBHR) model that was used to analyse the experimental data collected in this work. As this is an analytically derived model, they contributed during the analysis of the practical data presented within the publication. This was done through helpful discussions and jointly assessment on the data analysis. Ken Lewtas, Iain More also contributed with helpful discussions as industrial experts on the crystallisation of Biodiesel fuels compounds.

Part of the work in Chapter 8 of the thesis has appeared in publications as follows:
"The crystal morphology and growth rates of triclinic n-docosane crystallising from n-dodecane solutions", Journal of Crystal Growth, April 2015, Diana M. Camacho, Kevin J. Roberts, Ken Lewtas, Iain More.
I was the principal investigator on the research addressed by this publication as this work makes part of my research thesis. The contributions of the other authors were: Kevin J. Roberts as my research supervisor worked jointly with me analysing the experimental data and developing the experimental methodology presented in the publication. Ken Lewtas, Iain More as my industrial supervisors contributed with helpful discussions on the crystal growth of Biodiesel fuels compounds.

Acknowledgments

I would like to express my gratitude to:

Professor Kevin J. Roberts for his supervision, encouragement and support during my research.

Dr. Iain More and Dr. Ken Lewtas for sharing their extensive experience in the fuels industry through invaluable discussions.

Professor Dimo Kashchiev for his guidance, comments and invaluable advice during this research, particularly in the different aspects of crystallisation science.

Member of the Institute of Particle Science and Engineering (IPSE) for their continue support particularly to Dr Antonia Borissova for her advice and comments on the theoretical background of one of the methodologies underpinning this research.

I also gratefully acknowledge Infineum UK Ltd. for the funding of this research.

Abstract

Wax formation in diesel and biodiesel fuels at low temperatures is one of the major problems faced by the fuels industry as crystallisation of the saturated compounds present in these solutions can plug up filters and obstruct pipelines. Preventing wax formation in these multicomponent mixtures requires a good understanding of the crystallisation behaviour of both n-alkanes and Fatty Acid Methyl Esters (FAMEs). This work studies solutions of methyl palmitate and stearate in representative mixtures of diesel fuels and unsaturated esters solvents, providing an overall assessment of their solubility and nucleation kinetics. An in-depth analysis of the growth kinetics and crystal morphology for methyl stearate crystallising from n-dodecane, kerosene and toluene solvents is also presented.

To perform this study methodologies are developed for the assessment of nucleation kinetics and morphological indexation of crystal specific faces. Models for the analysis of crystal growth kinetics are also derived. These describe the effect in series of the diffusion of growth units within the bulk of the solution and a rate of incorporation of these units which is associated to the molecular structure of the crystal faces´ surface.

It was found that the solubility and crystallisation kinetics of methyl palmitate and stearate is very dependent on the solution environment in particular solvent type. Solubilities are higher in solvents whose molecules have more compact structures, such as in the case of toluene and methyl-cyclohexane and are lower in unsaturated methyl ester type solvents.

The nucleation process in these systems is found to be much more thermodynamically controlled in the case of diesel type solvents and show a greater kinetic influence in the case of unsaturated methyl esters solvents. The growth kinetics of methyl stearate crystals is found to be strongly associated to the level of solvation of these solutes molecules as well as to the chemical structure of the crystal-solution interface. Accordingly, the rate limiting step is suggested to be the integration of growth units to the surface of the crystal in the case of methyl stearate

growing from n-dodecane solvent, and more diffusional controlled in the case of methyl stearate growing from kerosene and toluene solvents. The morphology of methyl stearate crystals however is not found to be strongly influenced by solvent type, only showing changes as a function of supersaturation in the case of kerosene solvent.

Table of Contents

List of Figures

List of Tables

List of Symbols

a Dimensionless molecular latent heat of crystallisation

a Activity

a_e Activity of a saturated solution

A_0 Fixed needle cross sectional area (m^2)

$A_{i(hkl)}$ Surface area of individual forms (m^2)

A_{total} Total surface are of a crystal (m^2)

A_1 Growth parameter in B&S model

A_2 Growth parameter in the BCF model

A^* Surface area of nucleus (m^2)

b Dimensionless thermodynamic parameter

C Solution concentration (m^{-3})

C_e Equilibrium solution concentration (m^{-3})

C_s Solution concentration at the crystal solution interface (m^{-3})

C^*_{nuc} Equilibrium nucleus concentration (m^{-3})

C_0 Concentration of nucleation sites and/or instantaneously nucleated crystallites (m^{-3})

ΔC_{max} Maximum concentration difference (m^{-3})

d Dimensionality of crystallite growth

d_0 Molecular diameter (m)

d_{hkl} Inter-planar distances within morphological (hkl) forms

D Diffusion coefficient of colliding building units $(m^2 s)$

$\frac{dc_e}{dT}$ Rate of solubility change with temperature $(m^{-3}K^{-1})$

dG Change in Gibbs energy $(J\ mol^{-1})$

dS Change in entropy $(Jmol^{-1}K^{-1})$

dU Change in internal energy

dV Change in volume (m^3)

E_{att} Attachment energy

f Fugacity

$f_{i(real)}$ Fugacity of a compound at equilibrium

$f_{i(ideal)}$ Fugacity of a compound in ideal state

$f_{e,s}$ Molecular attachment frequency per growth site (s^{-1})

f^* Frequency of monomer attachment to the nucleus (s^{-1})

f_e^* Frequency of monomer attachment to the nucleus at $\Delta\mu = 0$ (s^{-1})

G Single crystal face growth rate $(m\ s^{-1})$

H_0 Fixed disk or plate thickness (m)

H Enthalpy $(Jmol^{-1})$

ΔH^E Enthalpy excess function $(Jmol^{-1})$

i^* Number of molecules in critical nucleus

J Nucleation rate $(m^{-3}s^{-1})$

k Boltzmann constant (JK^{-1})

k_d Docking rate $(mol\ m^{-2}s^{-1})$

k_G Growth rate constant $\left(\mathrm{m}^{\left(\frac{1}{m}\right)}s^{-1}\right)$

k_j Empirical parameter of nucleation rate $(m^{3(m_o-1)}s^{-1})$

k_J Nucleation rate constant $(m^{-3}s^{-1})$

k_{MT} Mass transfer coefficient $(m\ s^{-1})$

$\frac{1}{K_{MTOT}}$ Total resistance to mass transfer

k_n Nucleus numerical shape factor

k_v Crystallite growth shape factor $\left(m^{3-d}\right)$

m_0 Nucleation rate order

m, n Crystallite growth exponents

$M_{i(hkl)}$ Multiplicity of individual forms

N Number of crystallites

N_a Avogadro's number

N_{det} Detectable number of crystallites

P Pressure (Pa)

q Cooling rate $(K\ s^{-1})$

q_0 Parameter in the $u_c(q)$ dependence for both PN and IN $(K\ s^{-1})$

r Growth exponent

r Nucleus radius (m)

r^* Critical nucleus radius (m)

r_{MT} Rate of growth units transfer at the crystal solution interface $(molm^{-2}s^{-1})$

R' Effective crystallite radius (m)

R Single face growth rate $(m\ s^{-1})$

S Supersaturation ratio

S Entropy $(Jmol^{-1}K^{-1})$

ΔS^E Entropy excess function $(Jmol^{-1}K^{-1})$

T Solution temperature (K)

T_0 Temperature at which crystallites are instantaneously nucleated (K)

T_c Crystallisation temperature (K)

T_{diss} Dissolution temperature (K)

T_e Solution saturation (or equilibrium) temperature (K)

ΔT Undercooling (K)

ΔT_c Critical undercooling for crystallisation (K)

u Relative undercooling

u_0 Relative undercooling at the moment of crystallite IN

u_c Relative critical undercooling for crystallisation

U System internal energy

v_i Molar volume (m^3)

v_0 Volume of solute molecule in crystal (m^3)

V Volume of solution (m^3)

V_c Total volume of crystallites (m^3)

V_n Volume of individual crystallite (m^3)

W^* Nucleation work

x Mole fraction of solute in solution

x_f Mole fraction of solute in the liquid phase at a given crystallisation temperature

x_{ideal} Mole fraction of solute in ideal state

x_{real} Mole fraction of solute at equilibrium

X_1Concentration of colliding building units

z Zeldovich factor

α Fraction of crystallised volume

α_{det} Detectable fraction of crystallised volume γ Interfacial tension of crystal nucleus in HON (Jm^{-2})

γ Interfacial tension (Jm^{-2})

γ_{eff} Effective interfacial tension of crystal nucleus in $3D$ HEN (Jm^{-2})

$\gamma_{i(hkl)}$ Interfacial tension of individual forms (Jm^{-2})

ϒ Activity coefficient

λ Molecular latent heat of crystallisation (J)

Γ Complete gamma function

ψ Nucleation-activity factor

μ Chemical potential(J)

$\Delta\mu$ Supersaturation in terms of chemical potential difference (J)

σ Relative supersaturation

σ_s Relative supersaturation at the crystal solution interface

σ_{crit} Critical relative supersaturation

ρ Density

ξ Sticking coefficient

ω^* Transfer frequency of building units from adsorbed to integrated

ς_i Proportionality constant

ψ Activity factor

τ Induction time (s)

$\bar{g}_i^E$ Molar excess Gibbs free energy $(Jmol^{-1})$

$\bar{g}_{i(ideal)}$ Molar excess Gibbs free energy in ideal state $(Jmol^{-1})$

$\bar{g}_{i(real)}$ Molar excess Gibbs free energy at equilibrium $(Jmol^{-1})$

Δg_i Molar change in Gibbs free energy $(Jmol^{-1})$

ΔG^E Total excess Gibbs free energy $(Jmol^{-1})$

ΔG_v Free energy change per unit volume (Jm^3)

ΔH_f Molar enthalpy of fusion $(Jmol^{-1})$

ΔS_f Molar entropy of fusion $(Jmol^{-1}K^{-1})$

ΔH_m Molar enthalpy of melting $(Jmol^{-1})$

ΔS_m Molar entropy of melting $(Jmol^{-1}K^{-1})$

ΔH_{diss} Molar enthalpy of dissolution $(Jmol^{-1})$

ΔH_{mix} Molar enthalpy of mixing $(Jmol^{-1})$

ΔS_{diss} Molar entropy of dissolution $(Jmol^{-1}K^{-1})$

ΔS_{mix} Molar entropy of mixing $(Jmol^{-1}K^{-1})$

ΔC_p Molar heat Capacity $(Jmol^{-1}K^{-1})$

i Subscript to refer to a single compound

° Superscript to refer to a standard state

List of Abbreviations

$ASTM$ American Society for Testing and Materials

BX Biodiesel/diesel fuel mixtures

BCF Burton-Cabrera-Frank model

BFDH Bravais-Friedel-Donnay-Harker model

B&S Birth and Spread model

Btl Biomass to liquid

Cif Crystallographic information file

$CFPP$ Cold flow plugging point

CN Cetane number

CNT Classical Nucleation Theory

CP Cloud point

$CSFT$ Cold soak filtration test

DIC Differential Interference Contrast

DSC Differential Scanning Calorimetry

EN European norm

EVA Ethylene-vinyl acetate copolymer

$FAMEs$ Fatty Acid Methyl Esters

FVA Fumarate-vinyl acetate copolymer

GC Gas chromatography

HEN Heterogeneous nucleation

HON Homogeneous nucleation

IN Instantaneous nucleation

IV Iodine value

$KBHR$ Kashchiev-Borissova-Hammond-Roberts approach

$KJMA$ Kolmogorov-Johnson-Mehl-Avrami approach

$LTFT$ Low temperature flow test

$MSZW$ Metastable Zone Width

MTR Mass transfer

MW Molecular weight

$NERD$ Non-ester Renewable Diesel

PAA Poly-alkyl acrylates

PMO Palm oil

PN Progressive nucleation

PP Pour point

RIG Rough Interface Growth model

RSO Rapeseed oil

SBO Soybean oil

SD Standard deviation

SFO Sunflower oil

$UNIQUAC$ UNIversal QUAsiChemical

$2D$ Two dimensional

$3D$ Three dimensional

$C16{:}\,0$ Methyl palmitate

$C18{:}\,0$ Methyl stearate

$C18{:}\,1$ Methyl oleate

$C18{:}\,2$ Methyl linoleate

$C18{:}\,3$ Methyl linolenate

1. Introduction

Summary: The background underpinning this research together with aims and objectives of this study are presented. Details of the research´s project management and summary of the thesis layout is also provide

1.1. Research background

The decline of crude oil deposits and environmental legislations to reduce emissions and improve fuels economy is having a significant impact on fuels formulation and engine system design. The emission of greenhouse gases by motor vehicles and its effect on climate change has increased the pressure to reduce the level of CO_2 emissions by vehicles. This has advocated governments to look for substitutes sources of energy than rely on various forms of renewable energy which are gaining popularity. One of this "forms" of energy is bio-fuels which include liquid, solid or gaseous fuels produced from different bio-resources, derived through a number of different chemical processes. Under the framework of the Kyoto's protocol [1] the European Union has established a number of strategies to comply with the goals on the reduction of greenhouse gases emissions. Directives [2] that cover biofuels use have set an ambitious target of 10% renewable sources share in transport by 2020.

Among the biofuels used in transport, biodiesel is an immediate alternative to the traditional petrodiesel fuel and is commonly obtained through the trans-esterification of a triglyceride with methanol, to give a fatty acid methyl ester (FAMEs). FAMEs can be used as a direct substitute for petrodiesel or as a blending component in the final diesel fuel. However, its introduction has brought with it a number of challenges to the fuels industry for which one of the greatest is to comply with diesel fuels specifications to guarantee engines operability under cold weather conditions. Refineries, marketers and fuels producers are now operating under more rigorous conditions which include: tighter margins, supply and demand imbalances in fuels and ambitious environmental targets. Under these circumstances they are forced to incur in costly protective measures to ensure their fuel is fit for its purpose wherever its final destination might be [3].

The FAME products available in Europe today are often a mixture of different FAMEs manufactured from different feedstock which results in the final FAME composition being a function of cost, availability and performance. Recent EU directives, 2003/30/EC (Biofuels), 2009/28/EC (Renewable Energy Directive) and 2009/30/EC (Fuel Quality Directive), have led to an increasingly diverse source of

biomass feedstock for the manufacture of FAME. In addition to thus increasing amounts of FAME products manufactured from palm oil, soybean oil and animal fats is being imported into Europe.

In spite of all these issues there is an expectation in Europe to increase the use of biofuels in transport applications to meet environmental targets. Diesel quality in the EU is governed by EN590 where the maximum FAME content allowed is currently 7% v/v but there is a plan to increase to 10% v/v. Currently, in UK biodiesel fuels are used in blends of 5% Vol. biodiesel 95% Vol. diesel fuel but some other European countries are already using mixtures of up to 15% Vol. biodiesel.

The composition of FAMEs fuel is very different from that of diesel derived from fossil sources which is hydrocarbon in nature. For FAME derived from the most common feedstock the fatty acid distribution consist mainly of five C16 and C18 fatty acids: palmitic, stearic, oleic, linoleic and linolenic acids. This difference is important because the low temperature properties of the two different fuels are controlled by different solutions chemistry and composition. In petrodiesel the low temperature properties is controlled by the quantity and carbon number of the n-alkanes present. The longer chain n-alkanes have lower solubility and this influences their crystallisation behaviour. For FAMEs its low temperature properties are governed by the levels of the methyl esters of palmitic and stearic acids. At low temperatures these methyl esters can crystallise from a FAME to produce waxes, similar to those produced by n-alkanes in hydrocarbon diesel, which can subsequently plug filters and/or cause problems in fuels flow within fuel distribution systems (Fig. 1.1).

For a petrodiesel:FAME blend that is now commonly used in Europe the low temperature properties will be governed by both the n-alkanes that are present and the levels of methyl esters of palmitic and stearic acid, in the blend. The current formulation of biodiesel and petrodiesel/biodiesel fuel mixtures exhibit poor cold flow properties as indicated by relatively high cloud point (CP), pour points (PP) and cold flow plugging point (CFPP) as the saturated compounds in these mixtures tend to crystallize when they are exposed to low temperatures [4]. Solutions of FAMEs

have cloud (CP) and pour points (PP) that are 15-25 °C higher than those of petrodiesel fuel [5].

Numerous additives for petrodiesel have been synthesized and it has been reported they have had a positive effect on vehicle performance by depressing the Cold Flow Plugging Point (CFPP). Additives developed for petrodiesel fuels have been used on biodiesel fuels in an attempt to suppress the crystallisation of fatty acid methyl esters FAMEs, which crystallise at even higher temperatures that petrodiesel paraffin. However, the effect of petro-diesel additives on biodiesel mixtures has not had a relevant effect on improving their low temperature properties [6, 7]. Petrodiesel cold flow improvers (CFIs) decrease the pour point of B20 blend up to 18-20 °C, but do not affect the cloud point (CP) i.e. CFIs act by modifying crystal growth but do not inhibit crystallisation initiation [4]. Thus, currently the main challenge is finding effective chemistries to treat the most difficult biodiesel types [5].

In order to develop the appropriate technology to combat the poor cold flow behaviour at low temperature of biodiesel and diesel/biodiesel mixtures, it is of fundamental importance to understand from first principles crystallisation in these solutions.

Within the group of the Institute of Particles Science and Engineering (IPSE) substantial work has been done in investigating crystallisation of n-alkanes covering areas such as:

- Solubility and solution ideality
- Nucleation modelling and kinetics
- Morphological characterisation and growth kinetics
- Experimental and modelling studies of wax appearance temperatures
- Crystallographic characterisation of solid-state structures of single and mixed phase systems (n-alkanes and esters)
- SAXS/WAXS studies of the inter-molecular processes involved in the early stages nucleation and growth

- Prediction of the impact of cold flow additives on morphology and cloud points

The experience acquired through the study of n-alkanes crystallisation has allowed the definition of a set of experimental techniques, methodologies and modelling tools some of which have been applied to the study of representative systems associated to biodiesel fuel solutions in recent projects. However, there is still a need to develop a more systematic approach for the assessment of the solution state, phase separation and crystallisation kinetics of methyl esters systems.

This scenario provides the backdrop for the research addressed in this PhD thesis that aims to deliver a fundamental understanding of crystallisation phenomena of methyl palmitate and stearate as the main saturated compounds present in biodiesel fuels mixtures. For this purpose model solutions of these saturated esters are studied using as solvents representative compounds present in practical solvents of the fuels industry including: five diesel type hydrocarbons (n-dodecane, kerosene, toluene, n-heptane and methylcyclo hexane) and three unsaturated methyl esters (methyl oleate, linoleate and linolenate) which are used as single components solvent and in mixtures in the proportions as they are present in pal, soy and rapeseed FAME oil.

The crystallisation process of these systems is tackled comprehensively through the study of their solubility, nucleation kinetics, crystal morphology and crystal growth kinetics. This is expected to provide the bases for further research on the thermodynamic and kinetic behaviour of the wax precipitating from more complex-practical mixtures.

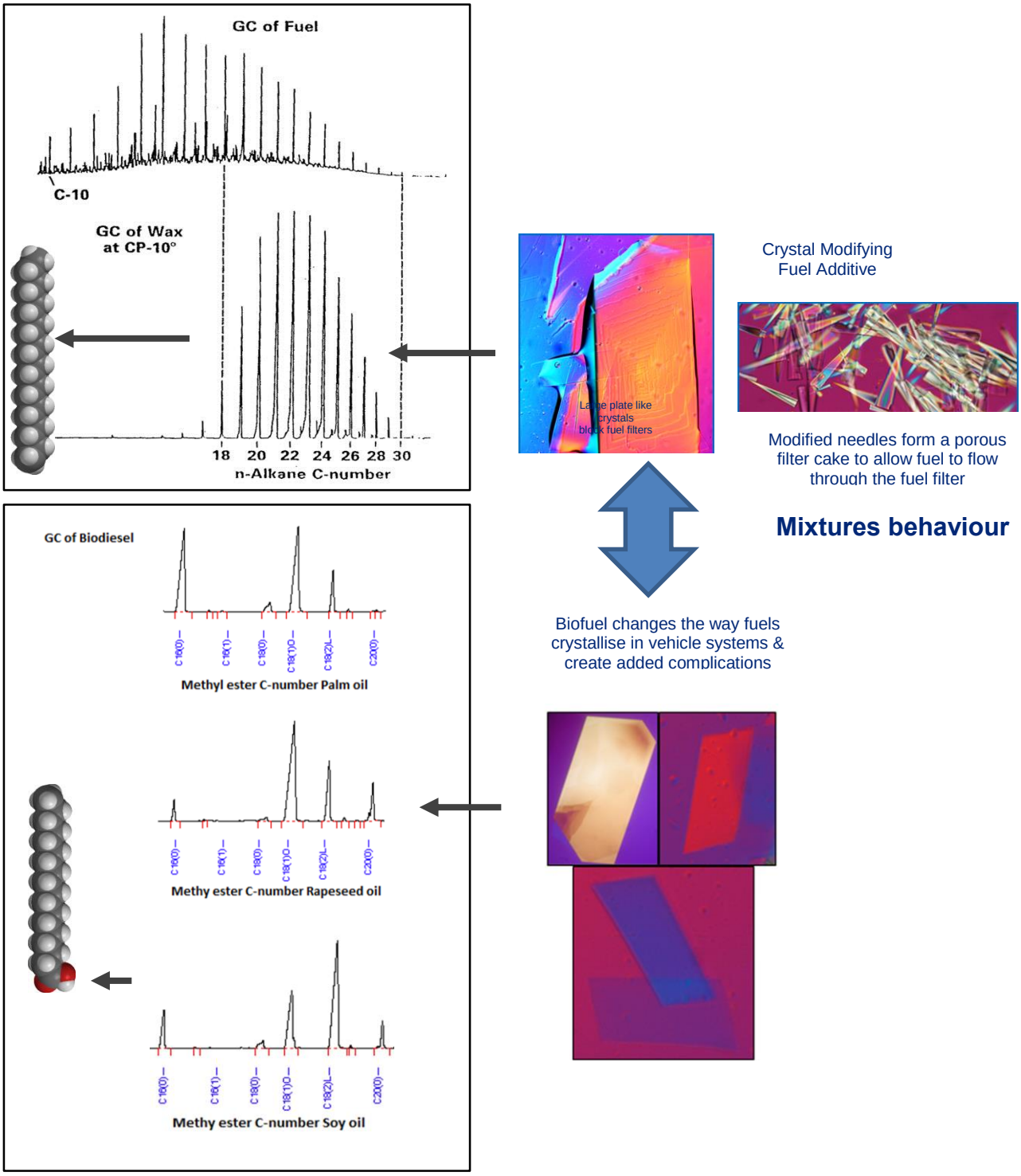

Figure 1.1 Schematic representation of the influence of biodiesel fuel chemistry on crystallisation diesel fuel. Pictures of n-alkanes crystals and chromatograms of diesel fuel provided by Infineum UK Ltda

1.2. Scope of research

The research question underlying this thesis is as follow:

What is the influence of solution composition on the solubility, phase separation & crystallisation of n-alkanes & methyl esters in practical fuel and biofuel systems?

This question is addressed through the following core objectives:

1. Develop a quantitative approach for the analysis of nucleation mechanism and kinetics from polythermal crystallisation data.
2. Assess the influence of solution composition on the solubilities, metastability (MSZW) & solution ideality of model solutions of n-alkanes and methyl esters in representative fuels solvents.
3. Examine the influence of solution composition on the nucleation kinetics of model solutions of n-alkanes and methyl esters crystallising from representative fuels solvents.
4. Establish a methodology to assess the influence of solvent on the morphology and growth kinetics of n-alkanes and methyl esters and apply it to model solutions of these compounds.
5. Define a methodology to predict the fractionation after crystallisation of complex mixtures and validate it from the crystallisation of representative biodiesel fuels solutions.
6. Apply the fractionation methodology to the assessment of solution's crystallisation of representative mixtures of diesel and biodiesel fuels.

1.3. Project management

This project was funded through industrial sponsorship from Infineum UK ltd. The research work was carried out at the Institute of Particle Science and Engineering (IPSE) at the University of Leeds under the supervision of professor Kevin J. Roberts, with the support of an interdisciplinary team: Co-supervision from Dr.

Robert Hammond and Dr. Xiaojun Lai and supervision from industry provided by Dr. Iain More and Dr. Ken Lewtas from Infineum UK Ltd.

Trimestral meetings with Infineum UK supervisors were carried out to present the work done and the progress made on achieving the outlined objectives.

The underpinning concepts used in the analysis of nucleation kinetics were developed through a visiting professorship awarded to Professor Dimo Kashchiev in the Institute of Particle Science and Engineering at the University of Leeds, with the financial support of the Leverhulme Trust (grant F10100A). Useful discussions on the nucleation model were regularly held with Dr. Antonia Borissova teaching fellow at the School of Process and Chemical Engineering (SCAPE).

The experimental methodology to calculate the number of crystals at the crystallisation temperature was developed with the help of Professor Joao Coutinho through collaboration with Infineum UK. The gas chromatography method used as part of this methodology was developed by Jenny Wilson from Infineum UK who also provided the initial training in this technique.

The diffusional growth kinetic model used for the analysis of crystal growth data was developed with the support of Professor Frans Muller from the School of Process and Chemical Engineering (SCAPE).

1.4. Structure of report

Following this chapter, Chapter 2 discusses the fundamentals of crystals and crystallography as well as the theoretical background on solubility, nucleation and crystal growth kinetics and morphology. It also provides a detailed theoretical review on the different methodologies to study nucleation kinetics.

Chapter 3 reviews the literature related to the cold flow behaviour and crystallisation in diesel and biodiesel fuels.

Chapter 4 provides information about the materials used in this research together with the instrumentation and experimental methodologies used for the collection and analysis of data related to this research.

Chapter 5 develops a methodology for the assessment of nucleation kinetics from polythermal experimental data.

Chapter 6 assesses the solubility, ideality and metastability of solutions of methyl palmitate and stearate in five representative compounds present in diesel fuels mixtures and three representative unsaturated methyl esters present in biodiesel fuels solutions.

Chapter 7 extends the assessment of representative methyl palmitate and stearate solutions to the analysis of nucleation kinetics using the methodology developed in chapter 5.

Chapter 8 introduces a methodology for the morphological indexation of specific crystal faces, presents the derivation of models for the assessment of crystals growth kinetics and provides a comprehensive analysis of the crystal growth kinetics and morphology of methyl stearate crystallising from n-dodecane, kerosene and toluene solvents.

Chapter 9 summarises the outcomes from this work, compares them with the aims and objectives of this thesis and makes suggestion for future development of this work.

A general description of the thesis content is presented schematically in Fig. 1.2.

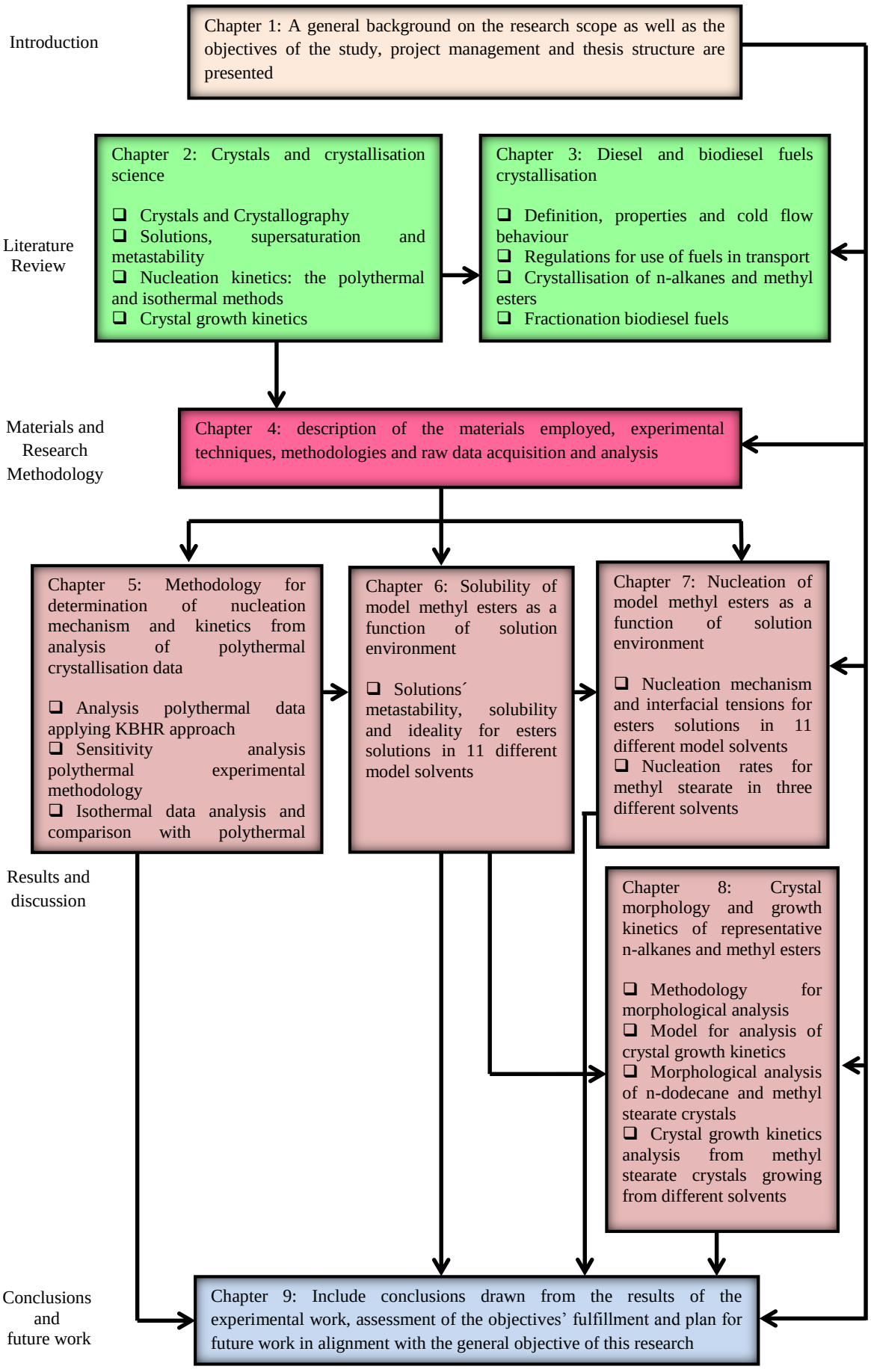

Figure 1.2 Schematic description of the thesis content

References

[1] L. Assunçao, Z. Zhang, United Nations Conference on Trade and Development., Domestic climate change policies and the WTO, United Nations Conference on Trade and Development, Geneva, 2002.

[2] E.P.a. Council, Directive 2003/30/EC of the European Parliament and of the Council in: E. Parliament (Ed.), European Union 2003.

[3] www.hartfuel.com, in: H.E. Publication (Ed.) The Global Bussiness of Fuel, 2015.

[4] G. knothe, R.O. Dunn, M.O. Bagby, Biodiesel: The use of vegetable oils and their derivatives as alternatives diesel fuels Oil Chemical Research, National Center for Agricultural Utilization Research, Agricultural Research Service, U.S. Department of Agriculture, Peoria, IL 61604, (2001).

[5] J.C.J. Bart, N. Palmeri, S. Cavallaro, Biodiesel science and technology : from soil to oil, Woodhead Publishing; CRC Press, Cambridge, Boca Raton, Fla., 2010.

[6] G. Knothe, J.H. Van Gerpen, J. Krahl, K. (Firm), The biodiesel handbook, in, AOCS Press, Champaign, Ill., 2005, pp. ix, 302 p. ill. 324 cm.

[7] K. Sangwal, Additives and crystallization processes : from fundamentals to applications, Wiley, Chichester, 2007.

2. Crystals and Crystallisation Science

Summary: discusses the fundamentals of crystals and crystallography as well as the theoretical background on solubility, nucleation and crystal growth kinetics and morphology. It also provides a detailed theoretical review on the different methodologies to study nucleation kinetics

2.1. Introduction

This chapter covers the fundamentals to understanding solutions´ crystallisation as a comprehensive processes controlled by the interplay between: solubility, nucleation and crystal growth kinetics. It begins with a review of the concept of crystals and their definition from the structural, chemical and morphological point of view to follow with an overview of solubility and solutions ideality explained through the solid-liquid equilibrium activity model. The concept of supersaturation as driving force for both nucleation and crystal growth processes is also given, followed by an outline of the most common approaches to characterise nucleation and crystal growth kinetics.

2.2. Crystals and crystallography

A crystal is a solid characterised by exhibiting a periodic three dimensional pattern in the arrangement of the component atoms or molecules. They can be described by defining the item to be repeated (motif) and the way in which it is repeated. An array of representative points of the repeated motif is known as a lattice. The points which make up the array are called lattice points. As the environment of each lattice point is identical, it is only necessary to select a representative part of the lattice, known as the unit cell, to define how the pattern is repeated.

The unit cell can be described using the length of its sides and the angles between them or by three vectors a, b and c (referred to as the crystallographic axes) as shown in Fig. 2.1. These characteristics of the unit cell are referred to as the lattice parameters or unit cell constants [1].

The inter-relationship between a, b, c, α, β & γ gives rise to a total of 7 crystal systems as shown in Table 2.1.[1, 2]. An example of a unit cell for Ibuprofen is illustrated in Fig. 2.2.

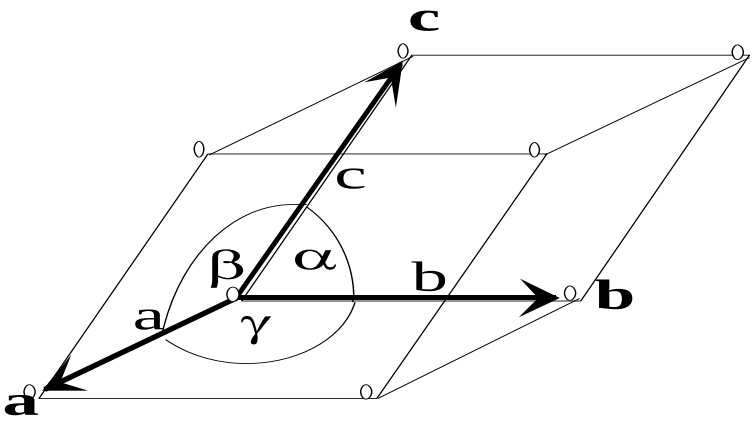

Figure 2.1 A three-dimensional unit cell, crystallographic axes a, b, c and the lattice parameters, a, b, c, α, β and γ

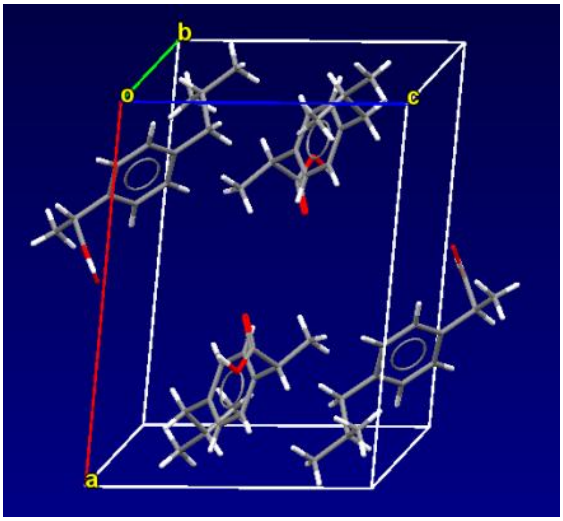

Figure 2.2 Examples of unit cell for Ibuprofen belonging to monoclinic P21/c; a 14.67, b 7.89, c 10.73, beta 99.36

Table 2.1 Seven crystal systems and examples

System	Axial lengths and angles	Example
Cubic	a=b=c, α=β=γ=90º	NaCl
Tetragonal	a=b≠c, α=β=γ=90º	TiO_2 , Urea
Orthorhombic	a≠b≠c, α=β=γ=90º	$(NH_4)2SO_4$
Rhombohedral or trigonal	a=b=c, α=β=γ≠90º	$CaCO_3$, α-Quartz
Hexagonal	a=b≠c, α=β=90º, γ=120º	Zn
Monoclinic	a≠b≠c, α =γ=90º≠β	Paraffin, sucrose
Triclinic	a≠b≠c, α≠β≠γ≠90º	$CuSO_4$ 5(H_2O)

To uniquely establish a crystal structure, the description of the atoms that make up the motif is also required. The location of an atom within the unit cell is defined by fractional coordinates using the crystallographic axes as coordinate systems. For instance an atom located at the body centre of a unit cell has fractional coordinates ½, ½, ½. It is half way along a, half way along b, and half way along c.

2.2.1. Crystal symmetry

It is possible to define the seven crystals systems in terms of the symmetry they possess. Likewise symmetry can be defined in terms of macroscopic symmetry elements such as rotation axes, mirror planes, inversion centres and rotation inversion axes. To describe all the symmetry elements that an object possesses a mathematical group known as a point group is used. For a crystal structure the symmetry elements of a point group are associated with every lattice point. The number of possible combinations of symmetry elements is limited by the fact that they must be compatible with the translational symmetry of the crystal lattice which restricts the crystallographic point groups to 32.

The unit cell symmetry is reflected in the arrangement of atoms in the crystal structure and in the physical and chemical properties of the crystal. Properties such as crystal growth rates, crystal shape, mechanical properties and surface chemistry are evidences of a given symmetry.

To fully describe the symmetry of a crystal structure is necessary to combine the 32 point groups with the 14 Bravais lattices through what is known as the space groups, all of which results in further types of symmetry elements [2].

Apart from the macroscopic symmetry elements crystals also have symmetry elements associated with the arrangements of atoms in the crystal structure. These are known as microscopic elements and include glide planes and screw axes [2].

2.2.2. Crystal geometry

As properties of crystals as well as properties and behaviour of crystalline surface change with direction it is always necessary to specify both planes and direction in crystalline structures. Crystal growth, dissolution rates, adsorption behaviour and hydrophobicity are some examples of the properties affected by direction.

Crystallographic directions can be defined by establishing the coordinates of a given point in a coordinates system whose origin is the origin of a unit cell. By convention the smallest integer coordinates are used to specify the direction which is enclosed in brackets. To specify any equivalent symmetrical direction a different notation is used. For example <110> represents not only the [110] but any of the following: $[\bar{1}10], [101], [\bar{1}01], [011]$ and $[0\bar{1}1]$ Fig. 2.3.

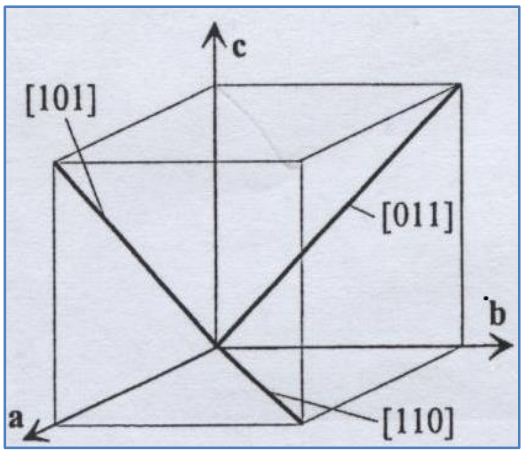

Figure 2.3 Example of equivalent symmetrical directions

Crystallographic planes are defined using the Miller indices defined as the reciprocals of the fractional intercepts which the plane makes with the crystallographic axes. When a plane is parallel to a given coordinate plane is consider to have an intercept of ∞ to the corresponding coordinate plane axes and therefore a Miller index of 0 is assigned to each of these axes. Examples of crystallographic planes are shown and Fig. 2.4.

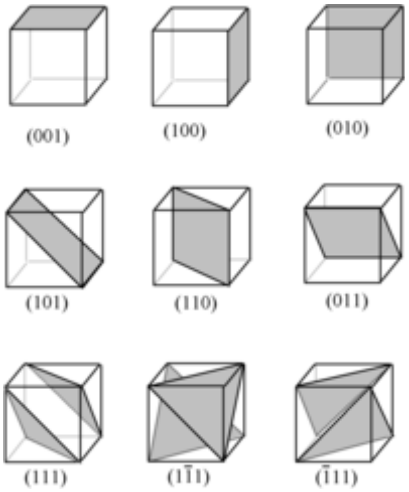

Figure 2.4 Example of Miller indices assigned to different planes

2.2.3. Crystal chemistry and polymorphs

Crystal chemistry relates to the influence that forces between molecules or particles and their size, shape, flexibility and rotational capability affect crystal structure. The nature of bonding in any solid is of considerable importance since it influences, either directly or indirectly, a wide range of properties, notably melting point and mechanical properties. Most organic solids are molecular in nature. While the atoms within a molecule are held together by strong covalent bonds, the molecules are saturated and only weak intermolecular forces exist between molecules.

Three factors are of particular importance in assessing the influence of intermolecular bonding on the properties of organic solids: the strength of the interaction, the distance over which the interaction exerts an influence and the extent to which the bonding is directional. Table 2.2. summarizes the main types of intermolecular bonding in organic solids.

Table 2.2 Typical bonding types in organic crystals

Type	Occurrence	Strength	Range
van der Waals	All atoms and molecules	Weak (1 - 10 kJ/mol)	short
Dipole-dipole	Between polar molecules only	Weak (3 - 4 kJ/mol)	long
Hydrogen bonding	Molecules containing O, N or F and a hydrogen bonded to one of these electronegative atoms	Strong (10 – 40 kJ/mol)	short
Ionic	Monatomic and molecular ions	Strong (10 – 50 kJ/mol)	short

In general organic solids conformed by large molecules are held together by relatively weak forces such as the Van der Waals. The relative strength of these interactions can also influence the crystal structure because this type of bonding do not exhibit directionality and therefore molecules maximise bond strength by minimising distance. Thus structures of molecular crystals will be determined by the ability of the molecules to pack closely together.

Polymorphism is defined as the existence of a compound in at least two different crystal structures. This is important because crystal structure can determine chemical or physical properties of a solid substance. Polymorphs can for instance have different melting points, solubility, optical properties etc.

2.2.4. Nature of crystal surfaces

Crystals grown from solution typically exhibit regular, planar facets. Although appearing flat, these crystalline surfaces are rarely so at the molecular level. The various features which make up the nanoscale surface topography of crystal face are closely related to the mechanisms by which crystals grow. Fig. 2.5 is a schematic representation of crystal surface in which the molecules, or growth units, are represented by cubes. The main attributes illustrated by this figure are (a) steps; (b) the terraces between them; (c) kink sites on the steps; and (d) terrace-adsorbed molecules. In this simplified model of a crystal surface, each cube represents a

molecule and can form a maximum of six bonds with surrounding cubes - one per face of the cube.

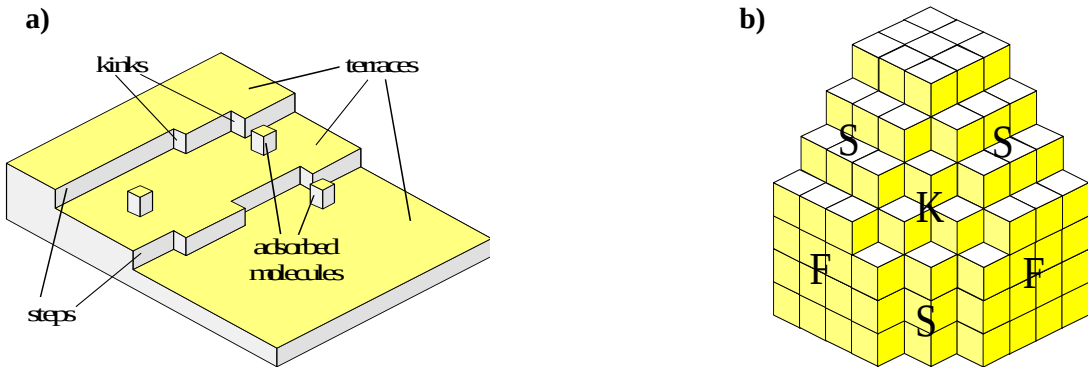

Figure 2.5 (a) Steps, terraces, adsorbed molecules and kink sites on a crystal surface; (b) Flat (F), stepped (S) and kink (K) faces [2]

This schematic crystal surface shows that at each featured site, an incoming molecule from the solution, would form a different number of bonds. A molecule adsorbed onto a terrace can form only one bond with the crystal surface. A molecule in contact with a step can form two bonds while a molecule incorporated at a kink site can form three bonds. A molecule placed in a kink site does not increase the surface area or, in other words, the surface energy of the crystal. When the molecules are assembled to form a crystal, three different types of crystal face can occur: flat or F faces, stepped or S faces and kink or K faces as shown in Fig. 1.5 b) [1, 2].

2.2.5. Crystal habit

The external shape of a crystal it is referred to as the crystal habit. The external form of a crystal is a polyhedron bounded by faces of various surface areas [3]. These polyhedrons are described using qualitative terms along with the Miller indices of the corresponding faces. Depending on the nature of the molecules and the way they will arrange within the crystal, each face will contain different functional groups, thus the crystal surface chemistry will depend strongly on the crystal habit [2].

The faceted crystals are bounded by the slowest growing faces and it follows that the crystal habit is determined by the relative growth rates of the possible faces for that

crystal structure [4, 5]. The growth rates at the same time will be influenced by solution´s supersaturation, solvents and the presence of impurities. One of the most relevant approaches to modify crystal morphology is the addition of impurities that can interact with a crystal surface through different mechanisms and slow the growth of a given face. An example of a plate-like crystal is given in Fig. 2.6.

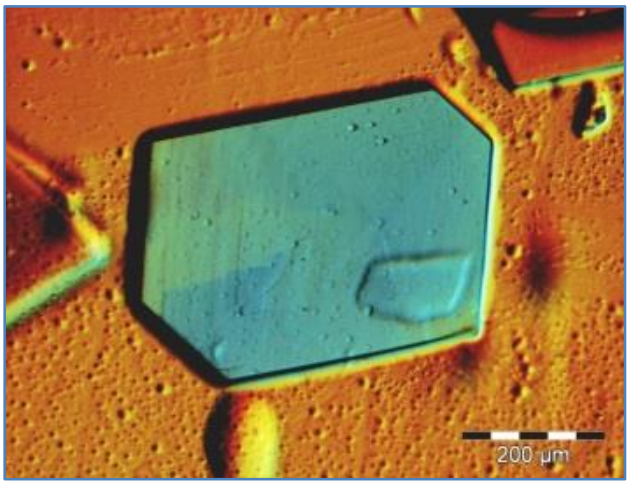

Figure 2.6 Examples of a plate-like crystal habit (methyl palmitate) [6]

2.3. Crystallisation in solutions

Crystallisation in solutions occurs when the initial homogeneous phase is subject to a change in its conditions leading to the formation of solid particles. Solid particles can be formed in a vapour, from a liquid melt or from liquid solutions [7].

In the formation of crystals three steps are involve:

1) Achievement of supersaturation
2) Nucleation: formation of crystal nuclei
3) Growth of Crystal nuclei to macroscopic size.

The driving potential for both nucleation and crystal growth is supersaturation, none of them can occur in a saturated or unsaturated solution [7]. Supersaturation may be generated by a number of methods: if the solubility increases with increasing the

temperature, for a given concentration reducing the temperature will generate supersaturation. If the solubility is relatively independent of temperature other methods can be used: evaporating a portion of the solvent, adding a third component to act with the solvent in order to decrease the solubility of the solvent at a given temperature. Similarly the third component can react with the solute forming an insoluble substance in a process called precipitation [7].

Crystallisation processes are all ruled by the equilibrium structure of the solid phase being formed; however in general is a non-equilibrium process which can be significantly affected by a number of factors such as crystallisation environment and nucleation and growth kinetics [1].

The analysis of crystallisation processes cannot be undertaken only from a thermodynamic point of view, but it also requires considering a kinetic approach that explain how crystals are formed and grow [8].

2.3.1. Solubility

A solution is a homogeneous mixture of two or more substances in a single phase. In liquid solutions, components are generally called solvents and solutes [1]. Fig. 2.7 describes the process of solution formation which occur in three distinct steps represented by ΔH_1, ΔH_2 and ΔH_3 and the overall enthalpy change is given by

$$\Delta H_{diss} = \Delta H_1 + \Delta H_2 + \Delta H_3 \tag{2.1}$$

For a solute to dissolve in a given solvent and form a homogeneous mixture, energy is required to break intermolecular forces between solvent (ΔH_1) and solute (ΔH_2) molecules. This energy (ΔH_3) is supplied when solute molecules are surrounded by solvent molecules through a process called solvation. Given that the enthalpy change (ΔH) in steps 1 and 2 are positive the dissolution would spontaneously proceed if the solute-solvent interactions are stronger i.e. $(\Delta H_{diss} < 0)$. However, if $(\Delta H_{diss} > 0)$ the process can still proceed but this would depend on whether or not the total

energy on dissolution is lowered. In this case spontaneous dissolution will be accompanied by an increase of entropy (S).

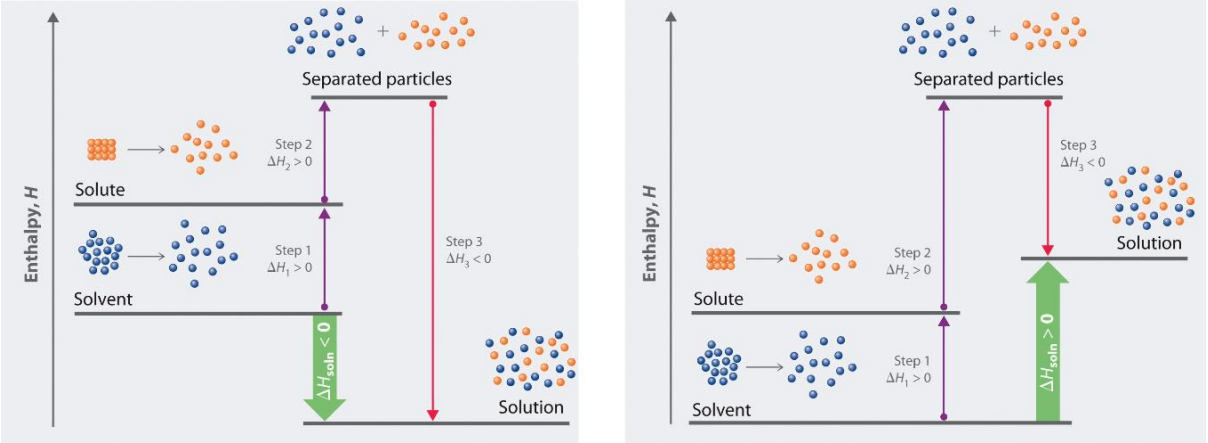

Figure 2.7 Enthalpy changes for the formation of a solution [9]

The amount of solute that a solvent can dissolve at certain temperature to form a saturated solution is called solute's solubility. In most cases the solubility of a solute in a solvent increases with temperature [1].

There is not a robust model that can accurately predict solubility and several approaches have been presented to predict solubility. The characteristic solubility curve of a solute in a given solvent is usually given as an exponential function in Temperature-Concentration coordinates [10].

2.3.1.1. Thermodynamic of phase equilibrium

If the properties of a closed system are maintained uniform (or is in internal equilibrium) during an irreversible process, then the system is characterised by two independent variables and a combined statement of the first and second law of thermodynamics is given by [11, 12]

$$dU = TdS - PdV \tag{2.2}$$

Where dU, dS and dV are, respectively small changes in energy, entropy and volume of the system when it undergoes a process and T and P are temperature and pressure.

If equation (2.2) is integrated to obtain the finite change in a thermodynamic property occurring from one state of equilibrium to another this results in expression (2.3)

$$\Delta U = U_2 - U_1 = \int_{S_1}^{S_2} TdS - \int_{V_1}^{V_2} PdV \tag{2.3}$$

In this case since U is a state function the result is independent of whether or not the system is maintained in internal equilibrium during the process.

Other extensive thermodynamic potentials can be obtained using different pairs of the four variable P, V, T and S as independent variables. For instance an expression for enthalpy change (dH) between two equilibrium states is given by

$$dH = TdS + VdP \tag{2.4}$$

Similarly, the change in Gibbs energy (dG) is given by

$$dG = -SdT + VdP \tag{2.5}$$

If the variation of G is restricted to occur at constant T and P then $dG_{T,P} \leq 0$, which means that in this case G tends towards a minimum in an irreversible process in a closed system and remains constant in a reversible process.

For a pure substance i a property known as the chemical potential (μ) is related to the temperature and pressure by the differential equation

$$d\mu_i = -s_i dT + v_i dP \tag{2.6}$$

Where s_i is the molar entropy, and $v_i$the molar volume

2.3.1.1.1. The concept of fugacity

The chemical potential for a pure ideal gas is given by

$$\left(\frac{\partial \mu_i}{\partial P}\right)_T = v_i \tag{2.7}$$

Using the ideal gas equation $v_i = \frac{RT}{P}$ and integrating at constant temperature, the chemical potential becomes a logarithmic function of the pressure ratio given by expression (2.8)

$$\mu_i - \mu_i^\circ = RT \ln \frac{P}{P^\circ} \tag{2.8}$$

Where the superscript ° refers to a standard state.

To generalise the application of this expression to any component in any system (solid, liquid or gas, pure or mixed, ideal or not) μ can be related to an auxiliary function easily identifiable with physical reality. The introduction of this function called fugacity (f) delivers

$$\mu_i - \mu_i^\circ = RT \ln \frac{f_i}{f_i^\circ} \tag{2.9}$$

This is so because for a component i in a mixture of ideal gases the fugacity is equal to its partial pressure $y_i P$ and since all systems approach ideal gas behaviour at very low pressures, the definition of fugacity is completed by limit $\frac{f_i}{y_i P} \to 1$ as $P \to 0$, with y_i the mole fraction of i [11, 12].

2.3.1.1.2. Equilibrium in a heterogeneous closed system

To define when two or more phases which are free to interact have reached a state of equilibrium it is necessary to introduce the equilibrium properties of the phases. The definition of chemical potential by Gibbs makes possible to determine the distribution of a component i between different phase 1, 2…π as at equilibrium the chemical potentials μ of component i in each phase are equal and therefore [11, 12].

$$\mu_i^1 = \mu_i^2 = \cdots = \mu_i^\pi \tag{2.10}$$

For phase 1 and 2 respectively equation (2.9) can be written as

$$\mu_i^1 - \mu_i^{\circ 1} = RT \ln \frac{f_i^1}{f_i^{\circ 1}} \tag{2.11}$$

$$\mu_i^2 - \mu_i^{\circ 2} = RT \ln \frac{f_i^2}{f_i^{\circ 2}} \tag{2.12}$$

Substituting equations (2.11) and (2.12) into equation (2.10) gives

$$\mu_i^{\circ 1} + RTln \frac{f_i^1}{f_i^{\circ 1}} = \mu_i^{\circ 2} + RTln \frac{f_i^2}{f_i^{\circ 2}} \tag{2.13}$$

If it is assumed that the standard state for the two phases are equal or $\mu_i^{\circ 1} = \mu_i^{\circ 2}$, $f_i^{\circ 1} = f_i^{\circ 2}$ then equation (2.13) becomes

$$f_i^1 = f_i^2 \tag{2.14}$$

This result meaning that the equilibrium conditions can also be stated in terms of fugacity.

2.3.1.1.3. Fugacity in liquid mixtures and the ideal solution

Fugacities in liquid solutions are expressed by defining an ideal liquid solution and describing its deviation from this ideal behaviour [11, 12].

The fugacity of compound i in a liquid solution can be related to the mole fraction (x_i) by

$$f_i^L = \Upsilon_i x_i f_i^\circ \tag{2.15}$$

Where γ_i is the activity coefficient and f_i° is the fugacity of i at the standard state.

In an ideal solution at constant temperature and pressure the fugacity of every compound can be taken as proportional to the mole fraction therefore

$$f_i^L = \varsigma_i x_i \tag{2.16}$$

Where ς_i is the proportionality constant dependent on temperature and pressure but independent of x_i. If $f_i^\circ = \varsigma_i$ then $\Upsilon_i = 1$.

2.3.1.1.4. Non ideal solution and activity

A non-ideal solution can be defined in terms of activity (a) since this parameter gives an indication of how active this compound is relative to its standard state, providing a measure of the difference between the compound´s chemical potential at the state of interest and that at its standard state [11, 12].

The activity of a compound i at an specific temperature, pressure and composition is given by the ratio of the fugacity of i to the fugacity of i in the standard state

$$a_i(T,P,x) = \frac{f_i(T,P,x)}{f_i(T,P^{\circ},x^{\circ})} \tag{2.17}$$

Thus from equation (2.15) the activity coefficient Υ_i is given by

$$\Upsilon_i = \frac{a_i}{x_i} \tag{2.18}$$

2.3.1.1.5. Excess functions

Excess functions are thermodynamic properties of solutions that are in excess of those of an ideal (dilute) solution at the same conditions of temperature, pressure and composition. For an ideal solution the excess function is zero [11, 12].

The molar excess Gibbs energy ($\bar{g}_i^E$) at constant T, P and composition is given by

$$\bar{g}_i^E = \bar{g}_{i(real)} - \bar{g}_{i(ideal)} \tag{2.19}$$

Where the subscript $real$ and $ideal$ refer a given solution property at equilibrium and at the ideal state.

Similarly, using the concept of fugacity for a compound i

$$\bar{g}_i^E = RT\left[\ln f_{i(real)} - \ln f_{i(ideal)}\right] \tag{2.20}$$

Thus inserting equation (2.16) into the $f_{i(ideal)}$ term

$$\bar{g}_i^E = RT\ln\left(\frac{f_i}{\varsigma_i x_i}\right) \tag{2.21}$$

As in an ideal solution $a = x_i$ when the standard fugacity $f_i^{\circ} = \varsigma_i$ then

$$a_i = \Upsilon_i x_i = \frac{f_i}{\varsigma_i} \tag{2.22}$$

And therefore equation (2.21) becomes

$$\bar{g}_i^E = RT \ln \Upsilon_i \tag{2.23}$$

Recalling that the total excess Gibbs free energy (ΔG^E) in a heterogeneous mixture is defined by

$$\Delta G^E = RT \sum_i x_i \ln \Upsilon_i \tag{2.24}$$

Excess functions for the entropy and enthalpy at constant pressure can be obtained from the partial derivatives of equation (2.24) delivering respectively [11, 13]

$$\Delta S^E = -\left(\frac{\partial \Delta G^E}{\partial T}\right)_P = -RT \sum_i x_i \frac{\partial \ln \Upsilon_i}{\partial T} - R \sum_i x_i \ln \Upsilon_i \tag{2.25}$$

$$\Delta H^E = \left(\frac{\frac{\partial \Delta G^E}{T}}{\partial T}\right)_P = -T^2 \left(\frac{\partial}{\partial T} \frac{\Delta G^E}{T}\right) \tag{2.26}$$

2.3.1.1.6. Regular and a-thermal solutions

Non-ideal solution can be classified in two limiting cases: regular or a-thermal solutions. For regular solutions $\Delta G^E \approx \Delta H^E$ which means that most of the deviation from ideality is due to excess in enthalpy of mixing [13]. Given that

$$\Delta G^E = \Delta H^E - T\Delta S^E \tag{2.27}$$

In a regular solution $\Delta S^E \approx 0$ and therefore from equation (2.25) it follow that

$$\ln \Upsilon_i \propto \frac{1}{T} \tag{2.28}$$

The second case is when $\Delta G^E \approx -T\Delta S^E$ in which case the deviation from ideality is mostly due to excess entropy of mixing or $\Delta H_E \approx 0$, therefore from equations (2.24) and (2.26)

$$\Delta H^E = -T^2 \left(\frac{\partial}{\partial T} R \sum_i x_i \ln \Upsilon_i \right) \tag{2.29}$$

In this case the $\ln \Upsilon_i$ are independent of T and thus these solutions are called a-thermal solutions. Solutions in which the component molecules are of nearly the same size but differ in intermolecular forces commonly behave like regular solutions. If the component molecules have very different sizes but do not differ significantly in their intermolecular forces the solution behaves like an a-thermal solution [13].

2.3.1.1.7. Solubility of solid in liquids

Solubility is a strong function of intermolecular forces between solvent and solute as in the absence of specific chemical effects, intermolecular forces between similar species conduce to lower endothermic heat of solution in comparison to those between dissimilar species. However, there are other factors that define whether a solid is soluble in a solvent or not. As solubility depends not only on the activity coefficient of the solute but also on the fugacity of the standard state to which that activity coefficient refers and on the fugacity of the pure solute [11, 12]

From equation (2.14) for a solute i the equation of equilibrium is

$$f_{i(pure\ solid)} = f_{i(solid\ in\ liquid\ solution)} \tag{2.30}$$

Or using equation (2.15)

$$f_{i(pure\ solid)} = \Upsilon_i x_i f_i^{\circ} \tag{2.31}$$

Therefore the solubility is given by

$$x_i = \frac{f_{i(pure\ solid)}}{\Upsilon_i f_i^{\circ}} \tag{2.32}$$

The standard state f_i° is arbitrary but must be at the same temperature as that of the solution. Usually this parameter is defined as the fugacity of pure, subcooled liquid at the temperature of the solution at a specified pressure.

As the two fugacities in equation (2.32) depend only on the properties of the solute ($f_{i(pure\ solid)} = f_i^{\circ S}$ and $f_i^{\circ} = f_i^{\circ L}$) then the molar Gibbs energy change for the solute going from solid (S) to liquid (L) is:

$$\Delta g_i = RTln\left(\frac{f_i^{\circ L}}{f_i^{\circ S}}\right) \tag{2.33}$$

And relating the Gibbs energy change to the corresponding enthalpy and entropy changes

$$\Delta H_i = \Delta H_{fus,i} + \int_{T_{f,i}}^{T} \Delta C_{p,i}\, dT \tag{2.34}$$

$$\Delta S_i = \Delta S_{fus,i} + \int_{T_{f,i}}^{T} \Delta C_{p,i}\, dT \tag{2.35}$$

Where the change in heat capacity $\Delta C_{p,i} = C_{p,i\,(liquid)} - C_{p,i\,(solid)}$, $T_{f,i}$ is the solute fusion temperature and ΔH_i, ΔS_i the enthalpy and entropy of fusion respectively.

At $T_{f,i}$ the entropy of fusion is related to the enthalpy of fusion by

$$\Delta S_{fus,i} = \frac{\Delta H_{fus,i}}{T_{f,i}} \tag{2.36}$$

Then using the relationship given by equation (2.27), substituting equations (2.34) to (2.36) in equation (2.33) and assuming that $\Delta C_{p,i}$ is constant over the temperature range, a general equation for the solid-liquid equilibrium is obtained

$$ln\left(\frac{f_i^{\circ L}}{f_i^{\circ S}}\right) = \frac{\Delta H_{fus,i}}{RT}\left[1 - \frac{T}{T_{f,i}}\right] - \frac{\Delta C_{p,i}}{R}\left(\frac{T_{f,i} - T}{T}\right) + \frac{\Delta C_{p,i}}{R} ln\frac{T_{f,i}}{T} \tag{2.37}$$

Recalling that at equilibrium $f_i^L = f_i^S$and that fugacity and activity are related by equation (2.22) then

$$\Upsilon_i^L x_i f_i^{\circ L} = \Upsilon_i^S z_i f_i^{\circ S} \tag{2.38}$$

Where Υ_i^L and Υ_i^S are the activity coefficients of component i in liquid and solid phases and x_i and z_i are the mole fractions of component i in liquid and solid phases. T is the saturation temperature corresponding to a solution concentration x_i.

Replacing equation (2.38) in (2.37) and re-arranging delivers

$$ln\left(\frac{\Upsilon_i^L x_i}{\Upsilon_i^S z_i}\right) = \frac{\Delta H_{fus,i}}{RT}\left[\frac{T}{T_{f,i}} - 1\right] + \frac{\Delta C_{p,i}}{R}\left(\frac{T_{f,i} - T}{T}\right) - \frac{\Delta C_{p,i}}{R} ln\frac{T_{f,i}}{T} \tag{2.39}$$

For an ideal solution of a single solid solute ($\Upsilon_i^L = 1$, Υ_i^S=1 and $z_i = 1$) equation (2.39) becomes

$$ln(x_i) = \frac{\Delta H_{fus,i}}{RT}\left[\frac{T}{T_{f,i}} - 1\right] + \frac{\Delta C_{p,i}}{R}\left(\frac{T_{f,i} - T}{T}\right) - \frac{\Delta C_{p,i}}{R} ln \frac{T_{f,i}}{T} \quad (2.40)$$

If it assumed that the change on $\Delta C_{p,i}$ is negligible over the range of temperature then a simplified model for the ideal solubility is obtained

$$ln(x_i) = -\frac{\Delta H_{fus,i}}{R}\left[\frac{1}{T} - \frac{1}{T_{f,i}}\right] \quad (2.41)$$

As $\Delta S_f = \frac{\Delta H_f}{T_f}$ equation (2.41) can be re-written in the form of the van´t Hoff model

$$ln(x_i) = -\frac{\Delta H_{fus}}{RT} + \frac{\Delta S_{fus}}{R} \quad (2.42)$$

In a non-ideal solutions the deviation from ideality can be accounted for on the right side of the van't Hoff expression rather than by means of activity on the left hand side and therefore the solubility could also be expressed as

$$ln(x_i) = -\frac{\Delta H_{diss}}{RT} + \frac{\Delta S_{diss}}{R} \quad (2.43)$$

Expression (2.43) shows that if the solubility (from observed experimental data) of a "single solute" solution is plotted in the form $ln\, x$ *vs* $1/T$, then from the slope and intercept of this line the enthalpy and entropy of dissolution "at saturation" can be obtained. As enthalpy depends on the solution composition, in this case ΔH_{diss} will be the differential heat of solution at saturation i.e the enthalpy change on dissolving a mole of a substance in a mole of "saturated solution".

2.3.2. Supersaturation and metastable zone width (MSZW)

2.3.2.1. Supersaturation

A solution that is in thermodynamic equilibrium with the solid phase of its solute at a given temperature is a saturated solution, and a solution containing more dissolved solute than that given by the equilibrium saturation value is said to be supersaturated [14].

The extent to which a solution exceeds equilibrium solubility can be expressed either by the concentration difference (ΔC), the supersaturation ratio (S) or the relative supersaturation (σ) respectively as given below

$$\Delta C = C - C_e \tag{2.44}$$

$$S = \frac{C}{C_e} \tag{2.45}$$

$$\sigma = \frac{C - C_e}{C_e} = S - 1 \tag{2.46}$$

where C is the solution concentration and C_e is the equilibrium concentration.

In terms of the change in solution temperature or supercooling, is given by

$$\Delta T = T_e - T \tag{2.47}$$

Where T is the temperature of the solution and T_e The saturation temperature Supercooling and supersaturation can be related by equation (2.48)

$$\Delta C = \left(\frac{dC_e}{dT}\right)\Delta T \tag{2.48}$$

Similarly, in terms of the chemical potential supersaturation is given by [1]

$$\Delta\mu = \mu_{solution} - \mu_{solid} \tag{2.49}$$

As chemical potential can be defined in terms of standard potential μ^0 and the activity a

$$\mu = \mu^{\circ} + RTln\, a \tag{2.50}$$

Thus supersaturation ratio S can be related to the chemical potential μ by

$$\frac{\Delta\mu}{RT} = ln\left(\frac{a}{a_e}\right) = ln\, S \tag{2.51}$$

Or

$$S = e^{\frac{\Delta\mu}{RT}} \tag{2.52}$$

Where a_e is the activity of the saturated solution

2.3.2.2. Metastable zone width (MSZW)

Regardless of the mechanism by which crystals are formed, a supersaturated solution can remain metastable until a critical level of supersaturation corresponding to the MSZW, is reached. The MSZW defines the kinetic limit of metastability and provides a useful indication of the ease with which crystallisation can occur.

In order to describe the conditions under which spontaneous nucleation would or would not occur, the terms *labile* and *metastable* zones need to be introduced. These definitions can be represented by means of a solubility – supersolubility diagram as in Fig. 2.8.

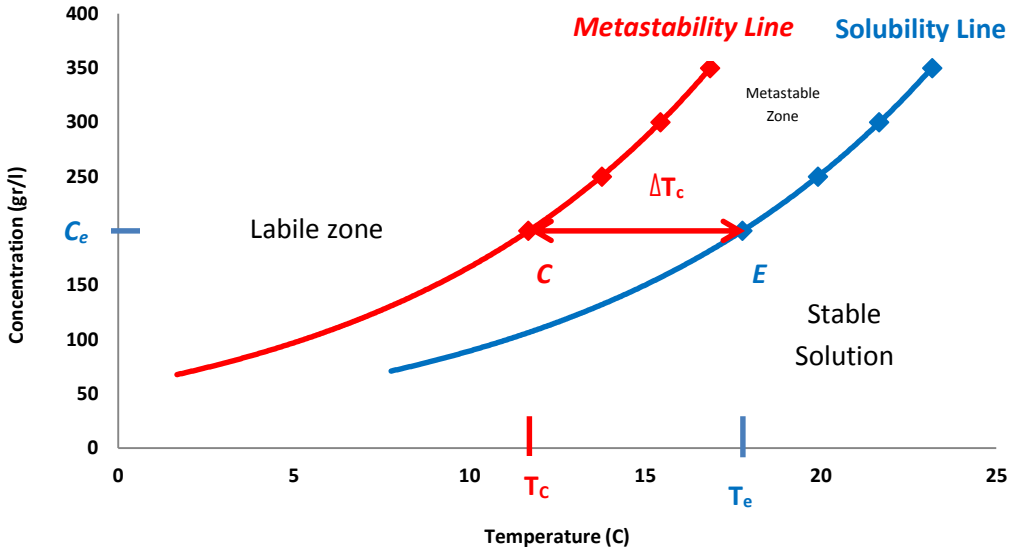

Figure 2.8 Solubility-Supersolubility diagram for a solution of a single component solute [14]

For C, T values below the solubility line the solution is stable, for C, T values above this line, it is metastable and can remain stable without precipitation for a long period of time. While the solubility line is fixed by thermodynamics the metastability line, is defined by a combination of thermodynamics and the process kinetics.

The value of this limit will greatly depend on the conditions that are established on the particular setup for its measuring and therefore will not be unique. The metastability line can be anywhere above the solubility curve depending on the nature of the nucleation and crystal growth processes. These, at the same time are influenced by a number of crystallisation environmental parameters such as the equilibrium temperature (T_e), cooling rate (q), solution agitation, presence of impurities and solvents among others [15, 16].

2.3.3. Nucleation

Nucleation refers to the birth of very small bodies of a new phase within a supersaturated homogeneous existing phase [17] and it is the first step of a crystallisation process. The control of a nucleation process is crucial in order to control the final crystal properties such as: number, size, polymorphism or crystal form among others [18]. A faster nucleation process will lead to the formation of many crystals of similar size.

Nucleation can take place either by a mononuclear or polynuclear nucleation mechanism [8]. The polynuclear mechanism occurs under conditions that favour the formation of statistically many nuclei and is often expressed in two different ways known as instantaneous nucleation IN and progressive nucleation PN. Whilst in PN new crystal nuclei are continuously formed in the presence of the already growing ones [8, 19], in the case of IN all nuclei emerge at once at the beginning of the crystallisation process to subsequently grow and develop into crystals [8, 20].

As in the case of IN all nuclei are formed simultaneously, at a specific time, the solution will contain a fixed number of crystallites of the same size, assuming they all grow at the same rate [8, 20]. This kinetic pathway is often followed by heterogeneous nucleation (HEN) which is favoured when strongly nucleation active sites are provided, e.g., when impurity molecules and foreign particles are present in the solution.

In the case of PN, the nuclei are formed during an extended period of time. Crystal nucleation and growth then occur simultaneously and the solution contains crystals of various sizes at any given point in time [8, 19]. Homogeneous nucleation (HON) as well as secondary nucleation and HEN on relatively weak nucleation-active sites can manifest themselves by means of this type of transformation. A simple scheme summarizing this classification is presented below.

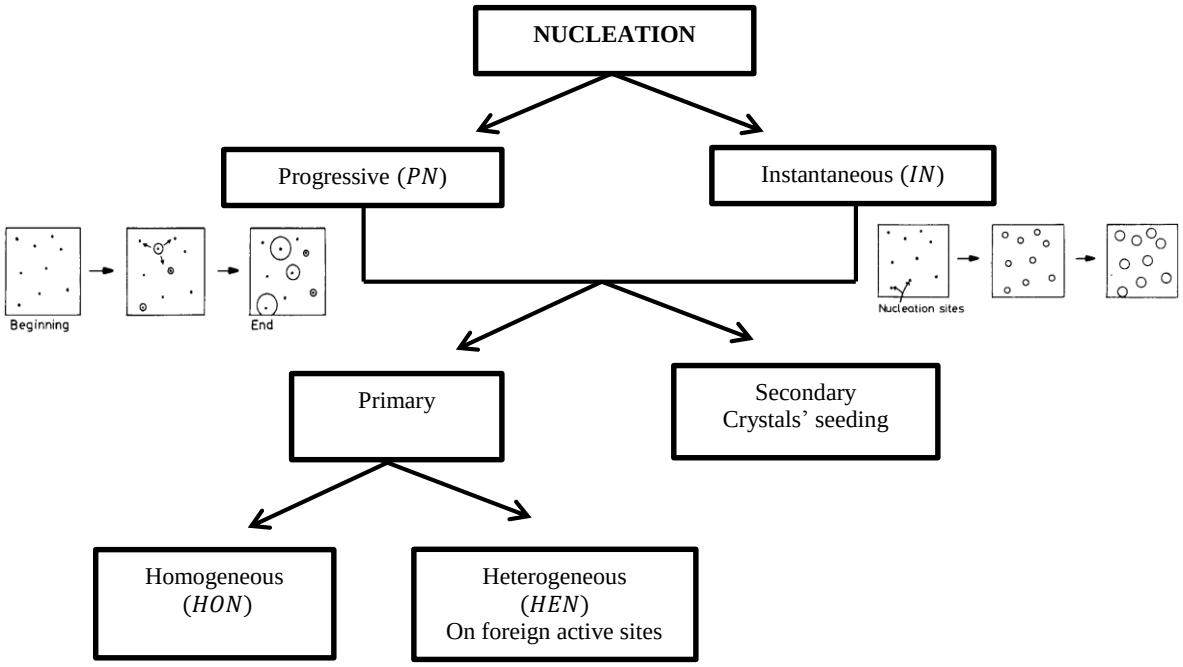

Figure 2.9 Schematic diagram highlighting the classification of the various mechanisms important in nucleation processes

Given that the sizes of critical nucleus typically range between 1 to 1000 there is still no accurate description of the nucleation process [21]. However, the most widely used nucleation model is given by what is called the classical nucleation theory (CNT). Although the classical nucleation theory was originally developed for vapour system involving condensation of vapour into liquid [1, 22], its application can be extended to solutions and melts.

However, the simplicity of this theory limits its application in certain cases. Several assumptions were made on the derivation of this model among which the most important are: the shape of molecular clusters is modelled as a spherical droplet with uniform internal density and sharp interface [22], nucleation occurs by addition of one growth unit or monomer at a time, the clusters formed are assumed to be stationary at their places without undergoing translation, vibration or even rotation.

Primary-homogenous nucleation can be explained through this theory.

2.3.3.1. Homogeneous Nucleation

In all instances, theories of primary nucleation stand that this process is a consequence of rapid local fluctuations on a molecular scale in a homogeneous phase that is in a state of metastable equilibrium [17]. Such primary nucleation is known as homogeneous (HON) or spontaneous [1, 14].

Due to the random motion of the particles in a supersaturated solution, particles can associate to form what is called a cluster, the clusters usually disappear quickly unless that enough particles associate to form an embryo where particles starts to form lattices and a new and separate phase is formed. If the supersaturation is long enough the embryo con grow further to form what is called a nucleus reaching a size where it is in thermodynamic equilibrium with the solution. A nucleus is defined as the smallest assemblage of particles that will not re-dissolve and can therefore grow to form a crystal [1, 8, 17].

A small crystal can be in equilibrium with a supersaturated solution, however this equilibrium is unstable, because if a large particle is also present in the solution, the smaller crystal will dissolve and the larger one will grow until the small crystal disappears (Ostwald ripening [17]).

2.3.3.1.1. Thermodynamics of nucleation

The thermodynamics of a nucleation process is better understood by looking at the free energy changes associated with nucleus formation. The change in free energy, assuming spherical nucleus are formed, is given by [1, 14].

$$\Delta G = 4\pi r^2 \gamma + \frac{4}{3}\pi r^3 \Delta G_v \tag{2.53}$$

Where ΔG is the overall excess of free energy associated with the formation of the crystal, γ is the interfacial tension between the crystal and its surrounding supersaturated fluid, ΔG_v free energy change per unit volume associated with the

phase change, $4\pi r^2\gamma$ is the surface contribution, and $\frac{4}{3}\pi r^3\Delta G_v$ is the volume contribution.

The volume effect on the free energy of a nucleus is associated with the decrease in free energy per molecule and has an r^3 dependence. The surface energy increase has a r^2 dependence and the sum of these two contribution yields the total free energy. Fig. 2.10 shows these two contributions to the free energy of a nucleus as a function of its radius. A nuclei smaller than the critical radius r_c will reduce its free energy by reducing its size therefore dissolution will be favoured. If a nuclei achieves a size greater than the critical radius r_c , grow will be favoured because this will lead to a decrease en free energy.

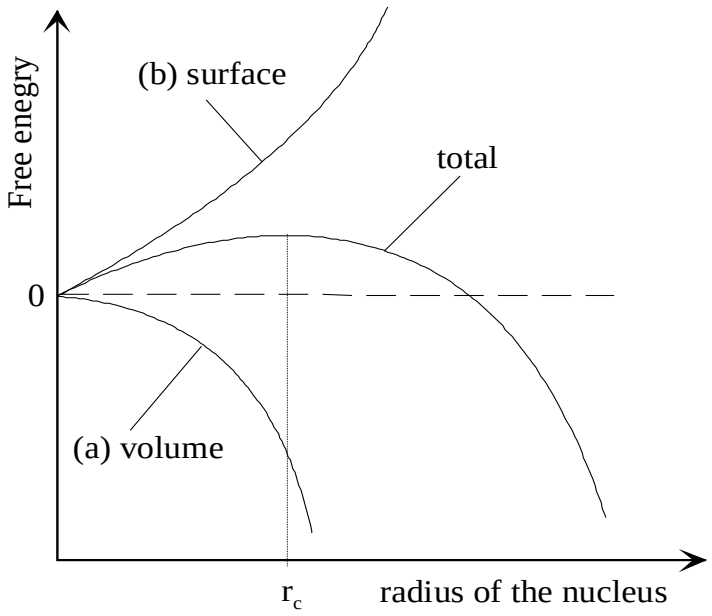

Figure 2.10 Free Energy Changes during nucleation

An expression for the critical radius of a spherical three dimensional nucleus can be obtained by maximizing equation (2.53), setting $\frac{d\Delta G}{dr} = 0$, which corresponds to the maximum value of free energy

$$\frac{d\Delta G}{dr} = 8\pi r\gamma + 4\pi r^2\Delta G_v = 0 \qquad (2.54)$$

Therefore

$$r_c = \frac{-2\gamma}{\Delta G_v} \tag{2.55}$$

Using equations (2.53) and (2.55) an expression can be also derived for critical free energy

$$\Delta G_{crit} = \frac{16\pi\gamma^3}{3(\Delta G_v)^2} = \frac{4\pi\gamma r_c^2}{3} \tag{2.56}$$

If the relationship between particle size and solubility, applied to solid-liquid systems is expressed by [1, 14]

$$ln\frac{C}{C_e} = \ln S = \frac{2\gamma v_0}{kTr} \tag{2.57}$$

an expression for ΔG_v is obtained

$$-\Delta G_v = \frac{2\gamma}{r} = \frac{kTln\,S}{v_0} \tag{2.58}$$

Where v_0 is the molecular volume.

Thus equation (2.56) can be also given in the form

$$\Delta G_{crit} = \frac{16\pi\gamma^3 {v_0}^2}{3(kTln\,S)^2} \tag{2.59}$$

Using equation (2.59) and expressing the rate of nucleation J in the form of an Arrhenius reaction rate equation

$$J = k_J\, exp\left(-\frac{\Delta G_{crit}}{kT}\right) \tag{2.60}$$

The nucleation rate e.g.the number of nuclei formed by unit time by unit volume can be expressed as [14]

$$J = k_J \, exp\left[-\frac{16\pi\gamma^3 v_0^2}{3k^3T^3(ln\,S)^2}\right] = k_J \, exp\left[\frac{-B}{(ln\,S)^2}\right] \quad (2.61)$$

Where k_J is the nucleation rate constant and k is the Boltzmann constant.

2.3.3.1.2. Kinetics of nucleation

Alternatively to the thermodynamic derivation of the nucleation rate model, the kinetics theory of nucleation approaches this process by describing how building units attach and detach to the clusters. According to the Szilard model of nucleation clusters grow and decay from a sequence of monomer attachment and detachment from the clusters [8]. Thus, the appearance of clusters is likely to results from a series of biomolecular reactions between monomers and n-mers (n=1,2,3…) as given by the model in equation (2.62)

$$[Z_1] + [Z_n] \rightleftharpoons [Z_{n+1}] \quad (2.62)$$

Where $[Z_1]$ and $[Z_n]$ are the chemical formula of the monomers and the n-sized clusters respectively.

This process will continue until equilibrium between these clusters is achieved.

The alternative expression for nucleation rate derived using the kinetic theory of nucleation is given by [8]

$$J = zf^*C^*_{nuc} \quad (2.63)$$

where the equilibrium nucleus concentration (C^*_{nuc}) is related to the concentration of nucleation sites (C_0) and the nucleation work W^* by

$$C^*_{nuc} = C_0 \, exp\left(-\frac{W^*}{kT}\right) \quad (2.64)$$

Combining equation (2.63) and (2.64) delivers

$$J = zf^{*}C_0\, exp\left(-\frac{W^{*}}{kT}\right) \tag{2.65}$$

where k_J in expression (2.61) is related to f^{*}, C_0 and the zeldovich factor z. The latter parameter reflects that not all clusters that reach the size of the critical nucleus will further growth into crystals.

In this expression the attachment frequency of monomers to the nucleus (f^{*}) is given by expression (2.66) and (2.67) for attachment of monomers controlled by volume diffusion or interface transfer respectively [8]

$$f^{*} = \xi 4\pi r^{*} D X_1 \tag{2.66}$$

$$f^{*} = \xi \omega^{*} d_0 A^{*} X_1 \tag{2.67}$$

where ξ is the sticking coefficient reflecting that not every building unit collision is an attachment, D the diffusion coefficient of colliding building units, X_1 the concentration of colliding building units, ω^{*} the transfer frequency of building units from adsorbed to integrated, d_0 the thickness of adsorbed surface layer and A^{*} the surface area of nucleus [8].

2.3.3.2. Heterogeneous Nucleation

Primary nucleation may also be initiated by suspended particles of foreign substances, and this mechanism is generally known as heterogeneous nucleation (HEN) [1, 14]. Foreign particles provide a surface for nucleation, decreasing the interfacial tensions to be overcome for nucleation to occur. Thus, the nucleation work decreases and nucleation rates drastically increase. The homogeneous nucleation interfacial tension γ is related to the effective heterogeneous interfacial tension γ_{eff} by

$$\gamma_{eff} = \psi\gamma \tag{2.68}$$

Where the activity factor ψ ranges between 0 and 1 and is associated to the contact angle between the nucleus and the heterogeneous particle.

2.3.3.3. Two steps nucleation

Given the increasing evidenced [18, 22, 23] that the classical nucleation model fails to explain the nucleation process in many cases, recent studies suggest nucleation follows a different mechanistic pathway to that accounted for through CNT.

This mechanistic pathway is generally called "two steps nucleation" and states that the nucleus appears inside pre-existing metastable clusters of several hundred nanometres in size, which consist of dense liquid and are suspended in the solution [18]. An alternative definition of this model, initially proposed for protein crystallisation, states that a cluster of molecules forms first followed by reorganization of that cluster into an order structure [22]. This metastable phase is likely to provide a suitable environment in which the necessary fluctuations for nucleation are more likely to occur [23]. A graphical description of this mechanism and comparison with the classical nucleation pathway is given in Fig. 2.11.

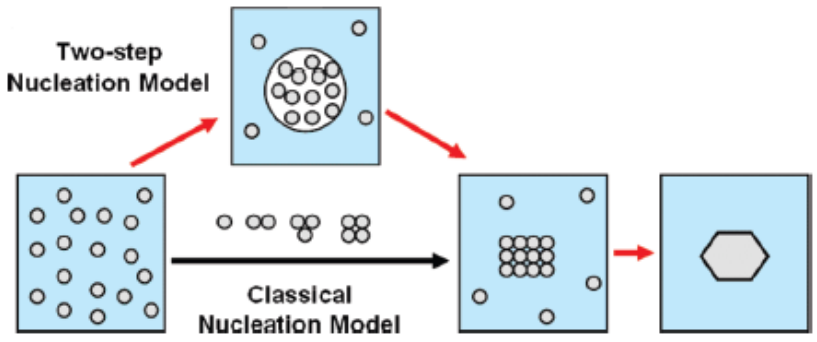

Figure 2.11 Different theoretical pathways for the nucleation process [22]

Studies on the two steps mechanism [24] have concluded that the main advantage of the formation of this transient intermediate phase is that the thermodynamic barrier

to nucleation is likely to either decrease or disappear. The transformation of clusters into crystal nucleus would follow a pathway in which two smaller energy barriers would have to be overcome rather than a large single one as is the case of CNT (Fig. 2.12). This conclusion is supported by [18] who suggested that the formation of a nuclei within a liquid-like droplet wound cause the nucleation barrier to disappear and the nucleation rate would only depends on the kinetics of cluster growth.

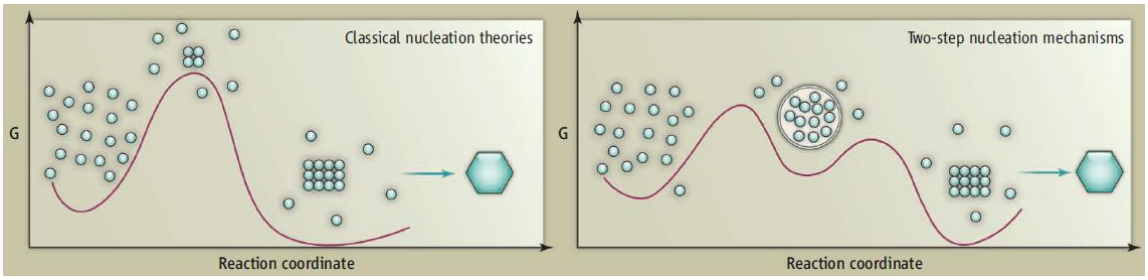

Figure 2.12 Free energy diagram for both CNT and two-step nucleation. While in CNT there is only one, large energy barrier, two smaller energy barriers need to be overcome for two-steps nucleation [24]

2.3.4. Methods to assess nucleation kinetics

The MSZW can be considered as a property of crystallisation for each system [25] and therefore its value can be related to the kinetics parameters of nucleation. A number of studies suggest the use of this concept, to determine and evaluate the kinetics of a given nucleation process.

The $MSZW$ is essentially the solution critical undercooling for crystallisation,(ΔT_c), expressed as the difference between the system saturation (or equilibrium) temperature (T_e) and the temperature (T_c) at which a detectable crystallisation commences: $\Delta T_c = T_e - T_c$.

Isothermal and polythermal crystallisation methodologies both use the concept of metastability to study crystallisation processes. The former generally makes use of expressions derived from classical nucleation theory to relate the induction time (τ) to the supersaturation ratio (S) in order to determine the nucleus interfacial tension and the nucleus size . To obtain crystallisation parameters, the polythermal

methodology generally uses expressions that predict the effect of the solution cooling rate q on the critical undercooling ΔT_c. Until recently, the interpretation of polythermal $\Delta T_c(q)$ data has been based on an essentially empirical methodology. In particular, researchers have mostly used Nyvlt's expression, derived from an empirical formula for the nucleation rate, which predicts a linear increase in $ln\,\Delta T_c$ with $ln\,q$ [26, 27]. However, whilst this relationship is most useful in terms of crystallisation process characterisation, this empirical approach has not contributed significantly to developing a mechanistic understanding of crystallisation processes. Later, Kubota [28] used the concept that for a given system, the extent of the measured $MSZW$ depends on the sensitivity of the method of detection employed to observe the first appearance of nuclei. He proposed a theoretical model, predicting also linearity between $ln\,\Delta T_c$ and $ln\,q$, which starts from the assumption that the measured $MSZW$ corresponds to the undercooling at which the number density of accumulated grown primary nuclei has reached a fixed (but unknown) value. Recently, employing the classical nucleation theory, Sangwal [15, 16, 29] obtained a $\Delta T_c(q)$ formula which provides physical insight into the parameters associated with it and which reveals linearity between $\frac{1}{(\Delta T_c)^2}$ and $\ln q$. More recently Kashchiev, Borissova, Hammond and Roberts ($KBHR$) developed an analytical approach [19, 20], based on that of Kolmogorov-Johnson-Mehl-Avrami ($KJMA$), which led to $\Delta T_c(q)$ expressions derived from the initial temporal evolution of either the fraction (α) of crystallised volume or the number (N) of nucleated crystallites. The expressions derived, when applied to experimental data, not only allow the determination of key parameters associated with both the nucleation and the growth processes, but also make it possible to gain an insight into the nucleation mechanism by differentiating between instantaneous nucleation (IN) and progressive nucleation (PN).

2.3.4.1. The polythermal method

In the polythermal method, the critical undercooling ΔT_c is measured as a function of the cooling rate q and the data collected are analysed by means of any of the approaches previously developed for the $\Delta T_c(q)$ dependence. In the case of the

Nyvlt approach [26, 27], the logarithms of q and ΔT_c are predicted to be linearly related. This $\Delta T_c(q)$ dependence was derived by assuming that the decrease in supersaturation is solely due to the depletion of solute by the nucleating crystallites. The effect of the subsequent growth of these crystallites on this decrease was not accounted for because Nyvlt's approach was developed for modelling the early stage of the crystallisation process, where the limit of metastability corresponds to the moment at which the first crystals are formed, where their surface areas can be considered to be negligibly small. At such a moment the solution concentration would hardly surpass the limit of metastability as a great amount of crystals would be formed leading to a rapid drop in supersaturation.[16, 26, 30-33]. In this particular case, through a material balance, the rate $\left(\frac{dC_e}{dT}\right)q$ of supersaturation change by cooling can be correlated to the nucleation rate as expressed through the following empirical formula:

$$J = k_j(\Delta C_{max})^{m_0} = \frac{dC_e}{dT}q \tag{2.69}$$

where J is the nucleation rate, $k_j$is an empirical parameter , m_0 is the order of nucleation, $\Delta C_{max} = \frac{dC_e}{dT}\Delta T_c$ and $\frac{dC_e}{dT}q$ represents the number of solute molecules precipitated per unit time and unit volume.

According to equation (2.69) $ln\,\Delta T_c$ depends linearly on $ln\,q$ and hence analysis of experimental $\Delta T_c(q)$ data in a $ln - ln$ correlation results in the determination of the two empirical parameters k_j and m_0.

Although widely used, the Nyvlt approach has received some criticism mainly due to its semi-empirical nature, as the two nucleation parameters used lack any direct physical significance and also the growth of the generated nuclei to detectable size is neglected [15, 19].

More recently, the $KBHR$ approach [19, 20] has led to alternative expressions that overcome some of the drawbacks of the previous approaches [15, 16, 26, 28, 29]. These expressions do not contain empirical parameters and allow PN-rulled

crystallisation to be distinguished from that mediated by IN, because while, in the former case the critical undercooling ΔT_c depends on both the nucleation and the growth rate of the crystallites, in the latter case, it is only controlled by the growth rate of the instantaneously nucleated crystallites provided their concentration C_o is independently known.

2.3.4.2. The isothermal method

Within the framework of classical theory of $3D$ nucleation, for the case of crystallisation by the polynuclear mechanism, an expression can be derived for the induction time τ as a function of the supersaturation $\Delta\mu$ which is the difference between the chemical potentials of the solute molecules in the solution and in the crystal. This expression is given by [3, 8]:

$$\tau = k_{md} e^{\frac{-\Delta\mu}{kT}} \left(1 - e^{\frac{-\Delta\mu}{kT}}\right)^{\frac{-md}{(1+md)}} exp\left[\frac{B'}{(1+md)\Delta\mu^2}\right] \tag{2.70}$$

Here, k_{md} is defined as

$$k_{md} = \left[\frac{(1+md)\alpha_{det}}{k_v z f_e^* C_s d_0^d f_{e,s}^{md}}\right]^{\frac{1}{(1+md)}} \tag{2.71}$$

where C_s is the concentration of sites in the system on which clusters of the new phase can form, f_e^* is the frequency of monomer attachment to the nucleus at $\Delta\mu = 0$, $f_{e,s}$ is the molecular attachment frequency per growth site at $\Delta\mu = 0$,and $d_0 \approx \left(\frac{6v_0}{\pi}\right)^{\frac{1}{3}}$ is the molecular diameter

The quantities B' and $\Delta\mu$ are given by:

$$B' = \frac{16\pi {v_0}^2 \gamma_{eff}^3}{3kT} \tag{2.72}$$

$$\Delta\mu = kT \ln S \tag{2.73}$$

where the supersaturation ratio S is defined by equation (2.45)

By combining equations (2.70) and (2.73), a relationship can be established for the dependence of τ on S:

$$\ln\left\{\tau[S(S-1)^{md}]^{\frac{1}{1+md}}\right\} = \ln k_{md} + \frac{B'}{(1+md)(kTln\,(S))^2} \tag{2.74}$$

Thus, a plot of $ln\left\{\tau[S(S-1)^{md}]^{\frac{1}{1+md}}\right\}$ vs. $\frac{1}{T^3(ln\,S)^2}$ is a straight line with a slope given by $\frac{16\pi v_0^2 \gamma_{eff}^3}{3(1+md)k^3}$

In this case, for a spherically shaped nucleus, r^* and i^*can be calculated from the equations:

$$r^* = \frac{2\gamma_{eff} v_0}{kTln\,S} \tag{2.75}$$

$$i^* = \frac{4\pi(r^*)^3}{3\,v_0} \tag{2.76}$$

2.3.5. Crystal Growth rates models and mechanism

The crystal growth from solution often involved two sequential processes which are the transport of growth units from bulk solution to the crystal-solution interface, followed by the incorporation of the growth units onto the crystal surface [34]. The former is referred as volume diffusion while the latter is known as surface diffusion. The rate of crystal growth will be determined by the slowest step between these two processes. The surface diffusion process can be described by the three growth mechanisms: birth and spread (B&S), BCF and rough interface growth (RIG) and is

closely related to the molecular nature of the crystal surface. Neither the diffusional nor the interfacial step will proceed unless the solution is supersaturated [1, 17].

2.3.5.1. The rough interface growth model

As illustrated by [35] (Fig. 2.13), if a crystal face is molecularly rough, there are many kinks sites on the surface through which the growth of the face will proceed.

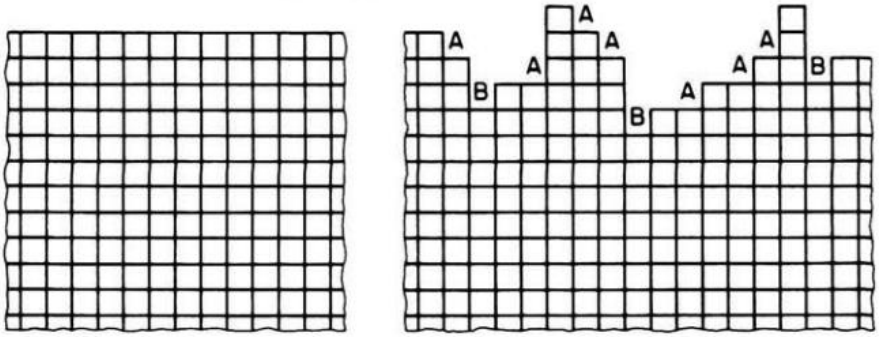

Figure 2.13 Graph comparing a crystal smooth surface (left) with a crystal rough surface (right) [35]

Any growth unit attached to the kinks will have greater chances to directly be incorporated to the surface and become a part of crystal [35]. The growth ($R\ (m/s)$) is then said to be continuous (or normal) and can be described by the Rough Interface Growth (RIG) model [36] given by equation (2.77)

$$R = k_G \sigma_s \tag{2.77}$$

where k_G is the growth rate constant and σ_s the solution´s relative supersaturation at the interface.

2.3.5.2. The B&S model

A second possibility is that the crystal face is molecularly smooth and therefore growth is then nucleation mediated. For faces molecularly smooth growth can

proceed only after the face roughens by nucleation of $2D$ clusters with edges having enough growth sites on them. The spreading of the $2D$ clusters is what fills a crystal monolayer and this leads to the growth of the crystal face (Fig 2.14). This mechanism is described by the Birth and Spread (B&S) model given by equation (2.78)

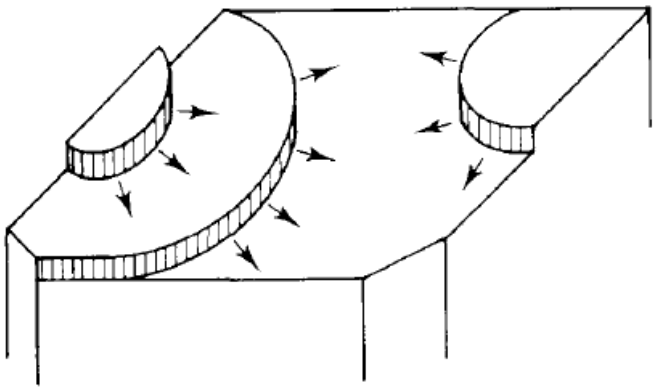

Figure 2.14 Schematic of B&S crystal growth process [37]

$$R = k_G {\sigma_s}^{5/6} exp\left(\frac{A_1}{\sigma_s}\right) \tag{2.78}$$

where A_1 is given by

$$A_1 = \frac{-\pi \gamma_{2D}^2}{3(kT)^2 \sigma_s} \tag{2.79}$$

In this expression $\gamma_{2D}$is the interfacial tension of the $2D$ nucleus

2.3.5.3. The BCF model

And finally, in the presence of points of emergence of screw dislocations the crystal face is stepped and exhibits spirals (or screw dislocations) (Fig. 2.15). In this case the growth rate is limited by the integration of a growth unit into the crystal at a step generated by lattice defects on the surface [37]. The dependence of the growth rate

on supersaturation can be described by the Burton-Cabrera-Frank (BCF) model [38] given by equation (2.80)

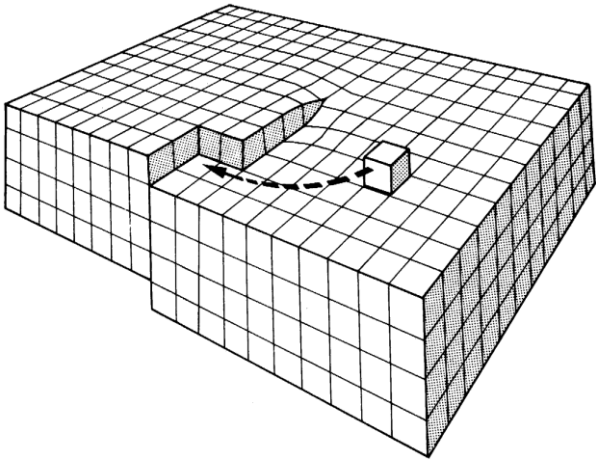

Figure 2.15 Squematic of growth mediated by screw dislocations [37]

$$R = k_G {\sigma_s}^2 tanh\left(\frac{A_2}{\sigma_s}\right) \tag{2.80}$$

For all of the three models $k_G \propto \beta$ where β is a kinetic coefficient that characterises the rate with which the growth units are incorporated into the lattice at the step. This rate is limited first of all, by de-solvation of the kinks and of the incorporating species and secondly, by the formation of new kinks at the surface of the crystal [38]

2.3.5.4. The power law

A general formula for the face of a crystal growing with time is given by

$$R = k_G(\sigma_s)^r \tag{2.81}$$

This law clearly described the RIG model and also represents the two limiting cases of the BCF equation ($r = 1\ or\ 2$). It can make a satisfactory approximation of the B&S model in a limited range of supersaturation [39].

The use of surface mechanistic models for the assessment of crystal growth should be treated with care as they only describe the kinetics at the crystal surface [40]. For instance studied the influence of volume diffusion on crystal growth, and found that this step can greatly influence the crystal growth rates, particular for crystallisation at high supersaturation. Similarly, the presence of impurities within a solution can greatly affect the mechanistic integration of growth units in different ways [1]. In some instances impurities can disrupt the formation of a growth layer which might result in retardation of crystal growth. The retardation of growth layer is known as "dead zone". In this case, for crystal growth to proceed the supersaturation level should be increased until it exceeds a given threshold limit.

2.4. Conclusions

This chapter provided the theoretical elements to understand the process of crystallisation. It initially presents a general description of crystals and crystallography followed by a detailed derivation of the activity model for the assessment of solubility.

A general review of nucleation kinetics is also presented through the concept outlined by the classical nucleation theory (CNT). Two methodologies for the assessment of nucleation kinetics are introduced: the polythermal and isothermal methods. A general description of the theoretical background used in the analysis of polythermal data is given. This is done with the aim of providing a platform to further present the detailed derivation of this model, as part of the development of a methodology to study nucleation kinetics presented in Chapter 5.

Surface growth kinetics models are also presented which described different mechanism of growth units integration. Similarly to the case of nucleation, this information serves as the theoretical background for the further derivation of a combined bulk/surface diffusion model for the assessment of crystal growth kinetics. This, model is part of a methodology presented in Chapter 8.

References

[1] J.W. Mullin, Crystallization, 4th ed., Butterworth-Heinemann, Oxford, 2001.

[2] K.J. Roberts, Advances in chemical engineering. PREN 5340M Course notes, School of process, environmental and materials engineering, University of Leeds, (2008).

[3] K. Sangwal, Additives and crystallization processes : from fundamentals to applications, Wiley, Chichester, 2007.

[4] P. Hartman, W.G. Perdok, On the relations between structures and morphology of crystals. II, Acta crystalligraphica 8, 49 (1955) 521-524.

[5] P. Hartman, W.G. Perdok, On the relations between structure and morphology of crystals. III, Acta crystalligraphica 8, 49 (1955) 525-529.

[6] H. Jiang, Molecular-Scale Effects of Additives on the Nucleation, Growth and Crystal Properties of Long-Chain Alkyl Methyl-Esters in: School of Process Environmental and Materials Engineering, University of Leeds, 2012.

[7] W.L. McCabe, J.C. Smith, P. Harriott, Unit operations of chemical engineering, 5th ed., McGraw-Hill, New York ; London, 1993.

[8] D. Kashchiev, Nucleation: basic theory with applications, Butterworth-Heinemann, Oxford, 2000.

[9] in: www.chemwiki.ucdavis.edu (Ed.), UCDAVIS, 2015.

[10] M. Broul, J. Nyvlt, O. Sohnel, Solubility in Inorganic Two-component Systems Elsevier 1981.

[11] J.M. Prausnitz, Molecular Thermodynamics of Fluid-Phase Equilibria, Prentice-Hall Inc., Englewood Cliffs N. J., 1969.

[12] R.E. Dickerson, Molecular thermodynamics, W. A. Benjamin, New York, 1969.

[13] D. Kondepudi, I. Prigogine, Modern Thermodynamics From Heat Engines to Dissipative Structures John Wiley & Sons Ltd. , West Sussex England, 1998.

[14] J.M. Coulson, J.F. Richardson, J.H. Harker, J.R. Backhurst, Coulson and Richardson's chemical engineering. Vol. 2, Particle technology and separation processes, 5th ed., Butterworth-Heinemann, Oxford, 2002.

[15] K. Sangwal, Novel approach to analyze Metastable Zone Width determined by the polythermal method: physical interpretation of various parameters, Crystal Growth and Design, 9 (2009) 942-950.

[16] K. Sangwal, A novel self-consistent Nyvlt-like equation for Metastable Zone Width determined by the polythermal method, Crystal Research and Technology, 44 (2009) 231-247.

[17] W.L. McCabe, J.C. Smith, P. Harriott, Unit operations of chemical engineering, 7th ed., McGraw-Hill, Boston ; London, 2005.

[18] P.G. Vekilov, The two-step mechanism of nucleation of crystals in solutions, Nanoscale, 2 (2010) 2346-2357.

[19] D. Kashchiev, A. Borissova, R.B. Hammond, K.J. Roberts, Effect of cooling rate on the critical undercooling for crystallization, Journal of Crystal Growth, 312 (2010) 698-704.

[20] D. Kashchiev, A. Borissova, R.B. Hammond, K.J. Roberts, Dependence of the Critical Undercooling for Crystallization on the Cooling Rate, J Phys Chem B, 114 (2010) 5441-5446.

[21] E.P. Wohlfarth, The Growth of Crystals from Liquids, North-Holland Publishing Company, Amsterdam, 1973.

[22] D. Erdemir, A.Y. Lee, A.S. Myerson, Nucleation of crystals from solution: classical and two-step model, Accounts of Chemical Research, 46 (2008) 621-629.

[23] H.K. Christenson, Two-step crystal nucleation via capillary condensation, Crystengcomm, 15 (2013) 2030-2039.

[24] A.S. Myerson, B.L. Trout, Nucleation from solution, Science, 341 (2013) 855-856.

[25] K.-J. Kim, A. Mersmann, Estimation of Metastable Zone Width in different nucleation processes, Chemical Engineering Science, (2001) 2315-2324.

[26] J. Nyvlt, Kinetics of nucleation in solutions Journal of Crystal Growth, 4 (1968) 377-383.

[27] J. Nyvlt, R. Rychly, J. Gottfried, J. Wurzelova, Metastable Zone Width of some aqueous solutions Journal of Crystal Growth, 6 (1970) 151-162.

[28] N. Kubota, A new interpretation of metastable zone widths measured for unseeded solutions, Journal of Crystal Growth, 310 (2008) 629-634.

[29] K. Sangwal, Recent developments in understanding of the metastable zone width of different solute-solvent systems Journal of Crystal Growth, 318 (2001) 103-109.

[30] H. Gurbuz, B. Ozdemir, Experimental determination of the Metastable Zone Width of borax decahydrate by ultrasonic velocity measurements Journal of Crystal Growth, 252 (2003) 343-349.

[31] N. Lyczko., F. Espitalier, O. Louisnard, J. Schwartzentruber, Effect of ultrasound on the induction time and the metastable zone widths of potassium sulphate Chem Eng J, 86 (2002) 233-241.

[32] O. Sahin, H. Dolas, H. Demir, Determination of nucleation kinetics of potassium tetraborate tetra hydrate Crystal Research and Technology, 42 (2007) 766-772.

[33] P. Sayan, J. Ulrich, Effect of various impurities on the metastable zone width of Boric Acid, Crystal Research and Technology, 36 (2001) 411-417.

[34] A.S. Myerson, Handbook of Industrial Crystallisation, Butterworth-Heinemann, Massachusetts, 2002.

[35] D. Elwell, H.J. Scheel, Crystal growth from high temperature solutions, Crystal Research and Technology, 11 (1975) K28-K29.

[36] J.D. Weeks, G.H. Gilmer, Dynamics of Crystal Growth, Advances in Chemical Physics 40 (1979) 157-227.

[37] R. Boistelle, J.P. Astier, Crystallization Mechanisms in Solution, Journal of Crystal Growth, 90 (1988) 14-30.

[38] W.K. Burton, N. Cabrera, F.C. Frank, The Growth of Crystals and the Equilibrium Structure of their Surfaces, Philos T R Soc A, (1951) 299-358

[39] J. Garside, Industrial Crystallization from Solution, Chemical Engineering Science, 40 (1985) 3-26.

[40] R. Janssen-van Rosmalen, P. Bennema, The influence of volume difussion on crystal growth, Journal of Crystal Growth, 29 (1975) 342-352.

3. Diesel and Biodiesel Fuels Crystallisation

Summary: A review of the literature related to the cold flow behaviour and crystallisation in diesel and biodiesel fuels is presented

3.1. Introduction

This chapter introduces the main concepts related to diesel and biodiesel fuels which are relevant to this research. An overview of the feedstocks, properties and technical issues of biodiesel fuels is presented, followed by a comparison with diesel fuel from the standpoint of the technical requirements for their use in diesel engines. Diesel and biodiesel cold flow behaviour is described in detail together with the approaches that are currently used to combat their poor low temperature properties.

As the main compounds in these fuels mixtures, a detailed review of the crystallisation of n-alkanes and methyl esters is also given addressing mainly morphological, crystallographic and kinetics studies.

3.2. Definition, structure and properties of diesel and biodiesel fuel

Originally biodiesels are defined as solutions of monoalkyl esters of long-chain fatty acids derived from renewable lipid feedstock such as vegetable oils or animal fats, for use in compression-ignition diesel engines [1]. However, recently debate about the concerns for the use of edible bio-sources in the production of biofuels, has led to increasing research to develop new production technologies. Biofuels obtained through these technologies belong to the second generation of biofuels and among others comprise the non-ester renewable diesel (NERD or bio-alkanes) [1].

The recent options available for the production of biodiesel, not only reveal a chemistry in transition but also a shift in process technology as the production of renewable fuels, require the conversion of carbohydrates (biomass) rather than hydrocarbons. This transition is illustrated in Figure (3.1) [1].

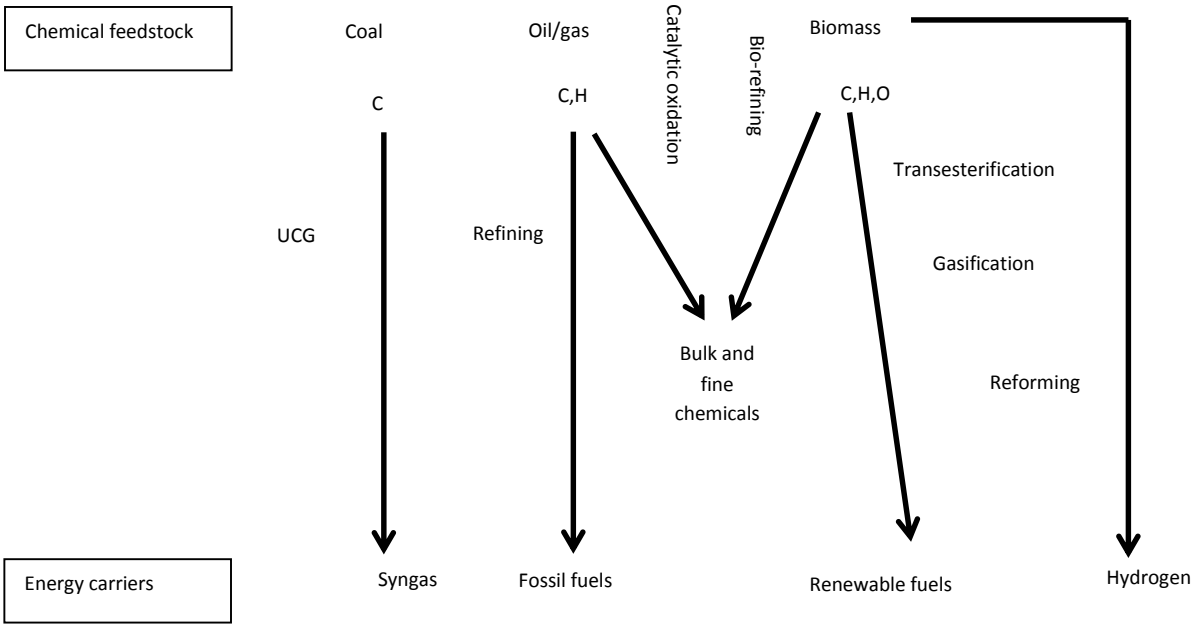

Figure 3.1 Chemistry transition of recent options available for the production of biodiesel

First generation of biodiesel fuels are produced through a catalytic alcoholysis transesterification from vegetable oils and animal fats. The process consists in separating the fatty acid esters, present in triglyceride by reacting of the latter with a primary alcohol, in the presence of a catalyst to obtain methyl esters and glycerine. The typical chemical reaction is illustrated below

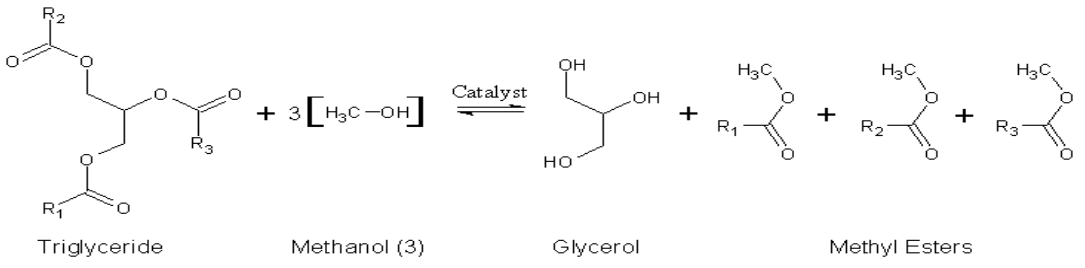

Figure 3.2 Chemical reaction for the production of biodiesel fuel from the transesterification of vegetable oils and animal fats

R_1, R_2, R_3 represent alkyl groups with a chain length ranging between C_{10} and C_{22} . Since natural oils are typically used in this process, the alkyl groups of the triglyceride are not necessarily the same [2]. Thus the product of this process is a

mixture of fatty acid methyl esters (FAMES) in which the main compounds are methyl esters of palmitic, stearic, oleic, lineolic and linoleic acids, however their proportion in the mixture will vary depending on the triglyceride feedstock. A typical fatty acid composition from the main first generation biodiesel feedstock is presented in Table 3.1.

Table 3.1 Typical fatty acid composition of the main biodiesel feedstock (wt%). The fatty acids are designated with a C followed with two numbers separated by a colon. The first number gives the number of carbon atoms in fatty acid molecule and the second the number of double bond present [3]

Oil/Fatty acid	Lauric C12:0	Myristic C14:0	Palmitic C16:0	Stearic C18:0	Oleic C18:1	Linoelic C18:2	Linolenic C18:3	Others
Rapeseed	-	-	4.2	2	60.8	20.6	9.2	3.2
Soybean	-	-	10.5	3.9	23.3	53	7.6	1.7
Palm	0.3	1.1	42.7	4.3	40.9	9.2	0.2	1.3
Sunflower	-	-	6.1	4.1	18.6	69	0.3	1.9
Olive	-	-	12.2	2.5	71.9	10.5	0.6	2.3
Peanut	0	0	11.2	3.2	45.5	31.7	0.4	8
Coconut	48.2	18.4	9.2	2.9	6.7	1.6	-	13
Tallow	0.1	2.3	23.1	15.4	45.8	3.5	0.6	9.2

A number of innovative processes, to convert biomass into biofuels are currently under developing. Second generation of biofuels are obtained from the conversion of forestry (branches, foliage, roots), agricultural residues (corn stover, straw) and waste stream. Bio-sources can be converted into biocrude through pyrolysis and thermochemical conversion. Biocrude is then turned into advanced biofuel using the currently refinery technology. Biomass to liquid (Btl or Synfuel) uses these bio-sources to produce biofuels through thermochemical pathways. The objective is to produce fuel components that are similar to those of current fossil-derived petrol (gasoline) and diesel fuels [4].

Advanced biodiesel can be produced via a number of routes such as: gasification of lignocellulosic materials or biogenic wastes which are then converted to Btl via the Fischer Tropsch process which converts a CH and O mixture into liquid hydrocarbons. In this process the feedstock is gasified in the first stage. The gas is then clean and adjusted to the ratio of the required hydrogen and carbon monoxide. The obtained balanced syngas undergoes a catalytic stage called a Fisher-Tropsch process in which carbon monoxide and hydrogen are converted into liquid

hydrocarbons. The catalysts used are generally based on iron and cobalt. The typical chemical reaction is shown below

$$(2n+1)H_2 + n(CO) \rightarrow C_nH_{2n+2} + nH_2O \quad (3.1)$$

Biodiesel can also be obtained from plant sugars via catalysis or biotechnology. The resulting biodiesel is a solution of hydrocarbons produced through a base catalysed condensation route. A scheme summarizing the processes available for the production of advanced biodiesel is presented in Fig. 3.3.

A third generation of biofuels will include those fuels obtained from algae oil than in the case of biodiesel will comprise a mixture of fatty acids and esters.

3.2.1. Comparison diesel and biodiesel fuel (first generation)

Biodiesels can be used in diesel engines both as pure and as a blend with petrodiesel and with little or no modification of the engine specifications, having the required properties to be considered as a good quality fuel with comparable properties to those of the petrodiesel [1]. Biodiesel/diesel blends are designated with a B followed by a number that refers to the percentage by volume of biodiesel present in the mixture. For instance B5 refers to a mixture in which 5% by volume is biodiesel fuel. A general characterisation that compares petrodiesel and first generation of biodiesel fuel is presented in Table 3.2.

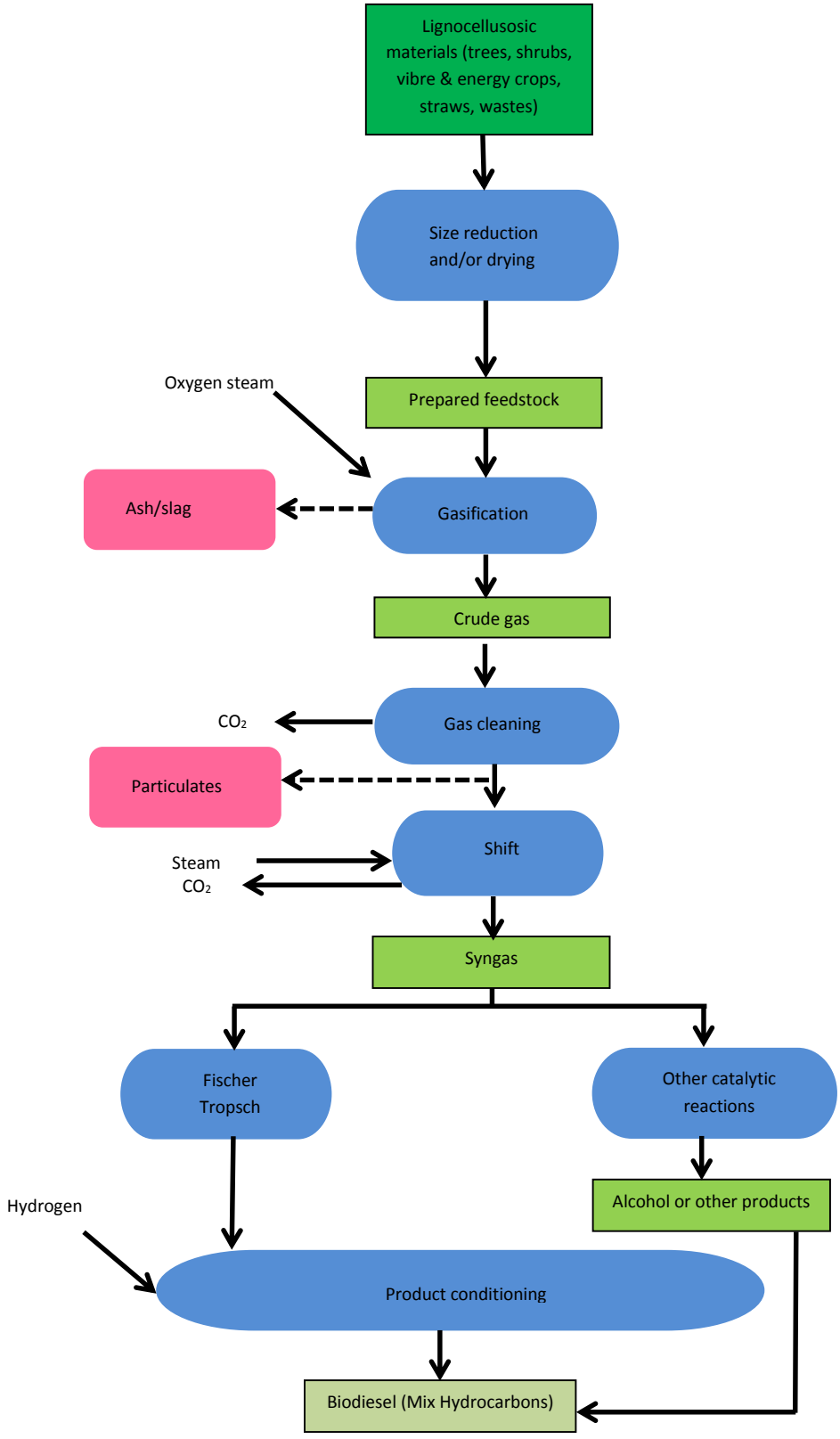

Figure 3.3 Scheme summarising the process to obtain biodiesel via catalysis or biotechnology [4]

Table 3.2 Comparative table of petrodiesel fuel and first generation biodiesel fuel

ATTRIBUTE	PETRODIESEL	BIODIESEL
HOW IS OBTAINED?	It is a hydrocarbon mixture obtained via the fractional distillation of crude oil between 200°C and 350°C at atmospheric pressure	Derived from vegetable oil triglyceride through the reaction with a primary alcohol (transesterification) to obtain methyl esters and glycerol. Normal conditions 65°C and a pressure of 20 psi
COMPOSITION	75% of petrodiesel is saturated hydrocarbons (primarily paraffins including n-, iso- and cycloparaffins) 25% aromatic hydrocarbons (naphthalenes and alkyl benzenes). The n-alkanes proportion and composition varies depending on the source of crude oil and refining conditions If petrodiesel is refined via a broad boiling distillate (BBD) n-alkanes range from C_{10} to C_{32} Using narrower band distillate (NBD) a smaller n-alkane distribution occurs from C_{15} to C_{27}	Consists of a range of methyl esters of a chain length between C_{10} and C_{22}, being the most common: Methyl Palmitate $C_{17}H_{34}O_2$ Methyl Stereate $C_{19}H_{38}O_2$ Methyl Oleate $C_{19}H_{36}O_2$ Methyl Linoleate $C_{19}H_{34}O_2$ Methyl Linoleanate $C_{19}H_{32}O_2$
SOURCES	Petroleum is typically found beneath the surface of the earth in accumulations known as fields	Sources of triglyceride include rapeseed oil, palm oil, sunflower oil, tallow, soybean oil, used kitchen oil, castor oil, jatropha oil and peanut oil

There are a number of technical and environmental advantages associated with the use of biodiesel fuel when compared with the traditional petrodiesel fuel. Important fuel properties include: lubricity, cetane number (CN), density, viscosity, heating value, sulphur, flash point, cloud point, distillation curve, carbon residue, ash and iodine value (IV). A comparison of these properties for petrodiesel and biodiesel (B100) fuel is given in Table 3.3.

Biodiesel increases engine and pumps life because it has excellent lubricating properties and has also higher cetane number than petrodiesel, indicating better ignition properties. One of the major advantages of using biodiesel fuel is the reductions of contaminants released to the atmosphere because biodiesels are free of sulphur or aromatics and results in substantial reduction of unburned hydrocarbons, carbon monoxide and particulate matter [5].

Table 3.3 Comparison of relevant technical diesel and biodiesel fuel properties [1]

Fuel property	Diesel	Biodiesel (B100)
Fuel standard	ASTM D 975	ASTM PS 121
Fuel composition	C_{10}-C_{21} Hydrocarbons	C_{12}-C_{22} FAME
Lower heating value, BTU/gal	131295	117093
Kin. Viscosity, @ 313 K	1.3-4.1	1.9-6.0
Specific gravity, kg/l @ 288K	0.85	0.88
Density, lb/gal @ 288K	7.079	7.328
Water, ppm by wt	161	500 max
Carbon, wt%	87	77
Hydrogen, wt%	13	12
Oxygen, by dif. Wt%	0	11
Sulphur, wt%	0.05 max	0.0-0.0024
Boiling point, K	461-616	455-616
Flash point, K	333-353	373-443
Cloud point, K	258-278	270-282
Pour point, K	238-258	258-283
Cetane number (CN)	40-55	48-65
Stoichiometric air/fuel ratio, wt/wt	15	13.8

In terms of nitrogen oxide emissions NO_x , biodiesel NO_x emissions are slightly greater than those of petrodiesel, however they can be reduced by modifications to the diesel engines or by using NO_x reduction technology, such us the use of a cerium-oxide catalyst that may have the potential to virtually eliminate NO_x emissions from both petrodiesel and biodiesel fuel [6].

Another positive feature of biodiesel is that the overall life-cycle production of wastewater from the production of biodiesel is 79% lower than that of the overall production from petrodiesel. Additionally the overall life-cycle production of hazardous solid wastes from biodiesels is 96% lower than overall production from petrodiesel [6]. In terms of the energy efficiency ratio, which represents the energy stored in the fuel compared with the total energy required to produce, manufacture transport and distribute the fuel. Biodiesels and petrodiesel have very similar energy efficiency ratios, however biodiesel is four times as efficient as petrodiesel in utilizing fossil energy [6].

With regard to biodegradability and toxicity biodiesel is far less dangerous than petrodiesel. Biodiesel fuel is not harmful to humans or the environment**.** In the event of a spillage biodiesel will degrade four times faster than petrodiesel fuel [6].

Unlike petrodiesel whose ignition temperature is about 56°C, biodiesels do not represent a danger when they are storage or shipped due to their higher flash point of about 126°C. What is more, tests have shown that the flash point of biodiesels blends increases as the percentage of biodiesel increases. However, due to the organic nature of biodiesel this is more susceptible to the growth of bacteria and mould than petrodiesel. Thus, in some cases it is necessary to add small quantities of biocides to store biodiesel, especially in warmer climates [6].

The energy content of biodiesels is about 10 to 12% lower than the petrodiesel (about 121,000 Btu compared to 135,000 Btu for number 2 diesel fuels), this is due to biodiesels oxygen content that is around 10% more than that of petrodiesel fuel. Higher oxygen content however results in more favourable emissions levels [6]. Generally speaking, although biodiesel offers a 7% average increase in combustion efficiency, the use of biodiesel results in about a 5% decrease in torque, power and fuel efficiency in diesel engines [6].

Biodiesel has some performance disadvantages such as material in-compatibility; filters, polypropylene and rubber materials are particularly vulnerable to B100. Although biodiesel is hydrophobic it can retain up to 20 times more water than regular diesel. This can create a favourable environment for biological attack on the fuel itself and also severe corrosion of the metal components of a fuel system [1].

Regardless evident biodiesel advantages, one of the major technical obstacles for the use of biodiesel is its cold-temperature performance as indicated by properties such as high cloud (CP), pour (PP) points and cold flow plugging point (CFPP) [7]. The wax that causes cold flow concerns mainly comes from saturated fatty acids, which are able to form highly regular crystalline structures easily. Thus the higher the proportion of saturated component in biodiesel solutions the higher the (CP), (PP) and (CFPP) [1].

Solutions of FAMEs have cloud (CP) and pour points (PP) that are 15-25 °C higher than those of diesel fuel [1]. Petrodiesel begins to cloud at about -7°C; this is the temperature at which paraffin wax crystals begins to form. Cloudy diesel fuel can clog fuel filters and cause problems in the performance of vehicle engines systems. If

the temperature decreases further, the diesel reaches the pour point, the temperature below which it will not pour. At this temperature diesel engine stops running. If the temperature decrease even further, to about -9,5°C diesel fuel reaches its gel point , when it becomes jelly [6].

Biodiesel reaches (CP) at the start of crystal formation of saturated components during cooling. (PP) occurs during further cooling below (CP) as a result of crystal growth and agglomeration involving not only saturated but also unsaturated components [1]. Although currently, there are well established additives to treat engines operability issues caused by traditional diesel fuel, these additives seem not to be very effective on biodiesel fuels as the formation of crystal in these solutions occurs at much higher temperatures. Additionally, low temperature properties are affected by fuels chemical composition which can influence crystal growth properties [1]. Some cold flow properties of selected vegetable oil and fat derived biodiesel are presented in Table 3.4.

Table 3.4 Low temperature properties of biodiesel fuels obtained from different biosources

Oil or fat	CP (K)	PP (K)	CFPP (K)
Linseed	273	264	
Olive	271	270	267
Palm	286	289	
Rapeseed	271	264	254-265
Soybean	273	271	266-271
Sunflower	275	270	271
Jatropha			270-273
Tallow	290	288	282

Several approaches to the low temperature problem of esters have been investigated including blending with conventional diesel fuel, winterization, additives, branched chain esters and bulky substituent in the chain [5, 8]. Numerous additives have been synthesized and it has been reported they have had the effect of lowering the PP and sometimes the CP [7]. Petrodiesel cold flow improvers (CFIs) decrease the pour point of B20 blend up to 18-20 K, but do not affect the cloud point. (CFIs) act by modifying crystal growth but do not inhibit crystal initiation. They do not have an influence on crystallisation onset nor on the total amount of crystals that form [7].

The main challenge currently is finding effective chemistries to treat the most difficult biodiesel types [1].

Other approaches have been suggested such as the use of fatty compounds derived materials with bulky moieties in the chain at additive level that will destroy the harmony of the crystallizing solid [7]. The use of branched alcohols, to obtain branched esters such as iso-propyl, isobutyl and 2-butyl instead of the methyl ester has also been suggested [9]. Branched esters have lower melting points, in the neat form these esters have shown a lower T_c (crystallization onset temperature) as determined by differential scanning calorimetry (DSC). For the iso-propyl ester of soybean oil by 7°-11 °C and for the 2-butyl ester soybean oil by 12-14 °C [9]. The CPs and PPs where also lowered. However it is well known that branched alcohols are more costly than the methanol and only isopropyl esters seems to be attractive in economic terms.

One of the best approaches to improve the cold-temperature flow properties of biodiesel is to modify the fatty acid composition of the raw material focusing in the key fatty acids limiting these cold-flow quality: palmitic (C16:0) and stearic (C18:0) acids [1].Winterization is probably the most promising approach in terms of reducing CP values, as the process consists on removing high melting point methyl esters from the biodiesel solution. This can be achieved by using different methods such as filtration of crystals after partial crystallisation of saturated compound. A number on unit process are employed commercially: dry, solvent and surfactant (detergent) fractionation [1]. Although winterisation leads to a decrease in cetane number (CN) it does not greatly compromise fuel quality [1].

3.2.2. Regulations and standards for the use of biodiesel fuels

In order to ensure that biodiesel complies with operability and environmental requirements some standards that contain both chemical and physical test quality have been issued. These quality specifications define what properties a biodiesel fuel must exhibit for use in a compression ignition engine.

In general these standards are issue by the American Society for Testing and Materials (ASTM). However in Europe the European Committee for Standardisation (CEN for its initials in French) has design some standards contained in the European Norm (EN). The ASTM covers standards for the production of Biodiesel B100 in the (ASTM D 6751). All commercial grade biodiesel has to comply with the (ASTM D 6751-08) specification if is going to be used in Diesel engines. US Biodiesel blend specification cover up to B5 in Diesel fuel (ASTM D 975-08a) and up to B20 (ASTM D 7467-08)) for use in on and off road diesel engine.

ASTM D 6751 standard has 14 standard methods to evaluate biodiesel properties of which ASTM D 2500 and ASTM D 7501 assess cold flow properties: cloud point (CP) and cold soak filtration (CSFT) respectively.

ASTM D 2500 consists in placing a small sample of fuel in a glass jar and cooling it at a constant cooling rate. The (CP) is determined visually by subjecting a sample to decreasing temperatures in a cloud point/pour point bath and checking the temperature at which any cloud is observed at the bottom of the jar. A typical set for the cloud point measurement is presented in Fig. 3.4.

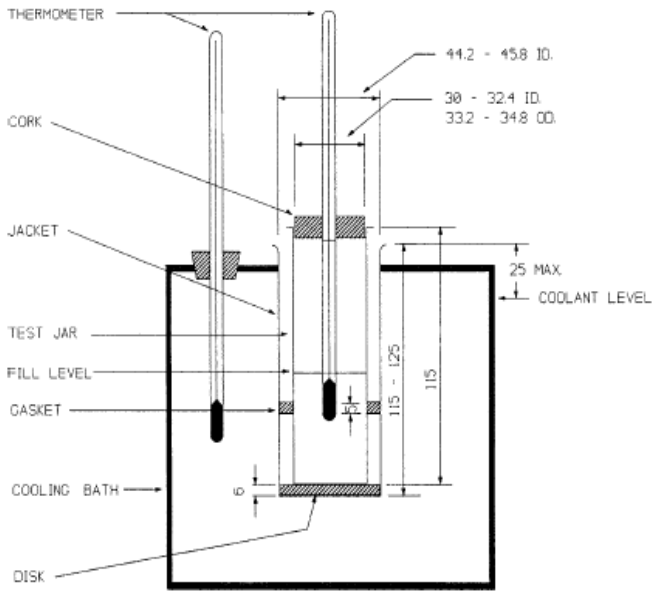

Figure 3.4 Typical apparatus set-up for the cloud point and the pour point tests

The CSFT recently received an official number ASTM D 7501-09. In this test the sample is chilled for a specified time and then allowed to warm to ambient temperature prior to filtering in a modified (ASTM D 6712) (Particulate Contamination in Middle Distillate Fuels by Laboratory Filtration) procedure. It measures the time in seconds it takes for a cold soak biodiesel to pass through two 0.7 µm filters and the amount of particulate matter (mg/L) collected on the filter. High filtration times indicate the potential for fuel filter plugging. The test might take up to 36 hours and is poorly reproducible and repeatable. There is no correlation between cloud point and CSFT. Failure in the CSFT can be caused by different variables such as: feedstock, incomplete glycerol removal or it may also indicate the fuel tested was previously subject to temperatures below the pour point.

Another test not included in ASTM D 6751 is the pour point (PP) ASTM D 97. It is very similar to test method D 2500.The sample is cooled at a specified rate and examined at intervals of 3°C for flow characteristics. At each test point, the sample inside the test jar is removed from the bath and tilted horizontally until a temperature is reached where the sample shows no movement. This temperature is recorded as the pour point [1] (See Fig. 3.4).

The biodiesel European Norm EN 14214 specify qualitative minimum standards for FAME as an automotive fuel for diesel engines. It addresses up to B5 blends and B100 and contains 26 quality parameters that are monitored by corresponding tests. In the European Union diesel containing up to 7% biodiesel is consider as diesel at all effects and is covered by normal diesel standard EN 590. Apart from the previously mentioned tests the European norm includes the cold filter plugging point CFPP test in EN 116 that has an equivalent in the ASTM D 6371-05.This parameter measures low-temperature operability limit. In general the CFPP is lower than the CP but higher than the PP. A sample is cooled under specified conditions and every 1 °C is drawn into a pipet under a controlled vacuum through a standardised wire mesh filter. The procedure is repeated for constant cooling rate until the wax crystals separated out of the solution is sufficient to stop or slow down the flow so that the time taken to fill the pipet exceeds 60 seconds or the fuel fails to return completely to the test jar before the fuel has cooled by a further 1 °C. The temperature at which the last filtration was commenced is recorded as the CFPP.

The ASTN D 4539-10 also assesses the filterability of diesel fuel through the low temperature flow test (LTFT). The temperature of a series of test specimens of fuel is lowered at a prescribed cooling rate. Commencing at a desired test temperature and at each 1°C interval thereafter, a separate specimen from the series is filtered through a 17-μm screen until a minimum LTFT pass temperature is obtained. The minimum LTFT pass temperature is the lowest temperature, expressed as a multiple of 1 °C, at which a test specimen can be filtered in 60 s or less.

3.3. Crystallisation of n-alkanes

The formation of wax out of petrodiesel solutions at low temperatures has been a traditional issue that limits vehicles operation. It is known that saturated paraffins crystallise at low temperatures forming crystals of large sizes that cause plugging of pipes, pumps and filters or that settles at the bottom of the fuel tank. To combat this problem crystals are generally modify to be small enough both less than about 0.01 mm prisms, to stay in suspension and less that 0.002 mm across to pass through the engine filters [10].

Crystallisation of n-alkanes, the main saturated components of petrodiesel fuel solutions, has been well studied. Previous work using single crystal and powder X-ray diffraction have characterised the solid-state properties for some of these compounds, suggesting they follow an overall scheme, in terms of the expected crystal structures as a function of the parity (n) of the number of carbon atoms within the molecule to be as follow: - triclinic, for n-alkanes with even carbon number $6 \leq n \leq 26$; - monoclinic, for $26 \leq n \leq 36$; and - orthorhombic for $n \geq 36$, and also for n odd $11 \leq n \leq 39$ [11].

Most single long-chain n-alkanes, generally grow from solutions as rhombic-shaped thin platelets with large and well-developed (001) faces together with much smaller (110) side faces. Polygonized growth spirals [12, 13] have been observed on the (001) faces when grown from n-alkane solutions (hexane, heptane) [14], in agreement with observations of wax crystals (see Fig. 3.5). This is consistent with n-alkane solvent molecules incorporating as impurities. Growth from more complex

solvents (cyclohexane) was found to result in no observable growth defects (spirals) [15] Although, these crystals are typically bounded by (110) faces some additional small faces can occur for orthorhombic and for monoclinic phases for growth near equilibrium and this often results in a crystal morphology with a more “hexagonal” habit [15].

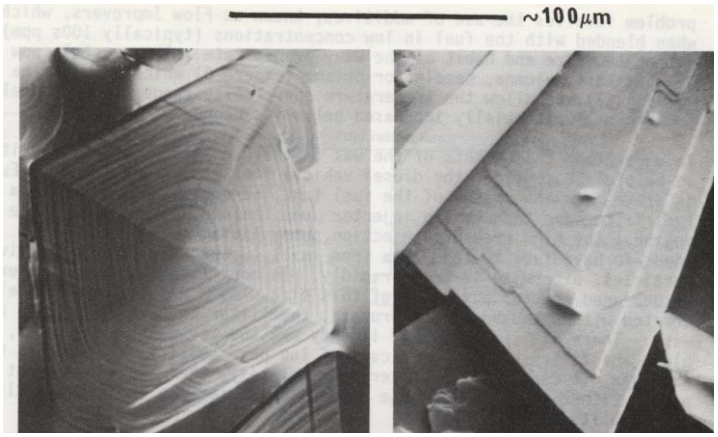

Figure 3.5 Wax crystals separating from diesel fuel: optical and scanning electron micrograph [10]

High molecular weight hydrocarbons can promote a more isotropic growth through co-crystallisation or lattice dislocation [16]. This is supported by the findings of Beiny et. al. [17] in which differences in crystal habits of n-dotriacontane n-$C_{32}H_{66}$ crystallised out of two different solvents were found. These differences were explained by the abilities with which the two solvents can adsorb on the growing crystal faces. The first solvent, n-heptane might be more easily incorporated than would be the second solvent, m-xylene in to the growing (110) faces and therefore create lattice defects from which growth originates. Furthermore n-heptane would also be expected to adsorb much more on the (001) face where methyl-methyl interactions of the n-heptane would be as strong as n-dotriacontane itself therefore inhibiting growth in the C direction resulting this in thinner plates.

N-alkane crystals show rapid growth on the AB plane and slow growth in the C direction. The most stable face is the (001) because the molecules in the AB plane have the strongest attachment energies (perpendicular to the n-alkane axes). These bonds result from the coordinated interactions of the many methylenes per n-alkane

molecule. Bonds in the C direction are relatively weak because they are mainly from the methyl-methyl interaction of adjacent molecules (see Fig. 3.6)

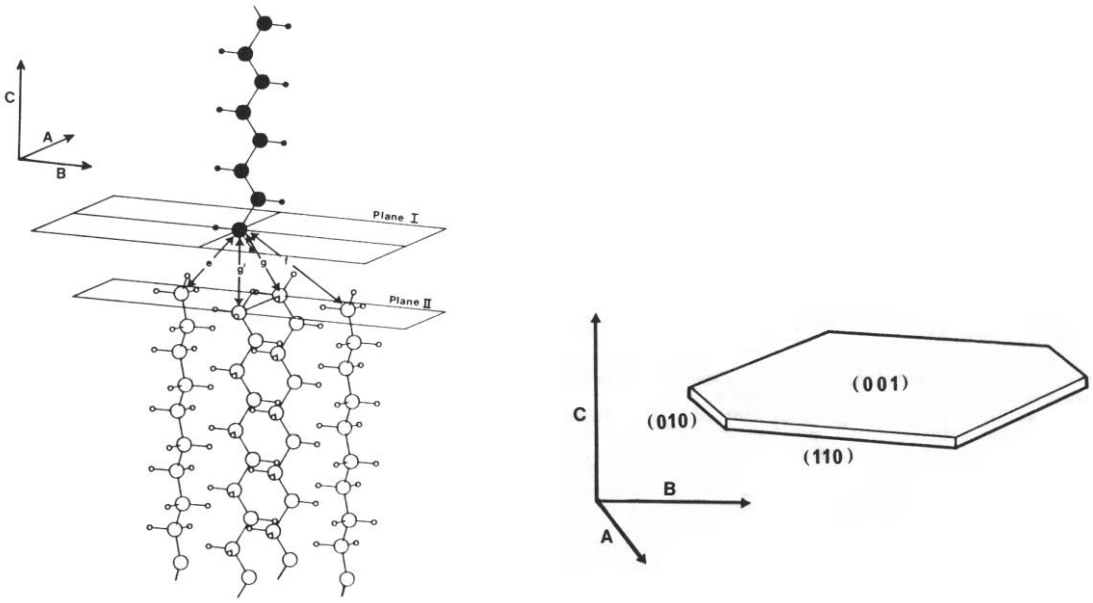

Figure 3.6 Left: Interactions of n-alkane molecules in adjacent crystal (001) planes, right: representation of a n-alkane crystal showing crystallographic axes and faces [10]

The influence of solution cooling on crystallisation of n-alkanes has also been studied. For example when the solution is cooled fast needle shaped crystals are formed. However, when they crystallise from hydrocarbon solvents at relative dilute concentrations and moderate slow rates of cooling, the crystal habits in general are thin plates [18]. It has been stated that crystallisation in these compounds always began with plate formation and rapid cooling cause the plates to curl at the edges [16].

Although the bulk crystallisation of n-alkanes has been studied extensively [19-26], the dynamics of this process and the complex nature of their crystal morphology have not so far allowed an extensive investigation to be made into their growth kinetics. Single long-chain n-alkane solutions systems crystallise comparatively easily and are characterised by small metastable zone widths (MSZW). This is associated with very fast lateral growth in which fully faceted crystals can be difficult to observe. Additionally, both the small thickness of the crystals together

with the - very low birefringence in the direction normal to the dominant morphological form add to the difficulty of their observation traditional microscopy.

In spite of this, some studies have been carried out to measure the growth rates of individual faces, mainly for crystals of n-alkanes with carbons chain lengths > 26, whose morphology is determined by crystallisation into either the orthorhombic or monoclinic structures. For instance, in the case of n-octacosane ($C_{28}H_{38}$) and n-hexatriacontane ($C_{36}H_{74}$), the observed crystals displayed a thin-lozenge plate-like morphology with well-developed (001) faces together with smaller (110) faces. Analysis of the growth rate kinetics measurements of the (110) faces was consistent with a dislocations-mediated [27] or two dimensional nucleation [28] growth mechanism for n-octacosane and n-hexatriacontane crystals, respectively. The observed crystal growth rates for these systems were found to be below 14 μm/s for supersaturations σ in the range of 0.007-0.15. The dominant (001) faces in the case of n-hexatriacontane crystals was found to develop by the slow incorporation of growth units by surface diffusion at the surface steps defined by the growth spirals [29, 30].

In the case of the n-alkane crystals, whose morphology is determined by crystallisation into the triclinic structure, such studies are scarcer due, in part, to the greater complexity in terms of preparing single crystals, controlling their growth and determining their corresponding crystal morphology. Some observations on the morphology of n-tetracosane ($C_{24}H_{50}$) crystallising from both n-hexane and n-octane solutions have been presented in Liu X-Y and Bennema P [31], together with the prediction of their morphologies using different models. However, the determination of the face-specific growth kinetics of these crystals has not as of yet been reported. Previous studies have been limited to only the development of instrumentation for collection of experimental data, e.g. associated with attempts to study the kinetics of n-eicosane ($C_{20}H_{42}$) crystallising from n-dodecane solutions [32].

3.3.1. The use of cold-flow improvers

The most traditional approach to improve n-alkanes cold flow behaviour is the use of additives [33]. They are classified in pour-point depressants, flow improvers, paraffin inhibitors and wax modifiers. The way these additives acts on modifying the n-alkanes solution cold flow properties is often well-known. However, it is difficult to generalise different n-alkane, solvent, additive systems due to the chemical structure of the additive and the complex composition of the diesel fuel that difficult understanding the mechanism of action of these additives.

Some of these additives can influence crystal growth to modify the crystal shape creating crystals with more compact shapes. In the case of plate-like crystal the modifiers can slow down the (110) faces growth by adsorbing into the faces. The habit modifiers additives all contain polymethylene segments and can be generally classified in: random copolymers such as Ethylene-vinyl ester copolymers from which one of the most representative are the ethylene-vinyl acetate copolymers (EVA). These are tailor made additives containing a co-crystallisable segment and a foreign segment comb-type polymers which have long polymethylene chains protruding from the polymer backbone. Examples of these additives are poly-alkyl acrylates (PAA) and fumarate-vinyl acetate copolymer (FVA) [33].

In some cases a well-defined effect of additives is observed. For instance when Ethylene-vinyl acetate copolymer (EVA) is used, the crystals formed from petrodiesel are much smaller and more numerous exhibiting more compact habit [33]. Soluble complexes at low temperatures are formed when European diesel fuel is treated with a polymer prepared from linear α-olefins with acrylic, vinylic and maleic unsaturated compounds. These additives also act as pour point depressants [33].

3.4. Crystallisation of biodiesel fuel and methyl esters

First generation of biodiesel fuels are generally a mixture of both saturated and unsaturated methyl esters from which the former represent an important proportion

of these solution and commonly contain methyl palmitate (C16:0) and stearate (C18:0). The cold-flow behaviour of biodiesel is determined to a great extent by the amount of saturated compounds present in its composition [34, 35]

Several approaches have been used to improve low temperatures properties of neat biodiesel including the blend of biodiesel with diesel fuel (BX systems). These blends have better cold flow properties than neat biodiesel solutions (B100). However, a more reliable approach that allows determining in a systematic way the more suitable mixtures has not been established due to the number of variables influencing crystallisation phenomena within these mixtures. The use of additives such as antioxidants and ozonised vegetable oils [36, 37] has also been suggested.

Among the additives a number of antioxidants DTBHQ (2,5-di-ter-butylhydroquinone), Ionox 220 [4,4´-methylenebis(2,6-di-tert-butylphenol)], Vulkanox ZKF [2,2´methylenebis(4-methyl-6-cyclohexylphenol)], Vulkanox BKF (2,2´-methylenebis(4-methyl-6-tert-butylphenol)] and Baynox (20% 2-6-di-tert-butyl-4-methylphenol dissolved in biodiesel) have been used to improve low temperature properties, however not all of them influence the stability to the same level as conclude from the stabilization factor that can vary between 1.89 and 13.07 depending on the origin of the biodiesel fuel. Stabilization factor defined as the ratio of the induction period in the presence of an additive to that without the additive (induction period determined by pour point) [33].

The influence of additives' concentration on the induction period is associated with the reduction in active aggregation/growth centres required for the formation of critical three dimensional nuclei. Selected additive molecule can bind to the saturated ester compound thus suppressing the onset of three dimensional nucleation. The dependence of the induction period on the concentration of different additives is given in Fig.3.7.

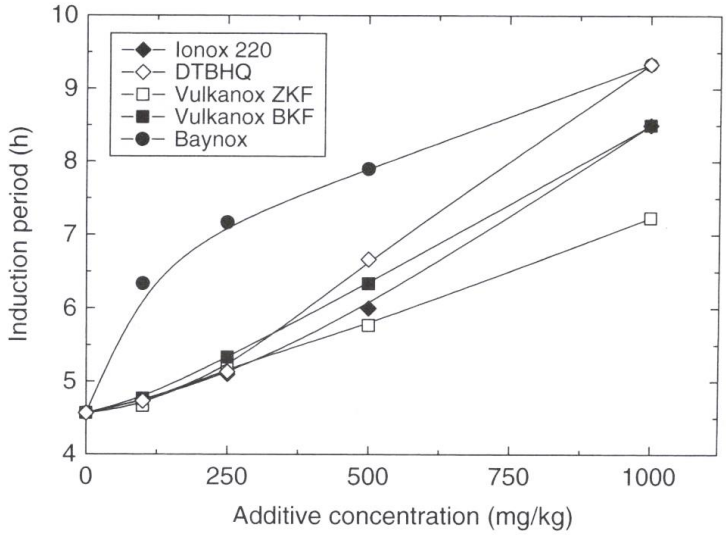

Figure 3.7 Dependence of induction period for instability (as determined by pour point) of rapeseed oil on the concentration of some selected additives [33]

Another common approach to improve low temperature properties of biodiesel is the use of ozonised vegetable oils derived from different vegetable oils sunflower (SFO), soybean (SBO), palm (PMO) and rapeseed oil (RSO). Migo et.al. [38] have shown the effect of 1% by weight of SFO, SBO, PMO and RSO on the cloud and pour points of biodiesel prepared from different vegetables oils. It was seen that a reduction in the biodiesel pour points occur when additive and biodiesel are prepared from the same vegetable oil due to the strongest interactions of their molecules. The pour point depressant is more effective when the average length of its hydrocarbons is the same as that of the main components of the biodiesel treated with the additive [38]. However ozonised oils had a relatively low influence on the treated biodiesel cloud point (CP). Ozonised PMO reduced the cloud points of SFO, SBO and RSO biodiesel by 2-3 °C and that of PMO biodiesel by 12-18 °C.

A study carried out by Migo et. al. [39] also addresses the effect of ozonised oils on the (PP) and (CP) of pure saturated and unsaturated components of biodiesel solutions and their binary and ternary mixtures in the presence of 1% ozonised additives. Observations of binary mixtures of C18:1 with C16:0 and C18:0 without and with 1% SFO showed that ozonised vegetable oil becomes less effective as (PP) depressant with increasing amount of saturated components especially C18:0 but leads to important reductions of the same parameter when the saturated component is

less than 10%. Furthermore observations on ternary mixtures of C16:0, C18:0 and C18:1 with total amount of saturated components less than 10% showed that (CP) and (PP) increases with increasing amount of C18:0 but that additive has not effect on the mentioned parameters if the mixture contains equal amount of the saturated components. The additive decreases the (CP) more than the (PP), decreases of 6 °C and 3 °C were observed respectively.

The mechanism of action of the additives on the crystallisation process may be explained by considering the physical blocking of the existing active growth [33]. When the crystal´s faces growth is blocked, by the adsorption of additive´s molecules on growth sites, nucleation is favoured to ease supersaturation this leading to the formation of numerous and smaller crystals. The way additives molecules interact with these growth sites is mainly determined by the functional groups present in them. Fig. 3.8 illustrates this. In general as saturated FAMEs contain long linear chain hydrocarbons, they assume flat surfaces. However, the double carbon-carbon bonds of the unsaturated compounds bent the geometry changing the flat geometry into a bent form. This giving a space for the accommodation of 1,2,3-trioxolane moieties of ozonised vegetable oil to be adsorbed into the bent geometry of the surface. Once this occurs growth will be blocked enhancing nucleation. The adsorption of additives molecules can also lead to a decrease in the interfacial free energy of the three dimensional nuclei, thus increasing the nucleation rate [33].

Fig. 3.9 shows polarised light micrographs of the morphology and seize distribution of crystalline agglomerates obtained from different biodiesel samples cooled from 40 °C down to -30 °C at 10 °C/min without and with 1% ozonised SFO additive. For SBO, SFO and RSO biodiesel samples the additive leads to the formation of much smaller rod-shaped crystalline aggregates. However, these additives do not modify significantly the morphology and number of agglomerates in palm oil biodiesel.

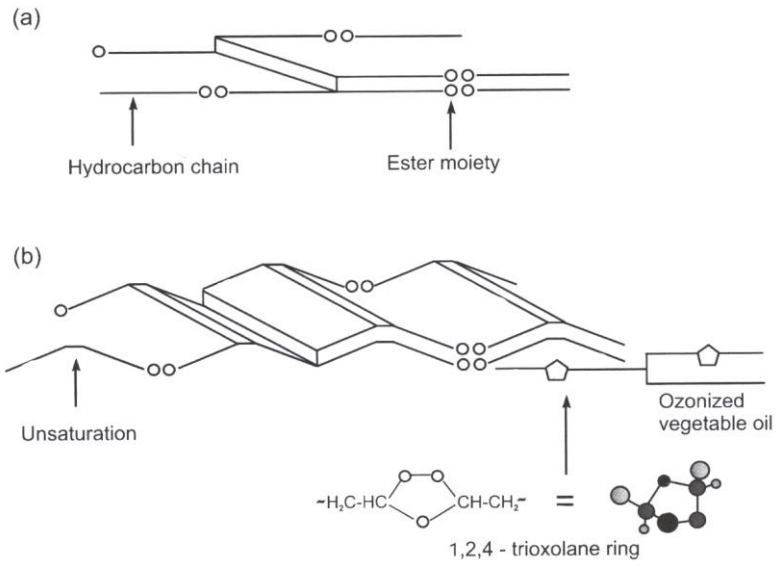

Figure 3.8 Schematic illustration of the geometry of lateral surfaces of (a) saturated and (b) unsaturated FAMEs. Unsaturation provides enough space to accommodate 1,2,4-trioxolane moieties of ozonised vegetable oil [33]

Some other studies [34, 39-41] also characterise the cold-flow behaviour of biodiesel fuel produced from different bio-resources, measuring certain properties such as: cloud point (CP), pour point (PP) and cold filter plugging point (CFPP) and the effect of cold-flow improvers on these properties. However, non-relevant fundamental investigations for saturated methyl esters such as methyl palmitate and stearate, have been reported on the two interrelated steps for crystallisation: nucleation and crystal growth. Morphological and kinetic studies on saturated methyl esters are scarce, not only due to the difficulty of obtaining reliable crystallographic information but also due to the difficulty of growing faceted observable crystals.

Limited structural information on methyl stearate suggests that this compound crystallises in two polymorphic forms: monoclinic and orthorhombic. The unit cell parameters of the stable monoclinic [42] form are thought to be a=5,61 Å, b=7.33 Å, C=106.6 Å, β=116.47º with crystal space group $\frac{A_2}{a}$. Similarly the unit cell parameters of the orthorhombic [43] form are a=5,61 Å, b=7.35 Å, C=95.15 Å with crystal space group $pnab$.

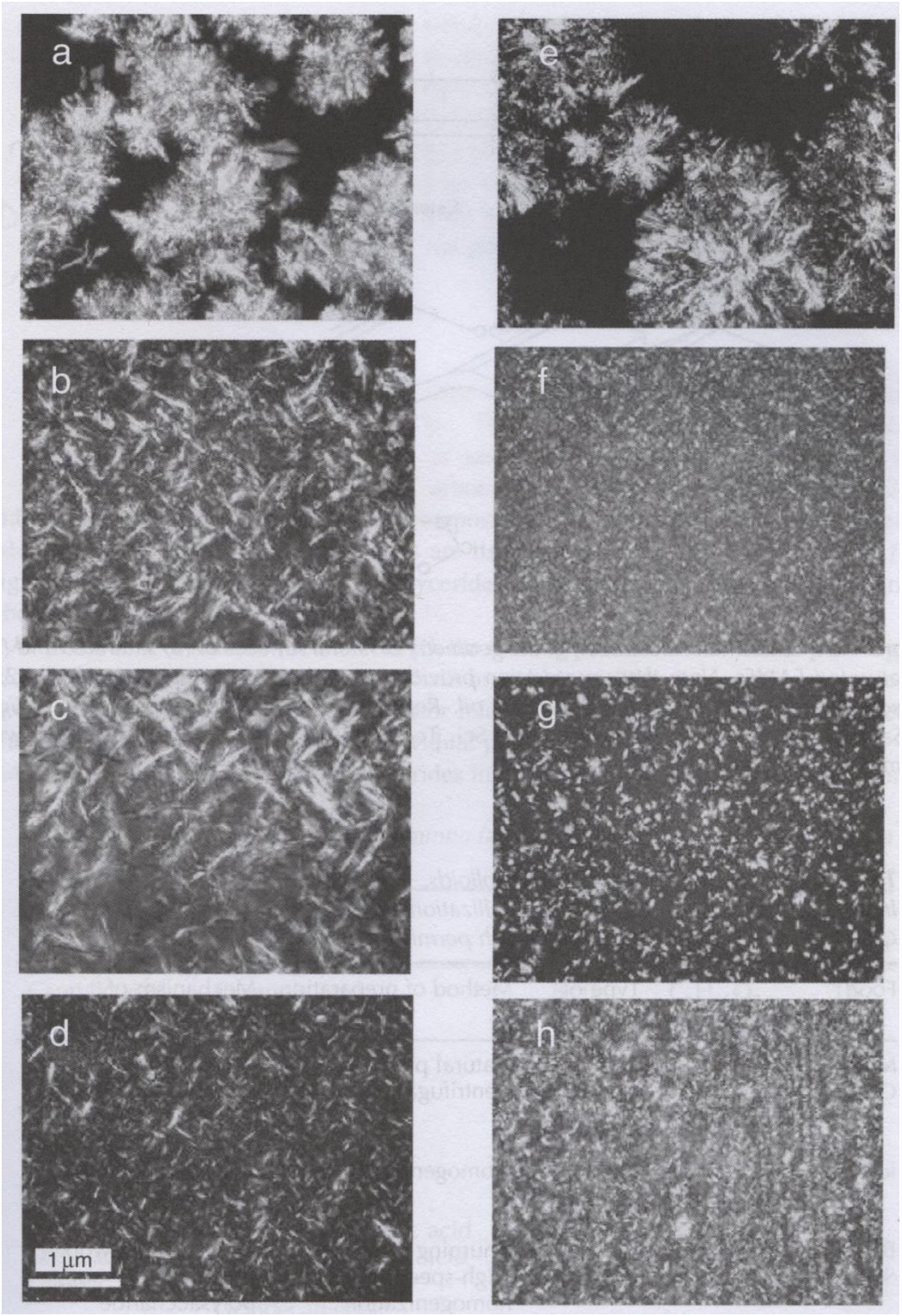

Figure 3.9 Polarised light micrographs showing the morphology and size distribution of crystalline agglomerates obtained from different biodiesel samples: (a-e) PMO diesel 10 ºC; (b-f) SBO diesel, 10 ºC; (c-g) SFO diesel, -20 ºC; (d,h) RSO diesel, -30 ºC. (a-d) neat biodiesel and (e-h) biodiesel with 1% ozonised SFO additive [33]

Observations of methyl palmitate and stearate crystals have shown that these compounds crystallise in a plate-like morphology, when grown from hydrocarbon solvents, in which the expected dominant (001) face is believed to growth via a screw dislocation mechanism as evidence of spiral growth on this face has been previously observed [44] (Fig.3.10).

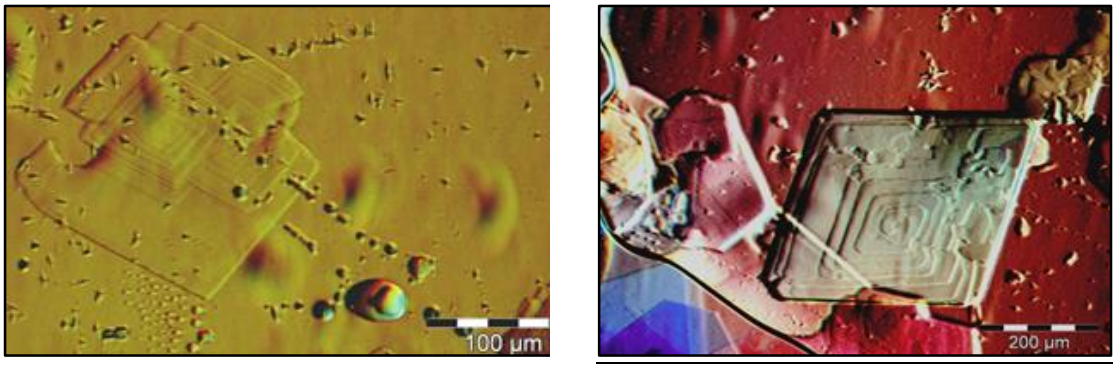

Figure 3.10 Left: methyl stearate crystal grown from a 30% solution with toluene at 3 °C, right: methyl palmitate crystal grown from a 30% solution with toluene solvent at -7 °C [44]

Growth of methyl palmitate and stearate crystals from unsaturated esters solvents results in a higher population of smaller and thinner crystals as shown in Fig. 3.11.

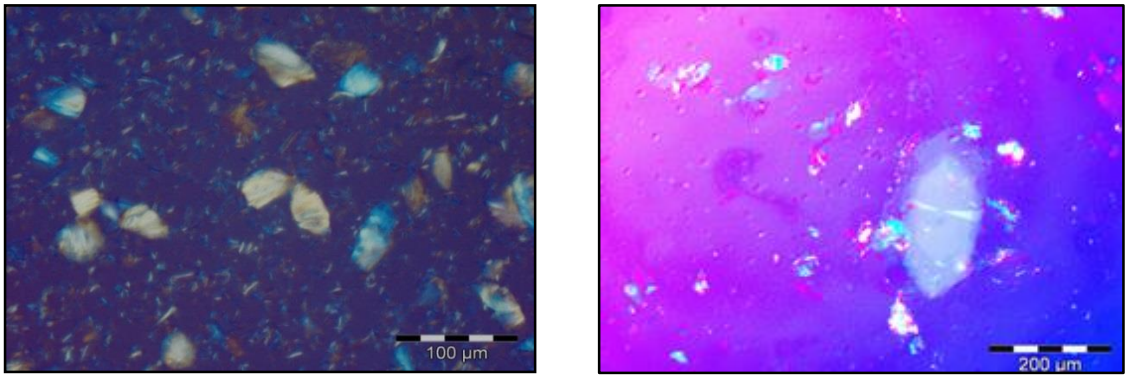

Figure 3.11 Left: methyl palmitate crystals grown from a 2.5% solution with methyl oleate solvent at -9 °C, right: methyl palmitate crystals grown from a 2.5% solution with methyl oleate solvent at -2 °C [44]

A project, addressing biodiesel/diesel mixtures cold flow activity using various additives in a Cold Climate Chassis Dynamotor (CCCD), suggested that a comprehensive approach should be used to study such complex systems [45]. Initially in this project samples of up to 20% by volume biodiesel fuel were studied

using differential scanning calorimetry (DSC) to assess thermal effects. The results reflected the complexity of these systems for which very broad DSC peaks were observed.

Thermal analysis over simpler systems were then carried out using n-dodecane as a solvent, to replicate some of the functionality of the diesel fuel, and a single component methyl ester either methyl stearate (C18:0) or methyl palmitate (C16:0) as a solute. It was observed that the onset of crystallisation increased with solute concentration and solute carbon chain length.

This work was expanded to using model systems with kerosene as a solvent. Thermal analysis was carried out with the aim of studying co-crystallisation of FAME with matching (or un-matching) chains n-alkanes compounds. The results suggested that co-crystallisation occurs when the FAME compounds are matched with the n-alkanes having the matching chain length. Fig. 3.12 shows that methyl stearate co-crystallise with n-C20 as given by a unique exothermal peak on cooling for solution composes of a binary mixture of methyl stearate and n-C20 in kerosene. On the other hand two peaks were observed when the solutions are made up of methyl stearate and n-C18 in kerosene indicating that crystallisation of these compounds takes place separately [45].

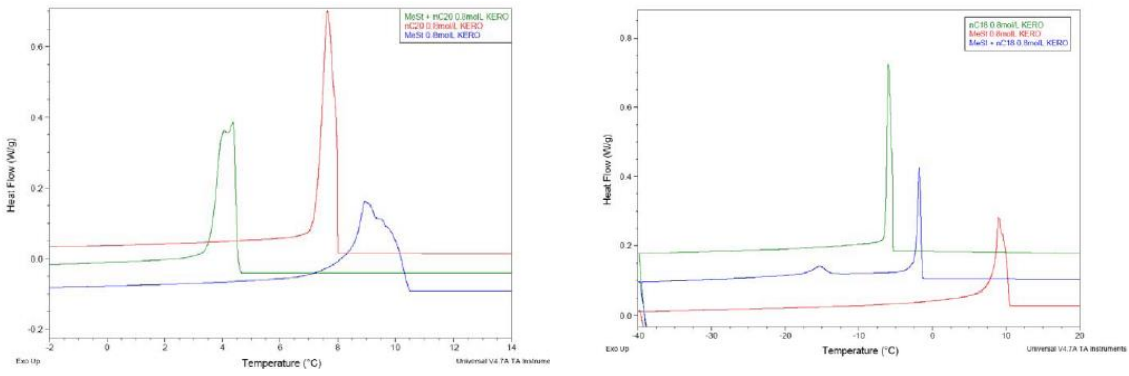

Figure 3.12 DSC curves for methyl stearate (C18:0) with matching and un-matching carbon chain lengths solutes crystallising from 0.8 mol solutions with kerosene. Left: the green curve represents C18:0/n-C20, the red curve represents n-C20 and the blue curve represents C18:0. Right: the green curve represents n-C18, the red curve represents C18:0 and the blue curve represents C18:0/n-C18 [45]

The same tendency was observed for solutions using methyl palmitate and n-alkanes as solutes in kerosene, for which co-crystallisation occurred between methyl palmitate and n-C18.

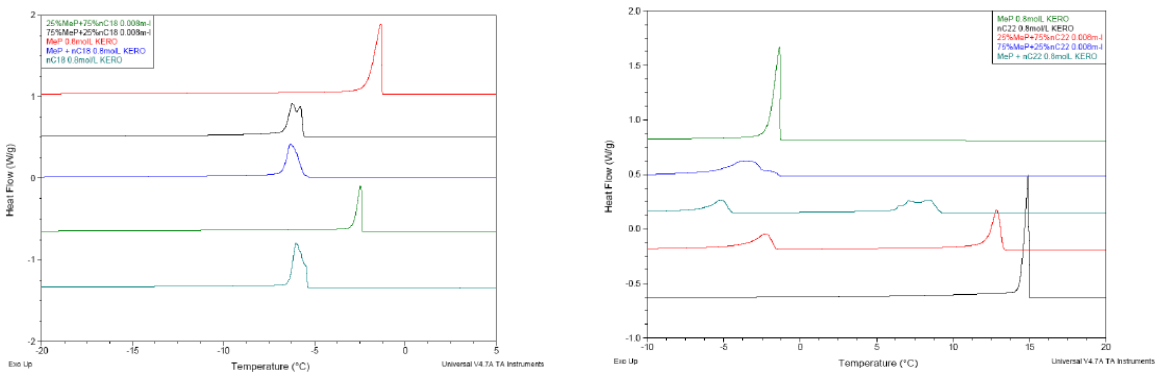

Figure 3.13 DSC curves for methyl palmitate (C16:0) with matching and un-matching carbon chain lengths solutes crystallising from 0.8 mol solutions with kerosene. Left: the green curve represents 25%C16:0/75%n-C18, the black curve 75%C16:0/25%n-C18, the red curve C16:0, the blue curve C16:0/n-C18 and the navy curve n-C18. Right: the green curve represents C16:0, the black curve n-C22, the red curve 25%C16:0/75%n-C22, the blue curve 75%C16:0/25%n-C22 and the navy curve C16:0/n-C22 [45]

As shown Fig. 3.13 this effect does not seem to be concentration dependant. A single peak is observed at three separate concentrations of the compounds used as solute, only with a change of position relative to the concentration of the solute components.

To validate these findings pictures of the crystals formed on cooling the same solution were obtained. The pictures showed that the crystals formed from mixtures of chain matched ester and straight chain alkane did not support the thermal analysis results. Rather than a single type of crystal as expected from a co-crystallised system a mixture of rough and faceted crystals was observed (Fig. 3.14) [45].

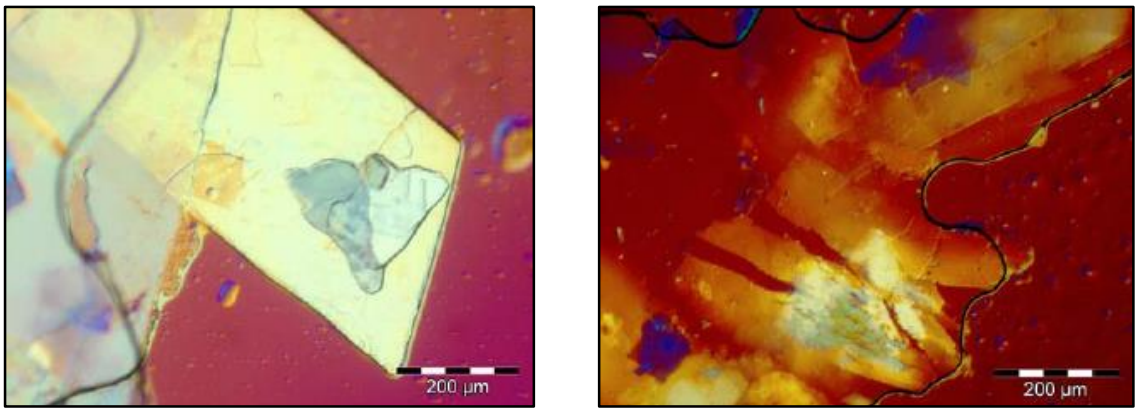

Figure 3.14 Crystals obtained from cooling crystallisation of solutions of methyl palmitate (C16:0) and octadecane (n-C18) [45]

As observed in Fig. 3.15 FAME crystals exhibited rough growth due to the high rate at which crystallisation occurs [45]. This is opposite to the n-alkanes case which generally produce faceted crystals as shown in previous work [46].

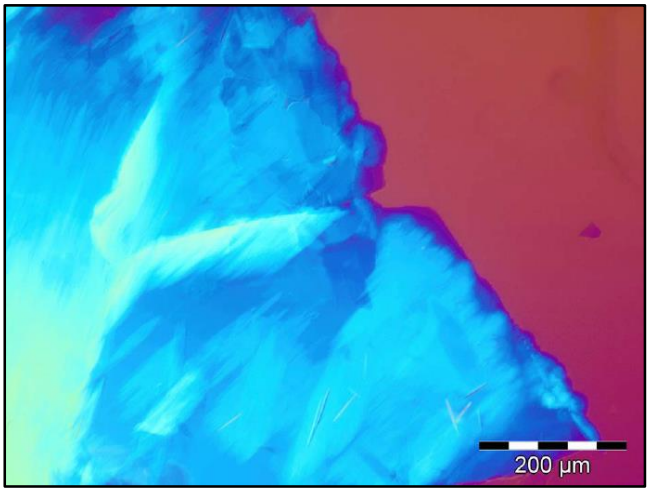

Figure 3.15 Example of rough FAME crystal growth [45]

3.5. Fractionation in biodiesel fuel mixtures

Dunn and co-workers have largely investigated the influence of the saturated esters and various alcohols on the low temperature behaviour of biodiesel [34, 35, 47, 48] . This work suggested that the higher melting points compounds are responsible for the low performance of biofuels under cold weather conditions as they would precipitate out of these solutions at relatively high temperatures. These findings lead

to the development of what is called “fractionation by crystallisation” as a suitable method to improve the cold flow properties of biodiesel fuel [49]. This methodology, in agreement with winterization process, consists in reducing the concentration of the higher melting point methyl esters (saturated esters), by separating them from the mixture after the fuel has been subjected to crystallisation. However, the efficient operation of these processes would depend on the capability of predicting both the composition of the materials that would precipitate below the CP of the fuel and the compositions of the liquid phase after partial crystallisation of a biodiesel and its new low-temperature characteristics [50, 51].

The effect of fractionation processes on improving the cold flow properties of soybean biodiesel was reported by Dunn et al. [49]. In this study a reduction of approximately 20 °C in the CP, PP, and CFPP values of the fuel was observed after the fractionation method was applied

Although a large body of work has been carried out on the crystallisation of n-alkanes and recently on the crystallisation of methyl esters, the fuels industry lacks a reliable tool capable of predicting the low temperature behaviour of real biodiesel and BX mixtures from the knowledge of the biodiesel/diesel composition [48]. This is mainly due to the complex composition of these solutions in which several compounds interact during the crystallisation process. The use of an appropriate model for predicting the behaviour of biofuels under cold weather conditions could not only help to evaluate the characteristics of a fuel but also to design fuels that meet the requirements for low temperature use and to design and operate fractionation processes [50].

Initial attempts on predicting low temperature properties of fuels addressed the prediction of CP temperatures through the use of the freezing point depression theory. (Holder and Winkler 1965) reported that this theory accurately predicted the low temperature behaviour of binary mixtures of long chain n-alkanes (either n-C20 or n-C28) in de-waxed gas oil. They observed that long chain n-alkanes crystallise independently rather than in a solid solution and therefore the use of the freezing point model was justified. This model is of the form of equation (2.39) but in it, Υ_i^S

and z_i are set equal to 1. Later Toro Vasquez et al. [52] employed the ideality model given by equation (2.40) to predict the low temperature behaviour of binary mixtures of tripalmitin and palm stearin in sesame seed oil solvent. Although in the former case the model predicted accurately the solution´s composition after crystallisation it deviated significantly in the latter case.

Additional investigations on binary and ternary mixtures of methyl esters were also carried out by Imhara et. al. [3]. The findings on the low temperature behaviour of these mixtures led to the development of a model to predict the CP values of biodiesel fuel. According to the analysis of these mixtures at the CP the methyl esters crystallised independently and in binary mixtures of saturated esters eutectic points were observed. Thus, in the solid-liquid equilibrium model (equation 2.39) Υ_i^S and z_i can be assumed equal to 1 for each of the saturated compounds present in a given esters solution. In addition to this Υ_i^L was set equal to 1 as non-ideality in liquid phase can be considered negligible when ambient pressure around the system is low, $\Delta C_{p,i}$ was assumed to be negligible and $T_{f,i}$ was equated to the measured cloud points of the pure esters. Thus the model developed to predict CP value of a given mixture is given by equation (3.2). It was reported that the CP of biodiesel fuel were accurately predicted by this model.

$$x_i = exp\left[\left(\frac{T - T_{f,i}}{RT}\right)\left(\frac{\Delta H_{fus,i}}{T_{f,i}}\right)\right] \tag{3.2}$$

Where x_i correspond to the molar fraction of either of the saturated esters present in the solution and T is equal to the cloud point (CP)

Although the models described can predict the CP values of some selected methyl esters mixtures, some investigations have reported they do not accurately predict the low temperature behaviour of real-practical fuels systems. For instance Dunn et al. [35, 53, 54] reported that the model given by Imhara et al. delivered a poor prediction of the cloud point of soy methyl esters (SME) oil. What is more, given

the assumptions made for the development of these models, not accurate prediction of the composition of the phases after crystallisation could be expected.

As a result of this, Dunn et al. [35] initially proposed the use of the activity model (equation 2.39) including the effect of the solution´s deviation from ideality. Later Coutinho and co-workers addressed the fractionation of traditional petro-diesel fuels, using a thermodynamic UNIQUAC model, for the estimation of liquid and solid phase activity coefficients [55, 56]. This model was tested in diesel fuels [57, 58] delivering accurate predictions for the compositions of both the precipitate and the liquid phase after crystallisation.

Given the increasing interest on biodiesel fuels this model was also applied to the prediction of CPs of fatty acid methyl and ethyl esters mixtures [59, 60]. However, it was observed that the use of this model present limited advantages when compared to a model in which no solid-solution was considered.

Further work [61] addressed the development of an activity model to predict fractionation of representative methyl esters mixtures. Two different versions of the UNIQUAC model together with a model assuming no formation of solid solution were tested. This was done by comparing the predictions of the model against experimental data collected for the fractionation of mixtures containing different molar fractions of C16:0, C18:0, C18:1, C18:2. It was shown that two of these models were capable of predicting the phase equilibrium of these solutions below the cloud point.

3.6. Conclusions

This chapter introduced the fundamental concepts related to the low temperature properties of diesel and biodiesel fuels solutions and presented an insight on how crystallisation science can be used to address biodiesel poor cold flow properties.

Initially a general background on biofuels is provided followed by a comparison of relevant properties of diesel and biodiesel fuel mixtures for their use in diesel

engines. The standards and norms associated with the regulation of the use of biodiesel fuel in transport is also presented.

A review of fundamentals studies on the crystallisation of n-alkanes and methyl esters is given, focusing on the investigations carried out on crystals morphology and crystallisation kinetics. This with the aim of providing the theoretical backdrop underpinning the research presented in sub-sequent chapters. Finally, a review of the models developed for the prediction of fractionation behaviour of practical fuels systems is provided.

References

[1] J.C.J. Bart, N. Palmeri, S. Cavallaro, Biodiesel science and technology : from soil to oil, Woodhead Publishing; CRC Press, Cambridge, Boca Raton, Fla., 2010.

[2] J.V. Gerpen, Biodiesel processing and production, Fuel Processing Technology 86 (2005) 1097-1107.

[3] H. Imahara, E. Minami, S. Saka, Thermodynamic study on cloud point of biodiesel with its fatty acid composition Fuel, 85 (2006) 1666-1670.

[4] E.B.T. Platform, Available from worldwide web http://www.biofuelstp.eu/btl.html, in, 2012.

[5] G. Knothe, Dependence of biodiesel fuel properties on the structure of fatty acid alkyl esters, Fuel Processing Technology, 86 (2005) 1059-1070.

[6] G. Pahl, Biodiesel : growing a new energy economy, Chelsea Green Pub., White River Junction, Vt., 2005.

[7] G. knothe, R.O. Dunn, M.O. Bagby, Biodiesel: The use of vegetable oils and their derivatives as alternatives diesel fuels Oil Chemical Research, National Center for Agricultural Utilization Research, Agricultural Research Service, U.S. Department of Agriculture, Peoria, IL 61604, (2001).

[8] G. Knothe, J.H. Van Gerpen, J. Krahl, K. (Firm), The biodiesel handbook, in, AOCS Press, Champaign, Ill., 2005, pp. ix, 302 p. ill. 324 cm.

[9] I. Lee, L.A. Johnson, E.G. Hammond, Use of branched-chain esters to reduce the crystallisation temperature of biodiesel JAOCS 72 (1995) 1155-1160.

[10] J. Garside, R.J. Davey, A.G. Jones, Advances in industrial crystallization, Butterworth Heinemann, Oxford, 1991.

[11] M. Broadhurst, An Analysis of the Solid Phase Behaviour of the Normal Paraffins, J. Res. Nat. Bur. Stds, 66A (1962) 241-249.

[12] R. Boistelle, D. Aquilano, Interaction Energy and Growth Mechanisms on Twinned and Polytypic Crystals of Long-Chain Even Normal-Alkanes . I. Interaction-Energy Calculations, Acta Crystallogr A, 33 (1977) 642-648.

[13] R. Boistelle, B. Simon, G. Pepe, Polytypic Structures of n-$C_{28}H_{58}$ (Octacosane) and n-$C_{36}H_{74}$ (Hexatriacontane), Acta Crystallogr B, 32 (1976) 1240-1243.

[14] C. Rinaudo, D. Aquilano, F. Abbona, Occurrence and Growth Mechanism of the Periodic Polysynthetic Twins in the Even n-Alkanes, Journal of Crystal Growth, 53 (1981) 361-368.

[15] R. Boistelle, in: E. Kaldis (Ed.) Current Topics in Material Science, North-Holland Publishing Co. , Amsterdam, 1980, pp. 413-480.

[16] M. Chichakli, F.W. Jessen, Crystal morphology in hydrocarbon systems, Industrial and Engineering Chemistry, 59 (1967) 86-98.

[17] D.H.M. Beiny, J.W. Mullin, K. Lewtas, Crystallisation of n-Dotriacontane from Hydrocarbon Solution with Polymeric Additives, Journal of Crystal Growth, 102 (1990) 801-806.

[18] B. Simon, R. Boistelle, Crystal growth from low temperature solutions Journal of Crystal Growth, 52 (1981) 779-788.

[19] A.R. Gerson, K.J. Roberts, J.N. Sherwood, A.M. Taggart, G. Jackson, The Role of Growth Environment on the Crystallization of Normal Alkanes in the Homologous Series from $C_{18}H_{38}$ to $C_{29}H_{60}$, Journal of Crystal Growth, 128 (1993) 1176-1181.

[20] K.J. Roberts, J.N. Sherwood, A. Stewart, The Nucleation of n-Eicosane Crystals from Solutions in n-Dodecane in the Presence of Homologous Impurities, Journal of Crystal Growth, 102 (1990) 419-426.

[21] S.R. Craig, G.P. Hastie, K.J. Roberts, J.N. Sherwood, Investigation into the Structures of Some Normal-Alkanes within the Homologous Series $C_{13}H_{28}$ to $C_{60}H_{122}$ Using High-Resolution Synchrotron X-Ray-Powder Diffraction, J Mater Chem, 4 (1994) 977-981.

[22] A.R. Gerson, K.J. Roberts, J.N. Sherwood, X-Ray-Powder Diffraction Studies of Alkanes - Unit-Cell Parameters of the Homologous Series $C_{18}H_{38}$ to $C_{28}H_{58}$, Acta Crystallogr B, 47 (1991) 280-284.

[23] A.R. Gerson, K.J. Roberts, J.N. Sherwood, X-Ray-Powder Diffraction Studies of Normal-Alkanes - a Re-examination of the Unit-Cell Parameters of $C_{24}H_{50}$ and $C_{26}H_{54}$, Acta Crystallogr B, 48 (1992) 746-746.

[24] S.R. Craig, G.P. Hastie, K.J. Roberts, A.R. Gerson, J.N. Sherwood, R.D. Tack, Investigation into the Structures of Binary, Tertiary and Quinternary-Mixtures of n-Alkanes and Real Diesel Waxes Using High-Resolution Synchrotron X-ray Powder Diffraction, J Mater Chem, 8 (1998) 859-869.

[25] S.R. Craig, G.P. Hastie, K.J. Roberts, Chain Length Dependent Polymorphism in Even Number n-Alkanes: Line Profile Analysis of Synchrotron Powder X-ray Diffraction Data, J Mater Sci Lett, 15 (1996) 1193-1196.

[26] S.R. Craig, G.P. Hastie, K.J. Roberts, J.N. Sherwood, R.D. Tack, R.J. Cernik, In-situ Study of the Solid-Solid Phase Transitions Occurring in Real Diesel Wax Crystalline Systems Using Differential Scanning Calorimetry and High-Resolution Synchrotron X-ray Powder Diffraction, J Mater Chem, 9 (1999) 2385-2392.

[27] R. Boistelle, A. Doussoulin, Spiral Growth Mechanisms of (110) Faces of Octacosane Crystals in Solution, Journal of Crystal Growth, 33 (1976) 335-352.

[28] B. Simon, A. Grassi, R. Boistelle, Cinétique de Croissance de la Face (110) de la Paraffine $C_{36}H_{74}$ en Solution, Journal of Crystal Growth, 26 (1974) 77-89.

[29] H.E. Lundagermadsen, R. Boistelle, Growth-Kinetics of the (001) Faces of Hexatriacontane ($C_{36}H_{74}$) in Solution, Journal of Crystal Growth, 46 (1979) 681-690.

[30] M. Rubbo, R. Boistelle, Dissolution and Growth-Kinetics of the (001) Faces of Normal-Hexatriacontane Crystals Grown from Heptane, Journal of Crystal Growth, 51 (1981) 480-488.

[31] X.-Y. Liu, P. Bennema, On the Morphology of Crystals of Triclinic Even Normal Alkanes: Theory and Observation, Journal of Crystal Growth, 135 (1994) 209-223.

[32] M. Rubbo, J.N. Sherwood, An Improved Method for the Measurement of the Rates of Growth and Dissolution of Crystals Under Isothermal Conditions, Journal of Crystal Growth, 61 (1983) 210-214.

[33] K. Sangwal, Additives and crystallization processes : from fundamentals to applications, Wiley, Chichester, 2007.

[34] R.O. Dunn, M.W. Shockley, M.O. Bagby, Improving the Low Temperature Properties of Alternative Diesel Fuels: Vegetable Oil-Derived Methyl Esters JAOCS, 73 (1996) 1719-1728.

[35] R.O. Dunn, Crystallisation behaviour of Fatty Acid Methyl Esters, JAOCS, 85 (2008) 961-972.

[36] R.O. Dunn, Effect of oxidation under accelerated conditions on fuel properties of methyl soyate (biodiesel), JAOCS, 79 (2002) 915-920.

[37] M. Mittelbach, S. Schober, The influence of antioxidants on the oxidation stability of biodiesel, JAOCS, 80 (2003) 817-823.

[38] N.U.S. Jr., V.P. Migo, M. Matsumura, Ozonized vegetable oil as pour point depressant for neat biodiesel, Fuel, 85 (2006) 25-31.

[39] N.U.S. Jr, V.P. Migo, K. Sato, M. Matsumura, Crystallization behavior of neat biodiesel and biodiesel treated with ozonized vegetable oil, European Journal of Lipid Science and Technology, 107 (2005) 689-696.

[40] C. Boshui, S. Yuqiu, F. Jianhua, W. Jiu, W. Jiang, Effect of Cold Flow Improvers on Flow Properties of Soybean Biodiesel Biomass and Bioenergy 34 (2010) 1309-1313.

[41] E. Odeigah, R.B. Janius, R. Yunus, Factors Affecting the Cold Flow Behaviour of Biodiesel and Methods for Improvement-A Review Pertanika J. Sci. & Technolog. , 20 (1) (2012) 1-14.

[42] S. Aleby, E. von Sydow, The Crystal Structure of Methyl Stearate, Acta Crystallographica, 13 (1960) 487.

[43] C.H. MacGillavry, M. Wolthuis-Spuy, Crystal structure of an Orthorhombic Modification of Methyl Stearate, Acta Crystallographica B26 (1970) 645-648.

[44] H. Jiang, Molecular-Scale Effects of Additives on the Nucleation, Growth and Crystal Properties of Long-Chain Alkyl Methyl-Esters in: School of Process Environmental and Materials Engineering, University of Leeds, 2012.

[45] Infineum UK, personal communication, December 6, 2011.

[46] K. Lewtas, R.D. Tack, Wax crystallisation in diesel fuel: habit modification and the growth on n-alkane crystals, in: Advances in industrial crystallisation, Butterworth Heinemann, Oxford, 1991, pp. 166-179.

[47] R.O. Dunn, M.O. Bagby, Low-temperature properties of trygliceride-based diesel fuels: transesterified methyl esters and petroleum middle distillate/ester blends, JAOCS, 72 (1995) 895-904.

[48] R.O. Dunn, Cold-flow properties of soybean oil fatty acid monoalkyl ester admixtures, Energy & Fuels, 23 (2009) 4082-4091.

[49] R.O. Dunn, Improving the cold flow properties of biodiesel by fractionation, in: www.intechopen.com Soybean - Applications and Technology, InTech, 2011, pp. 211-240.

[50] G. Knothe, "Designer" Biodiesel: Optimizing fatty ester composition to improve fuel properties, Energy & Fuels, 22 (2008) 1358-1364.

[51] S. Kerschbaum, G. Rinke, K. Schubert, Winterization of biodiesel by micro process engineering, Fuel, 87 (2008) 2590-2597.

[52] T.-V. J.F., B.-M. M., D.-A. M., R.-H. J., Crystallization kinetics of palm stearin in blends with sesame seed oil, JAOCS, 77 (2000) 297-310.

[53] G. Knothe, R.O. Dunn, Biodiesel: an alternative diesel fuel from vegetable oils or animal fats, in, Erhan SZ (ed) Industrial uses of vegetable oils. AOCS, Champaign, IL, 2005, pp. 42-89.

[54] R.O. Dunn, Crystallisation behaviour of Fatty Acid Methyl Esters, in, State of alternative fuel technologies (SAE Spec Publ SP-1274). Society of Automotive Engineers, Warrendale, PA, 2008, pp. 133-142.

[55] J.A.P. Coutinho, K. Knudsen, S.I. Andersen, E.H. Stenby, A local composition model for paraffinic solid solutions, Chemical Engineering Science, 51 (1996) 3273-3282.

[56] J.A.P. Coutinho, F. Mirante, J. Pauly, A new predictive UNIQUAC for modeling of wax formation in hydrocarbon fluids, Fluid Phase Equilibria, 247 (2006) 8-17.

[57] J.A.P. Coutinho, C. Dauphin, J.L. Daridon, Measurements and modelling of wax formation in diesel fuels, Fuel, 79 (2000) 607-616.

[58] J. Pauly, J.L. Daridon, J.M. Sansot, J.A.P. Coutinho, The pressure effect on the wax formation in diesel fuel, Fuel, 82 (2003) 595-601.

[59] J.C.A. Lopes, Et.al., Prediction of Cloud Points of Biodiesel, Energy & Fuels, 22 (2008) 747-752.

[60] L. Boros, Et.al., Crystallization behavior of mixtures of fatty acid ethyl esters with ethyl stearate, Energy & Fuels, 23 (2009) 4625-4629.

[61] J.A.P. Coutinho, M. Gonc-alves, M.J. Pratas, M.L.S. Batista, V.F.S. Fernandes, J. Pauly, J.L. Daridon, Measurement and modeling of biodiesel cold-flow properties, Energy & Fuels, 24 (2010) 2667-2674.

4. Materials and Methods

Summary: This chapter provides and overview of the materials used in this research, together with the instrumentation and experimental methodologies used for the collection and analysis of related experimental data

4.1. Introduction

This section describes the model compounds chosen for this study; followed by an overview of the instruments and methodologies employed for the collection, processing and analysis of related experimental data. The instrumentation includes a turbidimetric technique (Crystal 16®), Differential Scanning Calorimetry (DSC), microscopy and Gas Chromatography (GC). The methodologies to analyse experimental data are introduced and linked to sub-sequent chapters where detailed information is presented on the development of methodologies for the assessment of nucleation and crystal growth kinetics as well as crystals morphological indexation.

4.2. Materials

Model compounds present in both biodiesel and diesel fuels mixtures were chosen for this study. Two saturated methyl esters (methyl palmitate and stearate) and a long chain n-alkane (n-docosane) were selected as solutes. The esters are used in all subsequent chapters as part of a comprehensive analysis of their crystallisation behaviour. The n-alkane was used for the development of a methodology to characterise the morphology and growth kinetics of fuels type materials as presented in Chapter 8.

Eight different model solvents were chosen: five of them which are representative of diesel fuel mixtures (n-dodecane, kerosene, toluene, n-heptane and methyl-cyclohexane) and three unsaturated methyl esters (methyl oleate, linoleate and linolenate) which are representative compounds in biodiesel fuels mixtures. The latter were used both as single solvent components and mixed in the same proportions as they are present in palm, soy and rapeseed oil. Details of these materials are given in Table 4.1. and 4.2. Fig. 4.2 shows their corresponding chemical structures.

Table 4.1 Details of solutes and solvents used in the study

Material	Purity	Manufacturer
Methyl palmitate (C16:0)	96%	Sigma-Aldrich
Methyl stearate (C18:0)	96%	Sigma-Aldrich
N-docosane	99%	Sigma-Aldrich
Toluene	99%	Sigma-Aldrich
N-heptane	99%	Sigma-Aldrich
Methyl-cyclohexane	99%	Sigma-Aldrich
Methyl oleate (C18:1)	96%	TCI UK Ltd.
Methyl linoleate (C18:2)	95%	TCI UK Ltd.
Methyl linolenate (C18:3)	70%	TCI UK Ltd.

* For the purpose of this work methyl esters are designated with a C followed by two numbers separated by a colon. The first number corresponds to the number of carbons atoms in the chain including the carboxylic carbon and the second number corresponds to the number of double bonds in the ester molecule. No further purification of the materials was carried out

Kerosene was supplied by Infineum Ltd. comprising a mixture of hydrocarbons as presented in Table 4.2. Fig.4.1 shows the distribution of n-alkanes ranging from C_7-C_{18}.

Table 4.2 Composition of kerosene as obtained by 2D Gas Chromatography analysis

	Hydrocarbon	**Mass %**
Paraffins	n-alkanes	16.29
	Iso-paraffins	23.04
Cycloalkanes	Naphthenes	42.40
Aromatics	Alkyl Benzenes	7.60
	Benzocycloparaffins	6.80
	Naphthalenes	3.43
	Biphenyls/acenaphthenes	0.30
	Fluorenes	0.15

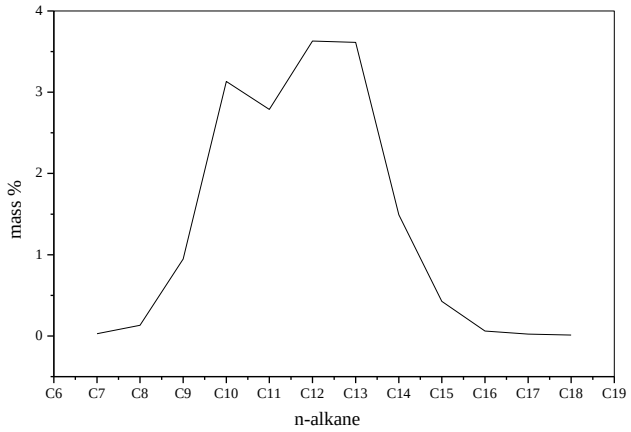

Figure 4.1 Kerosene n-alkane distribution as obtained by 2D Gas Chromatography analysis

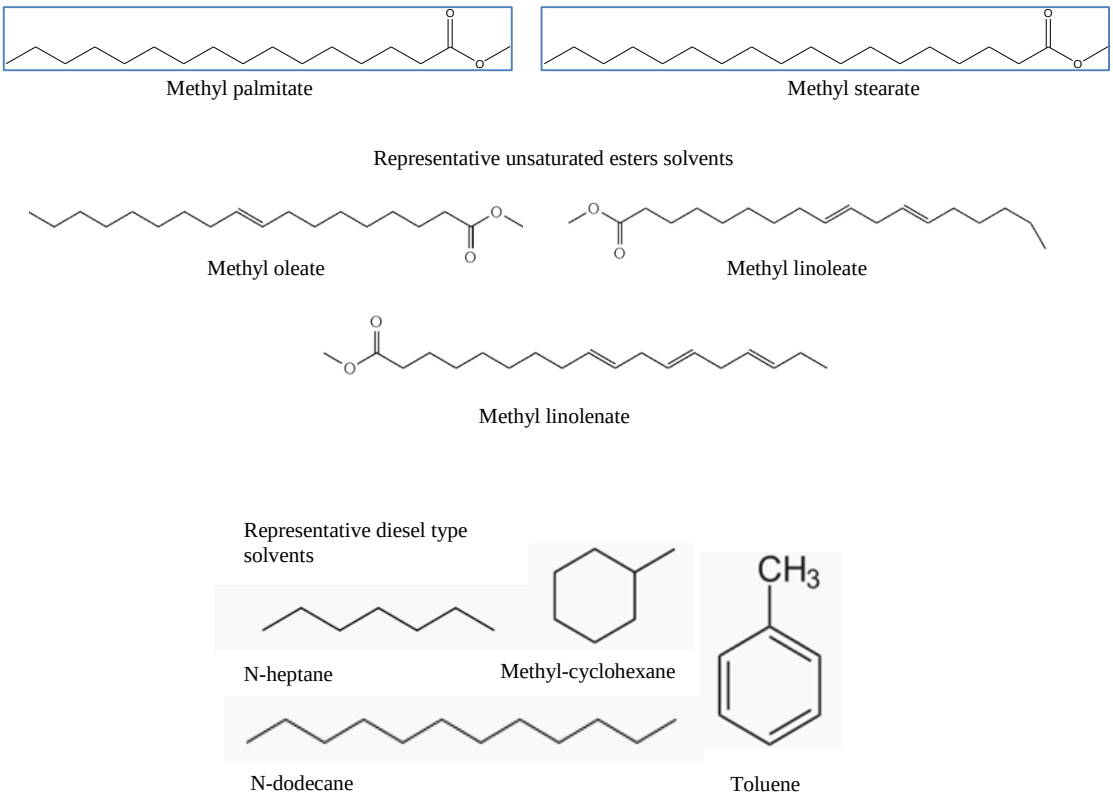

Figure 4.2 Representative chemical structures of solutes (methyl palmitate and stearate) and solvents selected for this study

4.3. Equipment and experimental procedure

4.3.1. Crystal 16

Crystallisation polythermal and isothermal experiments were carried out using the Avantium Crystal 16® system (Fig. 4.3) (see:http://www.crystallizationsystems.com/pharma/crystal16/). This provides a multiple reactor facility with four separate Peltier heated aluminium blocks, each of which has a capacity to hold four magnetically-agitated 1 ml solution vials. Each block can be individually programmed to follow a given temperature profile during which the variations in the solution turbidity are followed as a function of temperature.

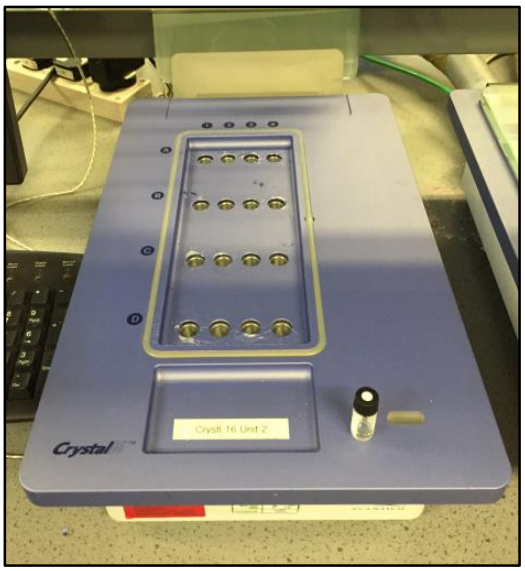

Figure 4.3 Avantium Crystal 16® unit showing the four independent heated reactor blocks and a HPLC sample vile

4.3.1.1. Equipment calibration

In order to ensure accurate measurement of temperatures, calibration of the Crystal 16® unit was required. Four vials containing each of the solvents used were placed in each of the blocks which were programmed to a specific temperature in the range of 20 °C to -8 °C. Whilst each block was kept at a chosen temperature, measurements of the actual temperature with ± 0.5 °C accuracy were carried out by positioning a thermocouple within each of the vials. The average of the four temperatures readings obtained in each block was plotted against the programmed temperature and fitted by a straight line, which was then used to correct the experimentally measured temperature values. An example of the temperature-calibration line obtained for kerosene solvent given by the expression $y = 0.96\,x + 1.34$ is presented in Fig. 4.4.

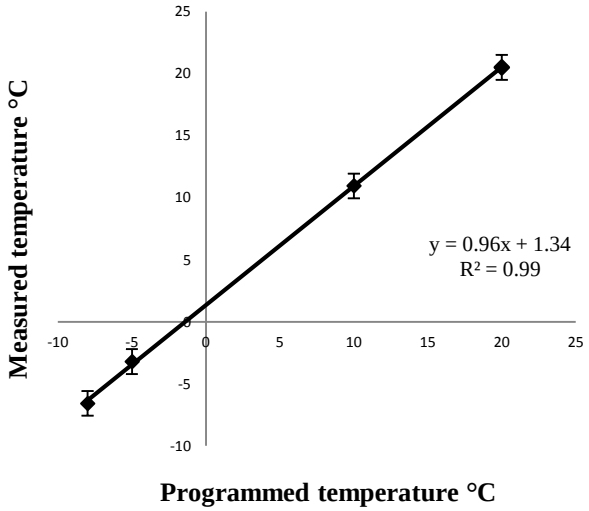

Figure 4.4 Temperature calibration for the Crystal 16® unit. Temperature at which the Crystal 16® is programmed is plotted against the actual temperature of the solvent as measured by a calibrated thermocouple

4.3.1.2. Polythermal measurements

In a polythermal methodology solutions are subject to heating and cooling cycles according to an established temperature profile. The crystallisation T_c and dissolution T_{diss} temperatures are estimated based upon the points in the turbidity profile at which sudden changes in light transmittance are detected.

The development of the methodology for collecting and analysing polythermal experimental data is part of the results of this research. Although the most suitable experimental procedure for the application of this method is defined in Chapter 5, a summary of the experimental parameters used for the collection of crystallisation data for the solutions studied is presented in this section. This is done with the aim of providing a methodologic overview to facilitate the fluent reading of this work. Table 4.3. shows the parameters used in both the heating and cooling segments as a function of solvent.

Table 4.3 Experimental parameters used for measurements of dissolution and crystallisation temperatures for C16:0 and C18:0 as a function of solvent

Solvent	Concentration $\left(\frac{g}{l}\right)$	Cooling rate q $\left(\frac{℃}{min}\right)$	Temperature cycles repeats
N-dodecane	200, 250, 300, 350	0.25, 1.00, 3.20, 9.00	5
Kerosene	200, 250, 300, 350	0.25, 1.00, 3.20, 9.00	5
Toluene	154, 192, 231, 269	0.25, 0.50, 1.00, 1.50	5
N-heptane	154, 192, 231, 269	0.25, 1.00, 2.00, 3.20	5
Methyl-cyclohexane	154, 192, 231, 269	0.25, 1.00, 2.00, 3.20	5
Methyl oleate	154, 192, 231, 269	0.25, 1.00, 3.20, 5.00	5
Methyl linoleate	154, 192, 231, 269	0.25, 1.00, 3.20, 5.00	5
Methyl linolenate	154, 192, 231, 269	0.25, 1.00, 3.20, 5.00	5
Mixtures as in palm, soy and rapeseed oil	154, 192, 231, 269	0.25, 1.00, 3.20, 5.00	5

The range of both concentrations and cooling rates for solutions of a given solvent were chosen to ensure accurate temperature profiles. This was achieved by setting temperatures profiles in which crystallisation was detected above -15 °C (lowest working temperature of the Crystal 16®) and a sufficiently wide range of cooling rates in compliance with both the equipment cooling power capacity and the methodology defined in Chapter 5. For the solutions where crystallisation was detected at lower temperatures a narrower cooling range had to be used due to the decrease in the equipment cooling capacity observed at these temperature levels.

4.3.1.3. Isothermal measurements

The isothermal method was applied to solutions of C18:0 crystallising from kerosene as part of the development of a methodology to study nucleation kinetics presented in Chapter 5. Therefore details on the procedure used for the application of this method are given in the sub-sequent chapter.

4.3.2. Rigs for observations of crystal morphology and growth

In-situ crystal growth studies for n-docosane crystals growing from n-dodecane were carried out using an experimental set-up described earlier [1]. This comprised an inverted optical polarising microscope (Olympus Optical IMT-2), operated in bright

field transmission mode, which was integrated with a Lumenera Infinity 3.3 megapixel CCD camera which captured crystal images as a function of time. The images were then analysed using the INFINITY ANALYZE software (http://www.lumenera.com/support/downloads/microscopy-downloads.php). The associated growth cell comprised a simple temperature-controlled annular tank (diameter 11 cm, depth 3.5 cm) sealed with two removable circular glass plates. The solution was secured within a 0.5 ml sealed UV glass cuvette with a path length of 1 mm. The temperature within the cell was measured using a PT100 temperature probe and controlled using a Haake F3 circulating water bath that circulates water through the growth cell. This is reported with an accuracy of ±0.2 corresponding to that of the PT100 probe. As the solution is placed within the cuvette, the exact temperature at a specific solution spot cannot be obtained due to the expected differences between the temperature of the circulating water and that of the solution isolated by the glass of the cuvette. However, this measurements are assumed to be accurate enough as the PT probe is placed as close as possible to the cuvette location and these ΔT are not considered to be relevant as the aim of this work is to observe the trend of the faces growth as a function of relative supersaturation σ and not to calculate any parameters as a function of absolute temperature. The overall system is shown in Fig. 4.5.

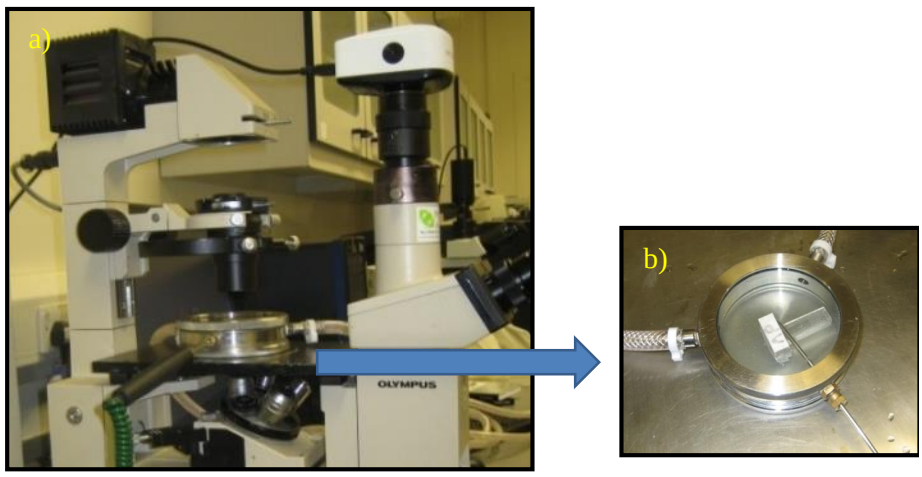

Figure 4.5 Experimental set up for crystal growth rates measurements, after [1]. (a) Olympus IMT-2 inverted optical polarising microscope integrated with Lumenera Infinity 3.3 megapixel CCD camera. (b) Enlarged picture of the crystal growth cell

To improve the contrast of the images obtained additional measurements for C18:0 crystals growing from three different solvents: n-dodecane, kerosene and toluene were carried out using an up-graded experimental set-up. This comprised an optical microscope (Olympus BX51), operated in Differential Interference Contrast (DIC) mode, which was integrated with a QImaging/QICAM camera which captured crystal images as a function of time. The images were then analysed using the QCapture Pro software (see: http://www.qimaging.com/products/software/qcappro7.php). The associated growth cell comprised a simple temperature-controlled rectangular tank (10 X 12 cm, depth 1.5 cm) sealed with two removable rectangular glass plates. The solution was secured within a 0.5 ml sealed UV glass cuvette with a path length of 1 mm which was placed within the cell as close to the objective lens of the microscope as feasible. The temperature within the cell controlled using a Huber Ministat 125 circulating water bath that circulates water through the growth cell. The overall system is shown in Fig. 4.6.

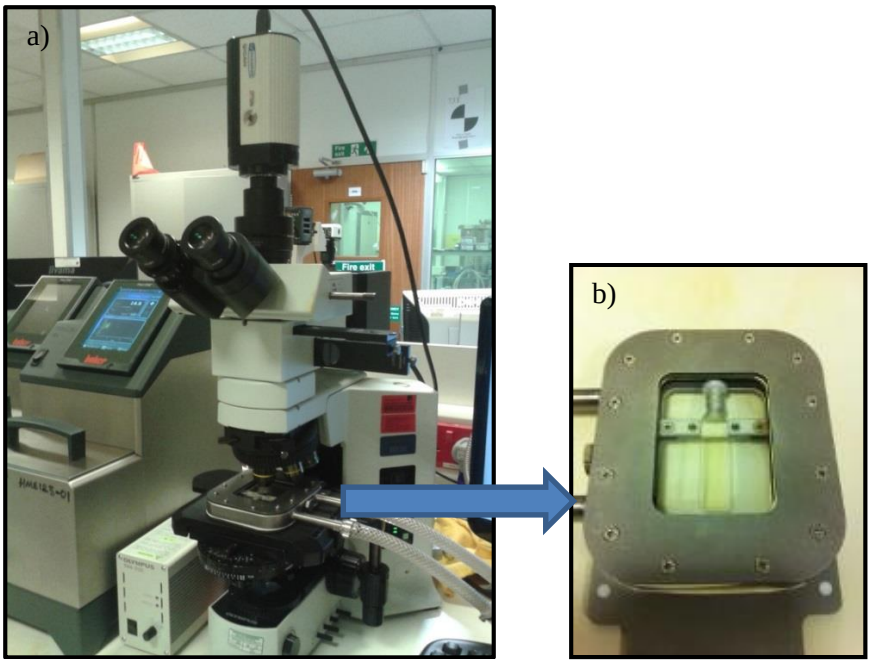

Figure 4.6 Experimental set up for crystal growth rates measurements, after [1]. (a) Olympus BX51 optical DIC microscope integrated with QImaging/QICAM camera. (b) Enlarged picture of the crystal growth cell

4.3.2.1. Experimental procedure

Due the operational working temperature range of the growth cells used, different concentrated solutions were chosen for the analysis. In the case of n-docosane in n-dodecane and C18:0 in n-dodecane and kerosene, solutions with concentrations of 350 g/l of solvent were chosen. Likewise a solution with concentration of 538 g/l was selected for C18:0 in toluene solvent. This allowed for an operation temperature range above 10 °C to avoid any condensation on the walls of the growth cell.

The examination of the crystal growth rates were carried out by crystallising the solutes from supersaturated solutions. The supersaturation required for crystallisation was created by decreasing the solution´s temperature from the equilibrium temperature T_e to different temperatures within the metastable zone. Although the supersaturation was set by decreasing the solution's temperature, circulating water through the cell, the growth of the crystals is only measured until the targeted temperature has been established as shown in Fig. 4.7. The supersaturation level at each temperature was calculated using expression (2.46).

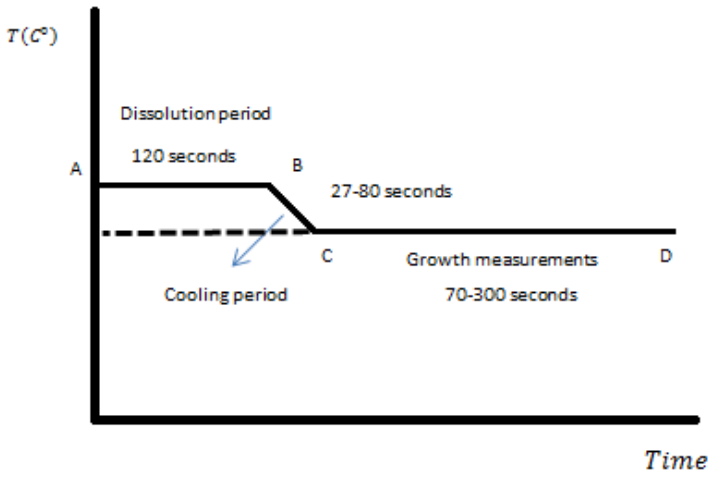

Figure 4.7 Description of the methodology used to reach the temperature at which the growth rate are measured. Typical values of the temperature profile for each segment are: AB (120 seconds), BC (27-80 seconds), CD (70-300 seconds)

The crystal morphology and subsequent growth of the observed crystals was followed by recording images at equal time-intervals, every 30 seconds for the two

lowest σ and every 20 seconds for the highest one for n-docosane in n-dodecane solutions. For solutions of C18:0 in the three solvents, every 5-20 seconds depending of the speed of the crystal growth in each system. Nine, six and four different σ levels were used for crystal growth measurements for n-dodecane, kerosene and toluene solvents respectively. The growth rates of the individual faces were obtained by following the increase with time of the normal distance from the centre of the projected two dimensional $(2D)$ crystal to the faces. Fig. 4.8 shows and example of the measurement procedure for an n-docosane crystal. This is a good approximation of the advancement of the corresponding $(hk0)$ faces as the growth rate of the expected dominant (001) face can be of around two orders of magnitude lower for both n-alkanes and methyl esters crystals. As the micrographs for n-docosane crystals were collected using the microscope in brightfield mode, the contrast of the image edges was found to be very low in terms of their reproduction. Therefore, as an aid to presentation, a perimeter to the crystals was drawn by visual examination using the tools in the image analysis software, in order to delimit the morphology of the crystals and facilitate the subsequent analysis of their respective growth rates. The crystals´ centre for both n-docosane and C18:0 crystals was further defined drawing lines that connected the crystals´ corners defined by the two most important observed faces.

For the most dominant crystal faces ten to fifteen measurements of the normal distance increase were obtained, while for occasional faces appearing with the crystal growth two to seven measurements were recorded.

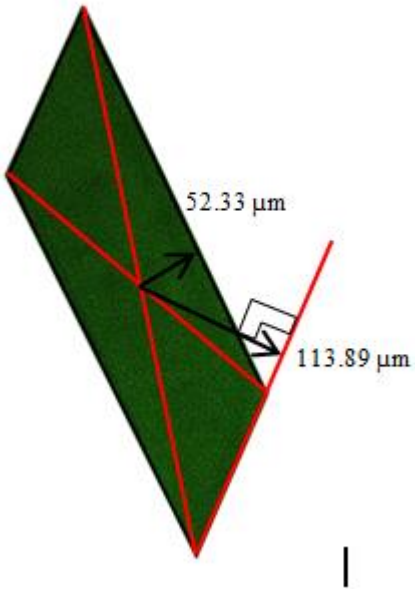

Figure 4.8 Example of measurement of normal distances from the centre of the projected (2D) crystal to the faces of a n-docosane crystal. The distances were obtained using the INFINITY ANALYZE software and the QCapture Pro software, for n-docosane and C18:0 crystal respectively, by drawing a perpendicular line to each face from the centre of the crystal

4.3.3. DSC measurements

The solutes latent heat of crystallisation and melting were measured using a Mettler Toledo Differential Scanning Calorimetry DSC 1 STAR^e system Fig. 4.9. This allowed monitoring the crystallisation transformation of individual 2-3 mg samples placed in aluminium standard 40 µl holders. The sample were subject to a temperature profile initiated by heating the solution up to 40 °C where it was held for an hour to ensure complete homogenization and then cooled to -15 °C where it was also held for an hour to allow equilibration. A constant rate of 0.25 °C/min was used in both the heating and cooling segments. The temperature cycle was repeated five times to obtain average values for the solute heat of crystallisation and melting obtained from the integration of the corresponding exothermic and endothermic peaks.

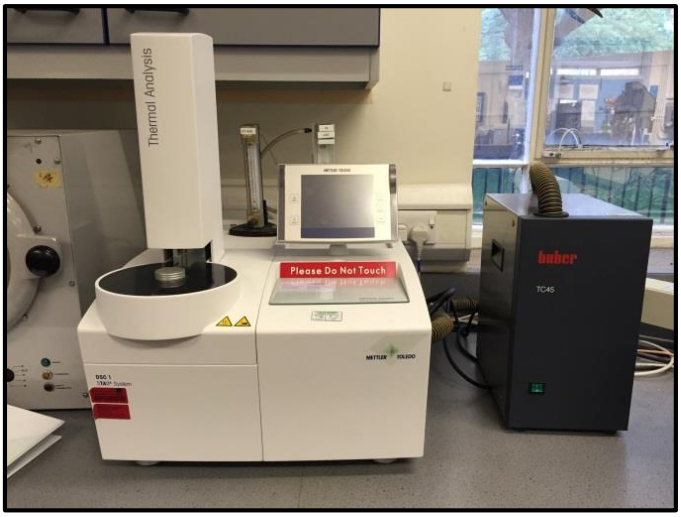

Figure 4.9 Mettler Toledo Differential Scanning Calorimetry DSC 1 STARe system

4.3.4. Crystallization set up and Gas Chromatography (GC)

To determine the total mass of crystals at a given crystallisation temperature, solutions of C18:0 in n-dodecane, kerosene and toluene were crystallised and further analysed using the system shown in Fig. 4.10. Four different solutions´ concentrations were used according to Table 4.3.

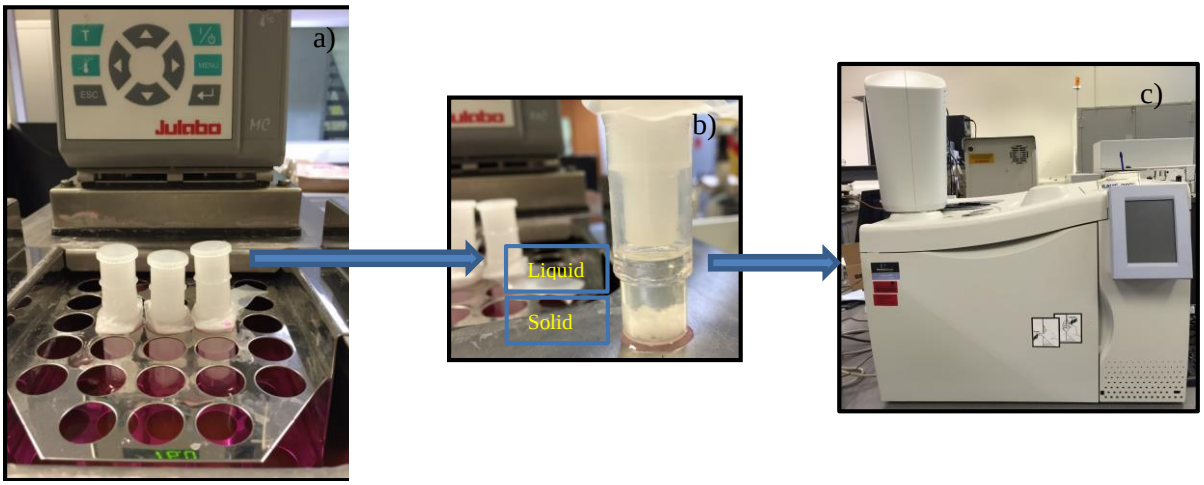

Figure 4.10 Typical experimental set up for the determination of the number of crystals at a given crystallisation temperature T_c. a) crystallisation bath b) filters for phase separation and c) gas chromatography equipment

This comprises syringeless filters which are placed within a thermostatic Julabo bath, set at a specific temperature, corresponding to the crystallisation temperature of the

solution under analysis at stagnant conditions. At each temperature three filters, each containing three millilitres of the solution are allowed to crystallise for a period of 24 hours after they were visible cloudy. Once the equilibration of the solution was reached, each sample was separated, by means of the filters, into the liquid phase containing no crystals and the precipitate which contain the solid crystals (however some liquid entrapped). The precipitate is then allowed to melt and a sample of each of the phases collected from each of the filters was analysed in a Perkin Elmer Clarus 500 Gas Chromatograph (GC) equipment using a SP^{TM} - 2380 column (Fused silica capillary column, 100m x 0.25 mm x 0.2 µm film thickness), with an oven program: initial temperature 140 deg for 5 min, Ramp at 4 deg/min to 240 deg, hold for 15 min.

From the chromatogram obtained from the GC analysis the fraction (percentage) of C18:0 in each phase (liquid and precipitate), at a specific crystallisation temperature, can be calculated from the average of the normalised area under the GC peaks from the three samples analysed. From these values the number of crystals at the related temperature can also be estimated using a procedure described in Chapter 7. This procedure is part of the methodology developed in this research to study nucleation kinetics.

4.3.5. Solutions preparation

All solutions were prepared on a 5 ml scale to equivalent solutions concentrations in grams per litres of solvent as specified in Table 4.3., using a weighing scale of $\pm$ 0.001 g accuracy to weigh the solute and a burette of 0.1 ml accuracy to add the solvent. The solutions were stirred for half an hour with an overhead motor stirrer at 700 rpm and room temperature. Once a homogeneous liquid solution was obtained, a Fisherbrand 100-1000 μl micropipette was used to distribute the solutions in the: 1 ml vials for use in the Crystal 16®, 0.5 ml UV glass cuvettes for use in the growth rig or syringeless filters, adding 3 ml to each of them, for use in the crystallisation rig.

4.4. Data analysis

4.4.1. Solubility

The polythermal data were used to establish the solubility and MSZW of the solutions studied by extrapolation of the $T_{diss}(q)$ and $T_c(q)$ lines to 0°C/min. The solubility was modelled according to the van't Hoff equation (2.43). The corresponding enthalpy ΔH_{diss} and entropy ΔS_{diss} of dissolution were estimated respectively from the slope and intercept with the y axes of these lines.

The solutions´ ideality was assessed by calculating activity coefficients (Υ) using the relationship given by expression (2.22) assuming that in an ideal solution activity (a) is equal to solution concentration (x_{ideal}) or $a = x_{ideal}$ and in a non-ideal solution $a = \Upsilon x_{real}$. At saturation (or equilibrium) these two expressions can be equated and therefore

$$\Upsilon = \frac{x_{ideal}}{x_{real}} \tag{4.1}$$

Thus from the plot in the same coordinate plane of the ideal solubility and the real solubility, the difference between the concentration at saturation (solubility) and that expected for ideality in the same range of temperature (T) will deliver the dependence of activity coefficient (Υ) on T, by the iterative calculation of this parameter through expression (4.1).

If $\Upsilon = 1$ the solution behaves ideally, $\Upsilon > 1$ the activity is higher than concentration and therefore the "effective concentration" will be lower than that at ideality (or less than ideal), $\Upsilon < 1$ the activity is lower than concentration and therefore the "effective concentration" will be higher than that at ideality (or more than ideal). This information can be used to infer information about the solvation of a solute in a solvent as for $\Upsilon > 1$ a significant more association of the solute molecules would be expected. For $\Upsilon < 1$ the molecules would more likely to exist as monomers.

To assess the influence of the solute and solvent molecules polarity on the solubility of methyl stearate (C18:0) its dipole moment was calculated in vacuum using three different methods: semi-empirical:AM1, Hartree-Fock:3-21G and DFT:B3LYP/6-31G* delivering values of 1.67D, 1.54D and 1.52D respectively. (K. Lewtas/ Lewtas Science & Technologies Ltd., personal communication, August 31st , 2015).

4.4.2. Nucleation kinetics

The Kashchiev-Borissova-Hammond-Roberts (KBHR) approach [2, 3] was used to assess nucleation kinetics. This approach uses polythermal crystallisation data to differentiate between two kinetics mechanisms: instantaneous (IN) and progressive nucleations (PN). IN is the case when all crystals are nucleated practically at the initial moment t=0 (within observational limits) and then only grow irreversibly. PN refers to the case when the crystals are continuously nucleated during the process. A detailed description of the derivation of this approach is provided in a subsequent chapter together with development of a reliable experimental method suitable for the application of the models´ expressions. The methodology applied to assess nucleation kinetics is part of the result of this research and is presented in Chapter 5.

4.4.3. Morphological analysis

A methodology for morphological analysis of n-alkanes and methyl esters crystals was developed as part of the results of this research. This uses the Bravais [4], Friedel [5], Donnay and Harker [6] (BFDH) and zone axis methodologies to predict the morphology of crystals for which no detailed crystallographic information is available. Crystals of n-docosane growing from n-dodecane were used to develop the methodology which is then applied to the case of C18:0 growing from n-dodecane, kerosene and toluene solvents. N-docosane crystallises in a triclinic structure, Z=1, $P\bar{1}$, with unit cell parameters a=4.289, b=4.823, c=29.544, α=86.237, β=70.661 and γ=72.097 [7] in good agreement with the predictions of Nyburg and Potworowski [8].

The assessment of the crystals´ morphology was carried out using modelling routines available in both Material Studio (http://accelrys.com/products/materials-studio/) and Mercury 3.1. (http://www.ccdc.cam.ac.uk/Solutions/CSDSystem/Pages/Mercury.aspx). The former was used to initially obtain an estimation of the likely crystal morphology by applying the Bravais [4], Friedel [5], Donnay and Harker [6] (BFDH) model, including a consideration of all possible Miller indices for comparison with the observed morphologies. This approach relates the external shape of a crystal to the internal crystallographic lattice dimensions and symmetry and states that:

> "After allowing for the reduction of the growth slide thickness from space group symmetry considerations, the most morphologically important forms (hkl), and hence those with the lowest growth rates, are those having the greatest inter-planar distance d_{hkl}" .

From the crystals´ unit cell parameters, a crystallographic information file (cif) was produced which provided a list of the most likely crystallographic planes, with the likelihood of their occurrence determined by the in ranking with respect to the highest d_{hkl} spacings. Using the BFDH approach, d_{hkl} spacings can be taken as being inversely proportional to the perpendicular distance from the centre of the crystals to the corresponding face, which in turn can be considered as a measure of the relative growth rate for the simulation of the crystal morphology.

The list of Miller indices delivered from the application of the BFDH approach was then used to further develop a specific methodology for indexation of n-alkanes and methyl esters crystals and is presented in chapter 8 as part of the results of this research.

4.4.4. Crystal growth mechanism

The crystal growth mechanism for C18:0 crystals growing from n-dodecane, kerosene and toluene was investigated by fitting the single faces growth rates dependence on supersaturation σ to the models derived in Chapter 8. These models

include the effect in series of the diffusion of growth units within the bulk and their rate of incorporation to the surface of the crystal, representing different interfacial growth mechanisms, in particular the rough interface (RIG), the Burton-Cabrera-Frank (BCF) and the birth and spread (B&S) models given by equations (2.77-2.80).

4.5. Conclusions

An overview of the equipment and experimental methodologies used for the analysis of the crystallisation process, of representative methyl esters solutions was presented. Given that, as part of the results of this research, three of the subsequent chapters present the development of methodologies for the assessment of: nucleation kinetics, morphology and crystal growth, the information included here was aimed to provide a general overview of the methodologic approach used for the comprehensive analysis of these solutions. The main experimental techniques described include a turbidimetric technique (Crystal 16®), gas chromatography (GC) and in-situ optical microscopy. The first two used to collect data for the assessment of solubility and nucleation kinetics whilst the latter for the assessment of morphology and crystal growth.

References

[1] T.T.H. Nguyen, R.B. Hammond, K.J. Roberts, I. Marziano, G. Nichols, Precision Measurement of the Growth Rate and Mechanism of Ibuprofen {001} and {011} as a Function of Crystallisation Environment, Crystengcomm, 16 (2014) 4568-4586.

[2] D. Kashchiev, A. Borissova, R.B. Hammond, K.J. Roberts, Dependence of the Critical Undercooling for Crystallization on the Cooling Rate, J Phys Chem B, 114 (2010) 5441-5446.

[3] D. Kashchiev, A. Borissova, R.B. Hammond, K.J. Roberts, Effect of cooling rate on the critical undercooling for crystallization, Journal of Crystal Growth, 312 (2010) 698-704.

[4] A. Bravais, Etudes Cristallographiques Paris:Gauthier Villars, 1866.

[5] G. Friedel, Bulletin De La Socit Franaise De Minralogie Et De Crystallographie, 30 (1907).

[6] J.D.H. Donnay, D. Harker, American Mineralogist, 22 (1937) 463.

[7] A.R. Gerson, K.J. Roberts, J.N. Sherwood, X-Ray-Powder Diffraction Studies of Alkanes - Unit-Cell Parameters of the Homologous Series $C_{18}H_{38}$ to $C_{28}H_{58}$, Acta Crystallogr B, 47 (1991) 280-284.

[8] S.C. Nyburg, J.A. Potworowski, Predictions of Unit Cells and Atomic Coordinates for the n-Alkanes, Acta Crystallogr B, B29 (1973) 347-352.

5. Methodology for Determination of the Nucleation Mechanism and Kinetics from Polythermal Crystallisation Data

Summary: A methodology for the assessment of nucleation kinetics from polythermal experimental data is developed

5.1. Introduction

A polythermal methodology to assess the mechanisms and the kinetics of solution crystallisation is described and used in connection with a recently proposed model for the dependence of the critical undercooling for crystallisation on the cooling rate (D. Kashchiev, A. Borissova, R. B. Hammond, K. J. Roberts, J Cryst Growth, 312 (2010) 698–704; J Phys Chem B, 114 (2010) 5441–5446) (Fig.5.1). The methodology is validated through analysis of experimental data measured for methyl stearate crystallising from kerosene solutions with concentrations from 200 to 350 g/l. The theoretical background of the model is initially presented, followed by the development of a suitable experimental method for the collection of experimental polythermal data.

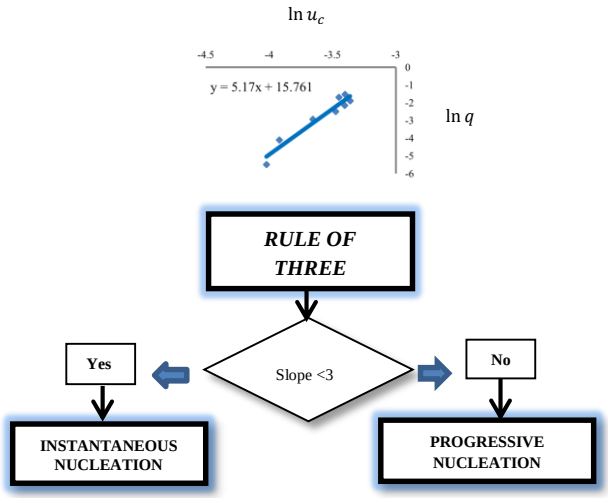

Figure 5.1 Schematic diagram summarising the conceptual approach used by the KBHR model

5.2. Methodology theoretical background

In this section a detailed derivation of the theoretical model used to analyse polythermal experimental data is given. The derivation is presented within the Chapter as part of the methodology development, in order to provide a more accessible account of the model´s fundamental background. This was originally presented in a comprehensive theoretical study [1, 2], that deals with the problem of the effect that the cooling rate (q) has on the metastable zone width $(MSZW)$.

Regardless of the mechanism by which the crystals are formed , the solution appears to remain unaffected until the level of supersaturation corresponding to the $MSZW$ is reached [3]. The $MSZW$ depends on the crystallites nucleation and growth kinetics, which in turn are influenced by a number of crystallisation environmental parameters such as the equilibrium (or saturation) temperature T_e, cooling rate q, solution agitation, presence of impurities and seeds and the solvents used [1, 3]. Alternative expressions for the $MSZW$ can be given in terms of either concentration or temperature. Among the most common are those for the maximum concentration difference (ΔC_{max}) and the critical undercooling ΔT_c. The former quantity is defined as:

$$\Delta C_{max} = C_{max} - C_e \tag{5.1}$$

where C_{max} is the solution concentration at the limit of metastability, and C_e is the equilibrium solution concentration (or the solubility).

Similarly, the critical undercooling ΔT_c is defined as:

$$\Delta T_c = T_e - T_c \tag{5.2}$$

where T_e and T_c are the solution equilibrium and crystallisation temperatures, respectively.

A dimensionless quantity associated with the critical undercooling ΔT_c is the relative critical undercooling (u_c) given by:

$$u_c = \frac{\Delta T_c}{T_e} \tag{5.3}$$

5.2.1. The *KBHR* Approach

According to the $KBHR$ approach, the dependence of $ln\,\Delta T_c$ on $ln\,q$ is not linear and manifests itself differently depending on the nucleation mechanism involved.

This approach applies to the early stage of crystallisation because of its treating the crystallites as not contacting each other. It makes use of the nucleation rate formula of the classical three dimensional $(3D)$ nucleation theory for stationary HON and HEN. As in practice the limit of metastability can only be registered when crystallites have already grown to a detectable size and/or number, the model presents expressions that relate this limit to either the fraction (α_{det}) of crystallised volume or the number (N_{det}) of nucleated crystallites at the detection point in which both the nucleation and the growth rates of the crystallites would have an influence.

The $KBHR$ approach is based on the Kolmogorov-Johnson-Mehl-Avrami $(KJMA)$ equation [4] for the time dependence of the fraction α of crystallised volume. This fraction is defined as:

$$\alpha = \frac{V_c}{V} \tag{5.4}$$

where V_c and V are the total crystallite volume and the solution volume respectively

5.2.1.1. Progressive nucleation case

The analytical performing of the integral in the $KJMA$ equation [1, 5] allows obtaining the dependence of the relative critical undercooling u_c on the cooling rate q at the early stage of the crystallisation when u_c meets the inequalities [1]:

$$u_c < 0.1, au_c < 1 \tag{5.5}$$

$$u_c < \left(\frac{2b}{3}\right)^{1/2} \tag{5.6}$$

Here, the dimensionless, molecular latent heat of crystallisation a, is defined by:

$$a = \frac{\lambda}{kT_e} \tag{5.7}$$

where λ is the molecular latent heat of crystallisation and k is the Boltzmann constant. The dimensionless thermodynamic parameter b of $3D$ nucleation is defined by

$$b = \frac{k_n v_o^2 \gamma_{eff}^3}{k T_e \lambda^2} \tag{5.8}$$

where k_n is the nucleus shape factor (e.g., $16\pi/3$ for spherical nuclei and 32 for cubic nuclei) [4], v_o is the volume occupied by a solute molecule in the crystal, γ_{eff} is the nucleus effective interfacial tension.

The final expression for the $u_c(q)$ dependence is derived [1] by accounting for the increase of either the number N of crystal nuclei or the crystallised volume fraction α with the steadily increasing undercooling (u) (see also Appendix A). For u_c determined by the number $N_{det}$of crystallites at the detection point this expression is of the form [1]:

$$ln\, q = ln\, q_0 + a_1\, ln\, u_c - \frac{a_2}{(1-u_c){u_c}^2} \tag{5.9}$$

Here the free parameters a_1, a_2 and q_0 are given by:

$$a_1 = 3 \tag{5.10}$$

$$a_2 = b \tag{5.11}$$

$$q_0 = \frac{V k_J T_e}{N_{det}\, 2b} \tag{5.12}$$

where k_J is the nucleation rate constant.

When equation (5.9) is derived by means of the fraction α_{det} of crystallised volume at the detection point, the parameters a_1, a_2 and q_0 read [1]:

$$a_1 = 3 + \frac{3nmd}{md+1} \tag{5.13}$$

$$a_2 = \frac{b}{md+1} \tag{5.14}$$

$$q_0 = T_e \left\{ \frac{\Gamma[(n+1)md+1] k_v a^{nmd} k_J k_G^{md}}{(n+1)^d \ (2b)^{(n+1)md+1} \alpha_{det}} \right\}^{\frac{1}{(md+1)}} \tag{5.15}$$

where Γ is the complete gamma function, d is the dimensionality of crystallites growth, i.e. 3 for spheres or cubes, 2 for disks or plates and 1 for needles, k_v is the crystallites growth shape factor, i.e. $\frac{4\pi}{3}$ for spheres, 8 for cubes, πH_0 for disks, $4H_0$ for square plates (H_0 is the fixed disk or plate thickness), and $2A_0$ for needles (A_0 is the fixed needle cross-sectional area), k_G is the growth rate constant, and n and $m > 0$ are the crystallite growth exponents which are related to the different growth mechanism [4]. The $n = 1$ case corresponds to growth mediated by diffusion of solute towards the crystallite or transfer of solute across the crystal/solution interface. The $n = 2$ case characterises growth controlled by the presence of screw dislocations in the crystallite. The parameter m ranges between ½ and 1: $m = 1/2$ is for growth controlled by undisturbed diffusion of solute, and $m = 1$ is for growth by diffusion of solute through a stagnant layer around the crystallite or for normal or spiral growth limited by transfer of solute across the crystal/solution interface. At $m = 1$ the crystallite radius increases linearly with time [1, 2, 4].

The parameters in the model expression (5.9) q_0, a_1 and a_2 all have a distinct physical meaning because a_1 relates to the crystallites growth as its value is determined by the growth exponents n, m and d, a_2 is a fraction of or equal to the thermodynamic nucleation parameter b, and q_0 is expressed by parameters of both the nucleation and the growth of the crystallites.

The critical radius of the nucleus (r^*) and the number (i^*) of molecules in the critical nucleus can be calculated from the equations [1]:

$$r^* = \frac{2\gamma_{eff} v_0}{\lambda u} \tag{5.16}$$

$$i^* = \frac{2bkT_e}{\lambda u^3} \tag{5.17}$$

5.2.1.2. Instantaneous nucleation case

In the case of IN a similar use of the $KJMA$ equation is possible [2, 5] within the limit established by inequalities (5.5) but now by taking into account that all crystal nuclei appear simultaneously with a concentration C_o at a moment t_o corresponding to relative undercooling u_0 defined as:

$$u_o = \frac{\Delta T_o}{T_e} \tag{5.18}$$

Here ΔT_o is given by:

$$\Delta T_0 = T_e - T_0 \tag{5.19}$$

where T_o is the solution temperature at the time t_o.

Thus the dependence of relative critical undercooling on the cooling rate can be expressed as [2]:

$$\ln q = \ln q_0 + \left(\frac{1}{m}\right) \ln\left[u_c^{(n+1)m} - u_0^{(n+1)m}\right] \tag{5.20}$$

In this expression $u_0 \geq 0$, $u_c > u_o$ and the parameter q_0 is given by:

$$q_o = \left[\frac{k_v C_o}{(n+1)^d \alpha_{det}}\right]^{\frac{1}{md}} a^n k_G T_e \tag{5.21}$$

If additionally, the undercooling u_0 at which all nuclei appear simultaneously is small enough to satisfy the inequality:

$$u_o^{(n+1)m} \ll u_c^{(n+1)m} \tag{5.22}$$

then equation (5.20) takes the Nyvlt-type form [2]

$$\ln q = \ln q_o + (n+1) \ln u_c \tag{5.23}$$

As shown by Kashchiev et al. [1], for a small range of q values equation (5.9) can also be expressed in the form of a Nyvlt-type equation:

$$ln\, q = ln\, Q + \left(3 + \frac{3nmd}{md+1} + \omega a_2\right) ln\, u_c \tag{5.24}$$

Here the parameter Q is related to q_o and a_2 in equation (5.9), and ω is a positive number.

Comparing the factor in front of $ln\, u_c$ in equation (5.23) for the case of IN with the one in equation (5.24) for the case of PN leads to the important findings of the $KBHR$ approach that this term is always less than three in the IN case and greater than three in the PN case because n, m and ω are positive numbers and typically $n \leq 2$ [2]. This so called "rule of three" [2] is practically very helpful in that when experimental $u_c(q)$ data are plotted in $ln\, q$ vs. $ln\, u_c$ coordinates and fitted by a straight line, the slope of the line will directly indicate the nucleation mechanism, PN or IN, governing the crystallisation process.

Although the application of the presented $KBHR$ expressions for the $u_c(q)$ dependence is restricted by inequalities (5.5), this restriction is not too severe, as even for rather low values of equilibrium temperature (e.g. $T_e = 273\ K$), the maximum critical undercooling ΔT_c satisfying the first of these inequalities would

have a value, large enough from experimental point of view ($27.3\,K$ for the above example). This means that in the above example only when ΔT_c > 27.3 the model would not be applicable.

A flow chart summary of the procedure needed to practically apply the $KBHR$ approach [1, 2] is given in Fig. 5.2*.

* A more detailed explanation of the derivation of the expressions here presented is available in the Appendix A.

Figure 5.2 Flowchart describing the procedure to follow in order to apply (KBHR) approach for the interpretation of metastable zone width data ($MSZW$) collected by means of the polythermal method

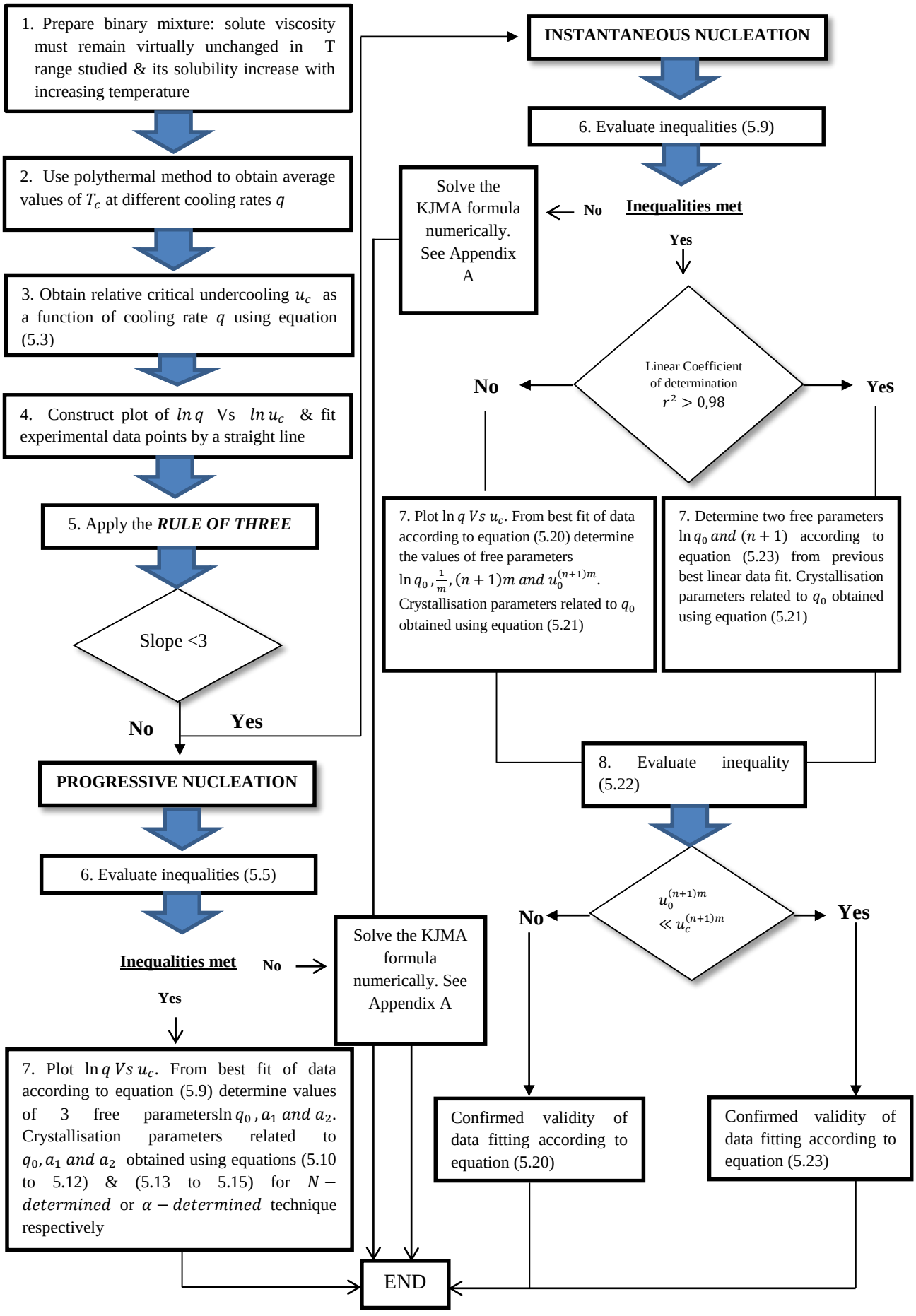

The following two sections include the experimental methodology and the steps required for the analysis of experimental data according to the $KBHR$ approach.

5.3. Development of experimental method

5.3.1. Polythermal measurements and data analysis

A large set of experimental $T_c\ (q)$ data was collected and analysed with the aim of validating an experimental procedure for the application of the $KBHR$ approach to crystallisation systems of practical interest.

Using the turbidimetric technique described in section (4.3.1) of the methodology solutions of methyl stearate (C18:0) in kerosene were analysed. They were subject to heating and cooling cycles, with each cycle initiated by heating the solutions up to 40°C where they were held for an hour to ensure complete homogenization and then cooled to 15°C where they were also held for an hour to allow equilibration. This temperature profile was applied at each solution's concentration using eight different rates 0.25, 1, 3.2, 5, 7, 9, 11 and 13 °C/min which were used in both the heating and cooling segments. At each rate the temperature cycle was repeated ten times to obtain average values for the crystallisation and dissolution temperatures T_c and T_{diss}. This approach was important in terms of improving the data fitting and minimising the standard deviation (SD) of the crystallisation temperatures T_c.

The crystallisation and dissolution temperatures were estimated based upon the points in the turbidity profile at which sudden changes in light transmittance are detected. Crystallisation temperatures were taken as the points at which the light transmittance suddenly decreased from 100% to at least 90% as in all measurements performed, this decreased was always of at least 10%. Similarly, dissolution temperatures were taken as the points at which the light transmittance increased from 0% to at least 20%. This was done as in some measurements a stabilisation period for the transmittance of the light was required, corresponding to a difference of no more than 0.5 degree, between the temperature at which the first change was detected and that of stabilisation of transmittance. Fig. 5.3 shows a typical

experimental profile together with a representative raw data set for one of the experimental runs.

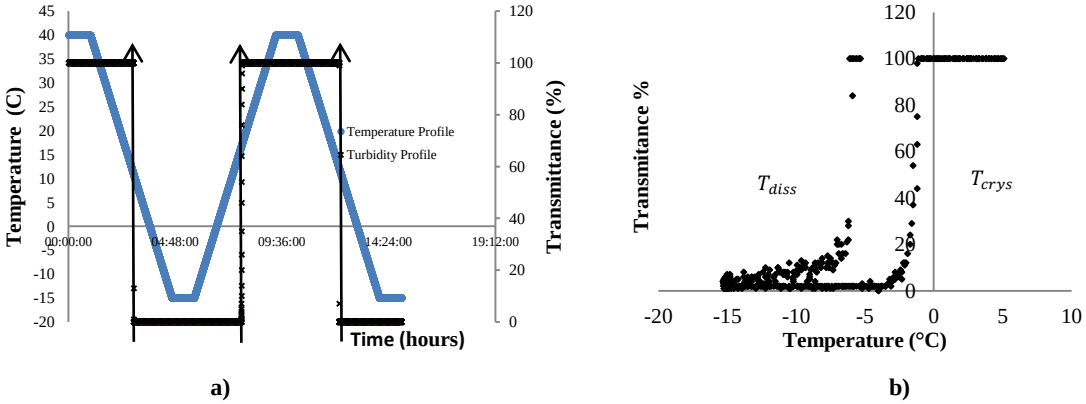

Figure 5.3 a) Typical experimental profile using Crystal 16® by applying the polythermal method. b) Representative turbidity profile in transmittance vs. temperature coordinates obtained by the application of a polythermal method

The $KBHR$ approach was applied to the process and used to analyse the polythermal data. At each concentration the average values of the dissolution and crystallisation temperatures were plotted as a function of cooling rate q. These data points were then fitted by straight lines to obtain the interrelationship of the $MSZW$ as a function of the cooling rate. The solubility-supersolubility curves were constructed out of the extrapolation of these lines to zero cooling rate from which the associated values of T_{diss} and T_c were determined. The extrapolation of the T_{diss} lines delivering the solution equilibrium temperature T_e. Fig. 5.4 gives an example of the extrapolation of the best linear fit to $T_{diss}(q)$ and $T_c(q)$ data points for a concentration of 200 g/l.

Using equation (5.2), at each concentration and cooling rate the critical undercooling ΔT_c was calculated from the average of the experimental crystallisation temperatures T_c and the corresponding solution equilibrium temperatures T_e. Then the relative critical undercooling u_c was obtained from equation (5.3).

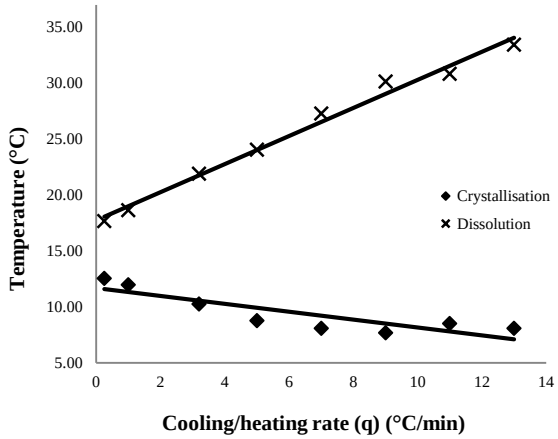

Figure 5.4 Extrapolation to zero cooling rate of the best linear fit of $T_{diss}(q)$ and $T_c(q)$ data points for a concentration of 200 gr/l. The best linear fits are represented by expressions $y = 1.25x + 17.77$ and $y = -0.35x + 11.67$ for $T_{diss}(q)$ and $T_c(q)$ respectively.

For each concentration, a plot of $u_c(q)$ data in $ln - ln$ coordinates was obtained and the data points fitted to a straight line from which the numerical value of the slope was used to assess the nucleation mechanism governing the process.

Following this, the data were analysed using the procedure summarised in Fig. 5.2 and the effective interfacial tensions γ_{eff} for the crystallite nucleus determined. Numerical values for r^* and i^* were calculated using equations (5.16) and (5.17), respectively.

5.3.2. Isothermal measurements and data analysis

With the aim of assessing the results obtained through the application of this methodology, nucleation parameters were also calculated using an isothermal method. Supersaturation values used for the isothermal methodology were chosen with reference to the characterization of the $MSZW$ determined using the solubility-supersolubility relationship given in Fig. 5.6. For each solution concentration four different temperatures within the $MSZW$ were chosen to carry out the isothermal crystallisation experiments. The $MSZW$ was typically about 6ºC (see Fig. 5.6). However, the measured induction times at temperatures corresponding to lower undercooling values were too long for practical measurements and so the data was obtained within a small temperature range (12-12.8 ºC, 14-14.8 ºC, 17-18 ºC and

17.8-18.5 ºC for 200, 250, 300 and 350 g/l, respectively), see tabulated values given in Table 6.6.

The 1 ml solutions were heated up to 10 °C above the corresponding solute dissolution temperature, in this case 28, 30, 32 and 33 °C for 200, 250, 300 and 350 g/l respectively. The solutions were held for an hour at this temperature to ensure homogenization, and then rapidly cooled down at a constant rate of 10 °C/min, down to the chosen temperature within the $MSZW$, where the supersaturated solutions were maintained and stirred until the onset of crystallisation was detected. The induction time τ was monitored by the change in the solution turbidity, from the time at which the solution reached the predetermined temperature to that of the crystallisation onset, which corresponds to the time at which the light transmittance suddenly decreases from 100%. For each concentration, four different temperatures were used together with four repeat measurements at each of the chosen temperatures. Fig. 5.5 shows an experimental temperature profile from one of the runs together with a representative raw data set.

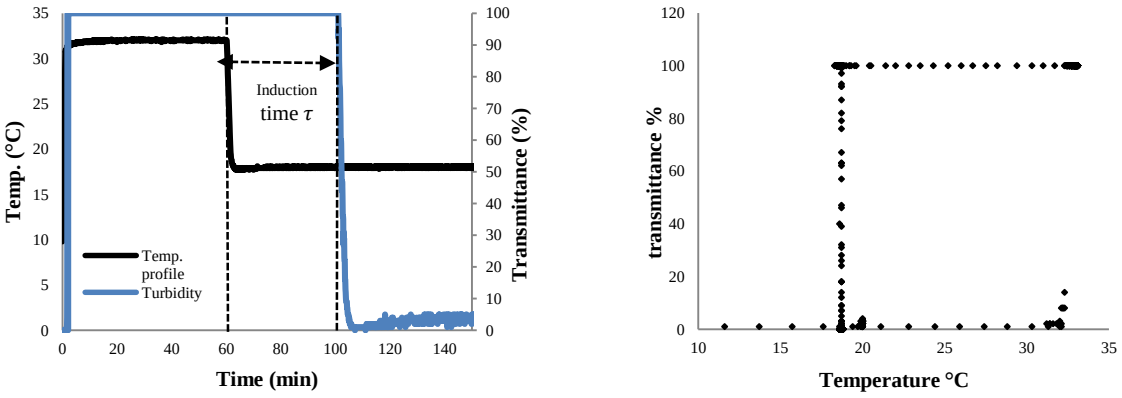

Figure 5.5 a) Crystal 16® typical experimental profile obtained by the application of the isothermal method b) Representative turbidity profile in transmittance vs temperature coordinates obtained by the application of the isothermal method

For each solution concentration, the average induction times τ for each of the chosen temperatures T were plotted in $\ln\left\{\tau[S(S-1)^{md}]^{\frac{1}{1+md}}\right\}$ vs $\frac{1}{T^3(\ln S)^2}$ coordinates and fitted by a straight line. The slopes of the lines were then used to obtain the effective

interfacial tensions γ_{eff} according to equation (2.74). The values of r^* and i^* were calculated using equations (2.75) and (2.76) respectively.

5.4. Methodology assessment

5.4.1. Polythermal data

The polythermal data were processed to obtain the solubility-supersolubility curves and nucleation parameters by applying the $KBHR$ approach. The average values for the collected crystallisation and dissolution temperatures and their standard deviations SD together with the critical undercooling ΔT_c at the corresponding concentrations and cooling rates are presented in Table 5.1. The correlation coefficients R^2 for the $T_{diss}(q)$ lines used to obtain equilibrium temperature T_e are presented in Table 5.3.

Fig. 5.6 shows the data points obtained for the equilibrium dissolutions and crystallisation temperatures at each concentration as described in detail in Sub-section 6.3.1. The solubility-supersolubility lines were plotted by fitting these data points using an exponential regression which in the case of the solubility curve delivers an expression of the form $y = 31.65e^{0.1037x}$.

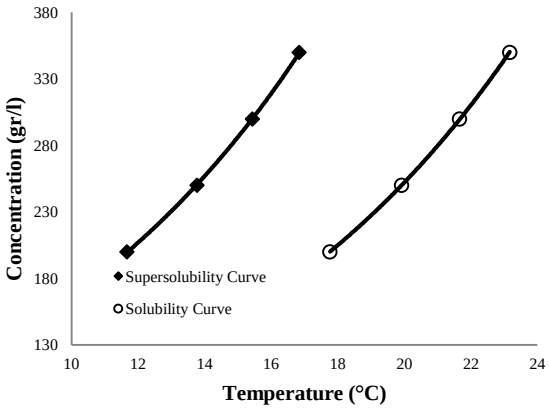

Figure 5.6 Solubility-supersolubility curve of methyl stearate in kerosene. Supersolubility curve data points obtained by extrapolating to the Y-axis the best linear fit of cooling rate q vs. crystallisation temperature T_c of the data obtained by the polythermal method at each concentration. Solubility curve data points obtained by extrapolating to the Y-axis the best linear fit of cooling rate q vs. dissolution temperature T_{diss} of the data obtained by the polythermal method at each concentration

For each concentration, the results of the relative critical undercooling u_c calculated at each cooling rate q are given in Table 5.2. The $u_c$values are within the limits specified by inequalities (5.5). This means that in all cases the experimentally obtained limit of metastability corresponds to a relatively low supersaturation for which the use of the $KBHR$ approach is justified.

For each concentration a plot of cooling rate q vs. relative critical undercooling u_c in *ln-ln* coordinates was then constructed to obtain the slope of the straight line fitting these data points. Fig. 5.7 presents the plot obtained for a concentration of 200 g/l for which the best linear fitting to the data is given by $y = 5.17x + 15.76$. The slope and the correlation coefficient R^2 of the best-fit straight line to the data at each concentration are presented in Table 5.3.

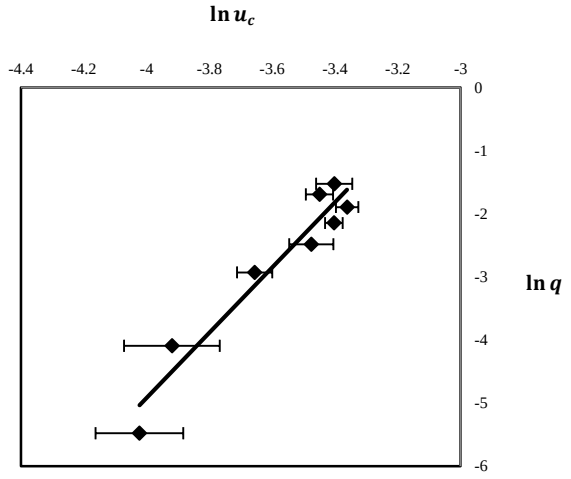

Figure 5.7 Plot of experimental data in ln q Vs ln u_c coordinates for methyl stearate in kerosene at a concentration of 200 g/l

In all cases the slopes of the lines are higher than 3, suggesting that crystallisation of methyl stearate in solution with kerosene proceeds via the PN mechanism. Thus, according to the $KBHR$ approach, equation (5.9) should describe the experimental data plotted in $ln\, q$ vs. u_c coordinates as detailed in the procedure to apply the $KBHR$ approach given in Fig. 5.2. To obtain the parameters a_1, a_2 and $ln\, q_0$, the fit of this equation to the experimental data was done using OriginPro 8.5.1. through a nonlinear least-square method . The values of these parameters for each of the

solution concentrations and the correlation coefficients for the fitting of equation (5.9) to the experimental data are presented in Table 5.3.

The best-fit curves that minimises the sum of squares of the deviations between the experimental $u_c(q)$ values and those calculated from equation (5.9) were obtained by setting $a_1 = 3$. An example of such a curve for the concentration of 200 g/l is presented in Fig. 5.8.

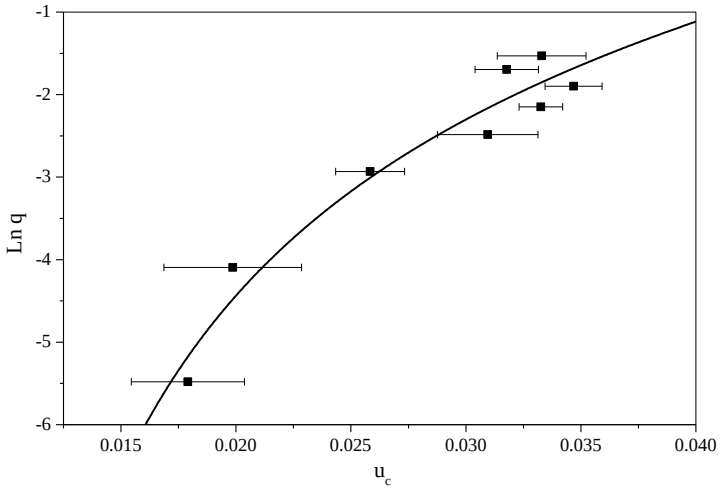

Figure 5.8 Increase in relative critical undercooling with the natural logarithm of cooling rate. The points represent the data for crystallisation of methyl stearate in solution with kerosene 200 g/l; the line illustrates the best fit according to equation (5.9)

As in all cases a_1 is set equal to 3, equations (5.11) and (5.12) can be used to proceed further. According to equation (5.11) a_2 equals b, a dimensionless thermodynamic parameter defined by equation (5.8) from which the γ_{eff} can be calculated. The results obtained for $\ln q_0$ yield the values of q_o, a parameter related through equation (5.12) to the nucleation rate constant k_J and the number N_{det} of crystallites at the detection point.

The effective interfacial tension γ_{eff} was evaluated from equation (5.8), using $v_o = 0.491\, nm^3$ [6], the calculated equilibrium temperatures T_e, the shape factor $k_n = \frac{16}{3}\pi$ for spherical nuclei and the molecular latent heat λ of crystallisation estimated to be $8.98\, x\, 10^{-20}\, J$ from measurements of the solute heat of crystallisation using DSC.

Table 5.1 Average dissolution and crystallisation temperatures as a function of cooling rate for methyl stearate in kerosene at solution concentrations 200, 250, 300 and 350 g/l. Standard deviation of crystallisation and dissolution temperatures. Critical undercooling ΔT_c calculated according to equation (5.2). Equilibrium temperatures T_e obtained from extrapolation of best-fit straight lines through $T_{diss}(q)$ data points

Rate ℃ /min	T_c (℃)	$SD\ T_c$ (℃)	T_{diss} (℃)	$SD\ T_{dss}$ (℃)	ΔT_c
200 g/l					
0.25	12.56	0.72	17.69	0.08	5.21
1.00	11.99	0.87	18.66	0.07	5.77
3.20	10.26	0.44	21.92	0.28	7.51
5.00	8.77	0.63	24.07	0.48	9.00
7.00	8.10	0.28	27.29	0.65	9.67
9.00	7.68	0.36	30.16	0.78	10.08
11.00	8.53	0.40	30.85	1.58	9.24
13.00	8.09	0.56	33.46	1.38	9.68
			T_e=17.77		
250 g/l					
0.25	14.88	0.63	19.59	0.09	5.04
1.00	14.16	0.84	20.81	0.18	5.76
3.20	12.15	0.50	24.85	0.39	7.78
5.00	10.82	0.41	28.49	0.42	9.10
7.00	10.27	0.54	31.88	0.67	9.66
9.00	9.09	1.00	34.12	0.96	10.83
11.00	10.49	0.49	36.30	2.04	9.44
13.00	10.54	0.30	38.78	0.46	9.38
			T_e=19.93		
300 g/l					
0.25	16.54	0.48	21.03	0.06	5.12
1.00	15.29	0.45	22.46	0.18	6.38
3.20	13.96	0.50	26.87	0.44	7.70
5.00	12.95	0.43	29.88	0.81	8.71
7.00	11.53	0.49	33.68	0.66	10.13
9.00	10.82	0.55	35.88	0.85	10.84
11.00	11.66	0.53	37.30	1.59	10.01
13.00	11.80	0.34	40.03	0.52	9.86
			T_e=21.66		
350 g/l					
0.25	17.75	0.47	22.19	0.10	5.42
1.00	16.85	0.28	23.71	0.18	6.32
3.20	15.12	0.50	28.29	0.53	8.05
5.00	14.33	0.45	31.44	0.93	8.84
7.00	13.31	0.42	35.36	0.81	9.86
9.00	11.69	0.31	37.52	0.94	11.48
11.00	12.86	0.40	38.96	1.34	10.31
13.00	12.91	0.45	40.12	0.38	10.26
			T_e=23.17		

Table 5.2 Relative critical undercooling u_c as a function of concentration and cooling rate for solution of methyl stearate in kerosene

	u_c			
Cooling rate $q\ \left(\frac{K}{s}\right)$	200 g/l	250 g/l	300 g/l	350 g/l
0.004	0.0179	0.0172	0.0174	0.0183
0.017	0.0199	0.0197	0.0216	0.0213
0.053	0.0258	0.0266	0.0261	0.0272
0.083	0.0310	0.0311	0.0296	0.0299
0.117	0.0333	0.0330	0.0344	0.0333
0.150	0.0347	0.0370	0.0368	0.0388
0.183	0.0318	0.0322	0.0340	0.0348
0.217	0.0333	0.0320	0.0335	0.0347

Table 5.3 Saturation temperatures and corresponding correlation coefficients of the best linear fitting of $T_{diss}(q)$ data; slopes of the best linear fit to data points in ln q vs. ln u_c coordinates and correlation coefficients; values of the free parameters a_1, a_2 and $ln\, q_o$ obtained from the data fitting in $ln\, q$ vs. u_c coordinates according to equation (5.9) and correlation coefficients (the values are for solution concentrations of 200, 250, 300, and 350 g/l, and the errors of the slope and the free parameters refer to the 95% confidence interval)

Con. (g/l)	$T_e(K)$	R^2, fitting $T_{diss}(q)$	Slope of best-fit straight line of $\ln u_c$ $vs. \ln q$	R^2, linear fitting	Nucleation Mechanism	a_1	$a_2 = b$	$\ln q_0$	$q_0\left(\frac{K}{s}\right)$	R^2, fitting equation (5.9)
200	290.77	0.99	5.17±0.57	0.93	PN	3	0.000654±0.000148	8.966±0.25	7834.0	0.94
250	292.93	0.99	4.82±0.59	0.92	PN	3	0.000543±0.000147	8.806±0.26	6673.5	0.93
300	294.66	0.98	5.05±0.47	0.95	PN	3	0.000629±0.000113	8.826±0.19	6811.2	0.97
350	296.17	0.96	5.06±0.51	0.94	PN	3	0.000698±0.000126	8.819±0.20	6761.1	0.96

Table 5.4 Interfacial tension, critical radius and number of molecules for nucleation of methyl stearate in kerosene at four solution concentrations (the Critical radius and number of molecules are calculated at $u_c = 0.035$ and 0.017

Concentration (g/l)	$\gamma_{eff}\ (mJ/m^2)$	$r^*(nm)$	i^*
200	1.74	0.54-1.12	1-12
250	1.64	0.51-1.05	1-10
300	1.72	0.54-1.11	1-12
350	1.79	0.56-1.15	1-13

Also, the critical nucleus radius r^* and number i^* of molecules at $u_c = 0.017$ and 0.035, the lowest and the highest experimentally determined relative critical undercoolings, were calculated from equation (5.16) and (5.17) respectively. The values obtained are given in Table 5.4.

A comparison of the correlation coefficients R^2 and the errors of the parameters shows that a better fit is obtained when a non-linear regression is applied, a result that should be expected in the scope of the $KBHR$ approach according to which the dependence of the critical undercooling on the cooling rate is not linear. It has been shown [1] that only in a sufficiently narrow q range $ln\, u_c$ and $\ln q$ are approximately linearly related, with the slope revealing the governing nucleation mechanism. A more elaborate statistical analysis comparing the goodness of the fitting models to describe the experimental $u_c(q)$ data reinforces the suitability of using equation (5.9) of the $KBHR$ approach for the polythermal data analysis. The standard deviations SD and covariance of the parameters in the two models are presented in Table 5.5.

Table 5.5 Standard deviation and covariance of the parameters in the linear regression model according to equation (5.24) and the parameters in the regression model according to equation (5.9)

Linear Fitting according to equation (5.24)						
Concentration (g/l)	Slope Standard Deviation (SD)	Intercept Standard Deviation (SD)	Covariance Slope-Intercept			
200	1.48	5.33	7.89			
250	1.39	5.00	6.95			
300	1.43	5.12	7.33			
350	1.44	5.12	7.38			
Fitting according to equation (5.9)						
Concentration (g/l)	$\ln q_0$ Standard Deviation (SD)	a_1 Standard Deviation (SD)	a_2 Standard Deviation (SD)	Covariance $\ln q_0 - a_1$	Covariance $\ln q_0 - a_2$	Covariance $a_1 - a_2$
200	34.42	10.92	0.0032	375.79	-0.11	-0.03
250	24.47	11.99	0.0034	453.88	-0.13	-0.04
300	22.63	11.16	0.0033	391.36	-0.11	-0.04
350	26.17	10.24	0.0032	326.06	-0.10	-0.03

A relatively high standard deviation is observed for the fitting according to equation (5.9), which also has an influence on the values of the covariance between the parameters $ln\, q_0$ and a_1. However the covariance is very low in all other cases. This suggests that the model according to equation (5.9) provides a good fit to the collected polythermal experimental data and can be used to proceed with further calculations.

The low values of the effective interfacial tension are an indication of a prevalence of HEN mechanism for the nucleation of the methyl stearate crystallites. These values have the order of magnitude of those reported earlier for HEN of m-ABA and L-His [7] and are very similar to those of other organic molecules such as eflucimibe [8], paracetamol [9], ketoprofen [10] and n-alkanes [11-14]. In the latter case, although some of the values are lower, there are others that are equivalent or very close to those obtained for methyl stearate crystals, as in the case of the interfacial tensions reported for $C_{20}H_{42}/C_{21}H_{44}$ and $C_{20}H_{42}/C_{22}H_{46}$ solute mixtures in solution with dodecane (see Table 5.9.).

Through the use of equation (5.12), the nucleation rate constant could also be estimated but this requires the corresponding values of N_{det}, the number of crystallites formed at the detection point, for which additional experimental work would be necessary.

The collection of all data presented above was not an easy task, as it required running 320 temperature cycles, each of which can last an average of three hours. Thus, a sensitivity analysis for the applied experimental methodology was carried out. Three additional scenarios were used with the aim of assessing the influence that reducing the number of cooling rates and/or temperature cycles would have on the parameters obtained by applying the $KBHR$ approach. It was found that reasonable interfacial tension values were still obtained even by a 50% reduction of the number of both the cooling rates and the T_c measurements. This analysis suggests that a reduced data set of four cooling rates q and five temperature cycles at each cooling rate would be sufficient for this work*. The experimental data were also analysed using the empirical Nyvlt approach. These results showed that the slopes of the lines obtained from best linear fit to the experimental data by employing the Nyvlt linearization can be 1.5 to 2.5 times lower than those obtained by best fit to the data in the coordinates corresponding to the $KBHR$ approach*

5.4.2. Isothermal data and comparison with the polythermal results

The analysis of the data for the induction time τ data as a function of the supersaturation ratio S was carried out in order to calculate nucleation parameters and compare them with those obtained by the analysis of the polythermal data. The average values of τ obtained as a function of S and the solution concentration are given in Table 5.6.

At each concentration, a linear dependence of $\ln\left\{\tau[S(S-1)^{md}]^{\frac{1}{1+md}}\right\}$ on $\frac{1}{T^3(\ln S)^2}$ was found with assumed $m = 0.5$ and $d = 2$, values corresponding to diffusion-controlled crystallite growth in two dimensions of space [4]. The choice of the d value is supported by pictures of methyl stearate crystals obtained experimentally, in

* Details of the sensitivity analysis are presented in the Appendix A of the supplementary material.

* Analysis of the experimental data using the Nyvlt approach along with a useful expression that relates the slopes of the experimental data linearization using the Nyvlt and the $KBHR$ approaches is presented the Appendix A.

which a plate-like morphology was observed. Interfacial tensions were calculated from the slopes of the straight lines predicted by equation (2.74). Fig. 5.9 shows an example of the plot obtained for a concentration of 200 g/l for which the best linear fit to the data is represented by $y = 6 * 10^7 x - 1.74$.

Table 5.6 Induction time as a function of supersaturation ratio for solutions of methyl stearate in kerosene. Solutions of 200, 250, 300, 350 g of solute per litre of solvent cooled to four holding temperatures within the corresponding metastable zone

$T(°C)$	$T(°K)$	*Average Induction time* (τ)(sec)	*Equilibrium concentration* C_e $(\frac{g}{l})$ *at the holding temperature*	*Supersaturation ratio* (S)
200 g/l				
12.0	285.0	240	109.87	1.57
12.3	285.3	675	113.34	1.54
12.5	285.5	915	115.72	1.51
12.8	285.8	3525	119.37	1.48
250 g/l				
14.0	287.0	345	135.19	1.60
14.3	287.3	600	139.46	1.56
14.5	287.5	2385	142.39	1.54
14.8	287.8	2430	146.89	1.50
300 g/l				
17.0	290.0	405	184.53	1.45
17.3	290.3	315	190.36	1.42
17.5	290.5	825	194.35	1.39
18.0	291.0	1395	204.69	1.34
350 g/l				
17.8	290.8	1155	200.49	1.52
18.0	291.0	2250	204.69	1.50
18.3	291.3	2505	211.16	1.46
18.5	291.5	4200	215.58	1.44

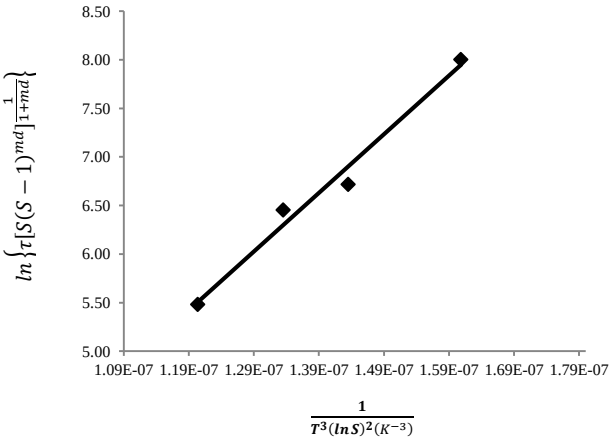

Figure 5.9 Linear fit of experimental $\tau(S)$ data plotted in $\ln\left\{\tau\left[S(S-1)^{md}\right]^{\frac{1}{1+md}}\right\}$ vs. $\frac{1}{T^3(\ln S)^2}$ coordinates (solution concentration of 200 g/l)

The calculated values of γ_{eff}, $r^*$and i^* are presented in Table 5.7. together with the values obtained by the polythermal method.

Table 5.7 Slopes of the best linear fit of experimental data plotted in $\ln\left\{\tau\left[S(S-1)^{md}\right]^{\frac{1}{1+md}}\right\}$ vs. $\frac{1}{T^3(\ln S)^2}$ coordinates and corresponding correlation coefficient, effective interfacial tension γ_{eff}, critical nucleus radius r^* and number i^* of molecules for nucleation of methyl stearate in kerosene at different concentrations. (r^* and i^* are given for the S values corresponding to $u = 0.035$ and 0.017, and the errors of the slope refer to the 95% confidence interval)

Con g/l	*Slope of the best linear fit of the experimental data plotted in* $\ln\left\{\tau[S(S-1)^{md}]^{\frac{1}{1+md}}\right\}$ *Vs* $\frac{1}{T^3(Ln\,S)^2}$ *coordinates*	R^2	$\gamma_{eff}\left(\frac{mJ}{m^2}\right)$ *Isothermal method*	$r^*(nm)$ *Isothermal method*	i^* *Isothermal method*	$\gamma_{eff}\left(\frac{mJ}{m^2}\right)$ *Polyhermal method*	$r^*(nm)$ *Polyhermal method*	i^* *Polythermal method*
200	(3±0.60) x 10^7	0.98	3.39	1.08-2.18	11-89	1.74	0.54-1.12	1-12
250	(3±1.92) x 10^7	0.80	3.39	1.05-2.12	10-81	1.64	0.51-1.05	1-10
300	(7±4.89) x 10^6	0.74	2.09	0.64-1.28	2-18	1.72	0.54-1.11	1-12
350	(1±0.70) x 10^7	0.86	2.35	0.72-1.46	3-27	1.79	0.56-1.15	1-13

A comparison of the parameter values shows that in all cases γ_{eff}, $r^*$and i^* calculated by means of the isothermal method are greater than those obtained by means of the polythermal method but are of the same order of magnitude. "The isothermal" γ_{eff} and r^* values are approximately 2, 2, 1.2 and 1.3 times greater than the "polythermal" ones for 200, 250, 300 and 350 g/l, respectively. These differences are reflected in a more noticeable increase of the critical nucleus number i^* of molecules obtained by means of the isothermal method where, for the lower concentrations of 200 and 250 g/l, it is between 7 and 11 times greater than that obtained by the polythermal method. However, for the higher concentrations of 300 and 350 g/l, the i^*values are only in the range of 1.5 to 3 times greater than those obtained by the polythermal method. For these concentrations, although the values of i^* calculated from the isothermal data are still greater than those obtained from the polythermal data, in both cases they are still in the range of typical values for HEN, well below 50 molecules.

It is important to notice that the supersaturation range in which crystallisation was detected through the polythermal analysis is considerably wider than that used to assess induction times through the isothermal method. This is so, because in the latter case the supersaturations where chosen within the $MSZW$ defined by the extrapolation to zero cooling rate of the $T_{diss}(q)$ and $T_c(q)$ dependences, which give

a $MSZW$ limited by higher crystallisation temperatures. This fact might explain the differences in the parameter values in the case of the lower solution concentrations for which two different nucleation mechanisms in the temperatures range of study may be present. However, to verify this assumption the use of a wider supersaturation range in the isothermal data analysis would be needed.

To further analyse these data, it is useful to determine the theoretical values of the interfacial tension γ for HON, which can be obtained with the aid of the Stefan-Skapski-Turnbull expression corresponding to spherical nuclei and given by [15, 16] :

$$\gamma = 0.514kT\frac{1}{{v_0}^{2/3}}\ln\frac{1}{N_a v_o C_e} \tag{5.25}$$

where N_a is Avogadro´s number, and C_e is the molar solubility.

The nucleation-activity factors (ψ) that control the value of the effective interfacial tension γ_{eff} can be calculated with the help of the formula

$$\gamma_{eff} = \psi\gamma \tag{5.26}$$

Table 5.8. lists the γ and ψ values obtained from equations (5.25) and (5.26) with the help of the γ_{eff} values calculated by both the polythermal and the isothermal method, using the corresponding molar solubility at $u = 0.035$ and 0.017.

Table 5.8 Interfacial tension for HON and nucleation-activity factor for 3D HEN as a function of solution concentration

$Con\ (g/l)$	$\gamma\left(\frac{mJ}{m^2}\right)$	ψ $from\ polythermal\ data$	ψ $from\ isothermal\ data$
200	7.24-8.42	0.24-0.21	0.47-0.40
250	6.73-7.95	0.24-0.21	0.50-0.43
300	6.32-7.59	0.27-0.23	0.33-0.28
350	5.99-7.24	0.30-0.25	0.39-0.32

Table 5.8. shows that for all concentrations the values of the nucleation-activity factor resulting from both the polythermal and isothermal analysis are well below the theoretical value of unity for HON. This indicates that HEN is the dominating mechanism controlling the methyl stearate formation in the whole temperature range studied.

The differences in the values of the nucleation parameters obtained by either the polythermal or the isothermal method could be attributed to the experimental methodology applied in the isothermal method. It was observed that induction time results are not very reproducible and repeatable and can vary significantly, even under the same experimental conditions, thus reflecting the stochastic nature of the nucleation process. The correlation coefficients for all concentrations show that a straight line does not fit the experimental data very well. As previously suggested by ter Horst and Jiang [7], to obtain accurate results from the application of the isothermal method, a probability distribution of the induction times at constant supersaturation ratio S should be constructed. To do that, however, an appreciable amount of time has to be spent for collecting the required experimental data, because a minimum of five values of the supersaturationn ratio S and eighty measurements of the induction time at each S value are suggested.

A comparative summary of interfacial tensions previously reported for organic compounds and the interfacial tensions obtained from both the polythermal and the isothermal methods is presented in Table 5.9.

Table 5.9 Previously reported values of interfacial tensions of some organic compounds and values obtained for the crystallisation of methyl stearate from kerosene by both the polythermal and the isothermal methods

Compound	Reported γ $\left(\frac{mJ}{m^2}\right)$
$m-ABA$ in water ethanol mixture	8.7
$m-His$ in water ethanol mixture [7]	5.1
Eflucimibe in ethanol and n-heptane mixture	
Polymorph A	5.17
Polymorph B [8]	4.23
Paracetamol in acetone-water mixtures [9]	1.4-2.8
Ketoprofen in acetone [10]	1.47
Liquid alkanes	
$C_{17}H_{36}$	7.20
$C_{18}H_{38}$	9.64
$C_{24}H_{50}$ [11]	8.20
Solutions of $C_{20}H_{42}$ + impurities (n-alkanes from $n-C_{18}$ to $n-C_{22}$) in Dodecane	
$C_{20}H_{42}$	0.389
$C_{20}H_{42}/C_{18}H_{38}$	0.775
$C_{20}H_{42}/C_{19}H_{40}$	0.844
$C_{20}H_{42}/C_{21}H_{44}$	1.713
$C_{20}H_{42}/C_{22}H_{46}$ [12]	1.170
$C_{22}H_{46}$ in Dodecane	
Mole fraction 10%	0.493
Mole fraction 15%	0.217
Mole fraction 20% [13]	0.315
$C_{24}H_{50}$ in Decalin	
2% mole fraction	0.69
7% mole fraction	0.64
19% mole fraction	0.29
$C_{24}H_{50}$ in Dodecane. (two Different nucleation mechanisms observed)	
HON	
1% mole fraction	0.86
5% mole fraction	0.74
19% mole fraction	0.49
HEN	
1% mole fraction	0.49
5% mole fraction	0.45
19% mole fraction [14]	0.29
Methyl stearate in kerosene (Polythermal method)	
200 g/l	1.74
250 g/l	1.64
300 g/l	1.72
350 g/l	1.79
Methyl stearate in kerosene (Isothermal method)	
200 g/l	3.39
250 g/l	3.39
300 g/l	2.09
350 g/l	2.35

5.4.3. Potential for further model development

The main advantage of the $KBHR$ approach is that it provides a quantitative account of the influence of cooling rate on the overall crystallisation process and hence provides an insight into the crystallite nucleation and growth mechanisms involved. The use of the complete set of expressions presented in this paper can deliver parameters such as e.g.: the nucleation rate constant k_J, the nucleus effective interfacial tension γ_{eff}, the crystal growth rate constant k_G and the crystallite growth exponents m and n. Additionally, the crystallites´ nucleation and growth rates could also be obtained by using these parameters in the respective formulae of the classical nucleation theory and the crystallite growth theories that model the temporal increase of crystallite radius through different mechanisms. The use of the mechanism-specific crystallite growth rate expressions presented by D. Kashchiev and A. Firoozabadi [17] will be addressed in future work.

Critically, the $KBHR$ approach provides a rational alternative to existing approaches based on empirical models. However, this approach is derived by making use of traditional expressions that rely on a number of simplifications and therefore there is more that could be done in the future, specifically to address the underlying molecular-scale interactions which are bound to be involved in directing and controlling the nucleation process [18, 19]. Clearly, an understanding of the nucleation kinetics at the molecular level is also required. In particular, the interactions between moieties or functional groups associated with the molecular building blocks of a nucleus known as “synthons”, need to be integrated within the model, and through this assess the relative balance between the bulk (intrinsic) synthons, which are fully co-coordinated in the crystallographic structure and the under-saturated surface (extrinsic) synthons which are present at the crystallite/solution interface. The latter will be much less co-coordinated to other solute molecules due to competition with solvent molecules. These synthons can be expected to provide the driving force for crystallisation processes such as crystallite nucleation and growth. A “synthonic engineering” approach has obvious value in that through it the initial stages associated with the molecular assembly of materials can be understood and quantified. This is especially useful in addressing the nature

of complex surface properties and the inherent anisotropy of many compounds, particularly those which crystallise in low symmetry structures. This is the case for many industrial materials such as fuels, confectionery products, pharmaceuticals and fine chemicals. In this regard, the shape of the particle needs further quantification, in a manner which draws down on the now comparatively routine application of the molecular modelling of dimers [20, 21], clusters [22-26], surfaces [18, 27, 28], point defects and additives [29-33] action on crystallisation. Such molecular scale modelling can be expected to have an impact e.g. using morphological modelling in the calculation of the volume of crystallites through the $KBHR$ approach. Similarly, the use of the classical nucleation theory for derivation of some of the expressions presented implies interfacial tension corresponding to the crystal equilibrium form, whereas in practice this parameter can vary significantly between the crystallographic forms that are present in the external crystal morphology. In this case, molecular modelling using grid search methods can be used to examine molecule/surface binding and to calculate the interfacial tensions as a function of solution composition [18, 27, 28]. This has been achieved through characterising the strength of the various surface-specific (extrinsic) synthons that contribute to the growth of the different habit faces [23], i.e.

$$\gamma_{particle} = \frac{\sum_{i=1}^{N} M_{i(hkl)} A_{i(hkl)} \gamma_{i(hkl)}}{A_{total}} \tag{5.27}$$

where N is the number of crystallographic forms (hkl) displayed in the external crystal morphology, $M_{i(hkl)}$ is the multiplicity of these individual forms, $A_{i(hkl)}$ is their surface area, $\gamma_{i(hkl)}$ is their interfacial tension and A_{total} is the total surface area of the crystal.

This approach could be applied, e.g., to segment the calculated interfacial tensions as obtained from the $KBHR$ model, to yield the inter-relationship between nucleus shape and surface chemistry with the resulting interfacial tensions derived for the individual crystal habit planes [18, 27]. This is valuable, given its potential application through the use of the Gibb-Thompson expression, to calculate solubility enhancement as a function of reduced crystal size [28]. Such an approach can also be

integrated with morphology prediction, with the potential to provide a more rigorous implementation of the model presented here, particularly in terms of defining a methodology for predicting the influence of crystallisation environment on the crystal growth rate [27, 29-32].

Molecular cluster modelling also provide a useful predictive way for modelling the stability of different polymorphs as a function of their crystal size. Linking this approach to the prediction of cluster size through the study presented in this paper, is potentially valuable in terms of being able to predict the correct crystallisation supersaturation needed to generate the required cluster size and thus, through this, to design the crystallisation processes needed to direct the polymorphic form desired [23, 25, 26].

A key future challenge, in terms of molecular scale predictions of nucleation behaviour, lies perhaps in trying to understand the inter-relationship (child-adult) between the incipient "crystal structure" present in the post-nucleation clusters (child) in relationship to that present in the fully formed micro/macro scale crystal structure (adult). For example, a sharp deviation between the structures of the material at the nanoscale with respect to that present in the bulk crystal structures could be taken to be indicative of a material's ease of crystallisation or "crystallisability". Aspects of this, have been recently addressed regarding the understanding of the crystallisability of L-glutamic acid and D-mannitol [23], and this work forms one of the focus areas in our current research.

5.5. Conclusions

A methodology was developed to assess the mechanisms and the kinetics associated with the crystallisation in solutions. This methodology makes use of the recently developed $KBHR$ approach in which polythermal experimental data are analysed to deliver important parameters of the kinetics of solutions crystallisation that otherwise could only be obtained by combined application of the isothermal and polythermal methods. This is particularly important, as obtaining these parameters in the case of

the isothermal method is stymied by the stochastic nature of nucleation which manifests itself in the large variation of the induction time for crystallisation.

Sensitivity analysis leads to the conclusion that a minimum of four different cooling rates spanning at least one order of magnitude, together with at least five repeats for crystallisation temperature values at each cooling rate are appropriate for a reliable experimental method.

A model system, methyl stearate crystallising from kerosene solutions, was used to test the developed methodology. The results obtained indicate that the crystallisation of methyl stearate in kerosene takes place by heterogeneous PN, i.e. the crystal nuclei are formed progressively on nucleation-active sites. The inferred values of the effective interfacial tensions are from 1.64-1.79 $\frac{mJ}{m^2}$ for solution concentrations in the range of 200 to 350 g/l respectively.

The application of the methodology can be extended to obtain additional crystal nucleation and crystal growth rate parameters but this requires the collection of additional experimental data. Chapter 7 presents additional analysis for methyl stearate crystallising from three different solvents.

References

[1] D. Kashchiev, A. Borissova, R.B. Hammond, K.J. Roberts, Effect of cooling rate on the critical undercooling for crystallization, Journal of Crystal Growth, 312 (2010) 698-704.

[2] D. Kashchiev, A. Borissova, R.B. Hammond, K.J. Roberts, Dependence of the Critical Undercooling for Crystallization on the Cooling Rate, J Phys Chem B, 114 (2010) 5441-5446.

[3] J.W. Mullin, Crystallization, 4th ed., Butterworth-Heinemann, Oxford, 2001.

[4] D. Kashchiev, Nucleation: basic theory with applications, Butterworth-Heinemann, Oxford, 2000.

[5] D. Kashchiev, A. Firoozabadi, Kinetics of the initial stage of isothermal gas phase formation, J Chem Phys, 98 (1993) 4690-4699.

[6] C.H. MacGillavry, M. Wolthuis-Spuy, Crystal structure of an Orthorhombic Modification of Methyl Stearate, Acta Crystallographica B26 (1970) 645-648.

[7] J.H. ter Horst, S. Jiang, Crystal nucleation rates from probability distributions of inductions times Crystal Growth and Design, 11 (2011) 256-261.

[8] S. Teychené, B. Biscans, Nucleation kinetics of polymorphs: induction period and interfacial energy measurements Crystal Growth and Design, 8 (2007) 1133-1139.

[9] R.A. Granberg, C. Ducreux, S. Gracin, A.C. Rasmuson, Primary nucleation of paracetamol in acetone-water mixtures Chemical Engineering Science, 56 (2001) 2305-2313.

[10] F. Espitalier, B. Biscans, C. Laguérie, Particle design Part A: nucleation kinetics of ketoprofen Chem Eng J, 68 (1997) 95-102.

[11] D. Turnbull, R.L. Cormia, Kinetics of crystal nucleation in some normal alkanes liquids The Journal of Chemical Physics, 34 (1961) 820-831.

[12] K.J. Roberts, J.N. Sherwood, A. Stewart, The Nucleation of n-Eicosane Crystals from Solutions in n-Dodecane in the Presence of Homologous Impurities, Journal of Crystal Growth, 102 (1990) 419-426.

[13] A.R. Gerson, K.J. Roberts, J.N. Sherwood, An Instrument for the Examination of Nucleation from Solution and Its Application to the Study of Precipitation from Diesel Fuels and Solutions of Normal-Alkanes, Powder Technol, 65 (1991) 243-249.

[14] B.D. Chen, L.J. Brecevic, J. Garside, Nucleation of tetracosane in hydrocarbon solvents, 12th symposium on industrial crystallisation, 2 (1993) session 4, 59-64.

[15] D. Kashchiev, Nucleation basic theory with applications, in, Butterworth Heinemann, Oxford ; Boston, 2000.

[16] D. Kashchiev, G.M. van Rosmalen, Review: nucleation in solutions revisited Crystal Research and Technology, 38 (2003) 555-574.

[17] D. Kashchiev, A. Firoozabadi, Induction time in crystallisation of gas hydrates, Journal of Crystal Growth, 250 (2003) 499-515.

[18] R.B. Hammond, K. Pencheva, K.J. Roberts, A structural-kinetic approach to model face-specific solution/crystal surface energy associated with the crystallization of acetyl salicylic acid from supersaturated aqueous/ethanol solution, Crystal Growth and Design, 6 (2006) 1324-1334.

[19] R.J. Davey, S.L.M. Schroeder, J.H. ter Horst, Nucleation of organic crystals-a molecular perspective, Angew Chem Int Edit, 52 (2013) 2166-2179.

[20] R.B. Hammond, C.Y. Ma, K.J. Roberts, P.Y. Ghi, R.K. Harris, Application of systematic search methods to studies of the structures of urea-dihydroxy benzene cocrystals, J Phys Chem B, 107 (2003) 11820-11826.

[21] R.B. Hammond, R.S. Hashim, C.Y. Ma, K.J. Roberts, Grid-based molecular modeling for pharmaceutical salt screening: Case example of 3,4,6,7,8,9-hexahydro-2H-pyrimido (1,2-a) pyrimidinium acetate, Journal of Pharmaceutical Sciences, 95 (2006) 2361-2372.

[22] R.B. Hammond, K. Pencheva, K.J. Roberts, Molecular modeling of crystal-crystal interactions between the alpha- and beta-polymorphic forms of L-glutamic acid using grid-based methods, Crystal Growth and Design, 7 (2007) 875-884.

[23] R.B. Hammond, K. Pencheva, K.J. Roberts, Structural variability within, and polymorphic stability of, nano-crystalline molecular clusters of L-glutamic acid and D-mannitol, modelled with respect to their size, shape and 'crystallisability', Crystengcomm, 14 (2012) 1069-1082.

[24] R.B. Hammond, S. Jeck, C.Y. Ma, K. Pencheva, K.J. Roberts, T. Auffret, An Examination of Binding Motifs Associated With Inter-Particle Interactions between Facetted Nano-Crystals of Acetylsalicylic Acid and Ascorbic Acid through the Application of Molecular Grid-Based Search Methods, Journal of Pharmaceutical Sciences, 98 (2009) 4589-4602.

[25] R.B. Hammond, K. Pencheva, K.J. Roberts, Simulation of energetic stability of facetted L-glutamic acid nanocrystalline clusters in relation to their polymorphic phase stability as a function of crystal size, J Phys Chem B, 109 (2005) 19550-19552.

[26] R.B. Hammond, K. Pencheva, K.J. Roberts, An examination of polymorphic stability and molecular conformational flexibility as a function of crystal size associated with the nucleation and growth of benzophenone, Faraday Discuss, 136 (2007) 91-106.

[27] R.B. Hammond, K. Pencheva, V. Ramachandran, K.J. Roberts, Application of grid-based molecular methods for modeling solvent-dependent crystal growth morphology:

Aspirin crystallized from aqueous ethanolic solution, Crystal Growth and Design, 7 (2007) 1571-1574.

[28] R.B. Hammond, K. Pencheva, K.J. Roberts, T. Auffret, Quantifying solubility enhancement due to particle size reduction and crystal habit modification: Case study of acetyl salicylic acid, Journal of Pharmaceutical Sciences, 96 (2007) 1967-1973.

[29] G. Clydesdale, R.B. Hammond, V. Ramachandran, K.J. Roberts, Molecular modelling of the morphology of organic crystals in the presence of impurity species: Recent applications to naphthalene, phenanthrene, and caprolactam crystals, Mol Cryst Liq Cryst, 440 (2005) 235-257.

[30] G. Clydesdale, R.B. Hammond, K.J. Roberts, Molecular modeling of bulk impurity segregation and impurity-mediated crystal habit modification of naphthalene and phenanthrene in the presence of heteroimpurity species, J Phys Chem B, 107 (2003) 4826-4833.

[31] R.B. Hammond, V. Ramachandran, K.J. Roberts, Molecular modelling of the incorporation of habit modifying additives: alpha-glycine in the presence of L-alanine, Crystengcomm, 13 (2011) 4935-4944.

[32] P. Mougin, G. Clydesdale, R.B. Hammond, K.J. Roberts, Molecular and solid-state modeling of the crystal purity and morphology of epsilon-caprolactam in the presence of synthesis impurities and the imino-tautomeric species caprolactim, J Phys Chem B, 107 (2003) 13262-13272.

[33] N. Anuar, W.R.W. Daud, K.J. Roberts, S.K. Kamarudin, S.M. Tasirin, Morphology and Associated Surface Chemistry of L-Isoleucine Crystals Modeled under the Influence of L-Leucine Additive Molecules, Crystal Growth and Design, 12 (2012) 2195-2203.

6. Solubility of Model Methyl Esters as a Function of Solution Environment

Summary: This chapter assesses the solubility, ideality and metastability of solutions of methyl palmitate and stearate in five representative compounds present in diesel fuels mixtures and three representative unsaturated methyl esters present in biodiesel fuels solutions

6.1. Introduction

The initial step to understand the mechanistic process underlying crystallisation of practical biodiesel and diesel/biodiesel solutions is the assessment of solubility of the saturated compounds present in these complex mixtures. In this chapter the solubility and solution´s ideality of model solutions of methyl palmitate (C16:0) and stearate (C18:0) as a function of solution environment are studied. Five different representative compounds present in diesel solutions were selected as solvents: n-dodecane, kerosene, toluene, n-heptane and methyl-cyclohexane, as well as three different unsaturated methyl esters: methyl linoleate, linoleate and linolenate. The latter are used both as single solvents and in combination in the same proportions as they are present in palm, rapeseed and soy oil in order to assess the relative importance of their proportions within the solution on the solubility and activities of the saturated methyl esters.

Enthalpies and entropies of dissolution and mixing as well as activity coefficients are calculated in order to assess the importance of chemical interactions, and molecular structure on the solubility of the model saturated methyl esters. These results are further used as inputs in subsequent chapters, to assess the kinetics of the crystallisation process of methyl palmitate and stearate and its dependence on solution environment.

The first section of the chapter presents the assessment of solubility and solution ideality for the methyl esters in the five model diesel type solvents. In the second section the analysis is extended to the unsaturated esters type solvents.

6.2. Solubility and solution ideality for methyl palmitate and stearate crystallising from model diesel type solvents

The solubility of C16:0 and C18: in n-dodecane, kerosene, toluene, n-heptane and methyl-cyclohexane solvents are analysed in this sub-section. Solubility related parameters are derived from the corresponding van´t Hoff plots, obtained from polythermal experimental data collected using a turbidimetric technique.

6.2.1. Polythermal data and van´t Hoff analysis

Using the polythermal experimental data obtained for C16:0 and C18:0 from five different model diesel type solvents their crystallisation T_c and dissolution T_{diss} temperatures were obtained as a function of cooling rate q and concentration. Some examples of these results are compared in Figs.6.1 and 6.2. The complete set of values for the T_c and T_{diss} as a function of cooling rate q are given in Table 6.1.

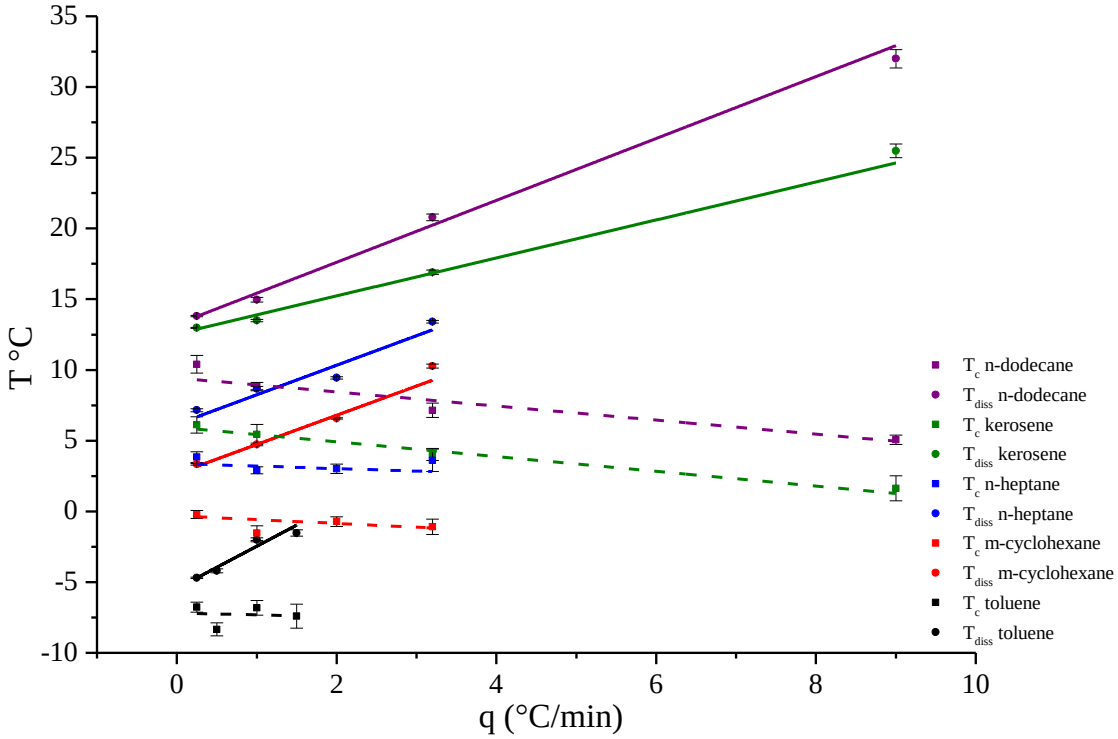

Figure 6.1 Crystallisation T_c and dissolution T_{diss} temperatures as a function of cooling rate q for solutions of methyl palmitate at a concentration of 250 g/l in n-dodecane and kerosene solvents and at a concentration of 192 g/l in toluene, n-heptane and methyl-cyclohexane solvents

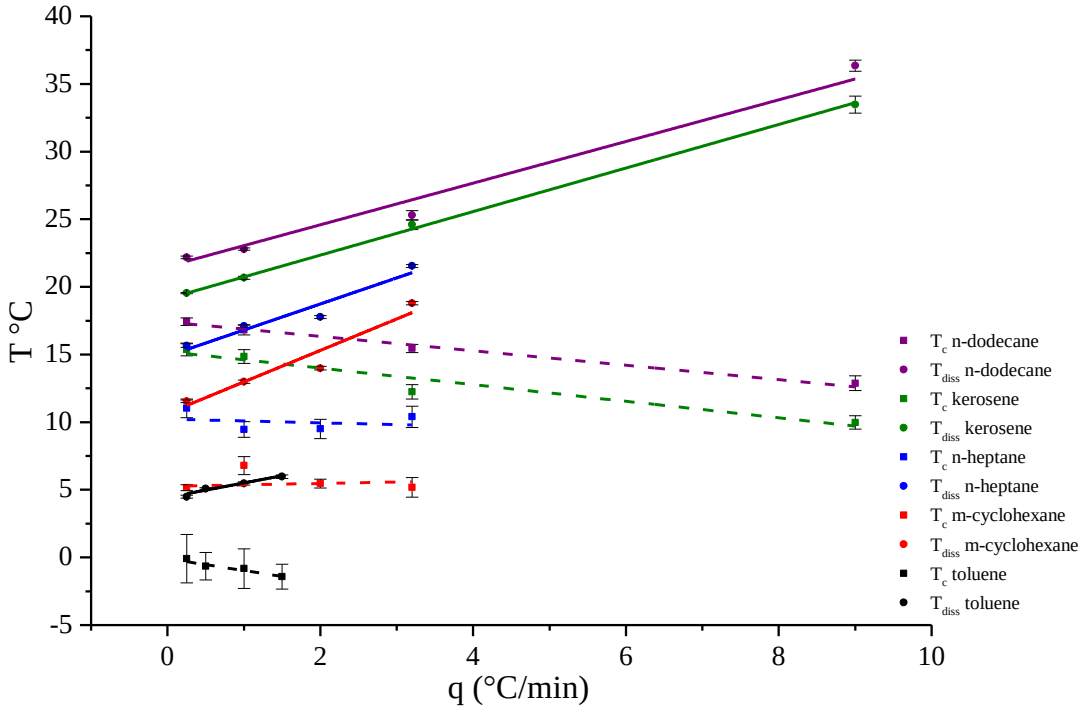

Figure 6.2 Crystallisation T_c and dissolution T_{diss} temperatures as a function of cooling rate q for solutions of methyl stearate at a concentration of 250 g/l in n-dodecane and kerosene solvents and at a concentration of 192 g/l in toluene, n-heptane and methyl-cyclohexane solvent

Table 6.1 Crystallisation T_c and dissolution T_{diss} temperatures as a function of cooling rate q and concentration for solutions of methyl palmitate and stearate in five different model diesel type solvents

	n-dodecane/Methyl palmitate							
$q\left(\frac{°C}{min}\right)$	$Con\left(\frac{g}{l}\right)$							
	200		250		300		350	
	T_c	T_{diss}	T_c	T_{diss}	T_c	T_{diss}	T_c	T_{diss}
0.25	8.34	12.22	10.39	13.80	11.85	15.31	12.27	16.13
1.00	7.51	13.29	8.87	14.96	10.95	16.32	11.51	17.72
3.20	5.77	18.84	7.15	20.78	9.16	20.82	9.86	22.62
9.00	3.31	30.61	5.06	32.00	6.76	31.77	7.01	35.20
	n-dodecane/Methyl stearate							
	$Con\left(\frac{g}{l}\right)$							
	200		250		300		350	
	T_c	T_{diss}	T_c	T_{diss}	T_c	T_{diss}	T_c	T_{diss}
0.25	15.81	19.67	17.43	22.19	18.84	23.04	19.76	24.18
1.00	15.03	20.71	16.82	22.80	18.56	23.94	19.18	25.49

3.20	13.61	23.47	15.45	25.30	17.15	26.29	17.90	29.22
9.00	10.86	35.37	12.88	36.36	14.56	36.72	14.67	36.85
	Kerosene/Methyl palmitate							
	$Con\ \left(\frac{g}{l}\right)$							
	200		250		300		350	
	T_c	T_{diss}	T_c	T_{diss}	T_c	T_{diss}	T_c	T_{diss}
0.25	3.91	11.51	6.12	12.97	9.61	13.05	10.73	14.20
1.00	2.22	11.84	5.45	13.49	8.33	14.51	9.59	15.68
3.20	0.74	15.28	4.03	16.91	5.95	18.81	8.08	20.02
9.00	-1.71	24.32	1.63	25.49	3.32	28.79	4.24	29.65
	Kerosene/Methyl stearate							
	$Con\ \left(\frac{g}{l}\right)$							
	200		250		300		350	
	T_c	T_{diss}	T_c	T_{diss}	T_c	T_{diss}	T_c	T_{diss}
0.25	12.43	17.66	15.37	19.54	16.73	21.03	17.81	22.19
1.00	11.76	18.67	14.85	20.67	15.53	22.34	16.95	23.65
3.20	10.11	22.11	12.24	24.59	13.91	27.02	15.28	28.18
9.00	7.66	30.75	9.98	33.47	11.24	36.01	11.90	37.58
	Toluene/Methyl palmitate							
	$Con\ \left(\frac{g}{l}\right)$							
	154		192		231		269	
	T_c	T_{diss}	T_c	T_{diss}	T_c	T_{diss}	T_c	T_{diss}
0.25	-10.65	-7.87	-6.78	-4.70	-5.06	-2.45	-3.76	-0.67
0.50	-10.39	-7.41	-8.35	-4.20	-5.16	-1.74	-3.67	0.24
1.00	-9.87	-5.16	-6.82	-2.01	-3.57	0.43	-1.57	2.50
1.50	-9.47	-5.16	-7.41	-1.53	-4.03	1.12	-2.52	3.51
	Toluene/Methyl stearate							
	$Con\ \left(\frac{g}{l}\right)$							
	154		192		231		269	
	T_c	T_{diss}	T_c	T_{diss}	T_c	T_{diss}	T_c	T_{diss}
0.25	-2.39	2.17	-0.10	4.48	1.06	6.20	2.92	7.69
0.50	-3.69	2.42	-0.65	5.09	0.78	7.13	3.03	8.79
1.00	-3.02	3.01	-0.83	5.47	0.30	7.71	2.34	9.39
1.50	-4.11	3.51	-1.42	5.97	0.13	8.39	1.85	10.26
	Heptane/Methyl palmitate							
	$Con\ \left(\frac{g}{l}\right)$							
	154		192		231		269	
	T_c	T_{diss}	T_c	T_{diss}	T_c	T_{diss}	T_c	T_{diss}
0.25	2.41	5.32	3.84	7.15	5.95	8.91	6.51	9.88
1.00	0.81	6.75	2.90	8.68	6.03	10.64	6.39	11.86
2.00	0.73	7.10	3.02	9.44	4.22	11.35	5.99	12.38

3.20	0.48	11.27	3.61	13.41	5.52	15.25	7.29	17.47
	Heptane/Methyl stearate							
	$Con\ \left(\frac{g}{l}\right)$							
	154		192		231		269	
	T_c	T_{diss}	T_c	T_{diss}	T_c	T_{diss}	T_c	T_{diss}
0.25	9.06	13.88	11.02	15.66	11.96	17.31	13.41	18.46
1.00	8.72	15.06	9.46	17.10	11.79	18.67	13.62	19.73
2.00	7.21	15.66	9.50	17.77	10.55	19.39	12.24	20.57
3.20	7.57	20.19	10.39	21.54	11.37	23.66	12.22	26.10
	Methyl-cyclohexane/Methyl palmitate							
	$Con\ \left(\frac{g}{l}\right)$							
	154		192		231		269	
	T_c	T_{diss}	T_c	T_{diss}	T_c	T_{diss}	T_c	T_{diss}
0.25	-2.12	1.56	-0.22	3.33	1.24	5.03	2.79	6.01
1.00	-2.70	2.92	-1.54	4.74	1.18	6.72	2.68	7.97
2.00	-3.73	4.55	-0.72	6.57	0.77	8.45	2.55	9.82
3.20	-3.79	8.14	-1.10	10.27	0.74	11.91	2.44	13.95
	Methyl-cyclohexane/Methyl stearate							
	$Con\ \left(\frac{g}{l}\right)$							
	154		192		231		269	
	T_c	T_{diss}	T_c	T_{diss}	T_c	T_{diss}	T_c	T_{diss}
0.25	4.92	9.71	5.17	11.54	8.31	13.24	9.86	14.60
1.00	4.79	10.79	6.79	13.00	8.36	15.24	9.65	16.16
2.00	3.71	12.04	5.46	13.99	7.28	15.58	8.90	17.44
3.20	3.61	15.78	5.18	18.79	7.33	20.55	9.54	22.32

The extrapolation to 0 °C/min of $T_c(q)$ and $T_{diss}(q)$ lines delivers the equilibrium saturation temperature T_e and the crystallisation temperature at the kinetic limit T_C for each of the solution´s concentrations. Table 6.2. shows these results together with the extent of metastability at different concentrations and the corresponding modelled van't Hoff lines.

Table 6.2 Solubility and supersolubility data of methyl palmitate and stearate in five different model diesel type solvents, together with the metastable zone width at each concentration within each solution system. van't Hoff model for the solubility data are also given according to expression (2.43)

	n-dodecane					
$Con\ \left(\frac{g}{l}\right)$	Methyl Palmitate			Methyl stearate		
	T_C	T_e	$MSZW$	T_C	T_e	$MSZW$
200	8.09	11.59	3.50	15.67	18.70	3.04
250	9.72	13.33	3.62	17.35	21.09	3.74
300	11.55	14.66	3.11	18.93	22.18	3.25
350	12.12	15.58	3.46	19.81	24.12	4.31
Van't Hoff model	$y = -9333.4\ x + 30.85$			$y = -7643.7\ x + 24.18$		
	Kerosene					
	Methyl Palmitate			Methyl stearate		
	T_C	T_e	$MSZW$	T_C	T_e	$MSZW$
200	3.23	10.68	7.45	12.28	17.25	4.97
250	5.98	12.31	6.33	15.16	19.21	4.05
300	9.08	12.76	3.69	16.33	20.86	4.53
350	10.55	13.98	3.43	17.69	22.01	4.33
Van't Hoff model	$y = -11740\ x + 39.37$			$y = -8396.2\ x + 26.83$		
	Toluene					
	Methyl Palmitate			Methyl stearate		
	T_C	T_e	$MSZW$	T_C	T_e	$MSZW$
154	-10.87	-8.36	2.51	-2.51	1.90	4.41
192	-7.38	-5.34	2.04	0.02	4.36	4.34
231	-5.35	-3.10	2.25	1.18	6.04	4.85
269	-3.97	-1.41	2.56	3.31	7.50	4.19
Van't Hoff model	$y = -5326\ x + 17.26$			$y = -7197.3\ x + 23.22$		
	Heptane					
	Methyl Palmitate			Methyl Stearate		
	T_C	T_e	$MSZW$	T_C	T_e	$MSZW$
154	2.00	4.57	2.56	9.08	12.92	3.83
192	3.38	6.42	3.04	10.30	14.97	4.66
231	5.89	8.26	2.37	11.87	16.45	4.58
269	6.18	9.02	2.84	13.68	17.21	3.53
Van't Hoff model	$y = -8487.4\ x + 28.01$			$y = -9541.4\ x + 30.70$		
	Methyl-cyclohexane					
	Methyl Palmitate			Methyl Stearate		
	T_C	T_e	$MSZW$	T_C	T_e	$MSZW$
154	-2.13	0.75	2.88	5.07	8.83	3.76
192	-0.64	2.48	3.11	5.93	10.52	4.59
231	1.30	4.34	3.05	8.47	12.44	3.97
269	2.81	5.20	2.39	9.73	13.55	3.82
Van't Hoff model	$y = -8401\ x + 28.00$			$y = -8557.3\ x + 27.59$		

The comparative plots of the solubility lines in the form of the van´t Hoff plot given by equation (2.43) for both C16:0 and C18:0 in each solvent are shown in Figs. 6.3 and 6.4 respectively. In the same plane of coordinates the line corresponding to the ideal solubility is also presented to allow for the assessment of the solutions´ ideality and solutions´chemical interactions.

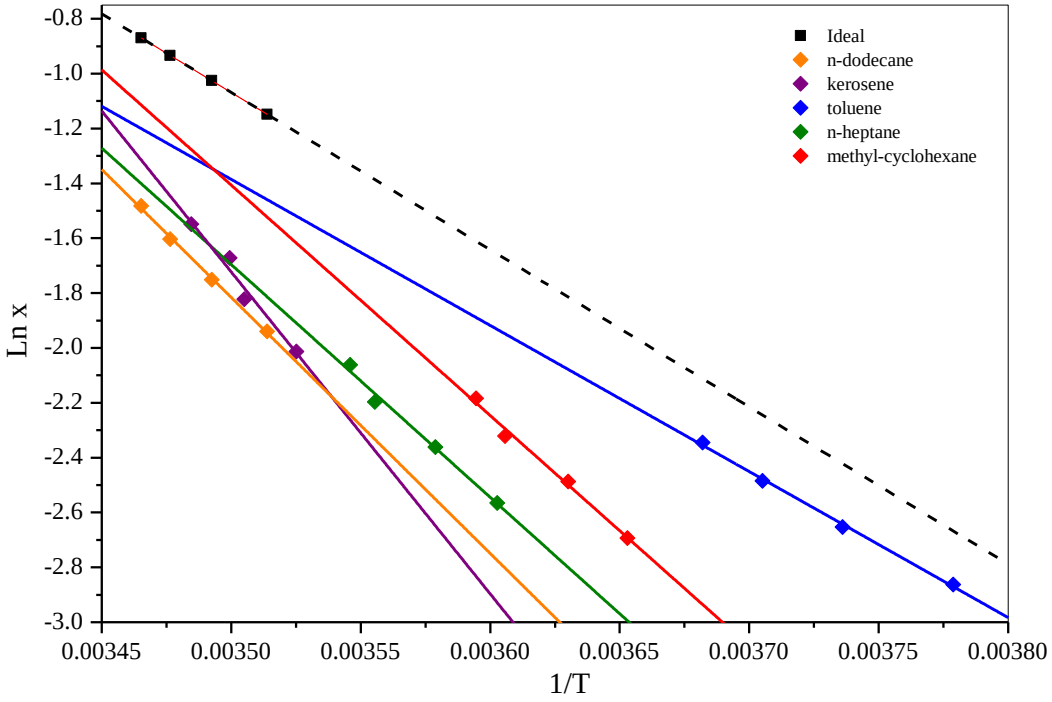

Figure 6.3 van't Hoff plot for methyl palmitate in five different model diesel type solvents. Solid lines represent experimental solubilities and the dashed line the ideal solubility. Experimental solubilities were obtained by extrapolation to 0 ºC of $T_{diss}(q)$ lines at four different solution's concentrations

The modelled lines representing the dependence of activity coefficient on temperature, enthalpies and entropies of dissolution as well as those of mixing (ΔH_{mix}) and (ΔS_{mix}) are presented in Tables 6.3. and 6.4. for C16:0 and C18:0 respectively. Enthalpy and entropy of dissolution were obtained respectively from the slope and intercept with the y axes of the corresponding van´t Hoff plots; while the subtraction of enthalpy and entropy of melting from these values delivered those of enthalpy and entropy of mixing. Enthalpy (ΔH_m) and entropy of melting (ΔS_m) are 47.67 $\left(\frac{KJ}{mol}\right)$ and 0.16 $\left(\frac{KJ}{mol\,K}\right)$ for C16:0 and 53.94 $\left(\frac{KJ}{mol}\right)$ and 0.17 $\left(\frac{KJ}{mol\,K}\right)$ for C18:0 respectively. The activity coefficient lines were obtained from iterative calculations of this parameter at four different temperatures using equation (2.22).

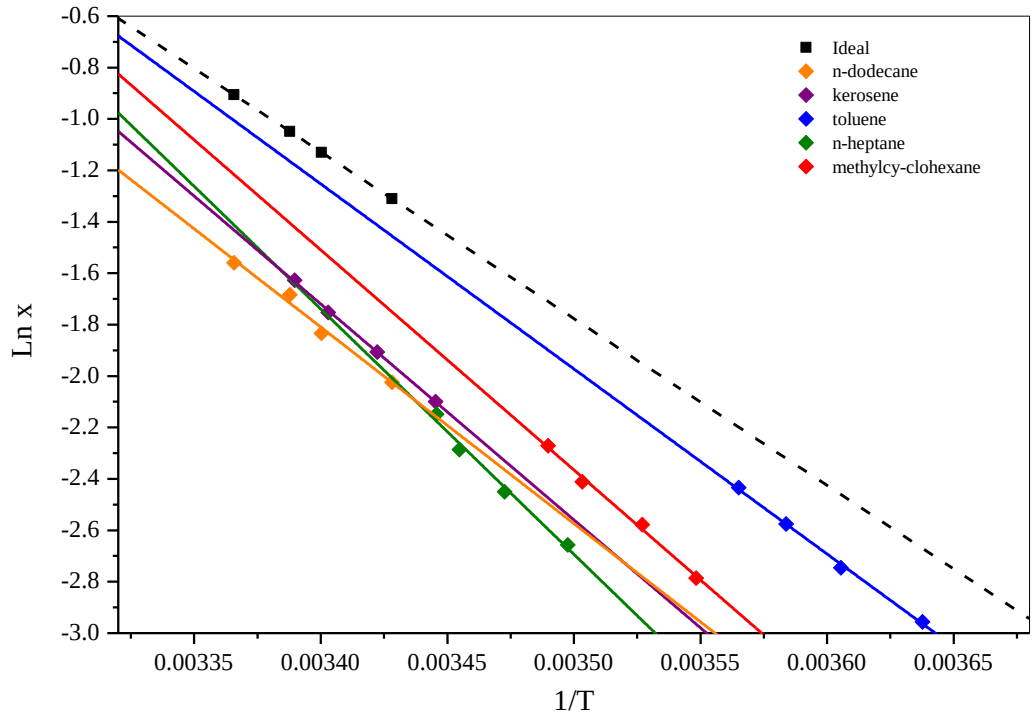

Figure 6.4 van't Hoff plot for methyl stearate in five different model diesel type solvents. Solid lines represent experimental solubilities and the dashed line the ideal solubility. Experimental solubilities were obtained by extrapolation to 0 ºC of $T_{diss}(q)$ lines at four different solution's concentrations

Table 6.3 Thermodynamic parameters derived from solubility data of methyl palmitate in solution with five different model diesel type solvents, together with the linear dependence of ϒ on *T*

	ΔH_{diss} (KJ/mol)	ΔS_{diss} $\left(\frac{KJ}{K\ mol}\right)$	ΔH_{mix} (KJ/mol)	ΔS_{mix} $\left(\frac{KJ}{K\ mol}\right)$	ϒ $1-15\ ^{\circ}C$	$\ln \Upsilon = aT + b$
n-Dodecane	77.60	0.26	29.93	0.10	3.53-1.91	$-0.044\ T + 1.31$
Kerosene	97.61	0.33	49.94	0.17	4.57-1.63	$-0.074\ T + 1.59$
Toluene	44.28	0.14	-3.39	-0.01	1.29-1.40	$0.006\ T + 0.25$
n-Heptane	70.57	0.23	22.90	0.07	2.82-1.72	$-0.035\ T + 1.07$
Methyl-cyclohexane	69.85	0.23	22.18	0.07	2.09-1.28	$-0.035\ T + 0.77$

Table 6.4 Thermodynamic parameters derived from solubility data of methyl stearate in solution with five different model diesel type solvents, together with the linear dependence of γ on T

	ΔH_{diss} (KJ/mol)	ΔS_{diss} $\left(\frac{KJ}{K\ mol}\right)$	ΔH_{mix} (KJ/mol)	ΔS_{mix} $\left(\frac{KJ}{K\ mol}\right)$	Υ $1-20\ ^{\circ}C$	$\ln \Upsilon = aT + b$
n-Dodecane	63.55	0.20	9.61	0.03	2.59-2.01	$-0.013\,T + 0.96$
Kerosene	69.81	0.22	15.87	0.05	2.83-1.85	$-0.022\,T + 1.06$
Toluene	59.84	0.19	5.90	0.02	1.35-1.14	$-0.009\,T + 0.31$
n-Heptane	79.33	0.26	25.39	0.08	3.85-1.91	$-0.037\,T + 1.39$
Methyl-cyclohexane	71.15	0.23	17.21	0.06	2.43-1.50	$-0.026\,T + 0.91$

6.2.2. Assessment of methyl palmitate and stearate solubility in five model diesel type solvents

van´t Hoff plots fit well to a linear model for all solutions studied. This indicating a consistent heat of fusion as a function of solution concentration, corroborating that the solid state form of the crystallising solute was the same within the corresponding range of temperature.

The solubility of methyl palmitate in all solvents is higher than that of methyl stearate due to its shorter carbon chain length which leads to lower intermolecular van der Waals forces between solute-solute molecules.

The highest solubility for both C16:0 and C18:0 is observed in toluene and decreases as function of solvent in the following order: toluene > methyl-cyclohexane > n-heptane > kerosene > n-dodecane. With the exception of n-heptane, this is in the same order of polarity/aromaticity. Fatty acid methyl esters are organic compounds with medium polarity due to the presence in their chemical structure of both a COO-alkyl group and a non-polar long hydrocarbon chain. The solubility trend could be justified in terms of the solvent polarity and the like-dissolves-like rule of thumb i.e. a non-polar compound will be dissolved by non-polar solvents and vice versa. Straight chain n-alkanes such as n-dodecane and n-heptane are non-polar molecules,

with dipole moment of 0.07 and 0 D respectively, which will have lower affinity with either methyl palmitate or stearate whose dipole moment calculated in vacuum ranges between 1.52 and 1.67 D. On the other hand toluene and methyl-cyclohexane will show better affinity due to a higher dipole moment of around 0.36 D. Kerosene is expected to deliver solubility higher than that of n-dodecane but lower than that observed in either toluene or methyl-cyclohexane due to its composition that comprises different types of hydrocarbons molecules including aromatic and cyclo-alkyl species.

In all cases the activity coefficients are higher than one or less than ideal (Tables 6.3. and 6.4), which given the clear dependence of Υ on temperature implies that solute-solute interactions are stronger than the solute-solvent ones. However, the significant lower values obtained in toluene together with the lowest enthalpy of mixing observed suggest that in these solutions solute-solvent interactions are significantly stronger than the same interactions in the other solutions´ systems.

These results follow a similar trend than that of the solubility in the sense that lowest activity coefficients were obtained in the case of toluene followed by methyl-cyclohexane in which the model saturated methyl esters have higher solubility.

Previous studies [1, 2] on the influence of molecular interactions on the ideality of representative organic molecules present in biodiesel fuels, have shown similar results. Infinite dilution activity coefficients calculated for mixtures of methyl esters and hydrocarbons compounds have also shown lower activity coefficients for mixtures of methyl esters with cyclo-alkyl and aromatic compounds than those observed in mixtures with straight chain hydrocarbons. A summary of these results is presented in Table 6.5.

Table 6.5 Activity coefficients for various solutions of saturated methyl esters and hydrocarbons compounds [1, 2]

	Methyl Palmitate	Methyl Stearate
n-Heptane	1.04-1.10	0.98
n-Dodecane	1.23	1.16
Cyclo-heptane		0.97
Methyl-cyclohexane		0.91
Toluene	0.65-0.66	

According to this it could be expected that dipole-dipole interaction between the modelled saturated solutes (C16:0 and C18:0) and toluene molecules are stronger, this creating at the same time induced dipoles that would make chemical interactions even stronger. It has been hypothesised that the low activity coefficients obtained in the case of toluene are likely to be to a great extend due to the polarising effect created by the delocalised electron cloud around the benzene ring. This could cause the distortion of the electron cloud around the solvent molecule inducing temporary dipoles among solute-solvent molecules which are very strong forces, in the case of the benzene ring, known as "London dispersion forces" [2]. This effect is manifested in the negative and very low ΔH_{mix} in toluene solvent, which could only results on these values due to a high released of energy on the formation of solute-solvent bonds.

The second highest solubility was observed for methyl-cyclohexane solvent. This could be attributed to the more compact structure of cyclo-alkyl molecules which could more easily solvate solute molecules than their straight-chain hydrocarbon counterparts. Similarly, the presence of the alkyl moiety will provide higher polarity than that of straight chain hydrocarbon for interaction with methyl ester molecules. The large carbon bond angles in small cycloalkanes make them more reactive thus facilitating the breaking of solvent-solvent interactions. In general, in this case more solvent surface area is available for binding to the solute molecule after molecular bonds within solute and solvent molecules have been broken. These conclusions are supported by the low enthalpy of mixing obtained in methyl-cyclohexane solvent which could be attributed to low energy required to break solvent-solvent interactions and/or higher energy released in the formation of solute-solvent bonds.

In the case of straight chain hydrocarbon solvents activity coefficients are higher for the modelled solutes in n-dodecane than in n-heptane. Similar results were observed for saturated methyl esters in solution with thirteen different straight chain hydrocarbons, in which there is a trend of increasing activity coefficient values with an increase in hydrocarbon chain length [1, 2]. It is interesting to note however that the Υ value obtained for methyl stearate in n-heptane at lower temperatures is much higher than that obtained in n-dodecane. From Fig.5.4 it can be seen that there is a cross point in which methyl stearate solutions become less ideal in n-heptane than in n-dodecane below approximately 18 °C, as activity is more dependent on T in the former case (see $\Upsilon(T)$ model in Table 5.4.) due to significantly higher ΔH_{diss}. Given that ΔH_{mix} is also higher in comparison with the other solvent systems, these results could imply that the energy released when forming solute-solvent interactions is significantly lower in the case of methyl sterate/n-heptane solutions. However, given that the cross-point of the two van´t Hoff lines is observed outside the range of $\ln x(T)$ measurements these conclutions would need to be validated by extending the range of analysis.

When comparing the solubility of the modelled saturated esters in hydrocarbon solvents with the same carbon number i.e. n-heptane, methyl-cyclohexane and toluene, it is clear that the aromatic solvent delivers the lowest activities coefficients followed by the cyclo-alkyl solvent which delivered lower activity coefficients that their straight chain counterpart. C16:0 solutions in n-heptane and methyl-cyclohexane showed the exact same values of entropy of dissolution and mixing and very close activity values. It seems that in this case, the chemical interactions between solute-solvent and solvent-solvent molecules are not affected to a great extent by the more compact structure of methyl-cyclohexane as just subtle lower values of the enthalpy of mixing were observed in methyl-cyclohexane solutions. In addition to this, due to the relatively high dependence of activities on temperature for methyl-cyclohexane and toluene solutions, there is a cross point at around 13 ℃ above which methyl-cyclohexane solutions become more ideal than those in toluene solvent. However, given that the cross point is observed well outside the range of $\ln x(T)$ observations this could indicate the presence of a different solid form at higher temperatures.

In the case of C18:0 solutions in the same three solvents, the lowest activities are observed in toluene and the highest in n-heptane solvent. However, it is important to note that C18:0/n-heptane solutions have a very high enthalpy of mixing in comparison to any other solvent making the activities coefficients more dependable on temperature. As observed in Fig. 6.4 activities in this solvent at lower temperature become the highest among the five solvent systems assessed. This is effect is likely to be due to the low release of energy when forming solute-solvent interactions at lower temperatures.

Comparing the behaviour of solutions of C16:0 in the three solvents showing the highest activities, lower values are observed at higher temperatures in kerosene followed by n-heptane and n-dodecane. On the other hand, at lower temperatures activity coefficients are lower in n-heptane followed by n-dodecane and kerosene. The noticeable dependence of activities on temperature for kerosene solutions can be evidence on the steep slope of the van't Hoff line (Fig. 6.3) which reduces significantly the solubility of C16:0 in this solvent at temperatures below 11 ºC where the lowest solubility among all solvents is observed. This issue is reinforced by high enthalpy and entropy of mixing in this case, likely to be due to the range of different compounds present in kerosene, especially the aromatic molecules, which not only differ in size but also will complicate chemical interaction with the solute. For C18:0 in the same systems activity coefficients follow a different trend with the activities in kerosene solutions being generally the lowest and more stable. A Cross point is observed between n-heptane and n-dodecane solutions at around 18 ºC below which deviation from ideality trend changed to be higher in n-heptane than in n-dodecane solutions. This effect as shown in Table 6.4. is due to the fact that the highest enthalpy and entropy of mixing are observed in this solvent i.e. lower proportion of released of energy in the formation of solute-solvent bonds in relation to the energy required to break solvent-solvent bonds is expected.

6.3. Solubility and solution ideality for methyl palmitate and stearate crystallising from model unsaturated methyl esters solvents

In this subsection the analysis of C16:0 and C18 solubility as a function of solution environment is extended to solutions in which the solvents are unsaturated methyl esters and mixtures of them. For this purpose methyl oleate, linoleate and linolenate where chosen as these unsaturated esters are present in the highest proportions in practical biodiesel mixtures.

6.3.1. Polythermal data and van´t Hoff analysis

Some chosen examples of the tendency of crystallisation T_c and dissolution T_{diss} temperatures as a function of cooling rate q and concentration are presented in Figs. 6.5 and 6.6. The complete set of values for the T_c and T_{diss} as a function of cooling rate q are given in Table 6.6

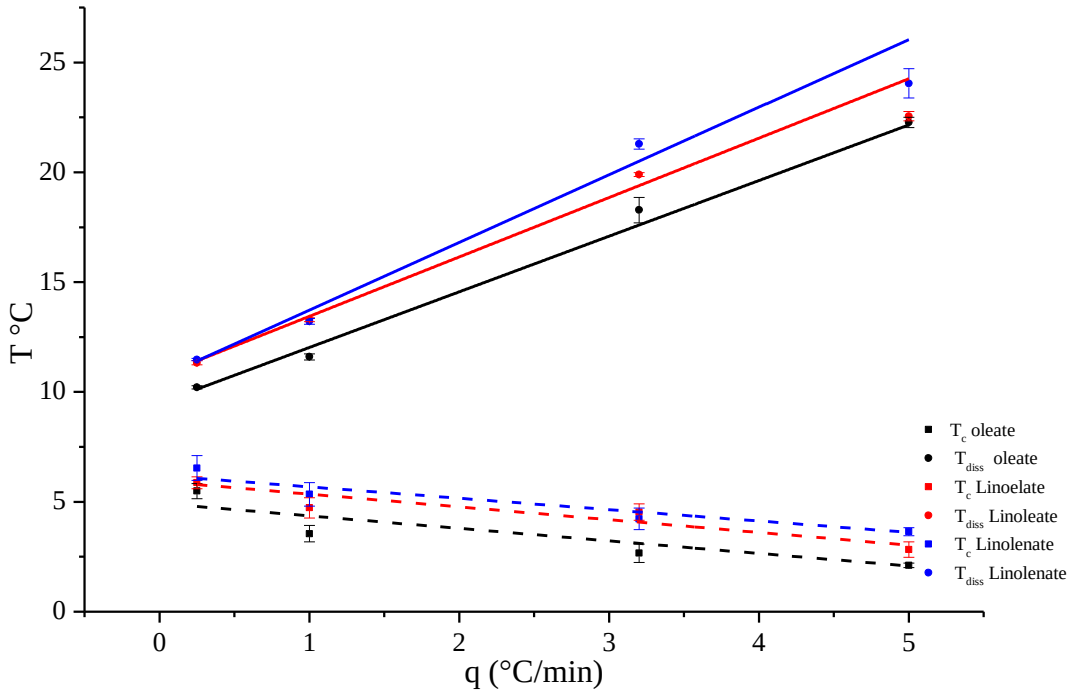

Figure 6.5 Crystallisation T_c and dissolution T_{diss} temperatures as a function of cooling rate q for solutions of methyl palmitate at a concentration of 192 g/l, in three different single unsaturated esters type solvents

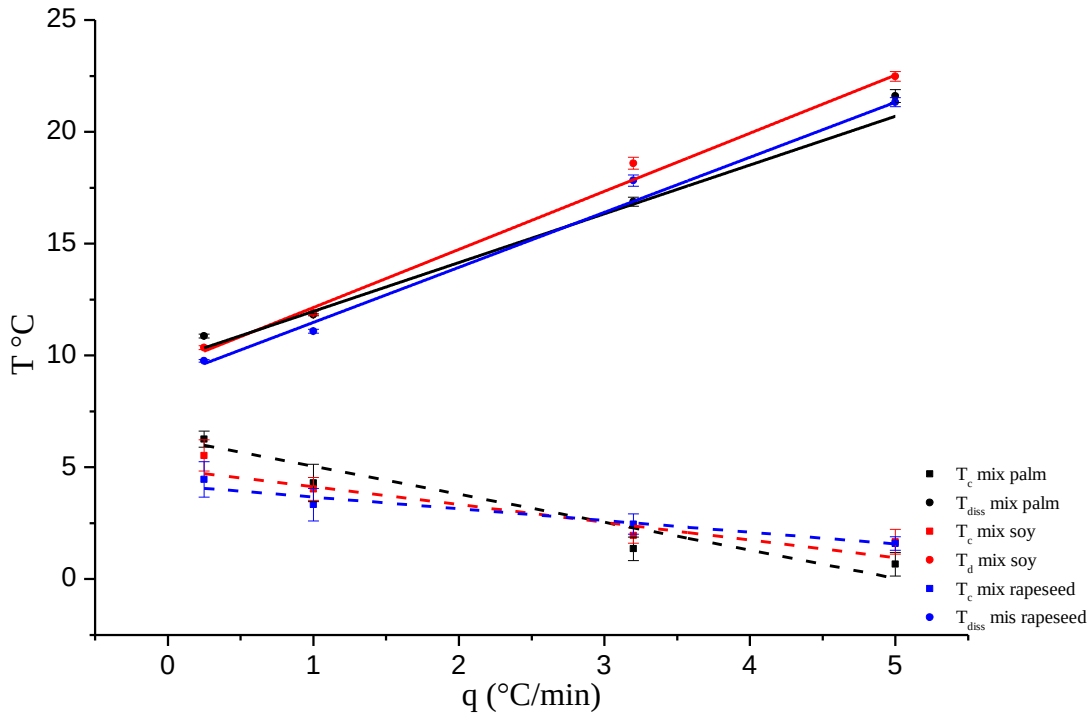

Figure 6.6 Crystallisation T_c and dissolution T_{diss} temperatures as a function of cooling rate q for solutions of methyl palmitate at a concentration of 192 g/l, in three different mixtures of unsaturated esters type solvents

Table 6.6 Crystallisation T_c and dissolution T_{diss} temperatures as a function of cooling rate q and concentration for solutions of methyl palmitate and stearate in six different unsaturated esters type solvents

	Methyl oleate/Methyl palmitate							
$q\left(\frac{°C}{min}\right)$	$Con\left(\frac{g}{l}\right)$							
	154		192		231		269	
	T_c	T_{diss}	T_c	T_{diss}	T_c	T_{diss}	T_c	T_{diss}
0.25	2.11	8.24	5.49	10.21	7.44	11.68	7.78	13.12
1.00	1.67	9.30	3.55	11.60	6.79	13.34	7.76	14.74
3.20	-0.33	15.33	2.66	18.28	5.05	20.24	5.72	22.53
5.00	-0.64	18.58	2.11	22.27	4.20	24.31	5.51	25.81
	Methyl oleate/Methyl stearate							
	$Con\left(\frac{g}{l}\right)$							
	154		192		231		269	
	T_c	T_{diss}	T_c	T_{diss}	T_c	T_{diss}	T_c	T_{diss}
0.25	13.34	18.58	14.84	20.16	16.54	21.82	18.42	23.28

1.00	13.40	20.04	14.60	22.33	16.16	24.21	17.51	25.60
3.20	11.14	27.20	13.85	30.24	15.65	31.70	17.33	33.37
5.00	7.86	27.71	10.39	30.68	13.18	33.01	14.07	35.03
	Methyl linoleate/Methyl palmitate							
	$Con\left(\frac{g}{l}\right)$							
	154		192		231		269	
	T_c	T_{diss}	T_c	T_{diss}	T_c	T_{diss}	T_c	T_{diss}
0.25	3.71	9.45	5.87	11.33	8.15	12.91	9.13	14.43
1.00	2.51	11.09	4.73	13.29	7.77	14.75	9.55	16.59
3.20	1.45	16.05	4.53	19.89	7.03	22.08	8.69	23.72
5.00	-0.81	20.45	2.83	22.56	3.41	26.12	5.23	28.94
	Methyl linoleate/Methyl stearate							
	$Con\left(\frac{g}{l}\right)$							
	154		192		231		269	
	T_c	T_{diss}	T_c	T_{diss}	T_c	T_{diss}	T_c	T_{diss}
0.25	13.03	18.33	14.93	20.23	17.47	21.79	18.53	23.26
1.00	12.81	20.01	15.27	22.44	16.73	23.78	17.95	25.64
3.20	11.11	26.52	13.85	29.50	16.33	31.04	17.55	33.34
5.00	8.95	30.22	12.49	32.74	14.93	34.64	15.75	37.72
	Methyl linolenate/Methyl palmitate							
	$Con\left(\frac{g}{l}\right)$							
	154		192		231		269	
	T_c	T_{diss}	T_c	T_{diss}	T_c	T_{diss}	T_c	T_{diss}
0.25	4.88	9.54	6.54	11.48	9.00	13.25	9.28	14.57
1.00	2.36	11.14	5.34	13.21	8.30	15.49	9.44	17.27
3.20	1.68	16.77	4.22	21.29	7.72	22.09	8.18	25.45
5.00	1.46	20.79	3.64	24.05	5.60	26.40	6.98	28.04
	Methyl linolenate/Methyl stearate							
	$Con\left(\frac{g}{l}\right)$							
	154		192		231		269	
	T_c	T_{diss}	T_c	T_{diss}	T_c	T_{diss}	T_c	T_{diss}
0.25	13.53	18.93	16.13	20.81	17.93	22.25	19.19	23.63
1.00	14.05	20.99	16.09	22.55	17.69	23.97	18.95	25.52
3.20	11.12	25.98	13.35	29.30	15.77	30.52	17.35	31.42
5.00	8.94	27.98	12.10	30.14	13.87	32.02	14.83	34.76
	Mix palm/Methyl palmitate							
	$Con\left(\frac{g}{l}\right)$							
	154		192		231		269	
	T_c	T_{diss}	T_c	T_{diss}	T_c	T_{diss}	T_c	T_{diss}
0.25	3.43	8.57	6.26	10.87	7.66	12.21	9.90	13.69
1.00	2.30	9.32	4.30	11.81	6.63	13.36	8.49	14.88
3.20	-1.41	13.08	1.35	16.88	3.96	18.38	6.14	20.24
5.00	-1.22	17.19	0.66	21.60	2.19	24.13	4.30	25.58
	Mix palm/Methyl stearate							

	$Con\ \left(\frac{g}{l}\right)$							
	154		192		231		269	
	T_c	T_{diss}	T_c	T_{diss}	T_c	T_{diss}	T_c	T_{diss}
0.25	13.00	18.36	14.38	19.94	16.20	21.40	17.75	22.99
1.00	12.86	19.82	14.74	21.58	15.91	23.32	17.25	25.30
3.20	10.96	26.92	13.81	28.62	15.59	30.36	17.01	33.01
5.00	9.34	31.03	11.93	32.24	13.34	35.40	15.39	37.64
	Mix soy/Methyl palmitate							
	$Con\ \left(\frac{g}{l}\right)$							
	154		192		231		269	
	T_c	T_{diss}	T_c	T_{diss}	T_c	T_{diss}	T_c	T_{diss}
0.25	3.79	8.45	5.53	10.35	8.81	12.13	8.95	13.61
1.00	1.39	9.81	4.03	11.89	6.73	13.95	8.49	15.39
3.20	-0.03	16.27	1.95	18.59	5.81	21.19	7.39	23.26
5.00	-0.83	20.11	1.67	22.48	4.21	25.00	4.95	27.16
	Mix soy/Methyl stearate							
	$Con\ \left(\frac{g}{l}\right)$							
	154		192		231		269	
	T_c	T_{diss}	T_c	T_{diss}	T_c	T_{diss}	T_c	T_{diss}
0.25	13.07	18.21	15.19	19.99	16.69	21.47	18.17	23.14
1.00	12.37	19.51	15.05	21.53	16.57	23.58	18.39	25.04
3.20	11.91	25.32	13.81	28.12	15.87	30.46	17.65	32.74
5.00	10.47	29.04	12.15	31.50	14.51	33.92	16.29	35.92
	Mix rapeseed/Methyl palmitate							
	$Con\ \left(\frac{g}{l}\right)$							
	154		192		231		269	
	T_c	T_{diss}	T_c	T_{diss}	T_c	T_{diss}	T_c	T_{diss}
0.25	3.00	7.60	4.46	9.76	7.76	11.60	8.53	12.82
1.00	0.74	8.99	3.33	11.08	7.03	13.30	7.96	14.64
3.20	-1.20	14.80	2.46	17.82	5.39	20.57	6.77	22.69
5.00	-0.88	18.38	1.59	21.32	3.77	22.79	4.80	26.84
	Mix rapeseed/Methyl stearate							
	$Con\ \left(\frac{g}{l}\right)$							
	154		192		231		269	
	T_c	T_{diss}	T_c	T_{diss}	T_c	T_{diss}	T_c	T_{diss}
0.25	12.45	17.67	14.27	19.53	15.14	21.05	17.45	22.45
1.00	11.81	18.62	12.72	20.20	14.70	22.43	16.26	23.54
3.20	9.50	22.33	11.04	25.18	10.41	26.56	13.85	29.59
5.00	6.22	27.45	9.62	28.50	11.60	32.40	12.84	33.68

Table 6.7. shows the equilibrium saturation temperature T_e and the crystallisation temperature at the kinetic limit T_C for each of the solution´s concentrations together

with the extent of metastability at different concentrations and the corresponding van't Hoff models.

Table 6.7 Solubility and supersolubility data of methyl palmitate and stearate in six different unsaturated esters type solvents, together with the metastable zone width at each concentration within each solution system. van't Hoff model for the solubility data are also given according to expression (2.43)

	Methyl oleate					
$Con\ \left(\frac{g}{l}\right)$	Methyl Palmitate			Methyl stearate		
	T_C	T_e	$MSZW$	T_C	T_e	$MSZW$
154	2.17	7.49	5.32	14.20	18.43	4.23
192	4.91	9.39	4.48	15.49	20.24	4.75
231	7.51	10.90	3.40	16.92	21.85	4.93
269	7.99	12.43	4.44	18.72	23.19	4.47
Van't Hoff model	$y = -7272.1\ x + 24.11$			$y = -8209.9\ x + 26.27$		
	Methyl linoleate					
	Methyl Palmitate			Methyl stearate		
	T_C	T_e	$MSZW$	T_C	T_e	$MSZW$
154	3.77	8.80	5.03	13.52	17.70	4.18
192	5.77	11.00	5.23	15.46	19.85	4.39
231	8.78	12.20	3.43	17.49	21.23	3.74
269	10.05	13.64	3.59	18.69	22.66	3.97
Van't Hoff model	$y = -7591.7\ x + 25.09$			$y = -7990.1\ x + 25.56$		
	Methyl linolenate					
	Methyl Palmitate			Methyl stearate		
	T_C	T_e	$MSZW$	T_C	T_e	$MSZW$
154	3.99	8.89	4.89	14.42	18.91	4.49
192	6.28	10.91	4.63	16.60	20.74	4.13
231	9.19	12.71	3.52	18.38	22.06	3.68
269	9.69	14.41	4.73	19.73	23.20	3.48
Van't Hoff model	$y = -6598.3\ x + 21.56$			$y = -9244.6\ x + 29.73$		
	Mix palm					
	Methyl Palmitate			Methyl Stearate		
	T_C	T_e	$MSZW$	T_C	T_e	$MSZW$
154	3.27	7.73	4.46	13.43	17.51	4.08
192	5.88	9.87	3.99	14.97	19.26	4.29
231	7.84	11.10	3.26	16.56	20.56	4.00
269	9.91	12.65	2.73	17.89	22.32	4.43
Van't Hoff model	$y = -7412.9\ x + 24.58$			$y = -8224.6\ x + 26.41$		
	Mix soy					
	Methyl Palmitate			Methyl Stearate		
	T_C	T_e	$MSZW$	T_C	T_e	$MSZW$
154	3.13	7.67	4.54	13.12	17.49	4.37
192	5.18	9.61	4.43	15.57	19.36	3.79
231	8.39	11.47	3.08	16.97	21.02	4.05
269	9.34	12.86	3.52	18.59	22.59	4.00
Van't Hoff model	$y = -6845.5\ x + 22.56$			$y = -7690.4\ x + 24.56$		

	Mix rapeseed					
	Methyl Palmitate			Methyl Stearate		
	T_C	T_e	$MSZW$	T_C	T_e	$MSZW$
154	2.22	6.94	4.72	13.04	16.71	3.67
192	4.26	9.00	4.74	14.09	18.70	4.62
231	7.93	11.20	3.26	15.11	20.09	4.98
269	8.80	12.02	3.22	17.39	21.55	4.16
Van't Hoff model	$y = -6669.2\ x + 21.99$			$y = -8117.0\ x + 26.10$		

The comparative plots of the solubility lines in the form of the van´t Hoff plot given by equation (2.43) for both C16:0 and C18:0 in each solvent are shown in Figs. 6.7 and 6.8 respectively.

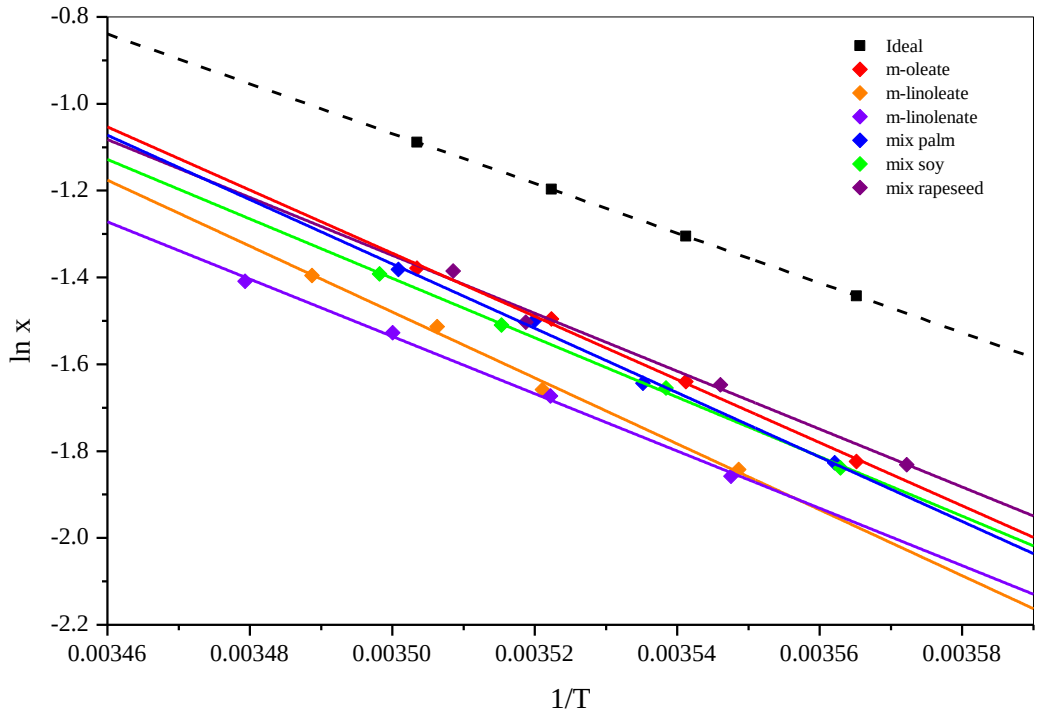

Figure 6.7 van't Hoff plot for methyl palmitate in six different unsaturated esters type solvents. Solid lines represent experimental solubilities and the dashed line the ideal solubility. Experimental solubilities were obtained by extrapolation to 0 ºC of $T_{diss}(q)$ lines at four different solution's concentrations

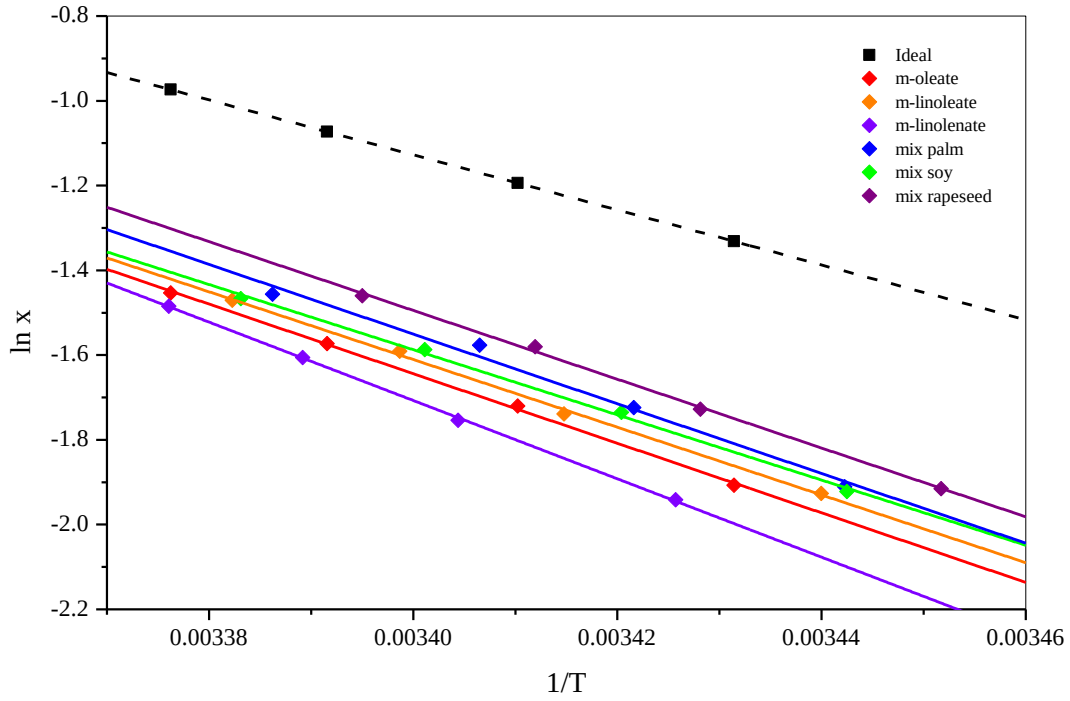

Figure 6.8 Solid lines represent experimental solubilities and the dashed line the ideal solubility. Experimental solubilities were obtained by extrapolation to 0 ºC of $T_{diss}(q)$ lines at four different solution's concentrations

The model lines representing the dependence of activity coefficient on temperature, enthalpies and entropies of dissolution and mixing for all systems are presented in Tables 6.8. and 6.9.

Table 6.8 Thermodynamic parameters derived from solubility data of methyl palmitate in solution with six different unsaturated esters type solvents, together with the linear dependence of γ on T

	ΔH_{diss} (KJ/mol)	ΔS_{diss} $\left(\frac{KJ}{K\ mol}\right)$	ΔH_{mix} (KJ/mol)	ΔS_{mix} $\left(\frac{KJ}{K\ mol}\right)$	Υ $1-15\ ^{\circ}C$	$\ln \Upsilon = aT + b$
Methyl oleate	60.46	0.20	12.79	0.04	1.65-1.26	$-0.019\,T + 0.52$
Methyl linoleate	63.12	0.21	15.45	0.05	1.98-1.43	$-0.023\,T + 0.70$
Methyl linolenate	54.86	0.18	7.19	0.02	1.81-1.56	$-0.011\,T + 0.60$
Mix palm	61.63	0.20	13.96	0.05	1.73-1.29	$-0.021\,T + 0.57$
Mix soy	56.92	0.19	9.24	0.03	1.64-1.35	$-0.014\,T + 0.51$
Mix rapeseed	55.45	0.18	7.78	0.02	1.52-1.29	$-0.012\,T + 0.43$

Table 6.9 Thermodynamic parameters derived from solubility data of methyl stearate in solution with six different unsaturated esters type solvents, together with the linear dependence of γ on T

	ΔH_{diss} (KJ/mol)	ΔS_{diss} $\left(\frac{KJ}{K\ mol}\right)$	ΔH_{mix} (KJ/mol)	ΔS_{mix} $\left(\frac{KJ}{K\ mol}\right)$	Υ $1-20\ ^{\circ}C$	$\ln \Upsilon = aT + b$
Methyl oleate	68.26	0.22	14.32	0.04	2.50-1.72	$-0.020\ T + 0.94$
Methyl linoleate	66.43	0.21	12.49	0.04	2.30-1.65	$-0.018\ T + 0.85$
Methyl linolenate	76.86	0.25	22.92	0.07	3.39-1.85	$-0.032\ T + 1.25$
Mix Palm	68.38	0.22	14.44	0.05	2.29-1.56	$-0.020\ T + 0.85$
Mix soy	63.94	0.20	10.00	0.03	2.10-1.61	$-0.014\ T + 0.76$
Mix rapeseed	67.49	0.22	13.55	0.04	2.12-1.47	$-0.019\ T + 0.77$

6.3.2. Assessment of methyl palmitate and stearate solubility in six model unsaturated methyl esters type solvents

In general solubility of C16:0 is higher than that of C18:0 in all solvents analysed i.e. decreases with the carbon chain length of the acid moiety. The results show that for C16:0 the highest solubility is observed in mixtures of unsaturated esters such as in rapeseed oil and then decreases in the following order: rapeseed mix > m-oleate > palm mix > soy mix > m-linoleate > m-linolenate. Solubility among the first four solvent systems do not differ more than 7%. Solubilities in m-linoleate and m-linolenate are very close in magnitude and differ from the most soluble systems by no more than 19%.

For C18:0 systems higher solubilities are also observed in mixed of unsaturated esters such as in rapeseed oil and then decreased in the following order: rapeseed mix > palm mix > soy mix > m-linoleate > m-oleate > m-linolenate. Solubility among the highest and lowest soluble system differs by around 24%. However, in general solubilities in the six different solvent compositions do not differ significantly likely due to the similarity in solvent's molecules dipole moment which range between 1.60 and 1.90 D [3].

In the case of C16:0 activity coefficients increase with increase in double bonds in the unsaturated ester solvent i.e. activities are lower in methyl oleate (1 double bond) followed by an increase in methyl linoleate (2 double bonds) and methyl linolenate (3 double bonds) solvents. This is likely to be a result of the increasing presence of cis- and trans- isomers with increase in double bonds, which will reduce the surface area of the solvent available for bond interaction due to the modified shape of cis- and trans- isomers molecules. Thus, this reducing the strength of chemical interaction between solute and solvent molecules. For the mixtures of the three unsaturated esters in the same proportions as they are present in palm, soy and rapeseed oil, the activities are very close to those values obtained for methyl oleate solvent, showing the lowest values for solvent proportions as in rapeseed oil, where methyl oleate constitutes approximately 60% of the total blend. In agreement with the previous assessment, activities for solvent proportions as in palm and soy oil are respectively slightly higher, although very close in magnitude, as their content of methyl oleate decreases to approximately 40% for palm oil and 23% in soy oil. In the latter case methyl linoleate constitutes the highest proportion of unsaturated methyl esters, around 53% delivering in this case higher activity coefficients.

Interestingly, even though ϒ values are relatively higher in C16:0/methyl linolenate solutions, ΔH_{diss} and ΔS_{diss} are the lowest for this solvent. It seems that in this case the solutions behave a-thermally i.e. enthalpy of dissolution is independent on temperature, which can be evidence by the lowest slope of the activity model. The van´t Hoff plots in this case are almost parallel to the ideal line making the enthalpy of dissolution very close to that of the enthalpy of melting. Thus, the deviation from ideality can be considered to be mostly due to entropic factors which is in agreement with the behaviour of a-thermal solutions. This behaviour could be the result of similar chemical interaction strengths between solute-solute, solvent-solvent and solute-solvents molecules.

C16:0 has less carbons than any of the solvent molecules and therefore van der Waals forces are likely similar to those between methyl linolenate molecules. This could be due to expected relative higher presence a of cis- and trans- isomers in this solvent that would reduce intermolecular forces between solvent molecules, this leading to relatively low enthalpies of dissolution. However, higher activities are

observed likely due to the fact that this effect is offset by a very low increase in entropy on mixing. Not much increase on the solution volume on mixing can be expected, as the presence of cis- and trans- isomers within the solvent would modify the shape of methyl linolenate molecules likely making their size very similar to that of C16:0.

Solutions of C18:0 in unsaturated solvents are less ideal than those of C16:0, however a similar trend in terms of solubility and ideality is observed. C18:0 solutions are also the least ideal in methyl linolenate solvent and the most ideal in mixtures of unsaturated esters such in rapeseed oil. Activities are higher using single unsaturated esters as solvents than mixtures of them such as in palm, soy and rapeseed oil. This may indicate that due to the equal number of carbons present in the solute and solvents molecules, the effect on the change in energy released with the formation of chemical interactions between solute-solvent molecules, caused by the presence of cis- and trans- isomers within the solvent, is less important than in the case of C16:0 solutions. In C18:0 solutions, solvent-solvent interactions would constitute a more important part of the enthalpy of dissolution, offsetting the decrease in energy released on mixing with increasing double bonds within solvent molecules.

6.4. Assessment of methyl palmitate and stearate solubility as a function of type solvent

A combined assessment of the solubility data obtained in the model diesel type solvents and unsaturated esters solvents shows that in general saturated methyl esters are more soluble in toluene, methyl-cyclohexane and n-heptane. The solubility of C16:0 in methyl oleate and the mixtures of methyl esters such as in palm, soy and rapeseed oil is very close in magnitude to that of C16:0 in kerosene. The solubility of the same solute in methyl linoleate and linolenate is lower and closer in magnitude to that observed in n-dodecane.

In the case of C18:0 solutions solubility in mixtures of unsaturated esters such as in rapeseed oil showed very close values to those observed in n-dodecane . Its solubility

in all other unsaturated esters solvents systems is lower than that in n-dodecane. This observation is interesting given that methyl stearate contain the same number of carbons as any molecules in the unsaturated solvents used.

This findings indicate that even though C16:0 and C18:0 molecules have very similar polarity than that of unsaturated methyl esters, the differences in molecular sizes between solute and solvent molecules would allow for a better solvation process by more compact or smaller molecular structures such as those of the model diesel type solvents.

6.5. Conclusions

An assessment on the solubility of C16:0 and C18:0 as a function of solution environment was carried out, delivering related parameters such as: enthalpy and entropy of dissolution and mixing and activity coefficients as a function of solution environment.

In all cases the solubility was observed to be less than ideal showing that solute-solute interactions are generally favoured over those between solute-solvent molecules. Both C16:0 and C18:0 showed the highest solubility in diesel type solvents with compact structures such as methyl-cyclohexane and toluene and aliphatic compounds with short carbon chain lengths such as n-heptane.

Solubility of C16:0 in all analysed unsaturated methyl esters solvents are very similar, generally decreasing with the increase in proportions of double-bonds within the solvent molecules. Similarly, the solubility of this compound in methyl oleate compares well with those observed in mixtures of unsaturated esters solvents in the same proportions as they are present in palm, soy and rapeseed oil. Although the results obtained for C18:0 in unsaturated methyl esters does not follow the same trend, solubility and activity coefficients only differ significantly for C18:0 in methyl linolenate solvent.

Comparatively, the solubility of the saturated esters (C16:0 and C18:0) in unsaturated methyl esters is similar in magnitude to those observed in kerosene and n-dodecane solutions for methyl palmitate and stearate respectively.

This information provides the bases for the analysis of nucleation and growth kinetics of the same model solutions as presented in Chapter 7 and 8 of this thesis.

References

[1] J.J. Scheepers, E. Muzenda, M. Belaid, Influence of structure on fatty acid ester-alkane interactions, International Conference on Chemical Engineering and its Applications, (2012) 93-102.

[2] J.J. Scheepers, E. Muzenda, M. Belaid, Influence of temperature and molecular structure on organics-biodiesel interactions using group contribution methods Proceedings - World Congress on Engineering III (2012).

[3] J.W. Smith, The dipole moments of some l
ong chaim molecules, J Chem Soc, (1933) 1567-1570.

7. Nucleation of Model Methyl Esters as a Function of Solution Environment

Summary: extends the assessment of representative methyl palmitate and stearate solutions to the analysis of nucleation kinetics using the methodology developed in Chapter 5

7.1. Introduction

Following the analysis of solubility of model saturated esters solutions the assesment is extended to the nucleation of methyl palmitate (C16:0) and stearate (C18:0) as a function of solution environment. This is done through the application of the KBHR approach introduced in Chapter 5 which allowed assessing the nucleation mechanism and obtain relevant nucleation parameters.

An in depth analysis is presented for methyl stearate crystallising from n-dodecane, kerosene and toluene solvents in order to extend the application of the $KBHR$ approach to obtain the number of crystals at the detection point N_{det} and the corresponding nucleation rates for these specific systems.

7.2. Nucleation mechanism and parameters for methyl palmitate and stearate crystallising from diesel type solvents

7.2.1. Experimental polythermal results

The values of relative critical undercooling u_c at the corresponding concentrations and cooling rates q were calculated from equation (5.3) using the equilibrium temperatures T_e from the solubility data and average values for the collected crystallisation temperatures T_c (Tables 6.1. and 6.2. Chapter 6). Table 7.1. shows these results for methyl palmitate and stearate crystallising from five different diesel type solvents. The $u_c$values are within the limits specified by inequalities (5.5). This means that in all cases the experimentally obtained limit of metastability corresponds to a relatively low supersaturation for which the methodology presented in Chapter 5 is justified.

Table 7.1 Relative critical undercooling (u_c) as a function of cooling rate (q) and concentration for solutions of methyl palmitate and stearate in five different diesel type solvents

	n-Dodecane							
	Methyl palmitate				Methyl stearate			
	$Con\ \left(\frac{g}{l}\right)$							
$q\ \left(\frac{K}{s}\right)$	200	250	300	350	200	250	300	350
0.004	0.0114	0.0103	0.0098	0.0115	0.0099	0.0125	0.0113	0.0147
0.017	0.0143	0.0156	0.0129	0.0141	0.0126	0.0145	0.0123	0.0166
0.053	0.0204	0.0216	0.0191	0.0198	0.0175	0.0192	0.0170	0.0209
0.150	0.0291	0.0289	0.0274	0.0297	0.0269	0.0279	0.0258	0.0318
	Kerosene							
	Methyl palmitate				Methyl stearate			
	$Con\ \left(\frac{g}{l}\right)$							
$q\ \left(\frac{K}{s}\right)$	200	250	300	350	200	250	300	350
0.004	0.0239	0.0217	0.0110	0.0113	0.0166	0.0131	0.0140	0.0143
0.017	0.0298	0.0240	0.0155	0.0153	0.0189	0.0149	0.0182	0.0172
0.053	0.0350	0.0290	0.0239	0.0206	0.0246	0.0238	0.0236	0.0228
0.150	0.0437	0.0374	0.0331	0.0340	0.0331	0.0316	0.0327	0.0343
	Toluene							
	Methyl palmitate				Methyl stearate			
	$Con\ \left(\frac{g}{l}\right)$							
$q\ \left(\frac{K}{s}\right)$	154	192	231	269	154	192	231	269
0.004	0.0087	0.0054	0.0073	0.0087	0.0156	0.0161	0.0178	0.0163
0.008	0.0077	0.0112	0.0076	0.0083	0.0203	0.0181	0.0188	0.0159
0.017	0.0057	0.0055	0.0017	0.0006	0.0179	0.0187	0.0182	0.0184
0.025	0.0042	0.0077	0.0034	0.0041	0.0218	0.0208	0.0216	0.0201
	n-Heptane							
	Methyl palmitate				Methyl stearate			
	$Con\ \left(\frac{g}{l}\right)$							
$q\ \left(\frac{K}{s}\right)$	154	192	231	269	154	192	231	269
0.004	0.0078	0.0092	0.0082	0.0089	0.0135	0.0137	0.0155	0.0131
0.017	0.0135	0.0126	0.0079	0.0093	0.0147	0.0191	0.0161	0.0124
0.033	0.0138	0.0122	0.0144	0.0107	0.0200	0.0190	0.0204	0.0171
0.053	0.0147	0.0101	0.0098	0.0061	0.0187	0.0159	0.0176	0.0172
	Methyl-cyclohexane							
	Methyl palmitate				Methyl stearate			
	$Con\ \left(\frac{g}{l}\right)$							
$q\ \left(\frac{K}{s}\right)$	154	192	231	269	154	192	231	269

0.004	0.0105	0.0098	0.0112	0.0086	0.0139	0.0189	0.0145	0.0129
0.017	0.0126	0.0146	0.0114	0.0091	0.0143	0.0132	0.0143	0.0136
0.033	0.0164	0.0116	0.0129	0.0095	0.0182	0.0178	0.0181	0.0162
0.053	0.0166	0.0130	0.0130	0.0099	0.0185	0.0188	0.0179	0.0140

In order to establish the nucleation mechanism for a solution system at a given concentration, a plot of cooling rate q vs. relative critical undercooling u_c in *ln-ln* coordinates was constructed to obtain the slope of the straight line fitting these data points. Fig. 7.1 and 7.2 present selected examples of the plots obtained for methyl palmitate and stearate in the different diesel type solvents. The slope and the correlation coefficient R^2 of the best-fit straight line to the data at four different concentrations within each system are presented in Table 7.2. and 7.3. for methyl palmitate and stearate solutions respectively.

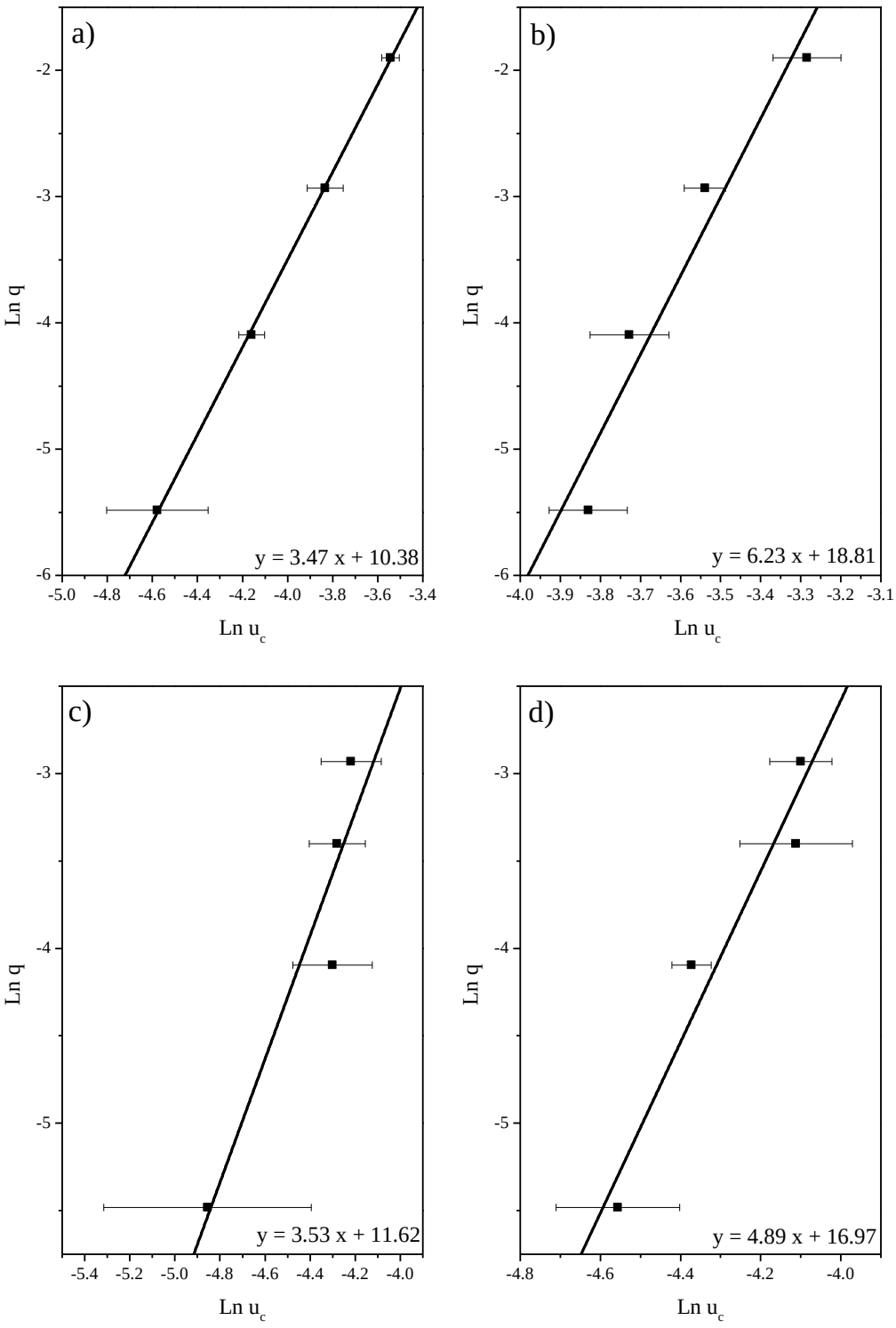

Figure 7.1 Experimental polythermal data in ln q vs ln u_c coordinates for methyl palmitate crystallising from a) n-dodecane and b) kerosene solvents at solution concentrations of 250 g/l and from c) n-heptane and d) methyl-cyclohexane solvents at solution concentrations of 154 g/l

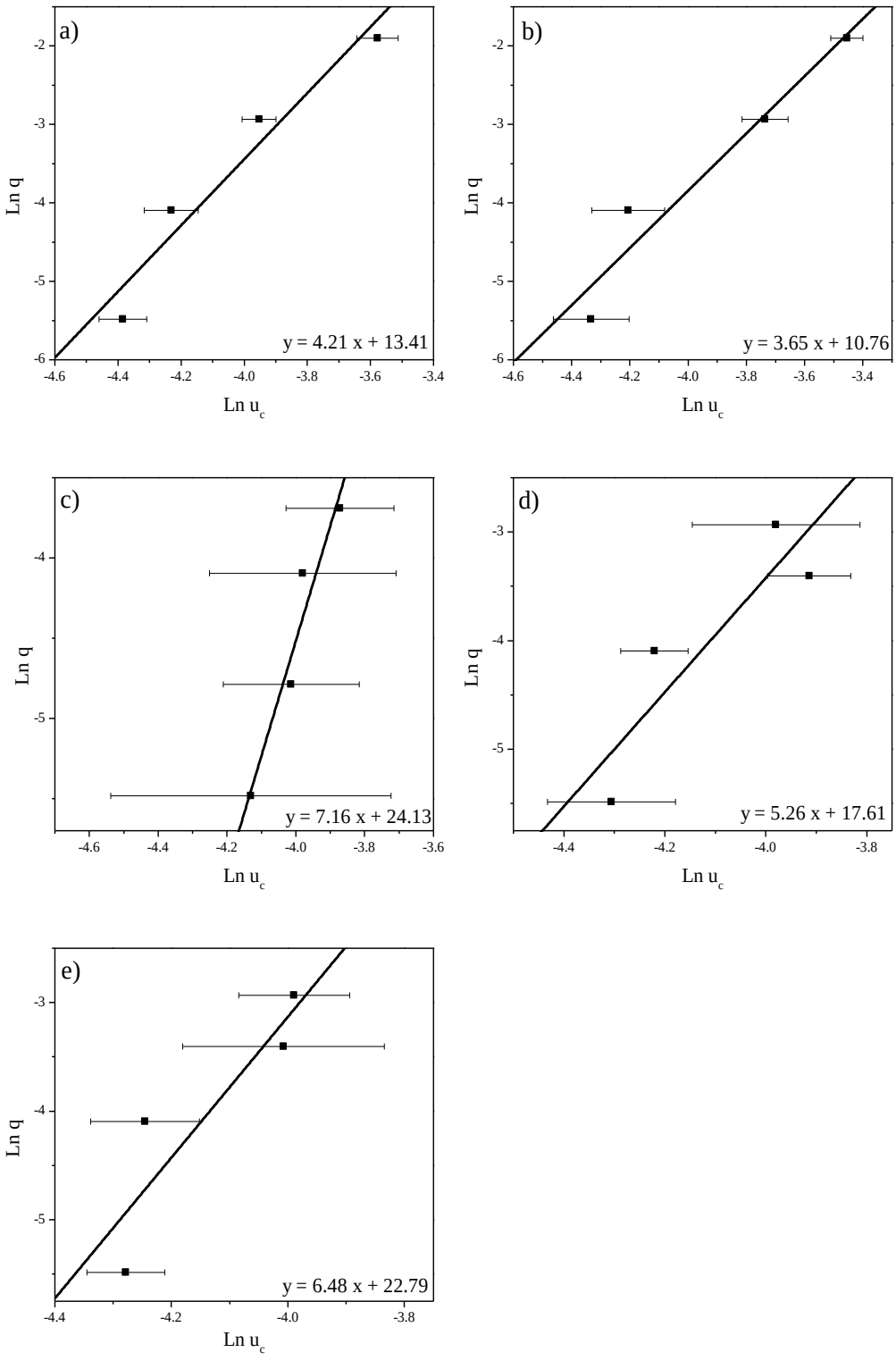

Figure 7.2 Experimental polythermal data in ln q vs ln u_c coordinates for methyl stearate crystallising from a) n-dodecane and b) kerosene solvents at solution concentrations of 250 g/l c) toluene at solution concentrations of 192 g/l, d) n-heptane and e) methyl-cyclohexane solvents at solution concentrations of 154 g/l

Table 7.2 Parameters obtained from the analysis of polythermal data of methyl palmitate crystallising from diesel type solvents: slopes of the best linear fit to data points in $ln\ q$ vs. $ln\ u_c$ coordinates and correlation coefficients; values of the free parameters a_1, a_2 and $ln\ q_o$ obtained from the data fitting in $ln\ q$ vs. u_c coordinates according to equation (5.9) and correlation coefficients (the errors of the slope and the free parameters refer to the 95% confidence interval)

Con. (g/l)	Slope of best-fit straight line of $\ln u_c \ vs. \ln q$	R^2, linear fitting	Nucleation Mechanism	a_1	$a_2 = b$	$\ln q_0$	$q_0\left(\frac{K}{s}\right)$	R^2, fitting equation (5.9)
n-dodecane								
200	3.70	0.97	PN	3	0.000120 ±0.000043	8.99±0.20	8.00E+03	0.99
250	3.47	1.00	PN	3	0.000052±0.000016	8.71±0.09	6.06E+03	1.00
300	3.38	0.98	PN	3	0.000052±0.000026	9.07±0.16	8.72E+03	0.99
350	3.63	0.96	PN	3	0.000120±0.000059	9.00±0.29	8.07E+03	0.98
Kerosene								
200	6.01	0.99	PN	3	0.001440±0.000135	8.27±0.16	3.89E+03	1.00
250	6.23	0.94	PN	3	0.001310±0.000304	9.12±0.48	9.15E+03	0.97
300	3.19	0.99	PN	3	0.000036±0.000022	8.40±0.10	4.44E+03	1.00
350	3.23	0.96	PN	3	0.000065±0.000060	8.60±0.28	5.41E+03	0.97
Toluene								
154	-2.34	0.93	-	-	-	-	-	-
192	0.30	0.02	-	-	-	-	-	-
231	-0.84	0.55	-	-	-	-	-	-
269	-0.36	0.34	-	-	-	-	-	-
Heptane								
154	3.53	0.89	PN	3	0.000024±0.000046	9.46±0.44	1.29E+04	0.89
192	3.18	0.18	-	-	-	-	-	-
231	2.28	0.31	-	-	-	-	-	-
269	-1.68	0.13	-	-	-	-	-	-
Methyl-cyclohexane								
154	4.89	0.94	PN	3	0.000168±0.000065	9.85±0.40	1.89E+04	0.95
192	3.98	0.37	PN	3	0.000108±0.000241	10.04±1.82	2.30E+04	0.41
231	12.52	0.80	PN	3	0.000692±0.000314	14.12±2.22	1.35E+06	0.81
269	18.02	0.94	PN	3	0.000645±0.000114	17.68±1.35	4.78E+07	0.96

Table 7.3 Parameters obtained from the analysis of polythermal data of methyl stearate crystallising from diesel type solvents: slopes of the best linear fit to data points in ln q vs. ln u_c coordinates and correlation coefficients; values of the free parameters a_1, a_2 and ln q_o obtained from the data fitting in ln q vs. u_c coordinates according to equation (5.9) and correlation coefficients (the errors of the slope and the free parameters refer to the 95% confidence interval)

Con. (g/l)	Slope of best-fit straight line of $\ln u_c \ vs. \ln q$	R^2, linear fitting	Nucleation Mechanism	a_1	$a_2 = b$	$\ln q_0$	$q_0 \left(\frac{K}{s}\right)$	R^2, fitting equation (5.9)
n-dodecane								
200	3.50	0.96	PN	3	0.000074±0.000042	9.29±0.26	1.08E+04	0.98
250	4.21	0.94	PN	3	0.000219±0.000087	9.35±0.38	1.15E+04	0.97
300	3.89	0.89	PN	3	0.000139±0.000109	9.54±0.60	1.39E+04	0.92
350	4.30	0.90	PN	3	0.000330±0.000169	9.10±0.55	8.92E+03	0.94
Kerosene								
200	4.92	0.95	PN	3	0.000521±0.000146	8.98±0.37	7.97E+03	0.97
250	3.65	0.94	PN	3	0.000132±0.000109	8.64±0.42	5.64E+03	0.95
300	4.22	0.99	PN	3	0.000262±0.000029	8.70±0.09	6.00E+03	1.00
350	3.93	0.95	PN	3	0.000239±0.000103	8.67±0.33	5.85E+03	0.97
Toluene								
154	3.98	0.56	PN	3	0.000176±0.000408	7.94±1.26	2.82E+03	0.57
192	7.16	0.94	PN	3	0.000683±0.000204	9.59±0.64	1.47E+04	0.94
231	6.65	0.55	PN	3	0.000709±0.000821	9.38±2.35	1.18E+04	0.55
269	6.42	0.79	PN	3	0.000532±0.000372	9.38±1.26	1.19E+04	0.78
Heptane								
154	5.26	0.79	PN	3	0.000320±0.000234	9.60±0.97	1.48E+04	0.82
192	3.96	0.33	PN	3	0.000182±0.000512	8.98±2.00	7.92E+03	0.35
231	6.39	0.49	PN	3	0.000601±0.000695	10.28±2.46	2.91E+04	0.53
269	4.94	0.59	PN	3	0.000187±0.000313	9.57±1.58	1.43E+04	0.58
Methyl-cyclohexane								
154	6.48	0.80	PN	3	0.000448±0.000287	10.24±1.21	2.80E+04	0.80
192	0.06	0.00	-	-	-	-	-	-
231	6.99	0.66	PN	3	0.000503±0.000452	10.44±1.86	3.42E+04	0.66
269	7.34	0.42	PN	3	0.000508±0.000615	11.42±3.21	9.08E+04	0.46

In all cases the slopes of the lines are higher than 3, suggesting that crystallisation of both methyl palmitate and stearate proceeds via the PN mechanism regardless the diesel type solvent. Thus, according to the $KBHR$ approach, equation (5.9) should describe the experimental data plotted in $Ln\, q$ vs. u_c coordinates. The parameters a_1, a_2 and $ln\, q_0$ for each of the solution concentrations within each solvent system and the corresponding correlation coefficients, are also given in Tables 7.2. and 7.3. Selected examples of the best-fit curves to the experimental $u_c(q)$ values are presented in Fig.7.3.

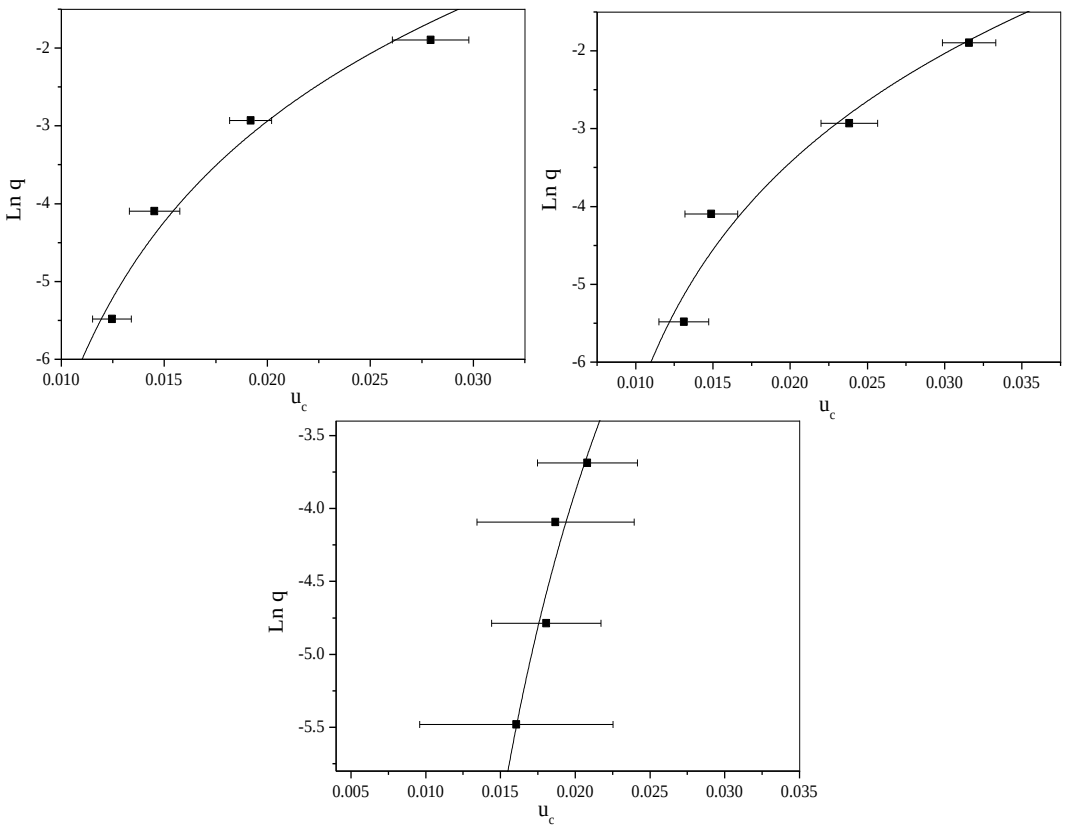

Figure 7.3 Increase in relative critical undercooling u_c with the natural logarithm of cooling rate q. The points represent the data for crystallisation of methyl stearate in solution with a) n-dodecane 250 g/l b) kerosene 250 g/l and c) toluene 192 g/l; the line illustrates the best fit according to equation (5.9)

Nucleation experimental data for C16:0 crystallising from toluene and n-heptane solvent did not show any correlation between the crystallisation temperature T_c and cooling rates q within the whole range of concentrations studied and the three highest concentrations in the former and latter case respectively, thus further assessment of these systems could not be performed.

The effective interfacial tension γ_{eff} was evaluated from equation (5.8), using $v_o = 0.491\, nm^3$ for the volume occupied by a single molecule within the crystal assuming orthorhombic unit cell parameter according to MacGillavry C., Wolthuis – Spuy M. Acta Cryst. (1970) B.26, 645 for both C16:0 and C18:0, the calculated equilibrium temperatures T_e, the shape factor $k_n = \frac{16}{3}\pi$ for spherical nuclei and the molecular latent heat λ of crystallisation which was estimated assuming the enthalpy of dissolution obtained from the solubility data can be equated to the enthalpy of

crystallisation. In addition to this, the critical nucleus radius r^* and number i^* of molecules were obtained from equation (5.16) and (5.17) respectively, calculated at u_c levels obtained using the T_c values corresponding to the extrapolation to 0°C/min of $T_c(q)$ lines, at each of the four concentrations within each solvent system. The results are given in Table 7.4. and 7.5. for methyl palmitate and stearate respectively.

Table 7.4 Nucleation kinetics parameters for methyl palmitate crystallising from five different diesel type solvents at four different solution concentrations. The interfacial tension and critical radius are calculated at u_c corresponding to $T_c$values obtained by the extrapolation to 0°C/min of ($T_c(q)$) lines

	x $\left(\frac{mol\ solute}{mol\ solution}\right)$	u_c	x_f	σ	$\gamma\left(\frac{mJ}{m^2}\right)$	$r^*(nm)$	i^*
n-Dodecane	0.144	0.0123	0.10	0.51	1.24	0.77	3.84
	0.174	0.0126	0.12	0.51	0.94	0.57	1.57
	0.201	0.0108	0.14	0.41	0.95	0.67	2.55
	0.227	0.0120	0.15	0.49	1.24	0.78	4.12
Kerosene	0.134	0.0262	0.04	2.07	3.32	0.77	3.85
	0.162	0.0222	0.07	1.44	3.23	0.88	5.82
	0.188	0.0129	0.10	0.79	0.97	0.46	0.80
	0.213	0.0120	0.13	0.63	1.19	0.60	1.87
Toluene	0.057	0.0095	0.05	0.22	-	-	-
	0.070	0.0076	0.06	0.15	-	-	-
	0.083	0.0083	0.07	0.17	-	-	-
	0.096	0.0094	0.08	0.22	-	-	-
n-Heptane	0.077	0.0092	0.06	0.33	0.68	0.62	2.02
	0.094	0.0109	0.07	0.40	-	-	-
	0.111	0.0084	0.09	0.25	-	-	-
	0.127	0.0101	0.09	0.39	-	-	-
Methyl-cyclohexane	0.068	0.0105	0.05	0.38	1.28	1.03	9.42
	0.083	0.0113	0.06	0.43	1.11	0.83	4.89
	0.098	0.0110	0.07	0.36	2.07	1.59	34.47
	0.113	0.0086	0.09	0.32	2.02	1.99	67.45

Table 7.5 Nucleation kinetics parameters for methyl stearate crystallising from five different diesel type solvents at four different solution concentrations. The interfacial tension and critical radius are calculated at u_c corresponding to $T_c$values obtained by the extrapolation to 0°C/min of ($T_c(q)$) lines

	x $\left(\frac{mol\ solute}{mol\ solution}\right)$	u_c	x_f	σ	$\gamma\left(\frac{mJ}{m^2}\right)$	$r^*(nm)$	i^*
n-Dodecane	0.132	0.0104	0.10	0.32	0.94	0.84	5.03
	0.160	0.0127	0.12	0.37	1.35	0.99	8.18
	0.186	0.0110	0.13	0.38	1.16	0.98	8.06
	0.210	0.0145	0.15	0.44	1.55	1.00	8.41
Kerosene	0.123	0.0171	0.07	0.66	1.91	0.94	7.16
	0.149	0.0138	0.10	0.50	1.21	0.74	3.46
	0.173	0.0154	0.11	0.55	1.52	0.84	4.99
	0.196	0.0147	0.13	0.54	1.48	0.85	5.33
Toluene	0.052	0.0160	0.03	0.55	1.18	0.73	3.26
	0.064	0.0156	0.04	0.49	1.86	1.17	13.75
	0.076	0.0174	0.05	0.58	1.88	1.07	10.44
	0.088	0.0149	0.06	0.49	1.71	1.13	12.45
n-Heptane	0.070	0.0134	0.04	0.59	1.76	0.98	7.97
	0.086	0.0162	0.05	0.69	1.46	0.67	2.59
	0.102	0.0158	0.06	0.66	2.18	1.02	9.19
	0.117	0.0122	0.08	0.54	1.48	0.90	6.30
Methyl-cyclohexane	0.062	0.0133	0.04	0.50	1.82	1.13	12.44
	0.076	0.0162	0.05	0.67	-	-	-
	0.090	0.0139	0.06	0.50	1.90	1.14	12.48
	0.103	0.0133	0.07	0.51	1.91	1.19	14.37

7.2.2. Comparative assessment of methyl palmitate and stearate nucleation from diesel type solvents

To help the visualization of the trend on the nucleation parameters as a function of solvent, Fig. 7.4 shows the averages of the values of each parameter obtained for the four solution concentrations analysed within each solution system. Table 7.6. highlights the solutions´ systems that stand out within some chosen relevant categories associated with specific nucleation parameters. These categories are defined in column one of the corresponding table.

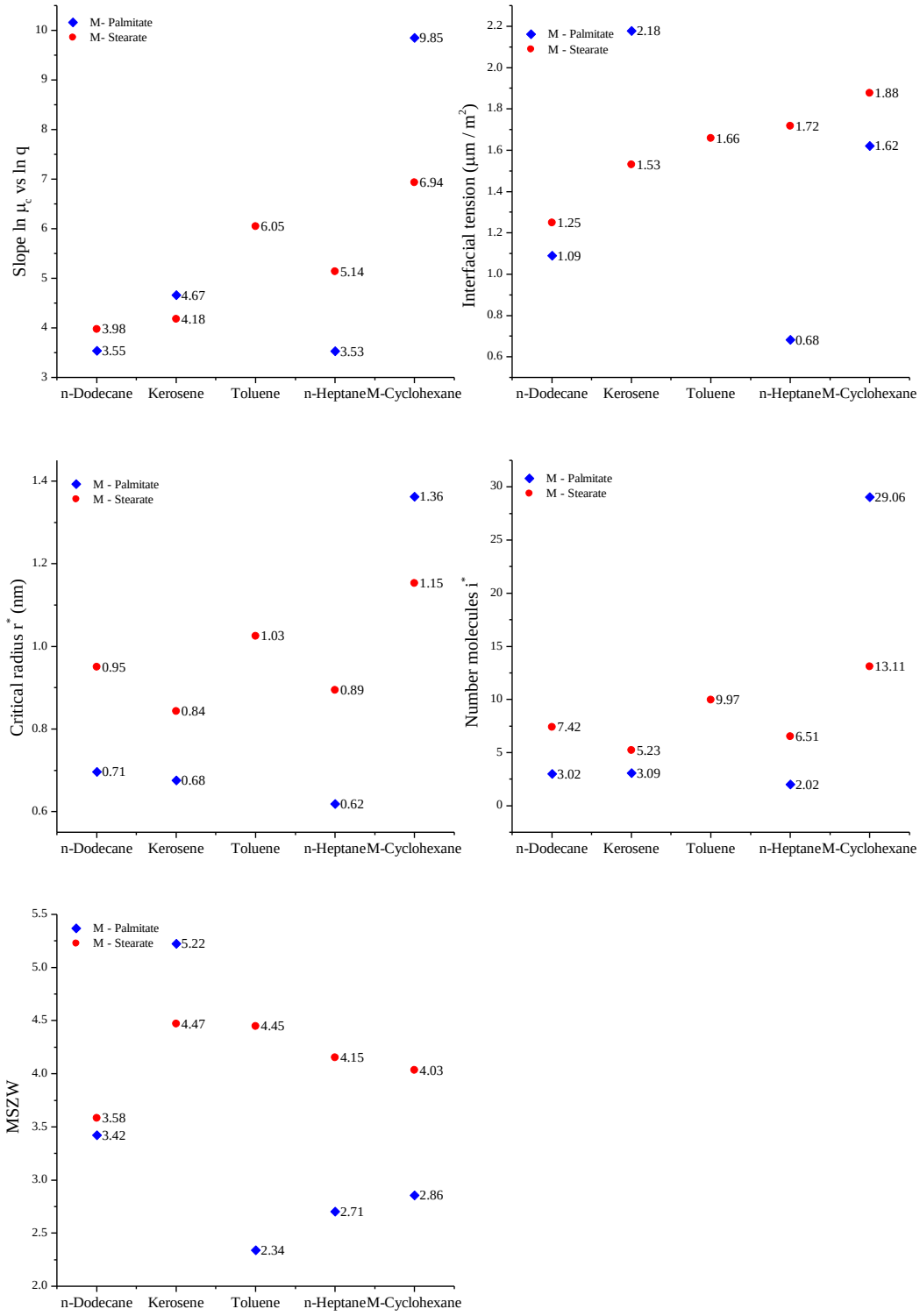

Figure 7.4 Comparative trend of nucleation kinetics parameters for methyl palmitate and stearate crystallising from five different model diesel type solvents. The data points correspond to the average of the relevant parameters obtained at four different solutions' concentrations

Table 7.6 Solution´s systems that stand out within a specific nucleation parameter category, for methyl palmitate and stearate crystallising from different diesel type solvents. Similarly, highlighted in red are the systems that stands out within each category

Category	C16:0 chosen solutions		C18:0 chosen solutions	
Higher slopes from the $ln\ q\ vs\ ln\ u_c$	C16:0/kerosene	**C16:0/methyl-cyclohexane**	C18:0/toluene	C18:0/methyl-cyclohexane
Lower slopes from the $ln\ q\ vs\ ln\ u_c$	C16:0/n-dodecane	**C16:0/n-heptane**	C18:0/n-dodecane	
Slopes from the $ln\ q\ vs\ ln\ u_c$ change significantly with concentration	C16:0/kerosene	C16:0/methyl-cyclohexane		
Higher interfacial tensions	**C16:0/kerosene**	C16:0/methyl-cyclohexane	C18:0/methyl-cyclohexane	
Higher r^* and i^*	**C16:0/methyl-cyclohexane**		C18:0/toluene	**C18:0/methyl-cyclohexane**
Lowest interfacial tensions	**C16:0/n-heptane**			
Lower MSZW	**C16:0/toluene**	C16:0/n-heptane	C18:0/n-dodecane	
Higher MSZW	**C16:0/kerosene**	C16:0/methyl-cyclohexane		

Although in most of the solution in diesel type solvents the analysis of polythermal data delivered higher slopes for the $ln\ q\ vs\ ln\ u_c$ lines in the case of C18:0 solute, nucleation in these solutions of both C16:0 and C18:0 is progressive in nature and similarly thermodynamically controlled as indicated by the close values of interfacial tensions obtained in all cases. Nucleation of C18:0 has a much closer thermodynamic dependence in all solutions´ systems with the exception of n-dodecane solvent as illustrated in Fig. 7.4.2 and 7.4.5 where similar values of interfacial tensions γ_{eff} and MSZW are observed independently of diesel solvent nature.

Regardless of this, some relevant mechanistic differences were observed within the solutions analysed, notably for crystallisation from kerosene and methyl-cyclohexane solvents. As indicated in Table 7.6 higher slopes of the $ln\ q\ vs\ ln\ u_c$ lines were obtained for C16:0 and C18:0 in methyl-cyclohexane, C16:0 in kerosene and C18:0 in toluene. These findings are in agreement with a lower observed kinetic dependence of crystallisation temperatures T_c on cooling rate q for the same systems, as indicated by the flatter tendency of these lines. According to classical theory in the nucleation rate (J) model given by equation (2.61), the thermodynamic

exponential function is related to the interfacial tension γ_{eff} and the nucleation rate constant k_J, which at the same time among others parameters is associated to the concentration of available nucleation sites C_0 and the frequency of attachment of the molecular building blocks to the nucleus, f^*. Given these correlations, as evidenced in this analysis where these systems also delivered higher interfacial tensions γ_{eff}, according to classical nucleation theory, nucleation within these solutions is much more thermodynamically controlled. The higher MSZW observed for nucleation to take place in solutions of C16:0 in kerosene and methyl-cyclohexane indicates that in this case a sufficient level of supersaturation was needed to overcome the thermodynamic barrier to nucleation characterised by the relative higher interfacial tension values.

In addition to this, the slopes of the $ln\ q\ vs\ ln\ u_c$ lines for C16:0 in kerosene and methyl-cyclohexane solutions showed a strong dependence on solution´s concentration (see Table 7.2.). These values indicate a decrease and an increase with concentration, on the thermodynamic influence on nucleation in the former and the latter case respectively. This effect is also illustrated by the values obtained for interfacial tensions as a function of concentration given in Table 7.4 and could be explained in terms of solubility. The activity coefficients of C16:0 in kerosene show a very strong dependence on temperature and the highest dependence among all solvents. These solutions become more ideal at higher concentrations levels and therefore the concentration of C16:0 (x_f) in the solution that is in equilibrium with the solid phase, at the corresponding crystallisation temperature T_c, are significantly lower at the lower solution´s concentrations Table 7.4. Given that interfacial tensions are inversely related to the equilibrium concentration, higher values of interfacial tensions were obtained at the lower solution´s concentration for C16:0 in kerosene solvent. The variability of the slopes of the $ln\ q\ vs\ ln\ u_c$ lines for solutions of C16:0 in methyl-cyclohexane, can be explained by flatter $T_c(q)$ lines obtained at the two highest solutions concentrations.

Although the low correlations of crystallisations temperature T_c on cooling rate q for C16:0 crystallising from toluene did not allow assessing nucleation using the KBHR approach, some relevant observations can still be made in the case. Interestingly,

given the low values of x_f (Table7.4.) in these solutions higher MSZW should have been observed to counteract the relatively high interfacial tension that could be expected under these conditions. However, whereas solubility of C16:0 in toluene solvent is the highest among all the solvents used, metastability in these solutions was observed to be the lowest. This might suggest that despite the expected higher values of interfacial tensions, the kinetics influence associated with the pre-exponential factor of the nucleation rate expression, would speed up the process due to higher concentration of nucleation sites C_0 available within the solution. The latter could be associated with the notable higher solubility of C16:0 in toluene providing higher concentration of molecules per unit volume.

On the other hand the lowest slopes of the $ln\ q\ vs\ ln\ u_c$ lines were observed in solutions of methyl esters with straight chain hydrocarbons such as C16:0 in n-heptane and n-dodecane as well as C18:0 in n-dodecane. The stepper $T_c(q)$ lines for these solutions are evidence of a more kinetically rate limited nucleation process, which is also in line with the lowest interfacial tensions obtained for the same systems (Fig. 7.4) among all solutions studied. This effect is likely to be the result of either low concentration of nucleation sites C_0 or low diffusion of molecules towards the nuclei due to the lower solubility of methyl esters in these solvents.

7.3. Nucleation rates for methyl stearate as a function of solution environment

An in depth analysis of nucleation was carried out for C18:0 crystallising from n-dodecane, kerosene and toluene with the aim of calculating nucleation rates using the interfacial tensions and the nucleation rate constant k_J obtained in the previous section.

Through the use of equation (5.12), k_J can be estimated from the corresponding values of N_{det}, the number of crystallites formed at the detection point. At a chosen temperature, this parameter can be obtained using the estimated fraction (percentage) in the precipitate and in the liquid after crystallisation, applying the methodology

described in section 4.3.4. to each of the solution systems. The mole fraction of C18:0 in the liquid phase was calculated using the following relationship

$$x_L = \frac{(average\ GC\ area\ C18{:}\ 0_P) * x_S}{(average\ GC\ area\ C18{:}\ 0_L)} \tag{7.1}$$

Where x is the mole fraction of C18:0, and L, P and S refer to the liquid, precipitate and homogeneous solution respectively.

Using the corresponding values of mole fraction, the mass of C18:0 per unit volume in the liquid phase can be obtained by solving the mass parameter in the molar fraction relationship. The mass of C18:0 in the solid phase per unit volume is therefore the difference between the initial mass of C18:0 in the homogenous solution and the mass in the liquid phase. This value can be converted to volume by dividing the mass of the solute in the solid phase by the corresponding density.

Finally, the number of nuclei per unit volume i.e. N_{det} as a function of solvent and solution concentration can be estimated from dividing the total volume of solid by the volume of a single nucleus. The latter can be obtained using the values of the critical radius assuming spherical nuclei.

The values of N_{det} obtained after the crystallisation of solutions at four different solution concentrations within each solvent system, are presented on Table 7.7. These correspond to the number of crystals calculated for methyl stearate crystallising at the T_C levels defined by the extrapolation to 0°C/min of $T_c(q)$ lines in each case.

Following this, the nucleation rate constants k_J can be calculated from equation (5.12) using $V = 1$, the corresponding equilibrium temperatures T_e, values of the dimensionless thermodynamic parameter b and values of the parameter q_0 for C18:0 as a function of solvent and concentration. Accordingly, nucleation rates can be calculated from expression (7.2)

$$J = k_J e^{\frac{-b}{(1-u)u^2}} \tag{7.2}$$

Nucleation rates values are also given in Table 7.7. Fig. 7.5. shows the trend of nucleation parameters as a function of solvent and solution concentration, to facilitate their correlation.

Table 7.7 Number of crystals at the detection point N_{det} and corresponding nucleation rates J for methyl stearate crystallising from three different solvents, at four different solution concentrations. The parameters are calculated at u_c corresponding to $T_c$values obtained by the extrapolation to 0 °C/min of $(T_c(q))$ lines

	x $\left(\frac{mol\ solute}{mol\ solution}\right)$	u_c	x_f	σ	N_{det}	$J\left(\frac{nuclei}{ml\ s}\right)$
n-dodecane	0.132	0.0104	0.10	0.32	7.24×10^{17}	2.00×10^{15}
	0.160	0.0127	0.12	0.37	4.85×10^{17}	2.12×10^{15}
	0.186	0.0110	0.13	0.38	3.44×10^{17}	1.41×10^{15}
	0.210	0.0145	0.15	0.44	1.54×10^{18}	6.21×10^{15}
Kerosene	0.123	0.0171	0.07	0.66	1.21×10^{19}	5.69×10^{16}
	0.149	0.0138	0.10	0.50	3.53×10^{19}	8.94×10^{16}
	0.173	0.0154	0.11	0.55	1.77×10^{19}	6.19×10^{16}
	0.196	0.0147	0.13	0.54	1.65×10^{19}	5.06×10^{16}
Toluene	0.052	0.0160	0.03	0.55	7.41×10^{17}	1.33×10^{15}
	0.064	0.0156	0.04	0.49	1.25×10^{17}	5.30×10^{14}
	0.076	0.0174	0.05	0.58	3.83×10^{17}	2.12×10^{15}
	0.088	0.0149	0.06	0.49	7.36×10^{16}	2.94×10^{14}

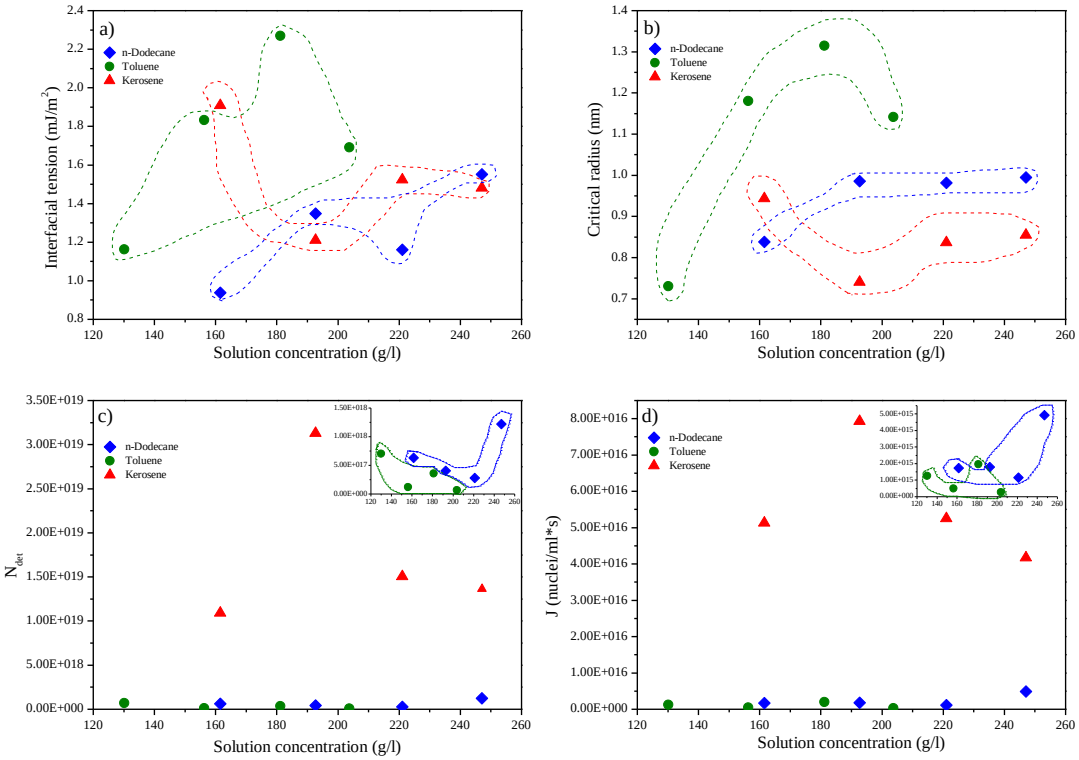

Figure 7.5 Comparison of nucleation kinetics parameters for C18:0 growing from n-dodecane, kerosene and toluene solvents at different solution concentrations. a) interfacial tension γ; b) critical radious r^* c) number of crystals at the detection point N_{det} and d) nucleation rates J

With the aid of the experimental data, model expressions can be obtained for the trend of the liquid that is in equilibrium with the solid after crystallisation as a function of temperature. These models are given by equations (7.3), (7.4) and (7.5) for methyl stearate crystallising from n-dodecane, kerosene and toluene solvent respectively. In these, y represents the concentration (in g/l) of methyl stearate in the liquid phase that is at equilibrium with the crystallised solid and x the corresponding crystallisation temperature.

$$y = 25.92e^{0.13\,x} \tag{7.3}$$

$$y = 33.39e^{0.12\,x} \tag{7.4}$$

$$y = 195.56e^{0.10\,x} \tag{7.5}$$

Using these expressions, the mass of solid that has crystallised at chosen undercooling levels (supersaturation levels) can be calculated to further obtain N_{det} values and nucleation rates (J) using equation (5.12) and (7.2) respectively. As an example, the trend of the nucleation rates (J) together with the critical radius (r^*) are plotted as a function of undercooling (u) as shown in Fig.7.6 for methyl stearate crystallising from n-dodecane, kerosene and toluene solvents. r^* values were calculated using the interfacial tension obtained at the highest solutions concentrations studied.

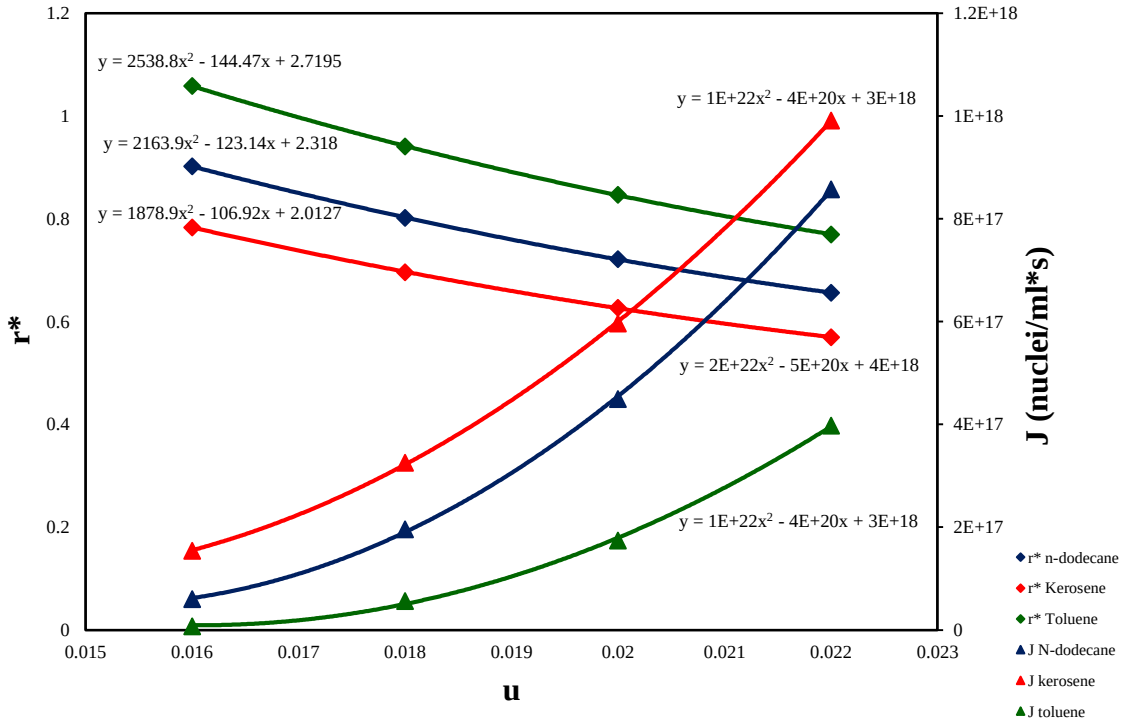

Figure 7.6 Tendency of critical radius (r*) and nucleation rates (J) as a function of critical undercooling (u) for C18:0 growing from n-dodecane, kerosene and toluene solvents

Nucleation rates were observed to be higher in kerosene followed by n-dodecane solvent. The lowest values of the rates delivered for toluene solvent could be associated with the higher interfacial tensions observed in this case. These values are likely influenced by the highest solubility of methyl stearate in toluene which would favour solute-solvent interactions over solute-solute ones. In addition to this, in toluene systems the fraction (x_f) of methyl stearate that remains in solution at the corresponding crystallisation temperatures, are lower in comparison to those in the

other two solvent systems, as crystallisation occurs at lower temperatures in this case. Thus, given that interfacial tensions are inversely related to x_f, higher values of this parameter should be expected. In these solutions a sufficient level of supersaturation is then required to overcome the free energy for nucleus formation, which can be evidence in the relative high levels of σ, at which nucleation took place even at such low T_c levels.

The dependence of T_c values on colling rates (q) is very similar in all cases as evidenced from the slope of the lines in Fig. 6.2. This suggesting, that the kinetics influence on nucleation is comparable in all systems. However, the higher values of interfacial tensions for methyl stearate in toluene solutions, indicate that in this case nucleation is a more thermodynamically controlled processed. On the other hand given that lower levels of interfacial tensions were observed in kerosene solutions, it is likely that under this condition nucleation is more kinetically controlled, hindered by the attachment frequency f^*. This could indicate that either volume diffusion or interface transfer of building units (molecules) would be rate limiting according to expressions (2.66) and (2.77). These conclusions are in line with a higher range of σ at which higher x_f values were calculated, allowing for both sufficient driving force for mass transfer and solute availability in solution that would reduce interfacial tension.

Interestingly, although similar values of interfacial tension to those of kerosene systems were obtained in n-dodecane solutions, the nucleation rates in the latter case were significantly lower by up to one order of magnitude. Given the expected lower strength of both solvent-solvent and solvent-solute intermolecular interaction, due to the non-polar nature of n-dodecane molecules, the diffusion of solute molecules should not be rate limiting and therefore sufficient levels of attachment frequency should be possible to reach. Based on these observations and accounting for the definition of nucleation rate given by equation (2.63), it is likely that in these systems nucleation rates are then hindered by the availability of nucleation sites C_0, due to the lower solubility of methyl steareate in n-dodecane that would allowed a lower amount of solute per unit volume.

7.4. Nucleation mechanism and parameters for methyl palmitate and stearate crystallising from unsaturated esters type solvents

7.4.1. Experimental results

For the crystallisation of methyl palmitate and stearate from unsaturated esters type solvents the relative critical undercooling u_c at the corresponding concentrations and cooling rates calculated from equation (5.3) are shown in Table 7.8. The $u_c$values are within the limits specified by inequalities (5.5), thus the use of the KBHR approach is justified. Similarly to the previous section and following the methodology Fig. 7.7 and 7.8 present selected examples of the $\ln q$ vs $\ln u_c$ plots obtained for methyl palmitate and stearate in the different unsaturated esters type solvents. The slope and the correlation coefficient R^2 of the best-fit straight line to the data at four different concentrations within each system are presented in Table 7.9. and 7.10. for methyl palmitate and stearate solutions respectively.

Table 7.8 Relative critical undercooling u_c as a function of cooling rate q and concentration for solutions of methyl palmitate and stearate in six different unsaturated esters type solvents

	M-Oleate							
	Methyl palmitate				Methyl stearate			
	$Con\ \left(\frac{g}{l}\right)$							
$q\ \left(\frac{K}{s}\right)$	154	192	231	269	154	192	231	269
0.004	0.0192	0.0138	0.0122	0.0163	0.0175	0.0184	0.0180	0.0161
0.017	0.0208	0.0207	0.0145	0.0164	0.0173	0.0192	0.0193	0.0192
0.053	0.0279	0.0238	0.0206	0.0235	0.0250	0.0218	0.0210	0.0198
0.083	0.0290	0.0258	0.0236	0.0243	0.0363	0.0336	0.0294	0.0308
	M-Linoleate							
	Methyl palmitate				Methyl stearate			
	$Con\ \left(\frac{g}{l}\right)$							
$q\ \left(\frac{K}{s}\right)$	154	192	231	269	154	192	231	269
0.004	0.0181	0.0181	0.0142	0.0157	0.0161	0.0168	0.0128	0.0140
0.017	0.0223	0.0221	0.0155	0.0143	0.0168	0.0156	0.0153	0.0159
0.053	0.0261	0.0228	0.0181	0.0173	0.0227	0.0205	0.0167	0.0173
0.083	0.0341	0.0288	0.0308	0.0293	0.0301	0.0251	0.0214	0.0234
	M-Linolenate							
	Methyl palmitate				Methyl stearate			

	$Con\ \left(\frac{g}{l}\right)$							
$q\ \left(\frac{K}{s}\right)$	154	192	231	269	154	192	231	269
0.004	0.0142	0.0154	0.0130	0.0179	0.0184	0.0157	0.0140	0.0136
0.017	0.0231	0.0196	0.0155	0.0173	0.0166	0.0158	0.0148	0.0144
0.053	0.0256	0.0236	0.0175	0.0217	0.0267	0.0251	0.0213	0.0198
0.083	0.0263	0.0256	0.0249	0.0259	0.0342	0.0294	0.0277	0.0283
	Mix Palm							
	Methyl palmitate				Methyl stearate			
	$Con\ \left(\frac{g}{l}\right)$							
$q\ \left(\frac{K}{s}\right)$	154	192	231	269	154	192	231	269
0.004	0.0153	0.0128	0.0121	0.0096	0.0155	0.0167	0.0148	0.0155
0.017	0.0193	0.0197	0.0157	0.0145	0.0160	0.0155	0.0158	0.0171
0.053	0.0326	0.0301	0.0251	0.0228	0.0225	0.0187	0.0169	0.0179
0.083	0.0319	0.0326	0.0314	0.0292	0.0281	0.0251	0.0246	0.0234
	Mix Soy							
	Methyl palmitate				Methyl stearate			
	$Con\ \left(\frac{g}{l}\right)$							
$q\ \left(\frac{K}{s}\right)$	154	192	231	269	154	192	231	269
0.004	0.0138	0.0144	0.0093	0.0137	0.0152	0.0143	0.0147	0.0149
0.017	0.0224	0.0198	0.0167	0.0153	0.0176	0.0147	0.0151	0.0142
0.053	0.0274	0.0271	0.0199	0.0191	0.0192	0.0190	0.0175	0.0167
0.083	0.0303	0.0281	0.0255	0.0277	0.0242	0.0247	0.0221	0.0213
	Mix Rapeseed							
	Methyl palmitate				Methyl stearate			
	$Con\ \left(\frac{g}{l}\right)$							
$q\ \left(\frac{K}{s}\right)$	154	192	231	269	154	192	231	269
0.004	0.0141	0.0161	0.0121	0.0122	0.0147	0.0152	0.0169	0.0139
0.017	0.0221	0.0201	0.0147	0.0143	0.0169	0.0205	0.0184	0.0179
0.053	0.0291	0.0232	0.0204	0.0184	0.0249	0.0263	0.0330	0.0261
0.083	0.0279	0.0263	0.0261	0.0254	0.0362	0.0311	0.0290	0.0296

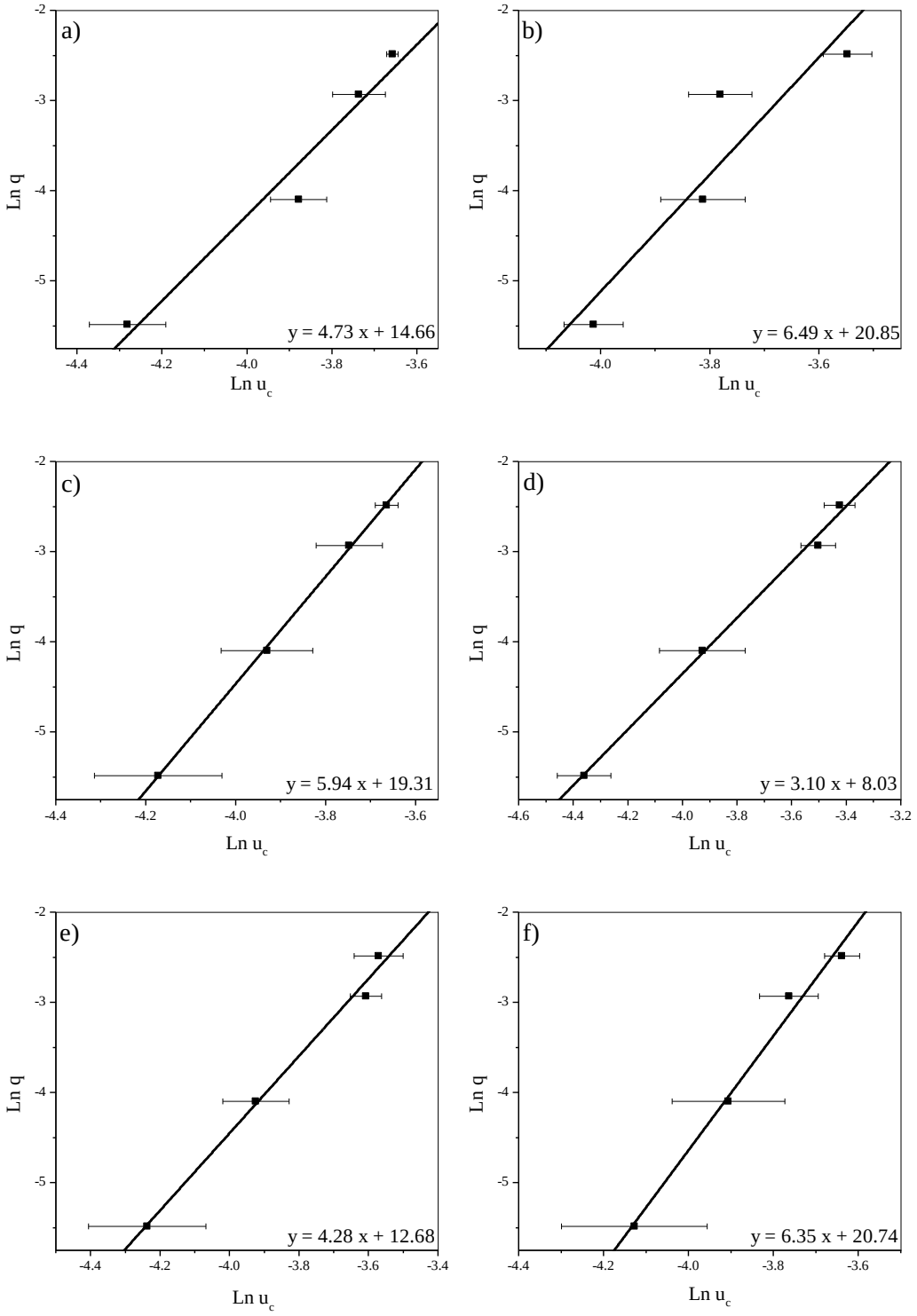

Figure 7.7 Experimental polythermal data in ln q vs ln u_c coordinates for methyl palmitate crystallising from a) m-oleate, b) m-linoleate, c) m-linolenate, d) mix palm, e) mix soy and f) mix rapeseed solvents at solution concentrations of 192 g/l

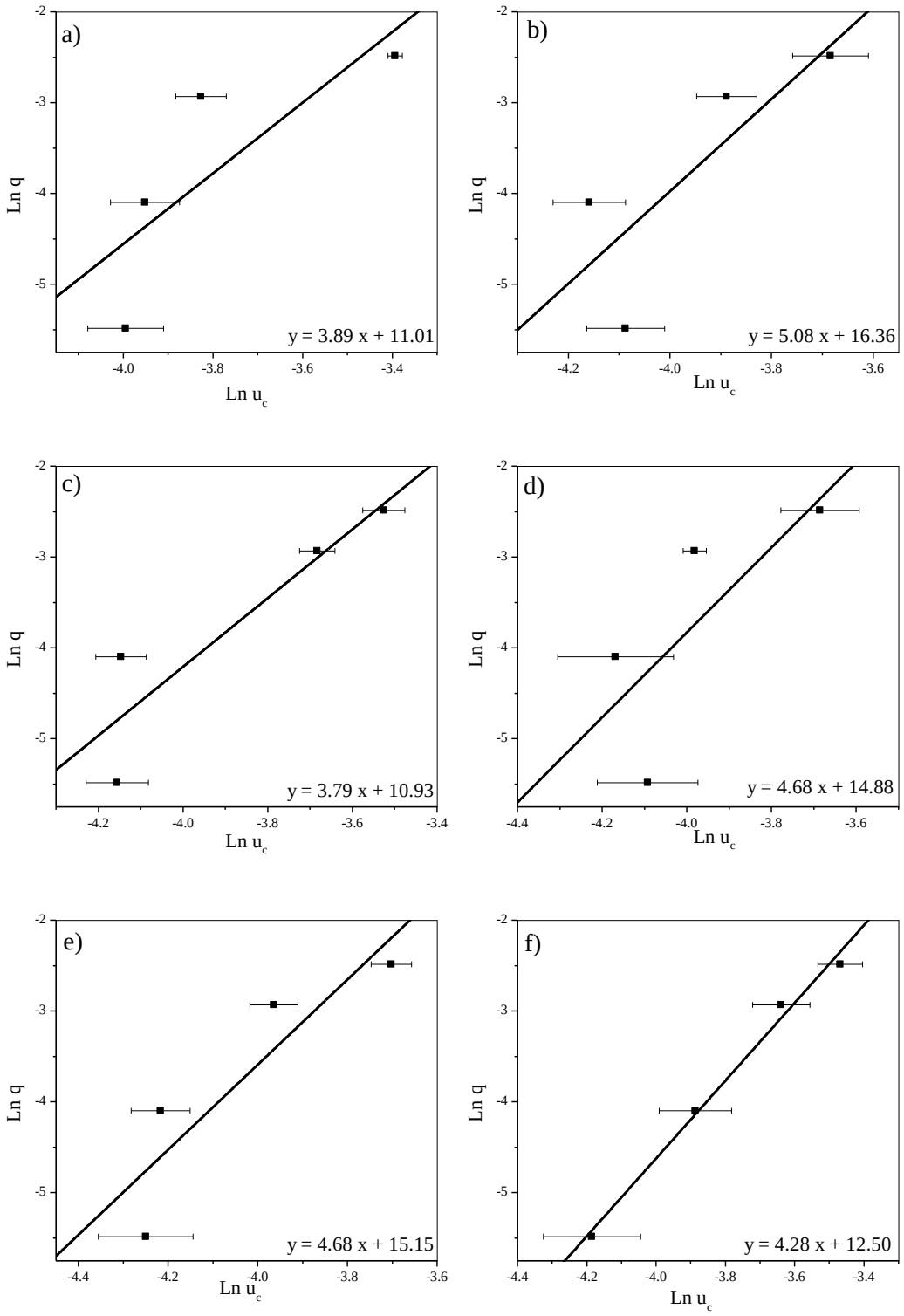

Figure 7.8 Experimental polythermal data in $ln\,q$ vs $ln\,u_c$ coordinates for methyl stearate crystallising from a) m-oleate, b) m-linoleate, c) m-linolenate, d) mix palm, e) mix soy and f) mix rapeseed solvents at solution concentrations of 192 g/l

Table 7.9 Parameters obtained from the analysis of polythermal data of methyl palmitate crystallising from unsaturated esters type solvents: slopes of the best linear fit to data points in $ln\, q$ vs. $ln\, u_c$ coordinates and correlation coefficients; values of the free parameters a_1, a_2 and $ln\, q_o$ obtained from the data fitting in $ln\, q$ vs. u_c coordinates according to equation (5.9) and correlation coefficients (the errors of the slope and the free parameters refer to the 95% confidence interval)

Con. (g/l)	Slope of best-fit straight line of $\ln u_c \ vs. \ln q$	R^2, linear fitting	Nucleation Mechanism	a_1	$a_2 = b$	$\ln q_0$	$q_0\left(\frac{K}{s}\right)$	R^2, fitting equation (5.9)
M-oleate								
154	6.19	0.92	PN	3	0.000889±0.000324	9.17±0.66	9.62E+03	0.93
192	4.73	0.96	PN	3	0.000256±0.000132	8.62±0.41	5.56E+03	0.94
231	4.28	0.96	PN	3	0.000185±0.000067	9.19±0.30	9.82E+03	0.97
269	5.52	0.82	PN	3	0.000476±0.000345	9.36±1.03	1.16E+04	0.82
M-linoleate								
154	4.79	0.92	PN	3	0.000569±0.000225	8.46±0.47	4.72E+03	0.95
192	6.49	0.85	PN	3	0.000920±0.000413	9.56±0.91	1.41E+04	0.87
231	3.18	0.68	PN	3	0.000119±0.000305	8.58±1.12	5.33E+03	0.70
269	2.88	0.48	IN	Analysis in Table 7.12.				
M-linolenate								
154	4.40	0.89	PN	3	0.000215±0.000199	8.28±0.58	3.95E+03	0.87
192	5.94	1.00	PN	3	0.000537±0.000062	9.28±0.17	1.07E+04	0.99
231	4.41	0.82	PN	3	0.000270±0.000188	9.47±0.77	1.30E+04	0.87
269	6.08	0.72	PN	3	0.000665±0.000569	9.64±1.53	1.54E+04	0.73
Mix palm								
154	3.47	0.94	PN	3	0.000136±0.000132	7.80±0.35	2.45E+03	0.95
192	3.10	1.00	PN	3	0.000017±0.000025	7.71±0.09	2.23E+03	1.00
231	3.03	0.96	PN	3	0.000026±0.000067	8.13±0.28	3.39E+03	0.96
269	2.71	0.99	IN	Analysis in Table 7.12.				
Mix soy								
154	3.79	0.97	PN	3	0.000122±0.000095	7.93±0.28	2.79E+03	0.96
192	4.28	0.99	PN	3	0.000238±0.000058	8.37±0.17	4.30E+03	0.99
231	3.08	0.96	PN	3	0.000003±0.000040	8.53±0.25	5.07E+03	0.96
269	3.88	0.81	PN	3	0.000211±0.000206	9.00±0.78	8.09E+03	0.85
Mix rapeseed								
154	3.92	0.95	PN	3	0.000152±0.000131	8.01±0.38	3.02E+03	0.94
192	6.35	0.99	PN	3	0.000664±0.000091	9.46±0.24	1.29E+04	0.99
231	3.78	0.94	PN	3	0.000135±0.000080	8.91±0.35	7.39E+03	0.96
269	3.94	0.88	PN	3	0.000171±0.000125	9.19±0.57	9.82E+03	0.91

Table 7.10 Parameters obtained from the analysis of polythermal data of methyl stearate crystallising from unsaturated esters type solvents: slopes of the best linear fit to data points in $ln\, q$ vs. $ln\, u_c$ coordinates and correlation coefficients; values of the free parameters a_1, a_2 and $ln\, q_o$ obtained from the data fitting in $ln\, q$ vs. u_c coordinates according to equation (5.9) and correlation coefficients (the errors of the slope and the free parameters refer to the 95% confidence interval)

Con. (g/l)	Slope of best-fit straight line of $\ln u_c \ vs. \ln q$	R^2, linear fitting	Nucleation Mechanism	a_1	$a_2 = b$	$\ln q_0$	$q_0\left(\frac{K}{s}\right)$	R^2, fitting equation (5.9)
M-oleate								
154	3.28	0.74	PN	3	0.000116±0.000366	7.85±0.94	2.58E+03	0.75
192	3.89	0.64	PN	3	0.000368±0.000584	8.44±1.37	4.63E+03	0.67
231	5.09	0.68	PN	3	0.000644±0.000584	9.28±1.44	1.07E+04	0.73
269	4.05	0.70	PN	3	0.000348±0.000414	8.77±1.15	6.45E+03	0.74
M-linoleate								
154	4.14	0.81	PN	3	0.000296±0.000288	8.67±0.84	5.83E+03	0.84
192	5.08	0.66	PN	3	0.000375±0.000490	9.23±1.53	1.02E+04	0.65
231	5.83	0.87	PN	3	0.000404±0.000167	10.27±0.73	2.90E+04	0.91
269	5.44	0.79	PN	3	0.000446±0.000272	10.04±1.04	2.29E+04	0.84
M-linolenate								
154	3.36	0.70	PN	3	0.000062±0.000402	7.71±1.01	2.23E+03	0.69
192	3.79	0.83	PN	3	0.000167±0.000250	8.35±0.77	4.22E+03	0.83
231	3.82	0.84	PN	3	0.000171±0.000192	8.76±0.71	6.39E+03	0.86
269	3.54	0.80	PN	3	0.000134±0.000203	8.76±0.81	6.38E+03	0.82
Mix palm								
154	4.27	0.83	PN	3	0.000277±0.000260	8.80±0.81	6.63E+03	0.84
192	4.68	0.55	PN	3	0.000320±0.000565	9.20±1.84	9.86E+03	0.55
231	4.70	0.63	PN	3	0.000373±0.000427	9.66±1.56	1.56E+04	0.67
269	6.49	0.74	PN	3	0.000697±0.000440	10.48±1.45	3.55E+04	0.79
Mix soy								
154	6.43	0.87	PN	3	0.000659±0.000259	10.19±0.83	2.66E+04	0.91
192	4.68	0.80	PN	3	0.000310±0.000255	9.45±0.97	1.27E+04	0.82
231	6.19	0.74	PN	3	0.000547±0.000372	10.44±1.40	3.42E+04	0.78
269	5.69	0.59	PN	3	0.000407±0.000492	10.13±1.98	2.51E+04	0.60
Mix rapeseed								
154	3.07	0.87	PN	3	0.000073±0.000189	7.93±0.58	2.78E+03	0.87
192	4.28	0.99	PN	3	0.000277±0.000039	8.29±0.10	3.98E+03	1.00
231	3.65	0.81	PN	3	0.000210±0.000303	7.98±0.75	2.93E+03	0.83
269	3.84	0.98	PN	3	0.000170±0.000048	8.32±0.15	4.10E+03	0.99

In most cases the slopes of the lines are higher than 3 with the exception of crystallisation of C16:0 from methyl linoleate and mixtures of unsaturated esters such as in palm oil solvents. For all systems that proceeds via the PN mechanism equation (5.9) should describe the experimental data plotted in $Ln\, q$ vs. u_c

coordinates. The parameters obtained a_1, a_2 and $ln\, q_0$ for each of the solution concentrations within each solvent system and the corresponding correlation coefficients, are also given in Tables 7.9. and 7.10. The effective interfacial tension γ_{eff}, the critical nucleus radius r^* and number i^* of molecules were evaluated from equation (5.8), (5.16) and (5.17) respectively using the same parameters and assumption given in the previous section. These results are given in Table 7.11. and 7.13. for methyl palmitate and stearate respectively.

Table 7.11 Nucleation kinetics parameters for methyl palmitate crystallising from unsaturated esters type solvents at four different solution concentrations. The interfacial tension and critical radius are calculated at u_c corresponding to $T_c$values obtained by the extrapolation to 0°C/min of $(T_c(q))$ lines

	x $\left(\frac{mol\ solute}{mol\ solution}\right)$	u_c	x_f	σ	$\gamma\left(\frac{mJ}{m^2}\right)$	$r^*(nm)$	i^*
M-oleate	0.161	0.0190	0.10	0.64	2.05	1.06	10.04
	0.194	0.0159	0.13	0.52	1.36	0.84	4.98
	0.224	0.0120	0.16	0.38	1.22	1.00	8.44
	0.252	0.0156	0.17	0.48	1.67	1.05	9.93
M-linoleate	0.158	0.0178	0.10	0.64	1.82	0.96	7.44
	0.190	0.0184	0.12	0.62	2.14	1.09	11.01
	0.220	0.0120	0.16	0.40	1.08	0.84	5.14
	0.248		0.18	0.40			
M-linolenate	0.156	0.0174	0.10	0.50	1.20	0.74	3.50
	0.188	0.0163	0.13	0.48	1.63	1.08	10.63
	0.217	0.0123	0.16	0.35	1.30	1.14	12.48
	0.244	0.0164	0.17	0.45	1.76	1.15	13.03
Mix palm	0.161	0.0159	0.10	0.53	1.11	0.67	2.56
	0.193	0.0141	0.13	0.44	0.56	0.38	0.47
	0.223	0.0115	0.16	0.38	0.64	0.53	1.30
	0.251		0.20	0.28			
Mix soy	0.159	0.0162	0.11	0.49	1.01	0.65	2.36
	0.191	0.0157	0.13	0.49	1.27	0.84	5.09
	0.221	0.0108	0.17	0.30	0.29	0.28	0.18
	0.249	0.0123	0.18	0.35	1.23	1.04	9.48
Mix rapeseed	0.160	0.0169	0.11	0.50	1.07	0.68	2.65
	0.193	0.0168	0.13	0.51	1.76	1.11	11.81
	0.222	0.0115	0.17	0.28	1.04	0.96	7.59
	0.250	0.0113	0.19	0.33	1.12	1.06	10.08

The analysis of polythermal data for methyl palmitate crystallising from methyl linoleate and a mixture of unsaturated esters such as in palm oil, at the highest

concentration levels, was done using the model given for IN according to equation (5.23). The concentration of crystal nuclei C_0 at the nucleation point was calculated from equation (5.21) for square plates with $k_v = 2\,x\,10^{-6}$ according, $\alpha_{det} = 1\,x\,10^{-10}$ which is a typical value for organic systems, $d = 2$ for two dimensional growth, $m = 1$, $k_G = 1\,x\,10^{-6}\,m/s$ which is a representative value for crystal growth of methyl esters, $a = 26$ according to equation (5.7) and T_e equal to 287 and 286 K for methyl linoleate and mix of esters such as in palm oil solvent respectively. The parameters obtained from the analysis are given in Table 7.12.

Table 7.12 Nucleation kinetics parameters for methyl palmitate crystallising from methyl linoleate and mixture of unsaturated esters such in palm oil at a concentration of 269 g/l. The parameters were obtained for instantaneous nucleation mechanism according to equation (5.23)

	n	q_0	$C_0\left(\frac{nuclei}{m^3}\right)$
C16:0 m-linolenate	2	2392	6.4 x 10^{-04}
C16:0 mix palm	2	1367	2.3 x 10^{-04}

The values obtained for the growth exponent parameter $n = 2$ suggests that growth of methyl palmitate is likely controlled by the presence of screw dislocations. Likewise the relative low values of C_0 coupled with the fact that at these concentrations the x_f values are higher than at any other concentration levels in these solutions systems, suggest that nucleation rates are strongly kinetically hindered. This could be the case as ideality is more dependent on temperature for methyl palmitate in methyl linoleate and proportion of methyl esters such as in palm oil. In this case at higher concentration level the ideality increases likely allowing the decrease of interfacial tension but at the same time increasing solute molecules solvation which will render in lower attachment frequencies f^*.

Table 7.13 Nucleation kinetics parameters for methyl stearate crystallising from unsaturated esters type solvents at four different solution concentrations. The interfacial tension and critical radius are calculated at u_c corresponding to $T_c$values obtained by the extrapolation to 0 °C/min of $(T_c(q))$ lines

	x $\left(\frac{mol\ solute}{mol\ solution}\right)$	u_c	x_f	σ	$\gamma\left(\frac{mJ}{m^2}\right)$	$r^*(nm)$	i^*
M-oleate	0.149	0.0145	0.10	0.51	1.14	0.68	2.70
	0.179	0.0162	0.11	0.60	1.68	0.90	6.19
	0.207	0.0167	0.13	0.61	2.03	1.05	9.90
	0.234	0.0151	0.15	0.52	1.66	0.95	7.30
M-linoleate	0.146	0.0144	0.10	0.50	1.53	0.95	7.22
	0.176	0.0150	0.12	0.50	1.70	1.01	8.79
	0.204	0.0127	0.14	0.43	1.70	1.19	14.48
	0.230	0.0134	0.16	0.44	1.76	1.17	13.67
M-linolenate	0.143	0.0154	0.09	0.64	1.00	0.50	1.07
	0.173	0.0141	0.11	0.56	1.40	0.76	3.81
	0.201	0.0125	0.14	0.49	1.41	0.87	5.60
	0.227	0.0117	0.16	0.45	1.30	0.85	5.33
Mix palm	0.148	0.0140	0.10	0.48	1.53	0.94	7.07
	0.178	0.0147	0.12	0.53	1.60	0.94	7.20
	0.207	0.0136	0.14	0.51	1.69	1.07	10.52
	0.233	0.0150	0.16	0.50	2.09	1.20	14.88
Mix soy	0.146	0.0150	0.10	0.49	1.95	1.20	14.63
	0.176	0.0130	0.12	0.43	1.52	1.08	10.81
	0.204	0.0138	0.14	0.45	1.84	1.23	16.04
	0.231	0.0135	0.16	0.42	1.67	1.14	12.66
Mix rapeseed	0.147	0.0127	0.10	0.43	0.97	0.67	2.55
	0.178	0.0158	0.11	0.56	1.52	0.84	5.02
	0.206	0.0170	0.13	0.63	1.38	0.71	3.09
	0.232	0.0141	0.16	0.48	1.29	0.80	4.38

7.4.2. Comparative assessment of methyl palmitate and stearate nucleation from unsaturated methyl ester solvents

Similarly to the analysis presented in the previous section Fig. 7.9 shows the averages of the values of each parameter obtained for the four solutions´ concentrations analysed within each solution system. Table 7.14. highlights the solutions´ systems that stand out within some chosen relevant categories associated with specific nucleation parameters.

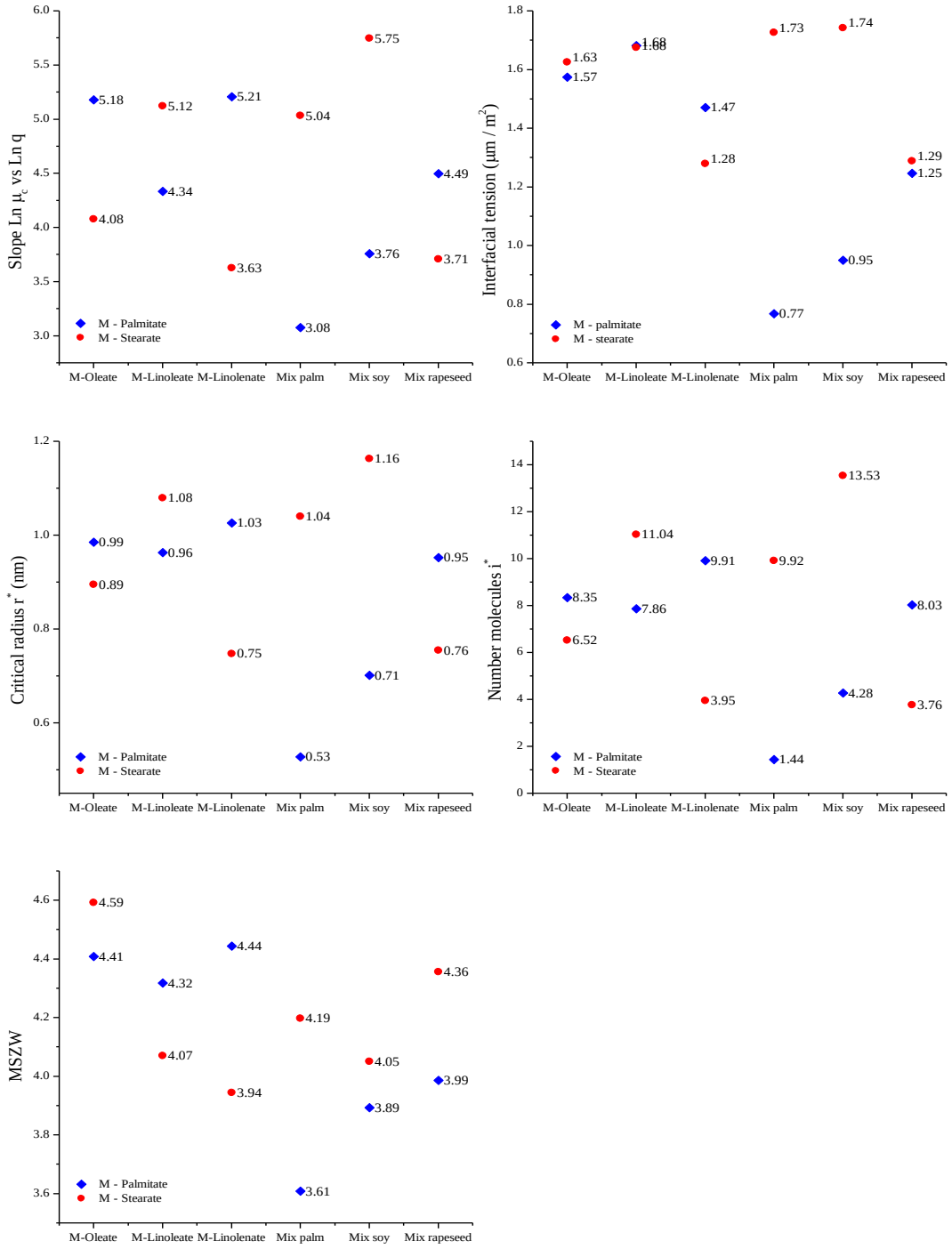

Figure 7.9 Comparative trend of nucleation kinetics parameters for methyl palmitate and stearate crystallising from six different unsaturated methyl esters type solvents. The data points correspond to the average of the relevant parameters obtained at four different solutions' concentrations

Table 7.14 Summary of solution´s systems that stand out within a specific nucleation parameter category, for methyl palmitate and stearate crystallising from different unsaturated esters type solvents. Similarly, highlighted in red are the systems that stands out within each category

Category	C16:0 chosen solutions		C18:0 chosen solutions	
Lower slopes from the $ln\ q\ vs\ ln\ u_c$	**C16:0/mix palm**	C16:0/mix soy	C18:0/m-linolenate	C18:0/mix rapeseed
Slopes from the $ln\ q\ vs\ ln\ u_c$ change significantly with concentration	C16:0/n-linoleate	C16:0/mix palm		
Lower interfacial tensions	**C16:0/mix palm**	**C16:0/mix soy**	C18:0/m-linolenate	C18:0/mix rapeseed
Lower r^* and i^*	**C16:0/mix palm**	**C16:0/mix soy**	C18:0/m-linolenate	C18:0/mix rapeseed
Lower MSZW	**C16:0/mix palm**	**C16:0/mix soy**	C18:0/m-linolenate	
MSZW changes significantly with concentration	C16:0/mix palm			

The differences in the nucleation mechanism and parameters for crystallisation of C16:0 and C18:0 from unsaturated methyl esters type solvents are not as noticeable as in the case of crystallisation from diesel type solvents. However, there is a relevant differentiation on the parameters observed for C16:0 crystallising from unsaturated esters mixtures such as in palm and soy oil and for C18:0 crystallising from methyl linolenate and unsaturated esters mixtures such as in rapeseed oil. The slopes for the $ln\ q\ vs\ ln\ u_c$ lines in these four solutions´ systems are lower than those observed in the other solutions. This indicating that nucleation is less progressive in nature and even evolves towards an instantaneous nucleation mechanism with increase in solution concentration, in the case of C16:0 crystallising from unsaturated esters mixtures such as in palm oil. These findings correlate with the fact that for the same solutions systems, lower interfacial energies γ_{eff}, as well as lower critical radius r^* and MSZW were obtained, in agreement with a more kinetically controlled nucleation process as evidenced from stepper $T_c(q)$ lines.

Given that C16:0 solubility is only significantly different in methyl linoleate and linolenate solvents similar de-solvation energies, and concentrations of nucleation sites C_0 should be expected in all other solutions systems. Therefore, according to the definition of the pre-exponential kinetic factor in the nucleation rate expression,

diffusivity of C16:0 is likely to be lower in mixtures of unsaturated esters such as in palm and soy oil and would be rate limiting.

In addition to this interestingly, in the case of C18:0 solute, a more kinetically controlled nucleation process was observed within the solutions with the lowest and highest solubility, methyl linolenate and mixtures of unsaturated esters such as in rapeseed oil respectively, where relevant differences in both de-solvation energies and C_0 should be expected. Given that rapeseed oil contains the highest proportion of methyl linolenate among all other combinations of methyl esters solvents, this could indicate that the diffusivity of C18:0 would be hindered by the existence of molecules with different sizes within the solvent due to methyl linolenate isomerism. In line with the previous comments it is relevant to mention that in the case of C16:0 solute, nucleation is clearly much more kinetically controlled in solutions where the solvents is constituted by a mixture of unsaturated esters as show by both lower slopes of the $ln\ q\ vs\ ln\ u_c$ lines and interfacial tensions (Fig. 7.8.1 and 7.8.2). This could be related to the presence of molecules with different shapes within the solvent, due to the isomerism of methyl linoleate and linolenate that would difficult molecular interactions and hinder diffusivity. On the other hand higher interfacial tensions were obtained for nucleation of C16:0 from single methyl esters solvents where a similarly thermodynamically controlled nucleation processed is manifested.

The slopes of the $ln\ q\ vs\ ln\ u_c$ lines for C16:0 crystallising from methyl linoleate and mixtures of methyl esters such as in palm oil, change significantly with concentration evolving from slopes values consistent with the PN mechanism to values consistent with the IN mechanism at the highest solutions´ concentrations. Although, interfacial tensions cannot be calculated from the IN model, this effect can be related to the variation of x_f with concentration (Table 7.11), whose influence at the higher concentration would reduce the interfacial tensions making the nucleation process a less thermodynamically controlled one. The results of the analysis for the IN mechanism at the highest solution´s concentration showed that the concentration of nuclei at the nucleation point are of the same order of magnitude in both cases.

7.5. Conclusions

The analysis of the nucleation of saturated methyl esters evidenced to be mainly progressive in nature strongly dependent on the interfacial tension when saturated esters are crystallising from diesel type solvents. Nucleation from unsaturated esters solvents, although essentially progressive evidenced a greater influence of the process kinetics; changing from a PN mechanism to a IN mechanism at higher solutions´ concentration, for nucleation of methyl palmitate from methyl linoleate and a mixtures of unsaturated esters as in palm fuel.

Calculated interfacial tensions ranged between 0.68 and 2.18 and 0.77 and 1.74 $\left(\frac{mJ}{m^2}\right)$ for saturated esters crystallising from diesel type solvents and unsaturated esters solvents respectively, in agreement with those values observed for other organic molecules. Extended analysis for methyl stearate crystallising from n-dodecane, kerosene and toluene solvents delivered nucleation rates ranging between 2.94 x 10^{14} and 8.94 x 10^{16} $\frac{nuclei}{ml\ sec}$.

Following this analysis the morphology and growth kinetic for methyl stearate crystallising from n-dodecane, kerosene and toluene solvents is also assessed in Chapter 8. The thorough assessment of these solutions system will provide the grounds for establishing an integrated approach to further extend the analysis to more solutions systems and to more complex mixtures.

8. Crystal Morphology and Growth Kinetics of Representative N-alkanes and Methyl Esters

Summary: This chapter introduces a methodology for the morphological indexation of specific crystal faces, presents the derivation of models for the assessment of crystals growth kinetics and provides a comprehensive analysis of the crystal growth kinetics and morphology of methyl stearate crystallising from n-dodecane, kerosene and toluene solvent

8.1. Introduction

The prediction of the crystal morphology and analysis of growth kinetics of n-alkanes and methyl esters crystals is essential to understand how to modify the shape of these crystals, for adequate flow in engines pipes lines. In agreement with this, a methodology to index specific (hkl) crystals faces is defined in this section. This methodology, based on a combined BFDH and zone axis method, is validated through the analysis of the crystal morphology of triclinic n-docosane, for which a preliminary assessment of the supersaturation dependence of the specific crystal faces growth rates is also provided. Using this methodology the assessment is then extended to study the influence of solvent on the morphology of methyl stearate crystals growing from n-dodecane, kerosene and toluene. This is combined with the mechanistic assessment of methyl stearate crystals´ growth, through the use of a set of model expressions that are derived to express the influence in series, of both the diffusion of growth units within the bulk and at the crystal-solution interface.

8.2. The crystal morphology and growth rates of triclinic n-docosane crystallising from n-dodecane solutions

This section addresses both the assessment of the crystal morphology and the measurement of the growth rates of the individual faces for n-docosane crystals growing from n-dodecane. This study allowed stablishing a methodology for the assessment of the crystals morphology when detailed structural information is not available such as in the case of both n-alkanes and methyl esters.

8.2.1. Morphological observations and crystal growth

Solubility data measured for n-docosane in n-dodecane was used to select the supersaturations levels at which both morphological observations and crystals growth measurements were carried out in these solutions The fitted parameters obtained according to the van´t Hoff plot were ΔH_{diss}= 63135.9 $\pm$ 617.6 $\frac{J}{mol}$ and ΔS_{diss}= 198.84 $\pm$ 2.19 $\frac{J}{mol\ K}$ (Unpublished work not included within the thesis).

Due to the very small MSZW of the system studied, i.e. ca. 2 °C, which is typical for n-alkanes systems [1-4], the growth and development of individual n-docosane crystals could only be followed within this limited temperature region resulting in only three different solutions supersaturations being practical for this study. Although the value of the highest relative supersaturation σ at which the observations were done only reached 5%, kinetic roughening of the side faces was already found to manifest itself at this point, thus further limiting the range for kinetic measurements even more. Additionally, the difficulty of growing faceted crystals only allowed single measurements to be obtained for the crystal growth at each supersaturation value and even within this limited range of measurements a significant amount of time (ca. a month) was required to carry out the experimental work.

Due to the very thin plate-like crystals observed, also typical of n-alkanes, the quality of the microscopy images obtained using brightfield illumination did not allow easy reproduction of the data obtained. Nonetheless, these observations were found to be sufficient to assess both the crystal morphology and growth rates for the individual habit faces. A representative sequence of these micrographs for the growth of the crystals observed at each supersaturation is shown in Fig. 8.1.

An assessment of these morphologies reveals that the crystal habit of the n-docosane crystals changed with increasing supersaturation from an irregular polygon towards a more regular shape. The regular quadrilateral shape of the crystals at higher supersaturation could suggest a new molecular arrangement in the crystal structure changing from the triclinic form expected to an orthorhombic structure more typical of even parity n-alkanes growth in the presence of a homologous impurity [3, 4].

The latter might be consistent with solvent incorporating at the higher supersaturations. In n-alkane crystallisation, is well known that the incorporation of lower carbon chain length n-alkanes into the lattices of crystals of even higher carbon chain lengths, can influence the arrangement of the molecules into the crystal structure.

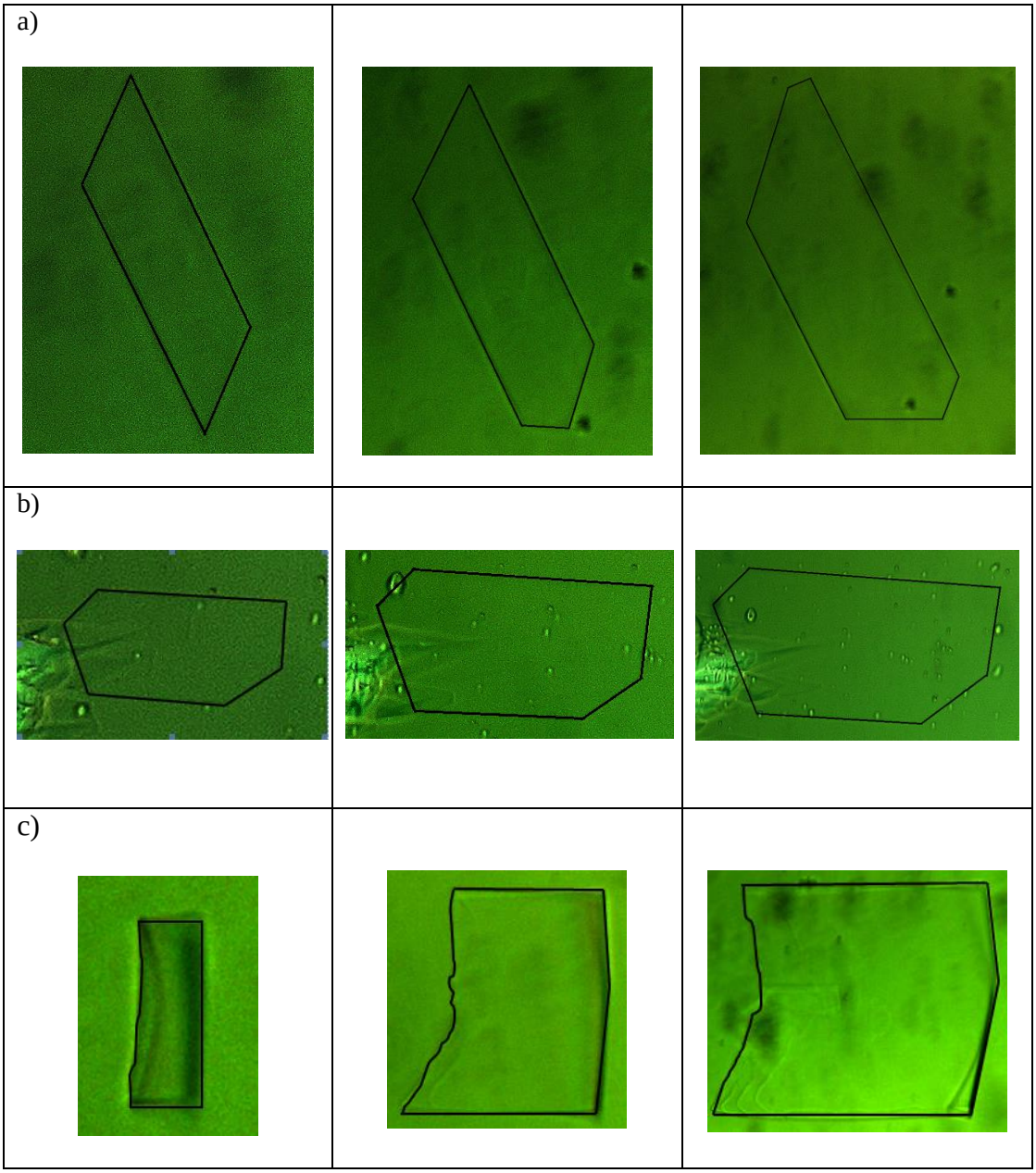

Figure 8.1 Optical micrographs showing the evolution of the growth of n-docosane crystals growing from a supersaturated n-dodecane solution for three different solution supersaturations (σ). The micrograph shown are a representative sequence of the crystal growth process at (a) 24.6 ºC (σ = 0.01); (b) 24.5 ºC (σ = 0.02); (c) 24.1 ºC (σ = 0.05)

However, even if this was the case the morphology observed at the highest supersaturation is not genuinely in agreement with that expected from a crystal structure based on an orthorhombic crystal system, where a lozenge shaped morphology dominated by four symmetrically equivalent {110} faces has been previously observed [5, 6].

Although the micrographs obtained at the two lowest supersaturations seemed to be associated with different crystal´s morphology a close comparisons of them revealed three coincidental internal angles that would allow the same indexation for three of the crystal faces. A fourth face in each case, however, was not found to be equivalent and would thus need independent indexation. In the case of the crystals obtained at the highest supersaturation, the indexation of the faces was not carried out as its morphology was not consistent with that associated with the same triclinic crystal structure.

8.2.2. Morphological indexing

Given the lack of detailed crystallographic information, the assessment of the n-docosane crystal morphologies was carried out using the Bravais [7], Friedel [8], Donnay and Harker [9] (BFDH) model, as described in the methodology section.

The list of Miller indices obtained was subsequently re-arranged by grouping the lattice planes with respect to those having a common zone axis $[uvw]$, defined as a crystallographic axis perpendicular to the set of two dimensional (2D) planes (hkl) satisfying the relationship

$$uh + vk + wl = 0 \tag{8.1}$$

The indices of the zone axis $[uvw]$ are defined with respect to two of its constituent lattices planes $(h_1k_1l_1)$, $(h_2k_2l_2)$ by:

$$\frac{u}{\begin{bmatrix} k_1 & l_1 \\ k_2 & l_2 \end{bmatrix}} = \frac{v}{\begin{bmatrix} l_1 & h_1 \\ l_2 & h_2 \end{bmatrix}} = \frac{w}{\begin{bmatrix} h_1 & k_1 \\ h_2 & k_2 \end{bmatrix}} \tag{8.2}$$

The planes with the lowest order of their Miller indices within each group were then examined in pairs, by modifying the corresponding cif. file in Mercury 3.1., to iteratively obtain morphology predictions onto the basal (001) plane, i.e. the most representative plane of the observed plate-like crystals. These projections were

segmentally compared with the micrographs of the crystals obtained experimentally. Essentially the law of rational indices was used, to define possible indices for the pairs of faces whose mutual orientation was consistent with the predictions. The results obtained were then combined and ranked in terms of the coincidental indices present in each pair, in order to generate putative crystal morphologies that satisfied the various pair-wise simulations.

Finally, once acceptable matches between the predicted and observed crystal edge orientations had been identified, the respective lengths of the projected edges in the predicted morphologies were adjusted in order to match their respective proportions as observed in the experimental observations. The latter was facilitated by varying the centre to face normal distances provided in the corresponding cif file. A schematic diagram summarising this overall methodology is given in Fig. 8.2.

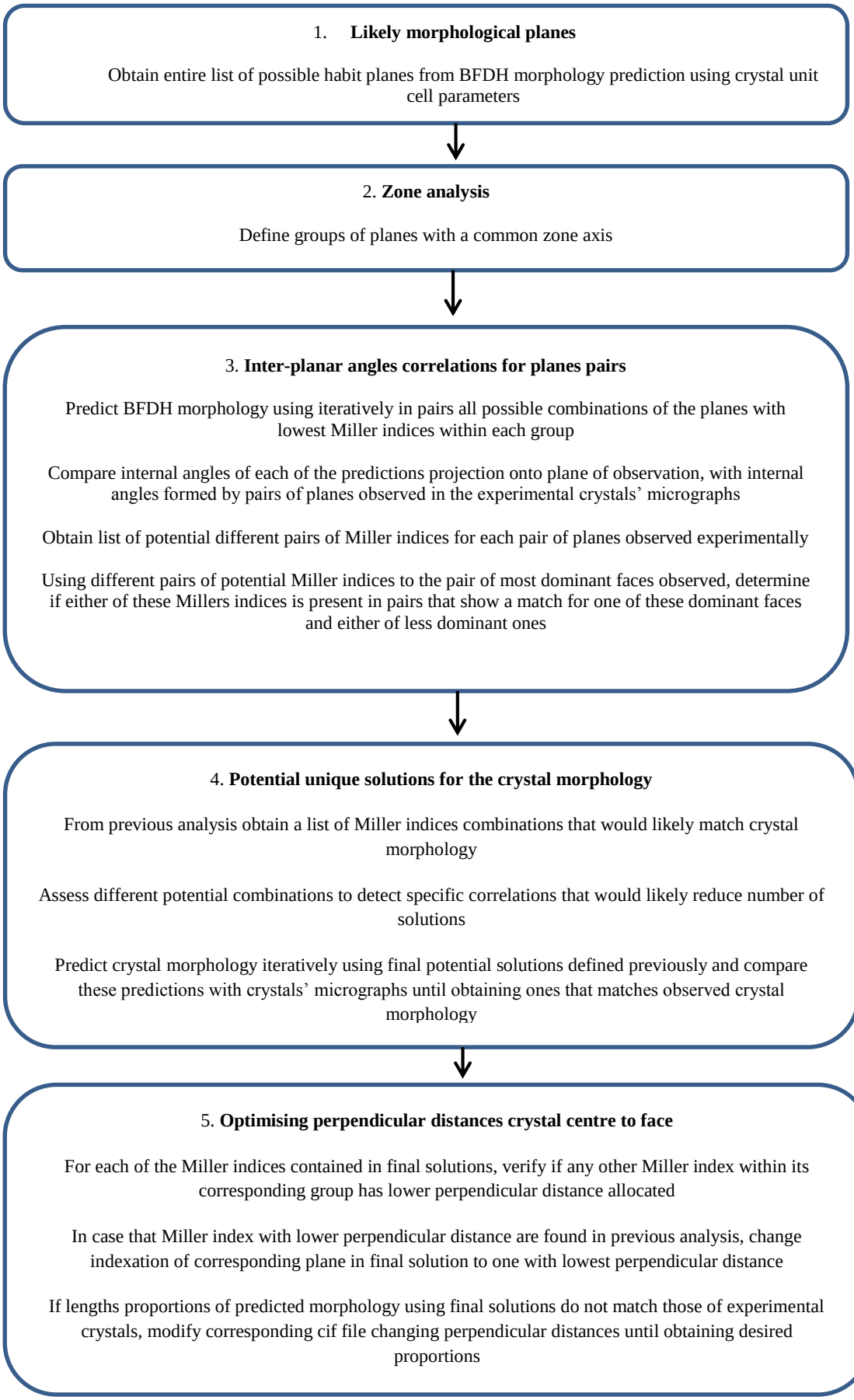

Figure 8.2 Flow chart describing the procedure to follow for the morphology indexation of observed n-docosane crystals, using iterative predictions of the BFDH morphology

The prediction for the morphology observed at the two lowest supersaturations was carried out following the procedure presented in Fig. 8.2. Mindful of the anisotropy of the known unit cell parameters for n-docosane with the magnitude of c >> a, b the indexation for the large crystal face was taken to be (001). BFDH analysis revealed 104 predicted crystal habit planes, including the dominant (001) plane, and 103 other possible indexations for the other four planes observed in the experimental morphology. In this case many of the d_{hkl} spacings were found to be very close and therefore, according to the methodology, these results were arranged by grouping the lattice planes into thirteen zones. These, together with the corresponding zone axis indexation, including the complete set of planes delivered by the BFDH prediction is given in the Appendix B. Table 8.1. shows a summary of this information including the different calculated zone axis and some representative planes featuring the range of d spacing values observed within each group.

The inter-planar angle correlation for the planes pairs using the annotation shown in Fig. 8.3, revealed a set of matches for the pairs of Miller indices as presented in Table 8.2.

Table 8.1 List of the predicted zone axis defining the different zone groups, representative (hkl) planes and d_{hkl} spacing within each group

Group	Zone axis $[uvw]$	Representative plane (hkl)	Inter-planar distance d_{hkl}
1	[1 0 0]	(010) (021) (031)	4.59 2.28 1.52
2	[0 1 0]	(100) (201) (301)	3.86 1.97 1.30
3	[1 -1 0]	(110) (221)	3.52 1.79
4	[2 -1 0]	(120)	2.30
5	[3 -1 0]	(130)	1.60
6	[1 1 0]	(1-10) (2-21)	2.59 1.31
7	[2 1 0]	(1-20)	1.75
8	[3 1 0]	(1-31)	1.30
9	[1 -2 0]	(210)	2.01
10	[3 -2 0]	(230)	1.43
11	[1 2 0]	(2-10)	1.61
12	[1 -3 0]	(310)	1.35
13	[2 -3 0]	(320)	1.30

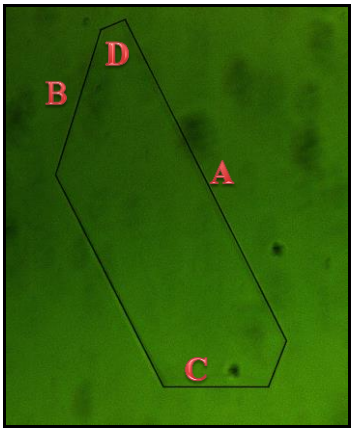

Figure 8.3 Example of initial designation of crystal's faces for the morphology as observed for the lowest supersaturation (σ = 0.01)

Table 8.2 Representative pairs of planes matching the inter-planar angles of pairs of faces for the morphology observed at the lowest supersaturation σ = 0.01. Planes designated according to Fig. 8.3

AB	BC	CD	AC	AD	BD
(010) (230)	(100) (010)	(1-10) (010)	(010) (110)	(010) (210)	(120) (320)
(010) (2-10)		(1-31) (010)	(1-20) (310)	(010) (320)	(100) (1-10)
(1-20) (100)			(1-10) (320)	(1-20) (110)	(100) (1-31)
(1-20) (130)			(130) (210)	(1-20) (320)	(1-10) (210)
(120) (1-31)			(1-31) (230)	(120) (2-10)	
(120) (210)				(100) (130)	
(100) (110)				(110) (1-10)	
(1-10) (310)				(110) (1-31)	
(130) (320)				(1-10) (230)	
(230) (310)				(1-31) (210)	
(2-10) (210)				(1-31) (320)	
(2-10) (320)				(230) (2-10)	

Even though in this case only one solution is possible for BC pairs, to facilitate the visualization of the solution for the entire morphology, a general cross-checking of the pairs was carried out. This, because in each pair combination, each Miller index can be allocated to either of the faces represented by that pair. Thus, starting with the AB pairs in Table 8.2. and cross-checking these with the other pairs' combinations yielded the likely Miller indices for the four crystal faces observed in the micrographs as shown in Table 8.3.

Looking at the results in Table 8.3., for instance, if (230) and (010) are the most likely Miller indices for faces A and B, then the C face could take one of either three Miller indices (1-31), (110) or (100). Likewise the D face could take one of either four Miller indices (1-10), (2-10), (210) or (320). However, in this case as observed in Table 8.2., only one combination is possible for BC pairs (100) (010) and two combinations are possible for CD pairs (010) (1-10) or (010) (1,-3,1). Therefore, only those set of planes in the possible solutions containing the (010) (100) and either (1-10) or (1,-3,1) indices, would be likely to deliver the prediction for the entire crystal indexation. This is the case of the set of planes in rows one, nine and twelve highlighted in Table 8.3.

Table 8.3 Likely combinations of Miller indices for the four faces of the experimental crystals observed at the lowest supersaturation σ = 0.01. Planes designated according to Fig. 8.3

	A	B	C			D			
1	(230)	(010)	(1-31)	(110)	(100)	(1-10)	(2-10)	(210)	(320)
2	(230)	(310)	(1-31)	(1-20)		(1-10)	(2-10)		
3	(1-10)	(310)	(320)	(1-20)		(100)	(110)	(210)	
4	(2-10)	(010)	(110)	(100)		(120)	(210)	(320)	
5	(2-10)	(210)	(130)			(120)	(1-10)	(1-31)	
6	(2-10)	(320)	(1-10)			(120)	(1-20)	(1-31)	(120)
7	(120)	(210)	(130)			(1-10)	(1-31)		
8	(120)	(1-31)				(100)	(110)		
9	(1-20)	(100)	(010)			(110)	(1-10)	(130)	(1-31)
10	(1-20)	(130)	(210)			(110)	(100)		
11	(320)	(130)	(1-10)	(210)		(1-20)	(1-31)	(120)	(100)
12	(110)	(100)	(010)			(1-10)	(130)	(1-31)	(1-20)

Arrangements of these indices considering all possible combinations among them are presented in Table 8.4. The comparison of the micrographs obtained at the lowest supersaturation, with the prediction of the corresponding BFDH morphology using these indices, showed that only the set of planes presented in rows one and thirteen in Table 8.4. would deliver a full match to the entire experimental morphology. Using these indices, further modification of the perpendicular distances from the centre of the crystal to the faces, in the corresponding cif files, gave a morphology prediction with lengths proportional to those observed experimentally.

As the planes used to carry out the analysis of the morphology were selected to represent a group of different planes with a common zone axis, then a ranking based on their respective d-spacing within these groups was done by using the BFDH method. (See Appendix B).

Table 8.4 Potential unique solutions of the n-docosane crystals morphology observed at the lowest supersatuarion σ = 0.01. Rows one and thirteen highlighted in the Table, represent the final unique solutions that match the entire crystal morphology. Planes designated according to Fig. 8.3

1	(230)A	(100)C	(010)B	(1-10)D
2	(2-10)	(100)	(010)	(1-10)
3	(210)	(100)	(010)	(1-10)
4	(320)	(100)	(010)	(1-10)
5	(230)	(100)	(010)	(1-31)
6	(2-10)	(100)	(010)	(1-31)
7	(210)	(100)	(010)	(1-31)
8	(320)	(100)	(010)	(1-31)
9	(1-20)	(100)	(010)	(1-10)
10	(110)	(100)	(010)	(1-10)
11	(130)	(100)	(010)	(1-10)
12	(1-20)	(100)	(010)	(1-31)
13	(110)A	(100)B	(010)C	(1-31)D
14	(130)	(100)	(010)	(1-31)

The analysis indicated the combination (230), (010), (100), (1-10) to be more likely than (233), (010), (102), (1-13). Likewise the combination (110), (100), (010), (1-31) was found to be more likely than (112), (102), (010), (1-33). However, the later prediction is more likely to occur due to its lower indexation. As the d-spacing of many of the planes within each group were so close in magnitude a more detailed analysis would be required to validate these findings. It should be noted that the calculation of the attachment energy (E_{att}) could be used for this purpose; but this information requires the optimised ($3D$) crystal structure of n-docosane which is not currently available. Fig. 8.4 compares the most likely morphology prediction with one of the micrograph of the experimental crystals observed at σ equal to 0.01. Likewise it presents the indexation for the morphology observed at the second supersaturation studied σ equal to 0.02, for which the same methodology was applied. The final prediction delivers the Miller indices (112), (102), (010) for the most dominant faces and (1-33) and (130) for the un-coincidental less dominant faces at σ equal to 0.01 and 0.02 respectively.

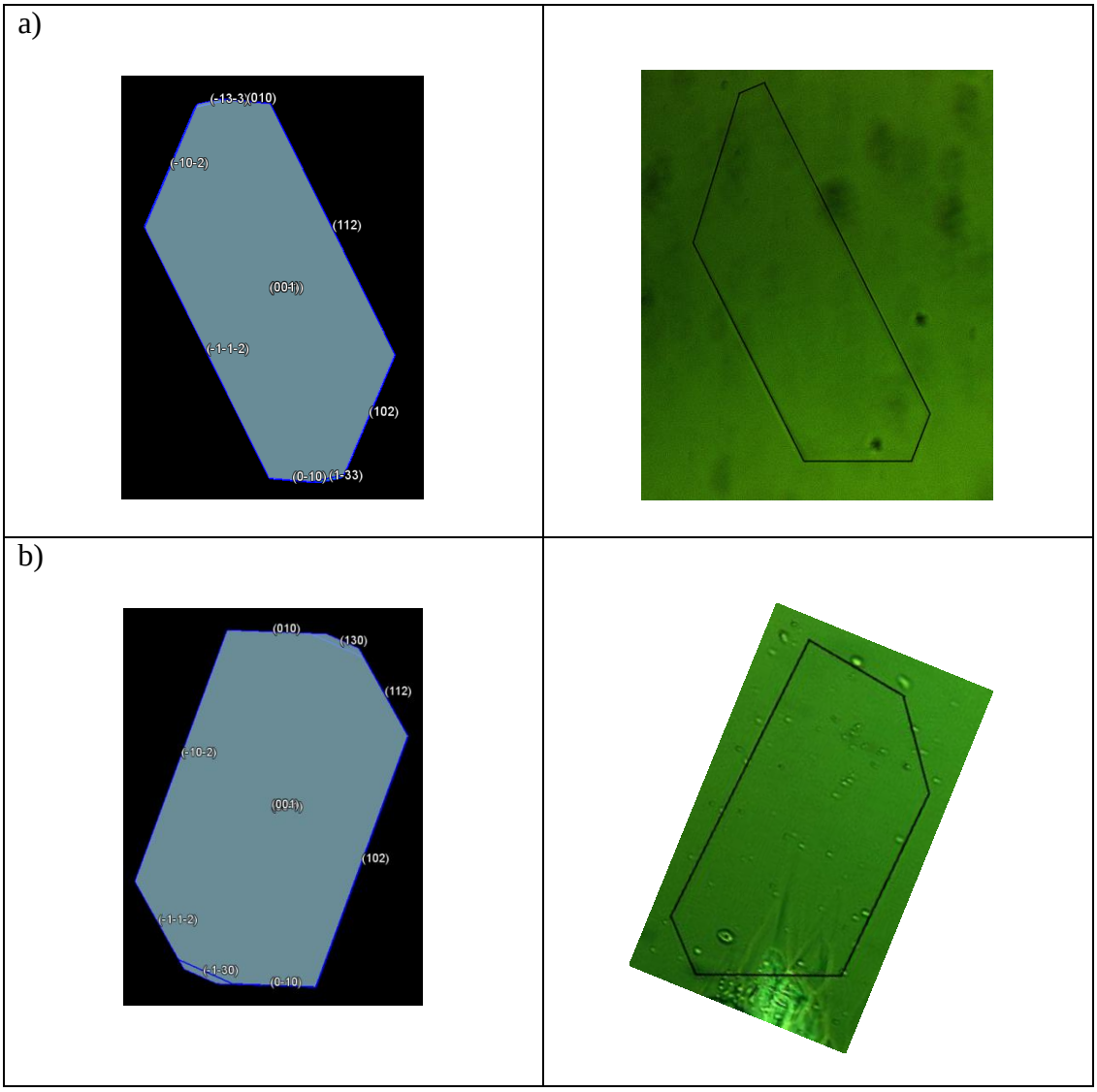

Figure 8.4 Predicted BFDH morphology of n-docosane crystals using the Miller indices in the obtained unique solutions and comparison with the crystals' micrograph at two different supersaturation a) σ=0.01 or T=24.6 ºC and b) σ=0.02 or T=24.5 ºC

8.2.3. Crystal growth rates as a function of supersaturation

The growth rates for the individual faces of n-docosane crystals as measured at each supersaturation are presented in Fig. 8.5

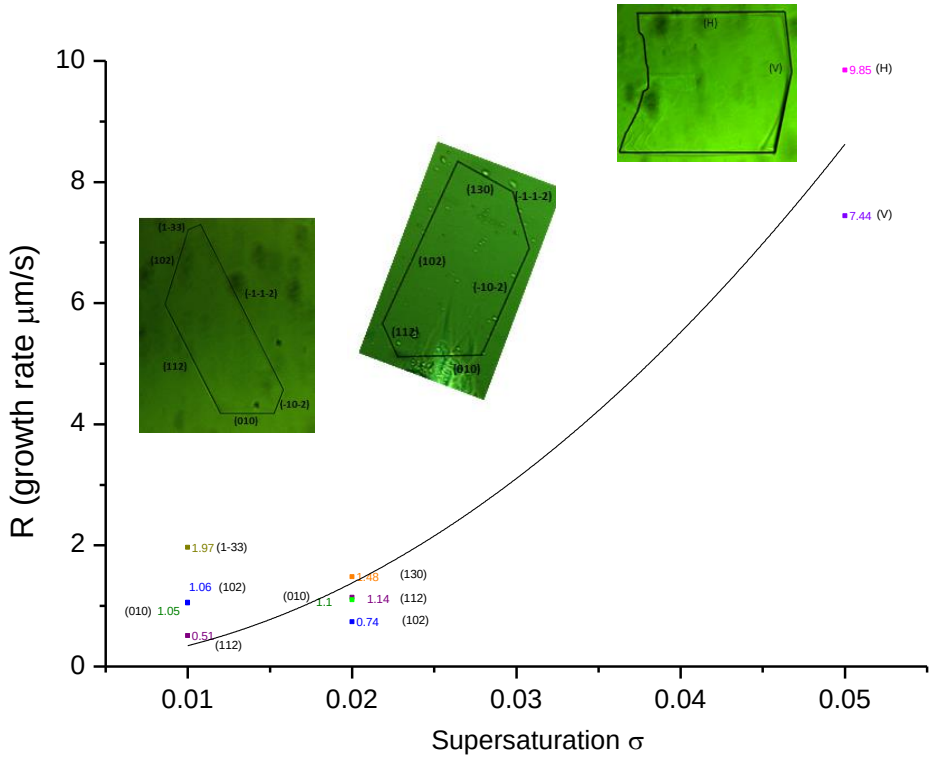

Figure 8.5 Comparative growth rates of individual faces of n-docosane crystals growing from n-dodecane at three different solution's supersaturations σ = 0.01, 0.02 and 0.05. Each of the colours assigned both to the symbol and R values represent each of the different crystal faces observed. The line represents the best fit of the data points through the BCF model

The growth rates for the (112) and (010) faces were found to increase as a function of supersaturation increase by 1%, while the growth of the (102) face decreases giving more importance to this face in the observed crystal morphology at σ equal to 0.02. The higher growth rates observed at the two lower supersaturation are for the less dominant non-coincidental (1-33) and (130) faces. However the growth rate of the (130) face observed at σ equal to 0.02 was found to be closer to the order of those rates observed for the (112) and (010) faces, which has an influence on the crystal morphology displayed, with the three faces having similar importance.

At the highest supersaturation σ equal to 0.05 the morphology observed was found to have changed considerably being defined by only two faces where growth rates are significantly higher than those measured for the crystal faces at lower supersaturation. Due to the high rates of these faces, the crystal morphology

displayed curvatures especially along the vertical faces (see label V in Fig. 8.5), which could be consistent with the early stages of kinetic roughening. Similar findings have been reported for other organic materials such as biphenyl and naphthalene crystallising from toluene in which roughening transition was observed at relative supersaturations below 1.5% [10]. Likewise, in the case of n-eicosane ($C_{21}H_{44}$) crystallising from n-hexane, observations of the growth morphology revealed roughening transitions to occur at relative supersaturations of around 3% [11].

A comparison of the growth rates values obtained with previously published data is shown in Table 8.5. These values which include those measured for similar organic systems are within the same order of magnitude of those presented in the present work.

Although the amount of experimental data collected is not sufficient at this stage to accurately assess the mechanistic regime of crystal growth based on $R(\sigma)$ models, a tentative assessment can still to be done. From Fig .8.5 it is clear that the data points do not follow a linear relationship whilst attempts to fit the data using the B&S model do not achieve convergence. However, the data seem to follow a parabolic rate dependence and fit well to the BCF type model which would be in agreement with growth via screw dislocations. In addition to this, the growth could be limited by volume diffusion as the experiments were carried out in stagnant solutions. However, the models used here to assess the growth mechanism only consider the interaction of molecules in the crystal surface. For a more accurate assessment of crystal growth, the combination of effects of both mass transfer and the molecular structure of the interface should be considered. These conclusions are merely speculative not only due to the lack of sufficient experimental data but also because the data collected at the higher supersaturation studied seem to be related to a different crystal polymorphic form.

Table 8.5 Comparative values of published growth rates values for individual faces of crystals of some inorganic and organic systems

Compounds	T (°C)	σ	Range of growth rates (μm/sec)	Ref.
Potash alum (111)		32	0.01-0.18	[12]
L-Glutamic Acid Length of needle-like crystals Width of needle-like crystals		 0.47- 0.5 0.47-0.5	 0.025 – 0.032 0.005 – 0.006	[13]
Tripalmitin (melt)	47 – 52		0.20 – 0.45	[14]
Paracetamol in 60% methanol and 40% water		0.25	0.30	[15]
Paracetamol in the [110], [010] and [001] direction		0.06 -0.26	0.020 – 0.160	[16]
Ibuprofen (001) and (011) faces in ethanl/water, ethyl acetate, acetonitrile and toluene		0.55-1.3	0.035-2.02	[17]
Hexatriacontane $C_{36}H_{74}$ in petroleum ether (110) face	17-22	0.22-0.7	0-2	[6]
Octacosane $C_{28}H_{58}$ in petroleum ether (110) face	12-22.75	0.007-0.15	0-14	[18]
Dotriacontane $C_{32}H_{66}$ in m-xylene	14.5	1-1.5	1-3	[19]
B and C polymorphs of stearic acid in butanone (110) face	16-25	0.012-0.3	0-2.8	[20]
B polymorph of stearic acid in decane (110) face		0.012-0.4	0-0.4	[21]
n-docosane in n-dodecane (010) (112) (102) and other not indexed faces	24.1-24.6	0.01-0.05	0.51-9.85	This work

8.3. Morphology and growth kinetics of methyl stearate as a function of crystallisation environment

In this section the morphology and growth kinetics of methyl stearate crystallising from three different solvents: n-dodecane, kerosene and toluene is analysed. A detailed morphological analysis methyl stearate crystals is presented using the methodology developed in the previous section and the crystals mechanistic growth regime is assessed through combined bulk and interface diffusional models whose derivation is presented in sub-section 8.3.2.

8.3.1. Morphological observations as a function of solution environment and crystal indexing

Using the set up for the measurements of crystal growth rates presented in the methodology, images of C18:0 crystals growing from three solvents were obtained. Depending on the initial assessment of the solutions behaviour different range of supersaturations within the MSZW were chosen for this analysis. In the case of n-dodecane solutions, growth was difficult to observe above 21 °C ($\sigma < 0.3$) and would occur too fast to be recorded below 20.2 °C ($\sigma > 0.39$). Similarly for kerosene solutions growth was difficult to observe above 18.3 °C ($\sigma < 0.45$) and would occur too fast below 17.8 °C ($\sigma > 0.52$). For toluene systems the growth would occur very fast even at high temperatures within the MSZW and therefore the range of assessed supersaturations was limited. A summary of the width of the metastable zone at the corresponding solution concentration together with the parameters used during the growth measurements for each system is presented in Table 8.6.

Table 8.6 Parameters used for the collection of crystals micrographs for methyl stearate crystallising from n-dodecane, kerosene and toluene solutions

	$Con\ \left(\frac{g}{l}\right)$	MSZW °C	Temperature range °C	Supersaturation (σ) range
n-dodecane	350	4.3 (19.8 – 24.1)	20.2 to 21.0	0.30 to 0.39
Kerosene	350	4.3 (17.7 – 22.0)	17.8 to 18.3	0.45 to 0.52
Toluene	538	4.3 (10.2 – 14.5)	13.5 to 13.9	0.04 to 0.08

Selected micrographs of the crystals observed in the range of supersaturations studied for the three solvents are shown in Fig. 8.6.

In general the crystals observed in all cases were very thin plate-like crystals. The assessment of C18:0 crystals morphology reveals that the crystal habit does not change with solvent except for the crystal habits observed in kerosene at the lowest supersaturations (σ). Although the habit observed at higher supersaturation in kerosene solutions are more elongated when compared to those obtained in the other two solvents, the internal angles of the observed crystals are equal in all cases. The lozenge shape of these crystals could suggests their morphology is based on either on a monoclinic or orthorhombic crystal system where crystals are bounded by <110> planes and the (001) plane. Lozenge crystals have previously been observed in methyl stearate and palmitate [22] or in crystals of similar molecules such as long-chain n-alkanes and stearic acid [21, 23, 24]. The morphology observed at the lowest supersaturations in kerosene solutions however could indicate that in this case, for certain levels of supersaturations these crystals develop a habit more consistent with a less symmetrical crystal system.

The prediction of the morphology for C18:0 crystals was carried out following the procedure presented in Fig. 8.1, using three different crystal structures that have been suggested for methyl stearate. The first two crystal structures correspond to monoclinic [25] and orthorhombic [26] crystal systems with space group $A2/a$ and $Pnab$ respectively and the third one to the monoclinic crystal system with space group $C2$. In the latter the unit cell parameters are: $a = 5.60\,\dot{A}$, $b = 7.39\,\dot{A}$, $c = 47.96\,\dot{A}$ and $\beta = 91.15$ ° (I. More/Infineum UK, personal communication, July 25, 2014)

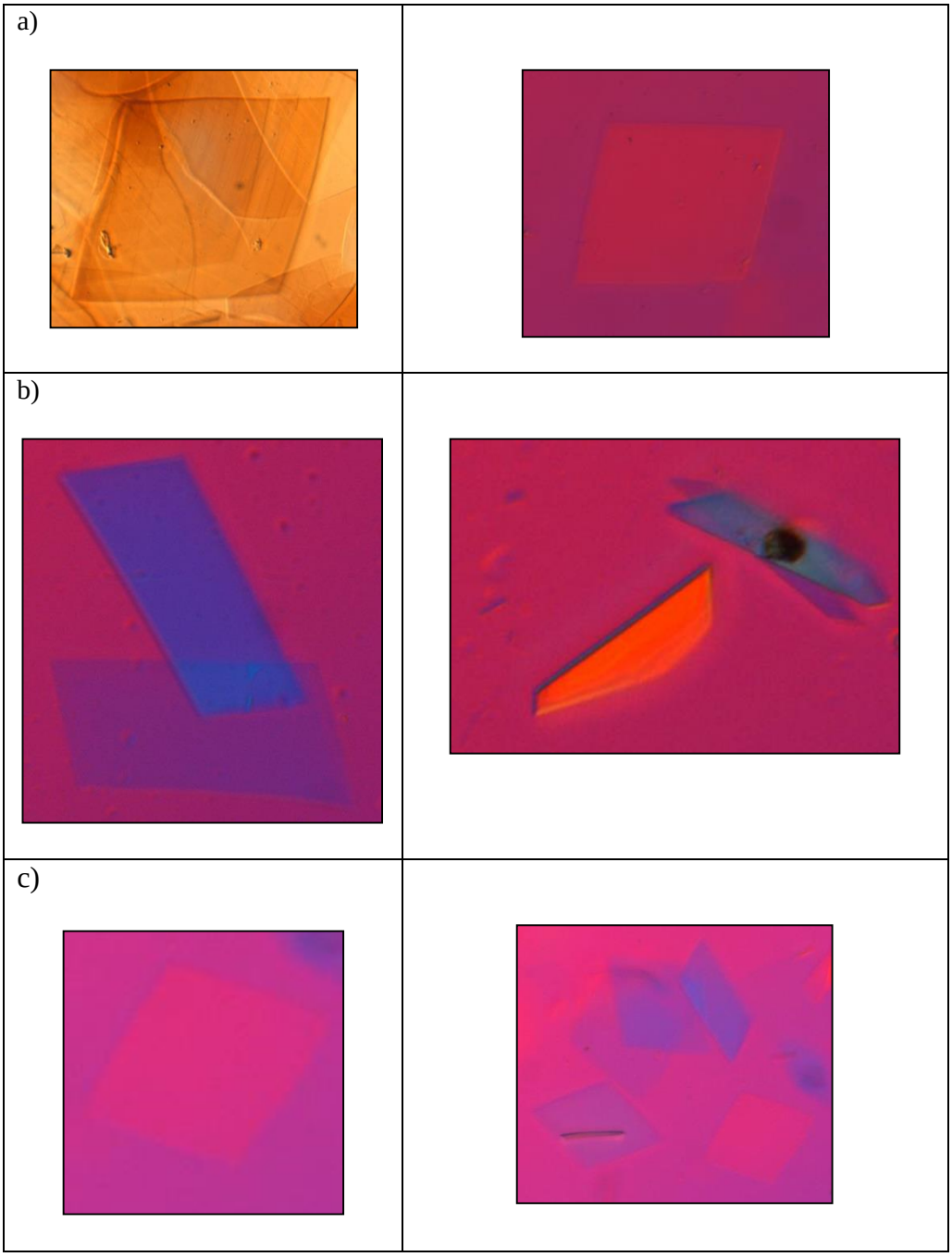

Figure 8.6 Optical micrographs showing the evolution of the growth of methyl stearate crystals growing from supersaturated n-dodecane, kerosene and toluene solutions for a selected solution supersaturations (σ). The micrograph shown are a representative sequence of the crystal growth process at (a) n-dodecane solution between 20.2 ºC and 21 °C (σ = 0.30-0.39); (b) kerosene solution: left/ between 17.8 ºC and 18.3 °C (σ = 0.45-0.52) right/ above 18.3 °C (σ < 0.45); (c) toluene between 13.5 ºC and 13.9 ºC (σ = 0.04-0.08)

BFDH analysis revealed 49, 81 and 147 habit planes for orthorhombic, monoclinic $(A2/a)$ and monoclinic $C2$ crystal systems respectively. The expected (001) plane is obtained in all prediction for the indexation of the larger crystals face perpendicular

to the c axes. According to the methodology, all other resulting indices were arranged by grouping the lattice planes into 9 zones for the first two crystal systems and into 17 zones for the latter. These groups with their corresponding zone axes indexation, including the complete set of planes delivered by the BFDH prediction are given in Appendix C. Table 8.7. shows a summary of this information featuring some representative planes and corresponding d spacing within each group.

Table 8.7 List of the predicted zone axis defining the different zone groups, representative (hkl) planes and d_{hkl} spacing within each group

Orthorhombic ($Pnab$)			
Group	Zone axis $[uvw]$	Representative plane (hkl)	Inter-planar distance d_{hkl}
1	[1 0 0]	(011) (020) (031) (042) (064)	7.33 3.68 2.45 1.84 1.22
2	[1-10]	(111) (220) (331)	4.46 2.23 1.49
3	[2-10]	(120)	3.08
4	[3-10]	(131) (260)	2.25 1.12
5	[0-10]	(200) (602)	2.81 0.94
6	[1-20]	(211) (420)	2.62 1.31
7	[3-20]	(231) (460)	1.85 0.92
8	[1-30]	(311) (620)	1.81 0.91
9	[2-30]	(320)	1.67
Monoclinic $A2/a$			
Group	Zone axis $[uvw]$	Representative plane (hkl)	Inter-planar distance d_{hkl}
1	[1 0 0]	(011) (020) (031) (042) (064)	7.31 3.67 2.44 1.83 1.22
2	[1-10]	(111) (220) (331) (442) (664)	4.07 2.07 1.37 1.03 0.68

3	[2-10]	(120) (242)	2.96 1.47
4	[3-10]	(131) (260)	2.19 1.10
5	[0-10]	(200) (402) (602)	2.50 1.24 0.83
6	[1-20]	(211) (420)	2.34 1.18
7	[3-20]	(231) (460)	1.74 0.87
8	[1-30]	(311) (620)	1.62 0.81
9	[2-30]	(320) (642)	1.52 0.75
Monoclinic $C2$			
1	[1 0 0]	(020) (062)	3.70 1.23
2	[-100]	(0-20) (0-62)	3.70 1.23
3	[1-10]	(110) (221) (331)	4.14 2.03 1.36
4	[-1-10]	(1-10) (2-21) (3-31)	4.14 2.03 1.36
5	[3-10]	(130)	2.21
6	[-3-10]	(1-30)	2.21
7	[0-10]	(200) (602)	2.50 0.82
8	[2-10]	(240)	1.49
9	[-2-10]	(2-40)	1.49
10	[1-30]	(310)	1.63
11	[-1-30]	(3-10)	1.63
12	[1-20]	(420)	1.18
13	[-1-20]	(4-20)	1.18
14	[3-20]	(460)	0.88
15	[-3-20]	(4-60)	0.88

16	[2-30]	(640)	0.76
17	[-2-30]	(6-40)	0.76

The inter-planar angle correlation for the plane pairs was carried out using the annotation in Fig. 8.7 both for the morphology observed at the lowest supersaturation in kerosene and the dominant morphology observed in all solvents.

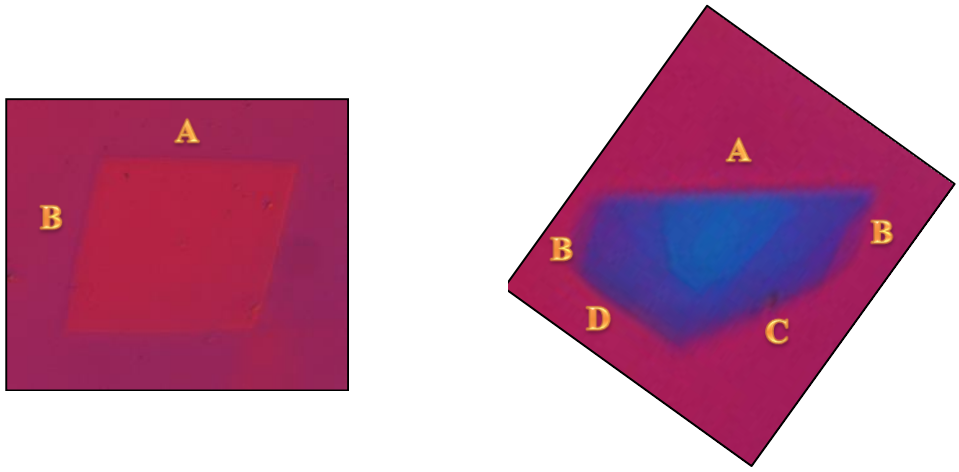

Figure 8.7 Example of initial designation of crystal's faces for the two morphologies observed for methyl stearate

As for the case of orthorhombic $Pnab$ and monoclinic $A2/a$ crystal systems the list of Miller indices obtained belong to the same zone axes groups, thus a single analysis could be carried out. This delivered only two pairs of miller indices matching AB inter-planar angles (111) and (1-11) or (011) and (311). However, due to the geometry of the space group the prediction for the pair wise (111) (1-11) is the only one delivering the expected crystal lozenge shape. The same analysis using monoclinic $C2$ crystal system delivered similar results with the pairs (110) and (1-10) or (240) and (2-40) matching the internal angle between A and B faces. This information is presented in Table 8.8.

In the case of the indexation for the morphology observed at the lowest supersaturation of kerosene solutions, the set of matches for the pairs of Miller

indices of the remaining inter-planar angles between BC/CD and BD faces are summarised also in Table 8.8. Miller indices for the BC and CD faces are presented within the same column as the inter-planar angles between these pairs of faces are coincidental.

Table 8.8 Likely combinations of Miller indices for the four faces of the experimental crystals observed at the lowest supersaturation σ<0.45 in kerosene solvent. Planes designated according to Fig. 8.7

	AB	BC or CD	BD
Orthorhombic and monoclinic	(111) (1-11) (011) (311)	(011)-(111) (120)-(200) (131)-(311) (200)-(231)	(011)-(211)
Monoclinic	(110) (1-10) (240) (2-40)	(020)-(1-30) (110)-(3-10) (110)-(4-20) (110)-(6-40) (130)-(1-30) (420)-(6-40)	(110)-(4-60) (240)-(3-10) (310)-(4-60)

Within the morphology delivered by the orthorhombic/monoclinic $A2/a$ crystal systems there is only a pair of Miller indices that match the inter-planar angles between BD faces, and one pair for AB faces, that also satisfies the faces present in the dominant lozenge shape morphology. This facilitates obtaining the solution for the entire morphology after cross-checking with the indices allocated for BC/CD pairs. If AB faces are allocated the pair (111) (1-11) and BD faces the pair (011) (211) then the solution for BD/CD pairs should contain either the Millers indices (011) or (211) together with either the (111) or (1-11) indices. The only pair that satisfice this condition is (011) (111). Therefore, the solution for the entire morphology is given by the indices (111) (1-11) (011) (211). Further modification of the perpendicular distance from the centre of the crystal to the faces, in the corresponding cif file, produce the morphology prediction with lengths proportional to those observed experimentally.

Among the Miller indices pairs delivered by the prediction using the monoclinic $C2$ crystal system, only three of these pairs matched BD faces inter-planar angles and two pairs matched those angles between AB faces. Using the same principle as in the

previous analysis, if AB pairs are given by the (110) (1-10) indices, then three options would be available for BC/CD faces: (110) (3-10), (110) (4-20) and (110) (6-40) and two pairs would likely satisfy BD faces (110) (4-60) and (240) (3-10). This is so because by crosschecking these pairs share either one of their two indices. Similarly, if AB pairs are given by (240) (2-40), then BD would be given by the pair (240) (3-10) and BC/CD faces would be likely indexed by the (110) (3-10) pair. A summary of the unique potential morphology solutions using these indices combinations is given in Table 8.9.

Table 8.9 Potential unique solutions of the methyl stearate crystals morphology observed at observed at the lowest supersaturation σ <0.45 in kerosene solvent. The row highlighted in the table represents the chosen final unique solution using monoclinic $C2$ crystal system

A	B	C	D
(110)	(1-10)	(3-10)	(460)
(110)	(1-10)	(4-20)	(460)
(110)	(1-10)	(6-40)	(460)
(110)	(1-10)	(3-10)	(240)
(240)	(2-40)	(110)	(3-10)

After performing the morphology predictions using the combinations in Table 8.9., the analysis suggests the indexation (110) (1-10) (3-10) (240) for the morphology observed at the lowest supersaturations in kerosene. Further modification of the perpendicular distance from the centre of the crystal to the faces, in the corresponding cif file, produce the morphology prediction with lengths proportional to those observed experimentally.

Fig. 8.8 compares the most likely morphology prediction, using either the orthorhombic/monoclinic $A2/a$ or monoclinic $C2$ unit cell parameters, with a micrograph taken from a selected experimental crystal. The selected micrographs feature both the dominant morphology observed in all solvents and that observed at the lowest supersaturations in kerosene systems. In the case of the final chosen morphology using the monoclinic crystal system with space group $A2/a$, the occasional face (011) is predicted for the habit observed at lower supersaturation in kerosene. This is in agreement with the morphology of the B monoclinic polymorph reported for stearic acid crystals [20, 21, 27].

a)

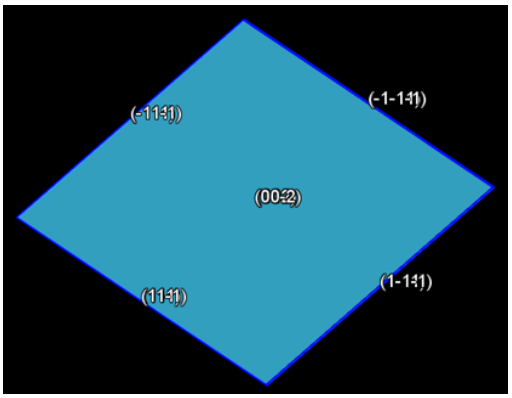
(-1-1-1)
(00-2)
(1-1-1)

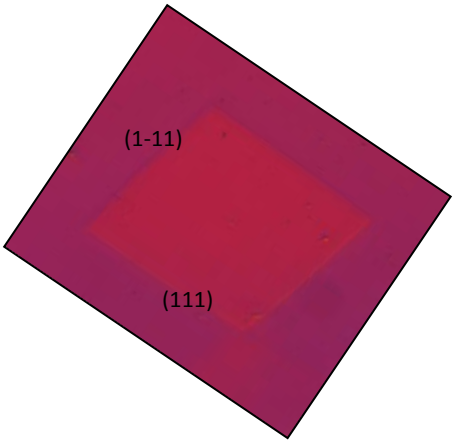
(1-11)
(111)

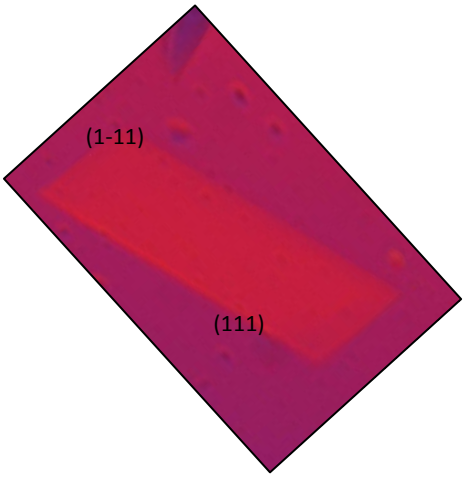
(1-11)
(111)

b)

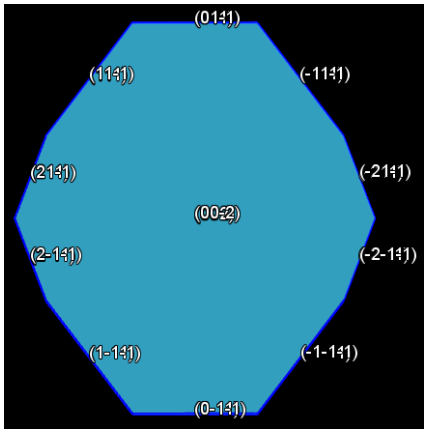
(01-1)
(-1-1)
(-2-1)
(00-2)
(-2-1)
(-1-1)
(0-1-1)

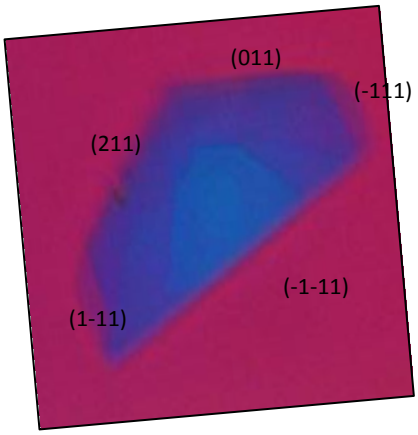
(011)
(-111)
(211)
(-1-11)
(1-11)

c)

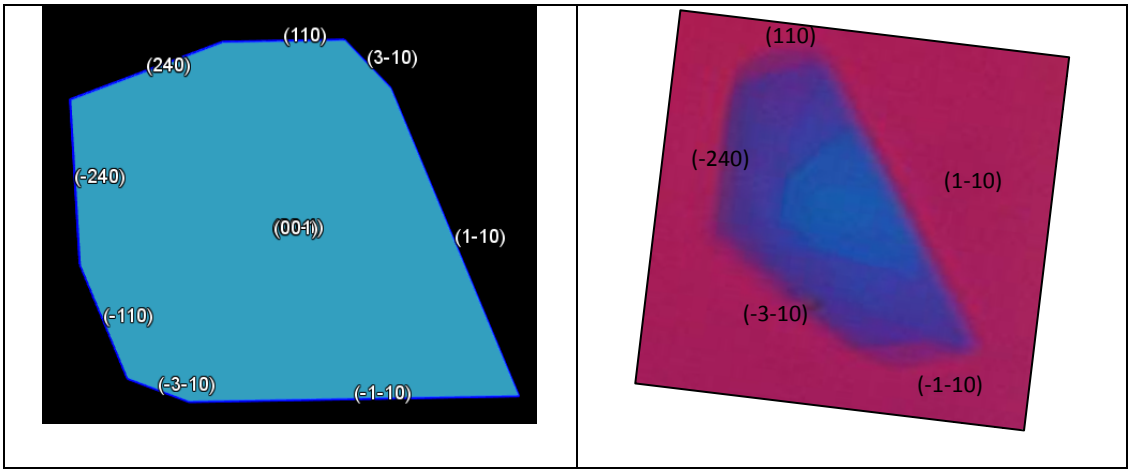

Figure 8.8 Predicted BFDH morphology of methyl stearate crystals using the Miller indices in the obtained unique solutions and comparison with the crystals' micrograph a) dominant morphology observed in three solvents b) predicted morphology using orthorhombic/monoclimic A2/a crystal system for kerosene crystals observed above 18.3 °C (σ<0.45) c) predicted morphology using monoclimic $C2$ crystal system for kerosene crystals observed above 18.3 °C (σ<0.45)

Given the asymmetrical nature of the crystals´ morphology observed at the lowest superaturations in kerosene the morphology predicted by the monoclinic crystal system C_2 seems to deliver the best match to those crystals observed experimentally. Thus the final chosen indexation is (110) (1-10) (-1-10) (-240) (-3-10).

8.3.2. Derivation of models for the analysis of crystal faces growth kinetics

Given the experimental method used to collect crystals´ growth rates, the measured growth rates are not only influenced by the incorporation of growth units into the crystal surface, but also by the diffusion of the growth units within the bulk of the solution. Thus, this effect needs to be accounted for.

In this case volume diffusion is followed by a "docking rate" that includes the effect of any of the three mechanisms on the crystal surface described by equations (2.77) to (2.81). As these two effects act consecutively, they have to share the driving force and the slower one will be rate determining [28]. Making an analogy to a circuit in which the resistors are arranged in a chain, the process can be represented by Fig. 8.9 This shows that the resistance to the diffusion of growth units in the bulk of the

solution is given by the inverse of the mass transfer coefficient k_{MT} and the resistance to mass transfer on the surface of the crystal is given by the inverse of the "observable docking rate".

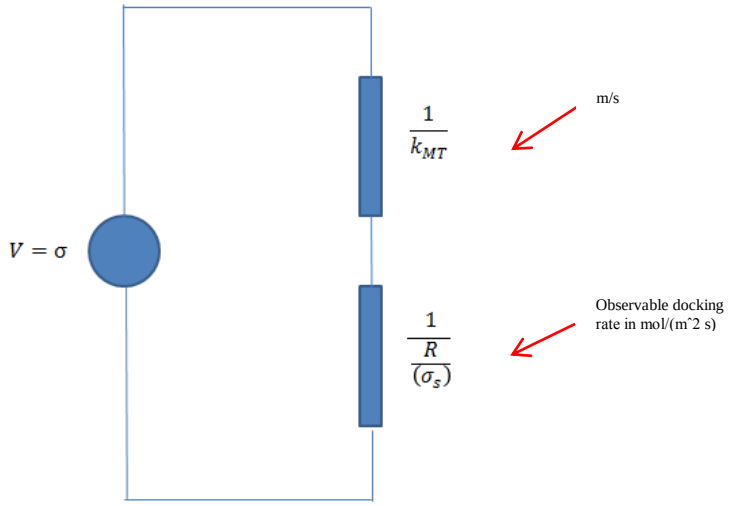

Figure 8.9 Representation of the mass transfer process for the growth of a crystal specific faces by an analogy to a circuit in which resistors are in series according to V=IR. V represents the driving force, I the flow of molecules towards the surface and R the resistant to this flow

If mass transfer on the surface is taken as a first order process then the rate of transfer r_{MT} is given by

$$r_{MT} = k_d(C_s - C_e) \tag{8.3}$$

where k_d is the observed incorporation rate constant, C_s the concentration at the crystal solution interface and C_e is the concentration at equilibrium

Given that r_{MT} is related to the rate of growth of a single face R by

$$r_{MT} = R\ C_e \tag{8.4}$$

Then

$$k_d = \frac{R}{\sigma_s} \tag{8.5}$$

Similarly mass transfer (MTR) would be represented by

$$\frac{MTR}{A} = k_{MT}(C - C_s) = k_d(C_s - C_e) \tag{8.6}$$

Or using equation (8.5)

$$\frac{MTR}{A} = k_{MT}(C - C_s) = \frac{R}{(\sigma_s)}(C_s - C_e) \tag{8.7}$$

where k_{MT} is the coefficient of mass transfer within the bulk of the solution, C the solution concentration and A is the effective mass transfer area

Expressing all terms in equation (8.7) using absolute supersaturation it becomes

$$\frac{MTR}{A} = k_{MT}(\sigma - \sigma_s)C_e = \frac{R}{\sigma_s}\frac{\rho_s}{MW_s C_e}\sigma_s C_e \tag{8.8}$$

Where ρ_s is the solute density and MW_s the solute molecular weight

Rearranging

$$(\sigma - \sigma_s) = \frac{MTR}{Ak_{MT}C_e} \tag{8.9}$$

and

$$(\sigma_s) = \frac{MTR}{A\frac{R}{\sigma_s}\frac{\rho_s}{MW_s}} \tag{8.10}$$

Thus summing driving forces

$$\frac{MTR}{A} = \frac{1}{\frac{1}{k_{MT}C_e} + \frac{1}{\frac{R}{\sigma_s}\frac{\rho_s}{MW_s}}}\sigma \tag{8.11}$$

Multiplying the denominator by $\frac{1}{\frac{MW_s}{\rho_s}}$ and making $k_{MT}^{'}\left(\frac{m}{s}\right) = \frac{k_{MT}C_e\, MW_s}{\rho_s}$ the growth of a crystal face with time can be expressed as

$$G\left(\frac{m}{s}\right) = \frac{1}{\frac{1}{k_{MT}^{'}} + \frac{1}{\frac{R}{\sigma_s}}}\sigma \tag{8.12}$$

Specific models describing the kinetics on the crystal surface can be inserted into equation (8.12) as R would depend on the mechanism with which the growth units will be attached to the crystal face. Thus using the power law given by equation (2.81) and additionally assuming $\sigma_s \approx \sigma$

$$G\left(\frac{m}{s}\right) = \frac{1}{\frac{1}{k_{MT}^{'}} + \frac{1}{k_G(\sigma)^{r-1}}}\sigma \tag{8.13}$$

Similarly for B&S crystal growth mechanism using equation (2.78)

$$G\left(\frac{m}{s}\right) = \frac{1}{\frac{1}{k_{MT}^{'}} + \frac{1}{k_G\,(\sigma)^{-1/6}\exp\left(\frac{A_1}{\sigma}\right)}}(\sigma) \tag{8.14}$$

And for the BCF crystal growth mechanism using equation (2.80)

$$G\left(\frac{m}{s}\right) = \frac{1}{\frac{1}{k_{MT}^{'}} + \frac{1}{k_G(\sigma)tanh\left(\frac{A_2}{\sigma}\right)}}(\sigma) \tag{8.15}$$

8.3.3. Mean growth rates and growth rates mechanism of the (110) and (1-10) faces of methyl stearate crystals as a function of growth environment

A sequence of images of methyl stearate crystals in a 0.5 ml cuvette crystallisation cell in three different solvents is shown in Fig. 8.10. An example of the type of plot used to obtain the mean growth rates of single faces is also shown in Fig. 8.11. The mean growth rates of the (110) and (1-10) faces of single crystals of methyl stearate growing from n-dodecane, kerosene and toluene are presented in Table 8.10.

Up to now no information has been yet reported on the growth of methyl esters crystals. However, the growth rates of stearic acid crystals growing from different solvent systems have been studied [20, 21, 29]. The values reported for the (110) face of these crystals (Table 8.5.) are within the same order of magnitude to those obtained in this work.

In general growth occurs quicker for crystals growing from toluene. In this case growth rates are within the same order of magnitude to those observed in the other two solvents but for supersaturations of much lower order of magnitude not surpassing 8%.

Using the indices predicted for the monoclinic $C2$ crystal system to identify the faces of the asymmetrical morphology; occasional observations of the (-3-11) face, at the lowest supersaturations in kerosene, showed this face grows at a rate of 0.16 μm/sec.

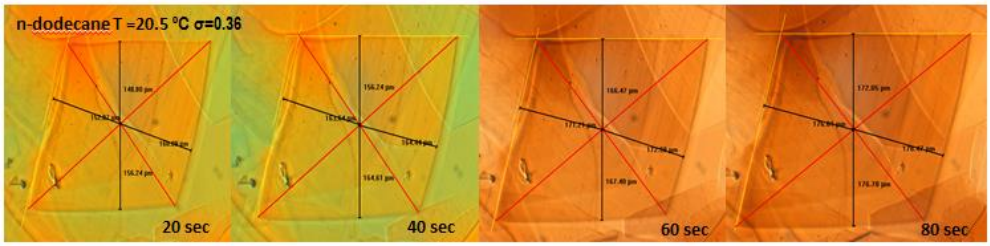
n-dodecane T =20.5 °C σ=0.36
20 sec
40 sec
60 sec
80 sec

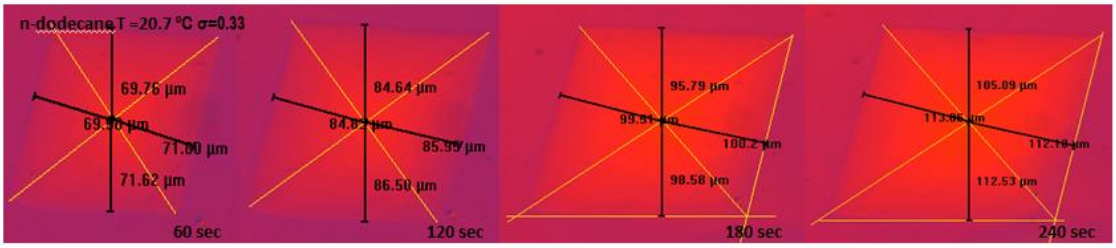
n-dodecane T =20.7 °C σ=0.33
69.76 µm
71.00 µm
71.62 µm
60 sec
84.64 µm
85.99 µm
86.50 µm
120 sec
95.79 µm
100.2 µm
98.58 µm
180 sec
105.09 µm
112.53 µm
240 sec

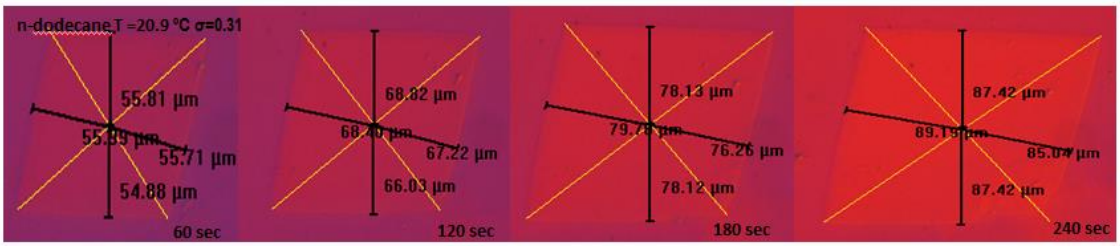
n-dodecane T =20.9 °C σ=0.31
55.81 µm
55.71 µm
54.88 µm
60 sec
68.82 µm
67.22 µm
66.03 µm
120 sec
78.13 µm
76.26 µm
78.12 µm
180 sec
87.42 µm
87.42 µm
240 sec

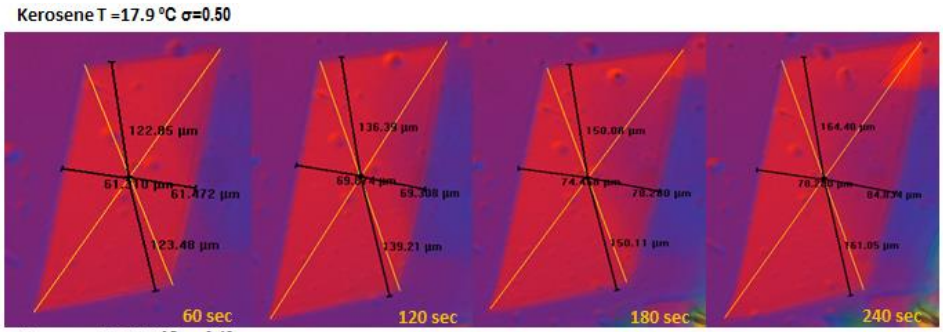
Kerosene T =17.9 °C σ=0.50
122.85 µm
61.472 µm
123.48 µm
60 sec
136.39 µm
69.308 µm
139.21 µm
120 sec
150.06 µm
78.280 µm
150.11 µm
180 sec
164.48 µm
84.834 µm
161.05 µm
240 sec

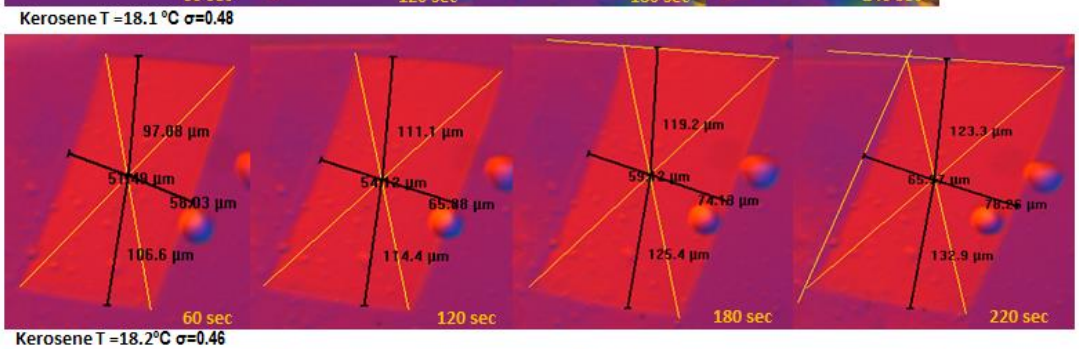
Kerosene T =18.1 °C σ=0.48
97.08 µm
58.03 µm
106.6 µm
60 sec
111.1 µm
65.88 µm
174.4 µm
120 sec
119.2 µm
74.18 µm
125.4 µm
180 sec
123.3 µm
78.26 µm
132.9 µm
220 sec

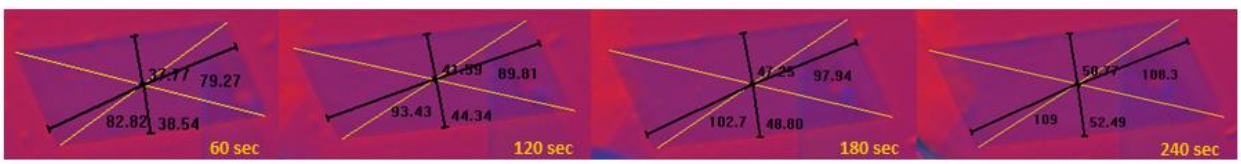
Kerosene T =18.2°C σ=0.46
37.17
79.27
82.82
38.54
60 sec
89.81
93.43
44.34
120 sec
97.94
102.7
48.80
180 sec
108.3
109
52.49
240 sec

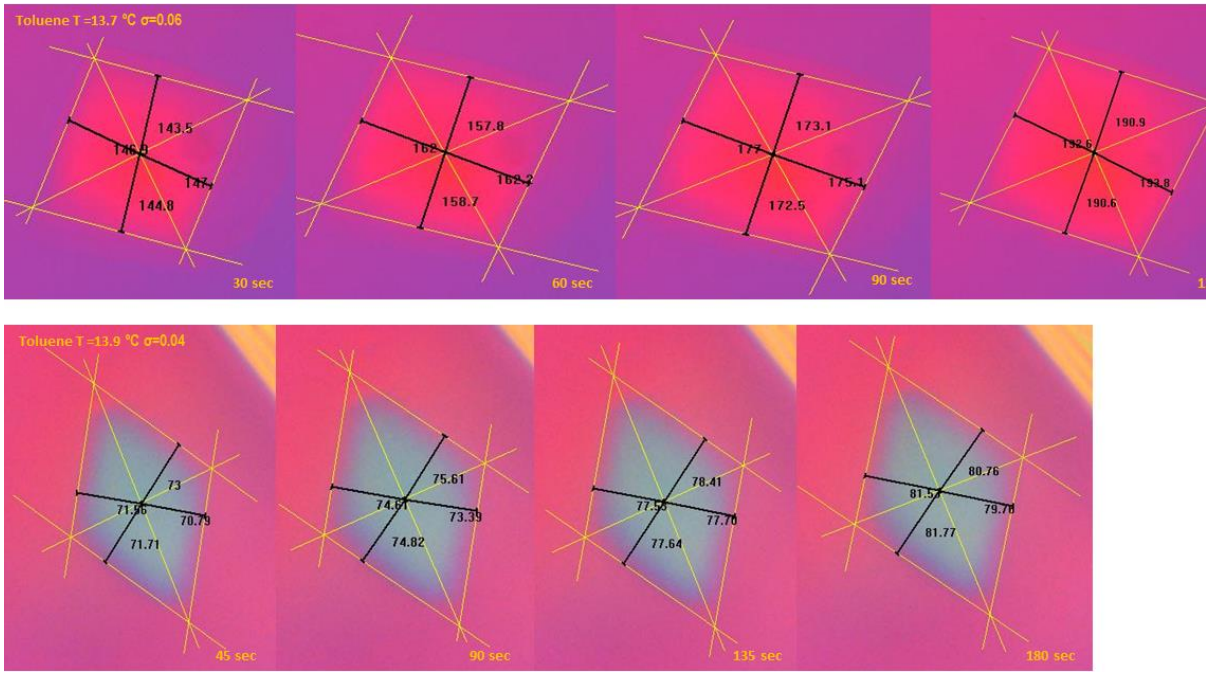

Figure 8.10 Sequences of optical micrograph of methyl stearate crystals grown in n-dodecane for σ=0.31 and 0.36, kerosene for σ=0.46 and 0.50 and toluene for σ=0.04 and 0.06, showing the growth of the crystals and their morphology as a function of solvent

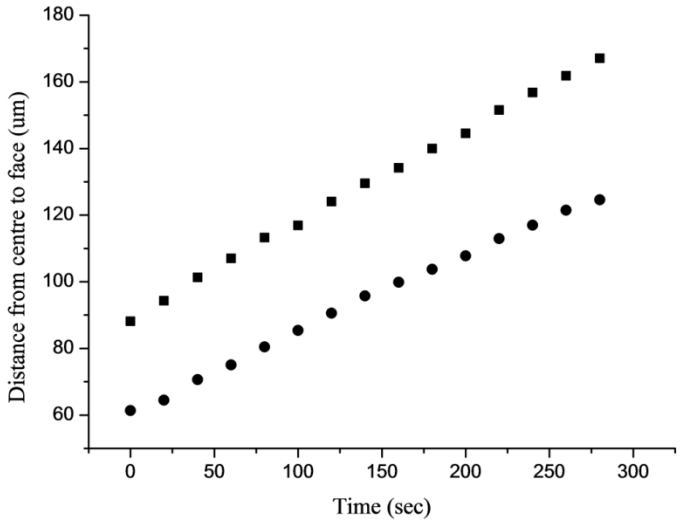

Figure 8.11 Plot of two measurements of the growth of the (110) face with time for methyl stearate crystals growing from n-dodecane at σ=0.33. Average of the slopes of the lines delivering the single faces growth rates

Table 8.10 Mean growth rates of (110) and (1-10) faces of methyl stearate crystals growing from n-dodecane, kerosene and toluene

Solvent	σ	No crystals	Mean growth rate $G(\mu m/s)$	
			G (110)	G (1-10)
n-dodecane	0.39	2	1.13	1.05
	0.38	2	0.66	0.70
	0.37	2	0.64	0.63
	0.36	2	0.34	0.34
	0.34	2	0.31	0.34
	0.33	2	0.25	0.26
	0.32	2	0.14	0.14
	0.31	2	0.13	0.14
	0.30	2	0.09	0.11
Kerosene	0.52	2	0.15	0.35
	0.50	2	0.11	0.25
	0.49	2	0.12	0.27
	0.48	2	0.08	0.15
	0.46	2	0.07	0.14
	0.45	2	0.02	0.01
Toluene	0.08	2	0.37	0.34
	0.06	2	0.27	0.27
	0.05	2	0.16	0.17
	0.04	2	0.02	0.03

To assess the mechanistic regime of crystal growth, the data collected for the (110) and (1-10) faces were fitted using to the models described by equations (8.13) to (8.15). However, given that experimental $G(\sigma)$ observations showed there is a critical supersaturation (σ_{crit}) below which growth does not proceed (Fig. 8.12 to 8.14), this parameter was introduced within the models to account for its effect by subtracting it from the term σ.

Figs. 8.12 to 8.14 show the best fits of these models to the experimental data for both the (110) and (1-10) faces for n-dodecane, kerosene and toluene solvents respectively. In addition to this, they also present the trend of the total resistance to transfer of growth units $\left(\frac{1}{K_{MTOT}}\right)$ as a function of driving force $(\Delta C = C - C_e)$, using the bulk and interface transfer coefficients obtained from the experimental data fitting. $\frac{1}{K_{MTOT}}$ is defined by the denominator of the $G(\sigma)$ expressions given by the corresponding mechanistic model assessed.

All relevant parameters obtained through this analysis are presented in Table 8.11. For comparative assessment, when more than one model fitted well to the experimental data all fitting lines were drawn and the corresponding modelled parameters were also given. For illustration, although a more accurate assessment of the rate limiting step can be done through Fig. 8.12 to 8.14 an estimation of both the resistance to transfer within the bulk and that at the interface are given in Table 8.11. using average values of σ and C^*within the range of study.

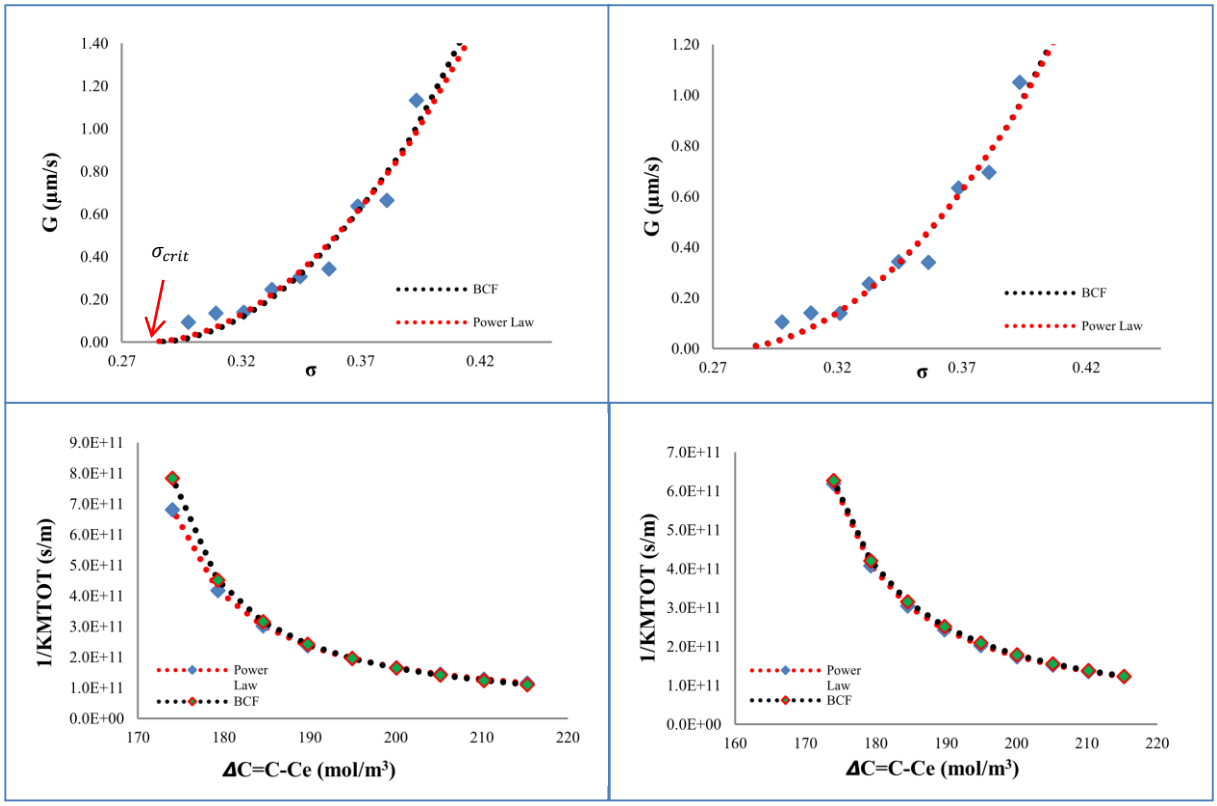

Figure 8.12 C18:0 growing from n-dodecane. For each set of four plots, above: G(σ) experimental data fitted to the power law and BCF models; below: trend of the total resistance to mass transfer as a function of ΔC using the parameters obtained from the data fitting to these models. Left refers to the (110) and right to the (1-10) faces respectively

Although the amount of experimental data collected is probably not enough to accurately determine the values of k_{MT} and k_G the fitting of the models presented to these data, can deliver relevant mechanistic information.

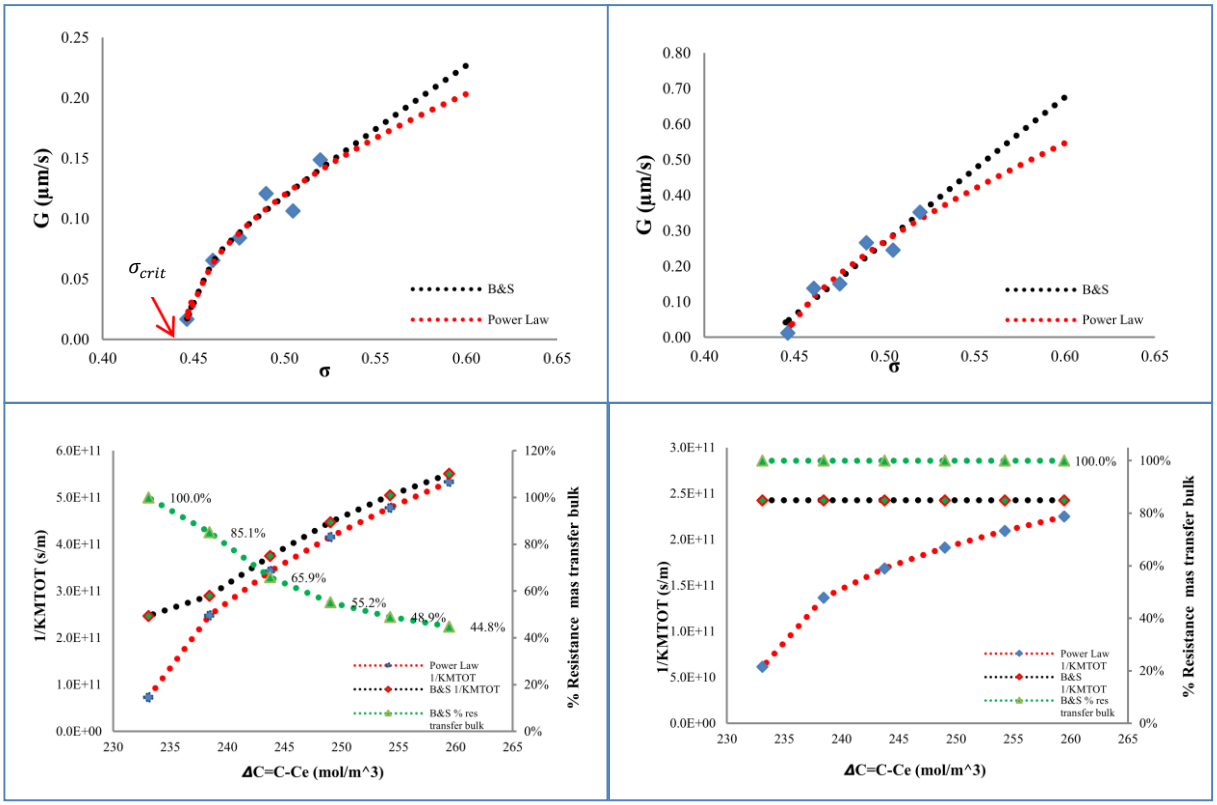

Figure 8.13 C18:0 growing from kerosene. For each set of four plots, above G(σ) experimental data fitted to the power law and B&S models; below: trend of the total resistance to mass transfer as a function of ΔC using the parameters obtained from the data fitting to these models. The green line shows the trend of the ratio of the resistance to mass transfer in the bulk to the total mass transfer resistance using the parameters obtained from the B&S model fitting. Left refers to the (110) and right to the (1-10) faces respectively

Whilst there is no direct-visual evidence of the presence of screw dislocations for the (110) and (1-10) faces of C18:0 crystals, the best fittings to the experimental data for C18:0 growing from n-dodecane solvent were obtained for the models given by both the power law and the BCF mechanism. Given that in the power law a value of r equal to 2 is associated with the BCF mechanism, this strongly suggests that growth in this case proceeds via screw dislocations. Since a linear dependence of $\frac{1}{K_{MTOT}}$ on ΔC is relevant to growth limited by bulk diffusion, Fig. 8.12 indicates that growth of C18:0 from n-dodecane is hindered by transfer of growth units at the crystal/solution interface. What is more the shape of the $\frac{1}{K_{MTOT}}(\Delta C)$ lines is coincident with that of the hyperbolic form given by the BFC mechanism but in opposite direction showing that as expected higher interfacial resistance would be placed at lower levels of driving force. The resistance to incorporation at the crystal/solution interface

$\left(\frac{1}{k_G(\sigma-\sigma_{crit})tanh\left(\frac{A_2}{(\sigma-\sigma_{crit})}\right)}\right)$ (calculated using average values of σ within the range of analysis) is significantly higher than the resistance to mass transfer within the bulk of the solution $\left(\frac{1}{k_{MT}'}\right)$ (Table 8.11.) this supporting surface integration as the rate limiting step.

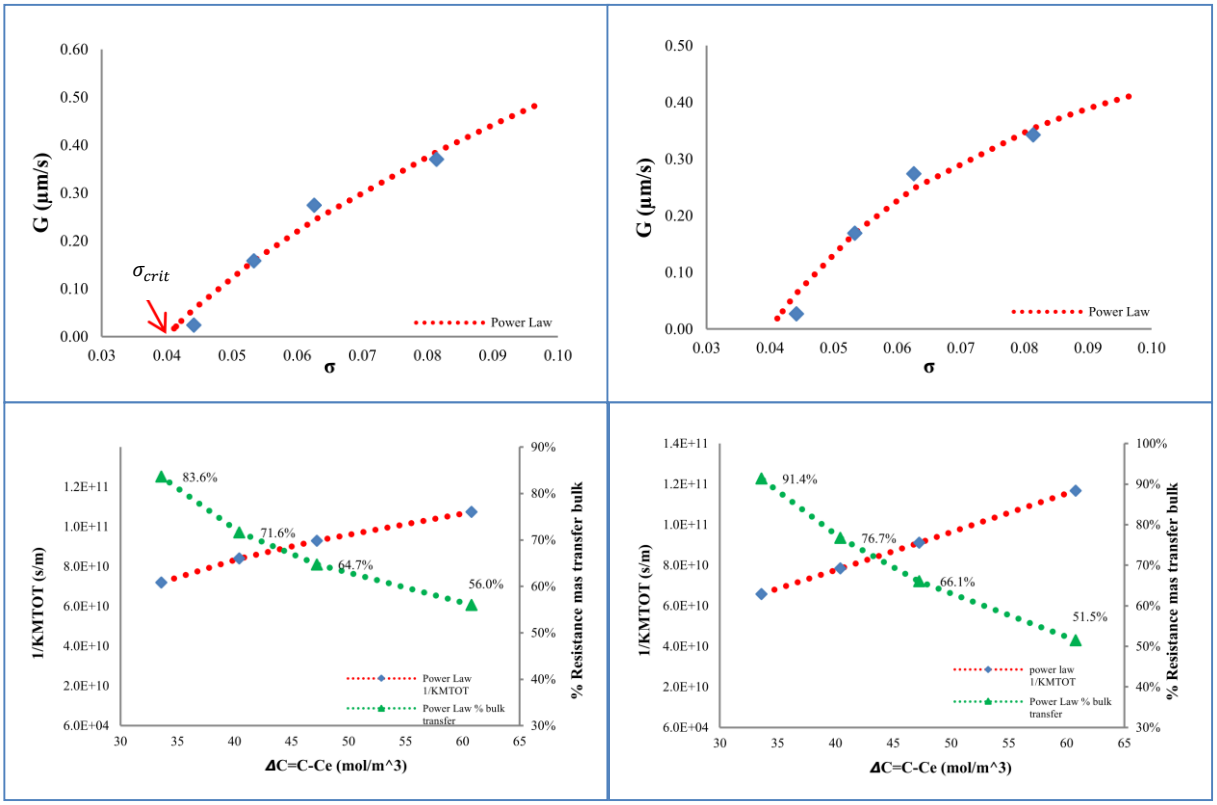

Figure 8.14 C18:0 growing from toluene. For each set of four plots, above: G(σ) experimental data fitted to the power law model; below: trend of the total resistance to mass transfer as a function of ΔC using the parameters obtained from the data fitting to this model. The green line shows the trend of the ratio of the resistance to mass transfer in the bulk to the total mass transfer resistance. Left refers to the (110) and right to the (1-10) faces respectively

Table 8.11 Crystal growth kinetics parameters obtained from the best fit of the models given from equation (8.13) to (8.15) to the experimental $G(\sigma)$ data

		n-dodecane		Kerosene		Toluene	
	Range σ studied	0.30 to 0.39		0.45 to 0.52		0.04 to 0.08	
Fitting model	Range of $\Delta C = (C - C_e)$ studied	174 to 215		233 to 259		34 to 61	
Power law Equation (8.13)	Faces	(110)	(1-10)	(110)	(1-10)	(110)	(1-10)
	$\frac{1}{k'_{MT}}$	**0.900 x 10^{10}**	**0.900 x 10^{10}**	**0.105 x 10^{9}**	**0.105 x 10^{9}**	**0.602 x 10^{11}**	**0.602 x 10^{11}**
	$k_{MT}\left(\frac{m}{s}\right)$	0.494 x 10^{-9}	0.494 x 10^{-9}	0.461 x 10^{-7}	0.461 x 10^{-7}	0.444 x 10^{-10}	0.444 x 10^{-10}
	$k_G\left(\frac{m}{s}\right)$	0.830 x 10^{-10}	0.752 x 10^{-10}	0.527 x 10^{-12}	0.194 x 10^{-11}	0.309 x 10^{-11}	0.731 x 10^{-12}
	$\frac{1}{k_G(\sigma-\sigma_{crit})^{r-1}}$	**0.185 x 10^{12}**	**0.193 x 10^{12}**	**0.368 x 10^{12}**	**0.177 x 10^{12}**	**0.305 x 10^{11}**	**0.274 x 10^{11}**
	σ_{crit}	0.28	0.28	0.45	0.45	0.04	0.04
	r	2.00	2.00	0.51	0.68	0.40	0.00
	R^2	93%	95%	94%	94%	96%	96%
B&S Equation (8.14)	$\frac{1}{k'_{MT}}$			**0.247 x 10^{12}**	**0.243 x 10^{12}**		
	$k_{MT}\left(\frac{m}{s}\right)$			0.196 x 10^{-10}	0.199 x 10^{-10}		
	$k_G\left(\frac{m}{s}\right)$			0.126 x 10^{-11}	0.100 x 10^{-11}		
	$\frac{1}{k_G(\sigma-\sigma_{crit})^{-1/6}\exp\left(\frac{A_1}{\sigma-\sigma_{crit}}\right)}$			**0.153 x 10^{12}**	**0.133 x 10^{3}**		
	σ_{crit}			0.44	0.44		
	A_1			0.04	1.00		
	R^2			94%	92%		
BCF Equation (8.15)	$\frac{1}{k'_{MT}}$	**0.900 x 10^{7}**	**0.900 x 10^{7}**				
	$k_{MT}\left(\frac{m}{s}\right)$	0.494 x 10^{-6}	0.494 x 10^{-6}				
	$k_G\left(\frac{m}{s}\right)$	0.817 x 10^{-10}	0.681 x 10^{-10}				
	$\frac{1}{k_G(\sigma-\sigma_{crit})tanh\left(\frac{A_2}{(\sigma-\sigma_{crit})}\right)}$	**0.195 x 10^{12}**	**0.208 x 10^{12}**				
	σ_{crit}	0.28	0.27				
	A_2	3.17	10.42				
	R^2	94%	95%				
Rate limiting step		Integration of growth units into the crystal surface		Diffusion of growth units within the bulk of the solution		Diffusion of growth units within the bulk of the solution	

The best fittings to the experimental data for C18:0 growing from kerosene solvent were obtained for the models given by both the power law and the B&S mechanism. However, since the fitting to the power law delivered r values of 0.51 and 0.68, and a value of r equal to 0.83 could be associated with the B&S mechanism, the parameters obtained via the fitting to this model were taken for this analysis. Fig. 8.13 shows that if this is the case the resistance to mass transfer within the bulk, would plays a more important role on the faces growth and would be rate limiting. This representing between, 44.8% to 100% of the total resistance to transfer of growth unit for the (110) face and 100% of the resistance for the whole range of σ studied for the (1-10) face. The differences in these proportions can be explained by the fact that the resistance to incorporation of growth units at the interface $\left(\frac{1}{k_G(\sigma-\sigma_{crit})^{-1/6}\exp\left(\frac{A_1}{\sigma-\sigma_{crit}}\right)}\right)$ (calculated using average values of σ within the range of analysis) for the (110) face is nine orders of magnitude higher than that of the (1-10) face (Table 8.11.). Considering that k_G values are of the same order of magnitude, this significant difference is due to the value obtained for the parameter A_1 which is inversely related to the $2D$ nuclei interfacial tension. Therefore the more elongated habit of the crystals observed in this case, is likely to be the result of differences between the molecular structures of the (110) and (1-10) faces in which the former would provide a less suitable surface for the formation of $2D$ nuclei, imposing a higher proportion of resistance to the face growth at the interface.

A fitting to the experimental data for C18:0 growing from toluene solvent was obtained only for the models given by the power law and similarly to the case of growth kerosene the resistance to mass transfer within the bulk is rate limiting. This effect is shown in Fig. 8.14 where the proportion of $\left(\frac{1}{k_{MT}}\right)$ to the total resistance to transfer $\left(\frac{1}{K_{MTOT}}\right)$ for both faces is above 50% all over the range of (σ) studied. Interestingly, this analysis delivered values of r equal to 0.4 and 0 for the (110) and (1-10) faces respectively, which cannot be associated to any of the interface kinetic models given by expression (8.13) to (8.15), this indicating that growth from toluene would be entirely controlled by the diffusion of growth units towards the crystal.

A comparison between the values obtained for the resistance to mass transfer within the bulk, using the best model fitting parameters, shows an interesting trend in which this resistance is one order of magnitude lower in toluene than in kerosene and four orders of magnitude lower in n-dodecane than in toluene. This result is likely to be due to the aromatic nature of toluene and the presence of both aromatic and cyclo-alkyl compounds in kerosene that would provide stronger solute-solvent interactions due to the more polar nature of solvent molecules. This condition would make difficult the de-solvation process and decrease the rate of transfer of the solute molecules.

The values obtained for the resistance to transfer at the interface are much more similar in magnitude, being only significantly lower for the (1-10) face of crystals growing from kerosene solvent where their values are eight and nine orders of magnitude lower than those observed in the other solutions likely due to very low resistance to the formation of $2D$ nuclei. This resistance is one order of magnitude higher in n-dodecane than in toluene solvents which could only be the case if the faces of crystals growing from toluene provide sufficient and larger number of kinks sites.

8.4. Combined assessment of methyl stearate crystallisation as a function of solvent

If a comprehensive assessment is carried out drawing on the finding within Chapters 6 to 8 for crystallisation of methyl stearate from n-dodecane, kerosene and toluene, it can be concluded that the crystallisation process in toluene systems will deliver a lower number of crystals, with bigger sizes in comparison to those crystals expected to be obtained from n-dodecane and kerosene solvents. This is due to lower nucleation rates (Fig. 7.5) and significantly higher crystal growth rates in this solution system. These findings are supported by observation of the crystallisation process under microscope in which fewer larger faceted crystals were observed growing at such significant rate that their growth could only be recorded at very low supersaturation σ below 8%. Given that diffusion of building units in toluene is rate limiting, this suggests that the surface of methyl stearate crystals growing from this

solvent would provide a more suitable structural environment in which greater concentration of sites (kinks) available for molecular attachment could be expected.

The number of crystals and nucleation rates were found to be higher in kerosene as lower interfacial tension γ were obtained in this case. If this is coupled with the fact that growth rates in these systems are around the same order of magnitude than those observed in n-dodecane solvent then it could be expected that crystallisation process in the former solvent will produce a larger population of crystals of smaller sizes.

8.5. Conclusions

A practical method for the indexation of the crystal faces of low symmetry materials was developed. This was validated through the characterisation of the morphology of n-docosane crystals for which tentative evidence is provided for solvent-induced polymorphic behaviour and kinetic roughening at higher supersaturations.

Typical growth rates of n-docosane crystals were found to be in the region 0.51 – 9.85 $\frac{\mu m}{s}$ over the relative supersaturation range of 0.01 – 0.05. The kinetic data was found to be consistent with the BFC interfacial growth mechanism.

Methyl stearate crystals growing from supersaturated n-dodecane, kerosene and toluene solutions, at supersaturation σ levels of 0.30-0.39, 0.45-0.52 and 0.04-0.08 respectively, showed that the crystal morphology changes only in the case of methyl stearate crystallising from kerosene at the lowest supersaturation levels.

Measurements of the growth rate for the indexed (110) and (1-10) faces of the dominant morphology of methyl stearate crystals are within the same range of magnitude in all solution´s systems studied, but for significantly lower values of supersaturation in the case of toluene solvent, where σ levels do not surpass 8%. These values range between 0.02 and 1.13 $\mu m/s$.

The tendency of methyl stearate crystals growth rates dependence on σ was consistent with the BCF growth mechanism in n-dodecane, the B&S mechanism in

kerosene and indicated the presence of a relative large number of kink sites in toluene solvent.

References

[1] A.M. Taggart, F. Voogt, G. Clydesdale, K.J. Roberts, An Examination of the Nucleation Kinetics of n-Alkanes in the Homologous Series $C_{13}H_{28}$ to $C_{32}H_{66}$, and their Relationship to Structural Type, Associated with Crystallization from Stagnant Melts, Langmuir, 12 (1996) 5722-5728.

[2] A.R. Gerson, K.J. Roberts, J.N. Sherwood, An Instrument for the Examination of Nucleation from Solution and Its Application to the Study of Precipitation from Diesel Fuels and Solutions of Normal-Alkanes, Powder Technol, 65 (1991) 243-249.

[3] K.J. Roberts, J.N. Sherwood, A. Stewart, The Nucleation of n-Eicosane Crystals from Solutions in n-Dodecane in the Presence of Homologous Impurities, Journal of Crystal Growth, 102 (1990) 419-426.

[4] A.R. Gerson, K.J. Roberts, J.N. Sherwood, A.M. Taggart, G. Jackson, The Role of Growth Environment on the Crystallization of Normal Alkanes in the Homologous Series from $C_{18}H_{38}$ to $C_{29}H_{60}$, Journal of Crystal Growth, 128 (1993) 1176-1181.

[5] P. Bennema, X.Y. Liu, K. Lewtas, R.D. Tack, J.J.M. Rijpkema, K.J. Roberts, Morphology of Orthorhombic Long-Chain Normal Alkanes - Theory and Observations, Journal of Crystal Growth, 121 (1992) 679-696.

[6] B. Simon, A. Grassi, R. Boistelle, Cinétique de Croissance de la Face (110) de la Paraffine $C_{36}H_{74}$ en Solution, Journal of Crystal Growth, 26 (1974) 77-89.

[7] A. Bravais, Etudes Cristallographiques Paris:Gauthier Villars, 1866.

[8] G. Friedel, Bulletin De La Socit Franaise De Minralogie Et De Crystallographie, 30 (1907).

[9] J.D.H. Donnay, D. Harker, American Mineralogist, 22 (1937) 463.

[10] L.A.M.J. Jetten, H. H.J., P. Bennema, J.P. van der Eerden, On the Observation of the Roughening Transition of Organic Crystals, Growing from Solution, Journal of Crystal Growth, 68 (1984) 503-516.

[11] X.Y. Liu, P. Bennema, J.P. van der Eerden, Rough-Flat-Rough Transition of Crystal Surfaces, in, Nature Publishing Group, 1992, pp. 778-780.

[12] J.W. Mullin, J. Garside, Crystallization of Aluminium Potassium Sulphate: a Study in the Assessment of Crystallizer Design Data: I: Single Crystals Growth Rates, II: Growth in a Fluidized Bed, Trans Inst Chem Eng, 45 (1967) 285-295.

[13] X.Z. Wang, J.C. De Anda, K.J. Roberts, Real-time measurement of the growth rates of individual crystal facets using imaging and image analysis - A feasibility study on needle-shaped crystals of L-glutamic acid, Chem Eng Res Des, 85 (2007) 921-927.

[14] A.G. Stapley, C. Himawan, W. MacNaughtan, T.G. Foster, A Computational Method for Extracting Crystallisation Growth and Nucleation Rate Data from Hot Stage Microscope Images, Crystal Growth and Design, 9 (2009) 5061-5068.

[15] C.T. Ó'Ciardhá, N.A. Mitchel, K.W. Hutton, P.J. Frawley, Determination of the Crystal Growth Rate of Paracetamol as a Function of Solvent Composition, Ind Eng Chem Res, 52 (2012) 4731-4740.

[16] S.D. Finnie, R.I. Ristic, J.N. Sherwood, A.M. Zikic, Morphological and Growth Rate Distributions of Small Self-nucleated Paracetamol Crystals Grown from Pure Aqueous Solutions, Journal of Crystal Growth, 207 (1999) 308-318.

[17] T.T.H. Nguyen, R.B. Hammond, K.J. Roberts, I. Marziano, G. Nichols, Precision Measurement of the Growth Rate and Mechanism of Ibuprofen {001} and {011} as a Function of Crystallisation Environment, Crystengcomm, 16 (2014) 4568-4586.

[18] R. Boistelle, A. Doussoulin, Spiral Growth Mechanisms of (110) Faces of Octacosane Crystals in Solution, Journal of Crystal Growth, 33 (1976) 335-352.

[19] D.H.M. Beiny, J.W. Mullin, K. Lewtas, Crystallisation of n-Dotriacontane from Hydrocarbon Solution with Polymeric Additives, Journal of Crystal Growth, 102 (1990) 801-806.

[20] W. Beckmann, R. Boistelle, Growth Kinetics of the (110) Face of Stearic Acid Growing from Butanone Solutions_Pure Solutions and in the Presence of an Emulsifier, Journal of Crystal Growth, 72 (1985) 621-630.

[21] W. Beckmann, Growth Kinetics of the (001) and (110) Faces of the B Modification of Stearic Acid Growing from n-Alkanes Journal of Crystal Growth, 79 (1986) 797-800.

[22] H. Jiang, Molecular-Scale Effects of Additives on the Nucleation, Growth and Crystal Properties of Long-Chain Alkyl Methyl Esters, PhD thesis, University of Leeds (2012).

[23] K. Sangwal, Additives and crystallization processes : from fundamentals to applications, Wiley, Chichester, 2007.

[24] H.E. Lundagermadsen, R. Boistelle, Growth-Kinetics of the (001) Faces of Hexatriacontane ($C_{36}H_{74}$) in Solution, Journal of Crystal Growth, 46 (1979) 681-690.

[25] S. Aleby, E. von Sydow, The Crystal Structure of Methyl Stearate, Acta Crystallographica, 13 (1960) 487.

[26] C.H. MacGillavry, M. Wolthuis-Spuy, Crystal structure of an Orthorhombic Modification of Methyl Stearate, Acta Crystallographica B26 (1970) 645-648.

[27] W. Beckmann, R. Boistelle, Growth-Kinetics of the (110) Face of Stearic-Acid Growing from Butanone Solutions Pure Solutions and in the Presence of an Emulsifier, Journal of Crystal Growth, 72 (1985) 621-630.

[28] J.W. Mullin, Crystallization, 4th ed., Butterworth-Heinemann, Oxford, 2001.

[29] W. Beckmann, S. Kammer, J. Meier, R. Boistelle, Growth-Kinetics of the (110) Face of the B-Polymorphs and C-Polymorphs of Stearic-Acid Growing from Octanone-2 Solutions, Journal of Crystal Growth, 74 (1986) 326-330.

9. Conclusions and Suggestions for Future Work

Summary: This chapters presents the outcomes from this work, compares them with the aims and objectives of this thesis and makes suggestion for future development of this work

This chapter seeks to: summarise the outputs of the thesis, confront these outputs with its aims and objectives and lay out the bases for future work. The chapter is sub-divided into three sections presenting the related information to each of these aspects.

9.1. Conclusions of this work

This work has examined the influence of solution environment on the solubility, phase separation and crystallisation kinetics of model biodiesel solutions systems including two saturated esters as solutes (methyl palmitate and stearate) crystallising from five representative compounds of diesel fuels (n-dodecane, kerosene, toluene, n-heptane and methyl-cyclohexane) and three representative unsaturated esters (methyl oleate, linoleate and linolenate). This work allowed:

- The calculation of the system's solubilities and activities together with their metastable zone widths (MSZW).
- The development of a new methodology to study nucleation from polythermal data [1] which enables the characterisation of the nucleation mechanism and nucleation kinetics. The methodology was applied to all the solutions studied delivering nucleation parameters such as interfacial tension and critical radius. Nucleation rates were also obtained for methyl stearate crystallising from n-dodecane, kerosene and toluene.
- The development of an experimental methodology to characterise the crystal morphology of plate-like crystals [2] which are representative of long-chain hydrocarbons and methyl esters. This methodology was applied to characterise the crystal morphology of n-docosane and methyl stearate crystals.
- The measurement of growth rates as a function of supersaturation for specific faces of n-docosane crystals growing from n-dodecane and methyl stearate crystals growing from n-dodecane, kerosene and toluene. Using these data the assessment of the crystal growth kinetics was carried out using a diffusional growth model also derived as part of this work.

9.1.1. Methodology for the determination of nucleation mechanism and kinetics from polythermal data

A methodology to assess nucleation kinetics and mechanism based on the KBHR approach was developed. This was done through the detailed analysis of polythermal experimental data collected for methyl stearate (C18:0) crystallising from kerosene. The methodology is of general application to the analysis of any single-solute solution system and showed to be a useful tool to get a physical insight of a nucleation process out of practical experimental measurements.

9.1.2. Solubility of model methyl esters as a function of solution environment

The assessment of the solubility of methyl palmitate (C16:0) and stearate (C18:0) in representative solvent compounds delivered parameters such as: enthalpy and entropies of dissolution and mixing as well as models for the dependence of activity coefficients on temperature. The analysis of solution ideality showed less than ideal behaviour as activity coefficients are all higher than 1. This indicating that there is a tendency for solute-solute interactions to be favoured over solute-solvent ones.

The solubility of saturated methyl esters in solvent compounds representative of diesel fuels mixtures showed to be very dependent on the ability of the solvent molecules to solvate solute ones. This is evidenced in the higher solubility of saturated esters in solvents whose molecules are compact such as in the case of toluene and methyl-cyclohexane. However, a slightly higher polarity in the case of toluene increased the solubility of the saturated esters significantly, as evidenced from the lowest enthalpies of dissolutions and mixing among all solutions studied for both methyl palmitate and stearate. In the case of unsaturated esters solvents, where all the molecules have similar polarity and size to that of the solutes, the solubility decreases with increase in double bonds in the solvents molecules. This is attributed to the higher presence of cis- and tran- isomers in the solvent with increase in unsaturation, which will cause the available area for chemical interactions with the solute to decrease.

The analysis of solutions ideality also provided the liquid phase activity models that could be used in the development of a solid-liquid equilibrium model as given by equation (2.39) for the prediction of cooling fractionation of biodiesel and diesel/biodiesel solutions.

9.1.3. Nucleation of model methyl esters as a function of solution environment

The analysis of methyl palmitate (C16:0) and stearate (C18:0) based on the KBHR approach showed that nucleation of saturated methyl esters is mainly progressive in nature strongly hindered by the interfacial tension when crystallisation occurs from diesel type solvents. Nucleation from unsaturated type solvents, although also mainly progressive in nature seems to be much more kinetically controlled.

Interestingly the solutions in which the kinetics is more rate limiting are those in which the solvent is constituted by a mixtures of different molecules such as in the case of kerosene and mixtures of unsaturated methyl esters. This could be attributed to the variability of chemical interactions, due to the differences in the size and shape of molecules present within the solvent, which would hinder nucleation as a result of lower solute diffusivities.

Regardless of these mechanistic differences the interfacial tensions values obtained within all solutions are of the same order of magnitude and range between 0.68 and 2.18 and 0.77 and 1.74 $\left(\frac{mJ}{m^2}\right)$ for saturated esters crystallising from diesel type solvents and unsaturated esters type solvents respectively.

In depth analysis of methyl stearate crystallising from n-dodecane, kerosene and toluene solvents delivered nucleation rates ranging between 2.94 x 10^{14} and 8.94 x 10^{16} $\frac{nuclei}{ml\ sec}$, with the highest rates predicted for methyl stearate crystallising from kerosene solutions where nucleation is likely to be more kinetically hindered.

9.1.4. Crystal morphology and growth kinetics of representative n-alkanes and methyl esters

9.1.4.1. Crystal morphology

A method was developed for the characterisation of the morphology of asymmetrical crystals such as those observed for n-alkanes and methyl esters. The application of this method, based on a combined BFDH and zone axis methodology, allowed characterising the morphology of n-docosane and methyl stearate crystals.

The morphological observations of n-docosane crystals changed with increasing in supersaturation, evolving from a habit consistent with a triclinic crystal system to a habit more representative of an orthorhombic structure. The morphological analysis delivered Miller indices (001), (112), (102), (010), and (1-33) or (130) based on the expected triclinic crystal structure, for the two habits observed at the two lower supersaturations studied.

Morphological observation of methyl stearate crystals were the same in all solvents (n-dodecane, kerosene and toluene) except for the lowest supersaturation levels in kerosene in which there was a less symmetrical habit. The indexation of the latter allowed for the identification of the crystal system that would predict the most likely morphology - the monoclinic C_2 crystal system. This analysis delivers the Miller indices (110) and (1-10) for the crystal habit observed in the three solvents and (110), (1-10), (-1-10), (-240) (-3-10) for the habit observed in kerosene at lower supersaturations.

9.1.4.2. Growth kinetics

The growth rates for n-docosane crystals growing from n-dodecane solvent were found to be 0.51 – 9.85 $\frac{\mu m}{s}$ for a supersaturation (σ) range between 0.01 – 0.05. The kinetic data was consistent with the BFC interfacial growth mechanism.

Measurements of the growth rate for the indexed (110) and (1-10) faces of methyl esters crystals as a function of solvent were within the same range of magnitude but for significantly lower values of supersaturation in toluene solvent, which were lower than 8%. The growth rates measured in toluene are close in magnitude to those observed in kerosene, ranging from 0.02 to 0.37 $\mu m/s$ and are around half those observed in n-dodecane solutions, in which these values range from 0.09 to 1.13 $\mu m/s$. Measurements of the growth for the (110) face in the case of kerosene solutions, are much lower in magnitude compared to those for the (1-10) face, ranging from 0.02 to 0.15 $\mu m/s$, which gives these crystals an elongated lozenge shape. Similar growth rates values were observed between the (110) face and the (1-10) face for crystals growing from n-dodecane and toluene solvents. The tendency of the growth rates dependence on σ was consistent with the BCF growth mechanism in n-dodecane, the B&S mechanism in kerosene and indicated the presence of a relative large number of kink sites in toluene solvent.

9.1.5. Combined assessment of methyl stearate crystallisation as a function of solution environment

Table. 9.1. is provided as an illustration of the comprehensive assessment that was carried out for methyl stearate crystallisation, using the methodologies developed within this research. In this case conclusions are drawn up for methyl stearate crystallising from n-dodecane, kerosene and toluene solvents. This assessment includes: solubility, nucleation and crystal growth kinetics as well as crystals´morphological analysis thus providing an overall insight on how the thermodynamics, the kinetics of the process and the chemistry of these solutions are influencing the crystallisation of methyl stearate as a function of solution environment.

Table 9.1 Summary of parameters obtained through the combined assessment of solubility, morphology and nucleation and crystal growth kinetics of methyl stearate in three different solvents

		n-Dodecane		Kerosene		Toluene	
Solubility	Solubility	Lowest		Intermediate		Higher	
	Υ (20℃)	2.01		1.85		1.14	
	$\Delta H_{diss}\left(\frac{KJ}{mol}\right)$	63.55		69.81		59.84	
	$\Delta S_{diss}\left(\frac{KJ}{mol\,K}\right)$	0.20		0.22		0.19	
	$\Delta H_{mix}\left(\frac{KJ}{mol}\right)$	9.61		15.87		5.90	
	$\Delta S_{mix}\left(\frac{KJ}{mol\,K}\right)$	0.03		0.05		0.02	
Conclusion	All systems behave less than ideal as activities are higher than one. However, higher values in n-dodecane followed by kerosene solutions indicate either solute-solute or solvent-solvent interactions are favoured in these systems. Solute-solvent interactions are similar to those of solute-solute in toluene solutions as activities close to 1, this is further supported by the lowest enthalpy of mixing. The highest values of both enthalpy of dissolution and mixing in kerosene solution evidence strong dependence of activities on temperature.						
Nucleation	Average slope $\ln q$ vs $\ln u_c$	3.98		4.18		6.05	
	Mechanism	PN		PN		PN	
	Range σ	0.32-0.44		0.50-0.66		0.49-0.58	
	Range $\gamma_{eff}\left(\frac{mJ}{m^2}\right)$	0.94-1.55		1.21-1.52		1.18-1.88	
	Range r^*	0.84-1.00		0.74-0.94		0.73-1.17	
	Average N_{det}	7.73 x 10^{17}		2.04 x 10^{19}		3.31 x 10^{17}	
	Average $J\left(\frac{nuclei}{ml\,s}\right)$	2.94 x 10^{15}		6.47 x 10^{16}		1.07 x 10^{15}	
Conclusion	Relatively higher values of interfacial tensions in toluene seem to hinder nucleation in this solvent. Although interfacial tension values are close in n-dodecane and kerosene solutions, nucleation in the former is one order of magnitude lower. This could indicate less available nucleation sites in these solutions, due to the low solubility of methyl stearate in n-dodecane.						
Morphology	The morphology observed in all cases was the same except for the lowest supersaturation levels in kerosene in which there was a less symmetrical habit. The indexation of the latter allowed for the identification of the crystal system that would predict the most likely morphology - the monoclinic C_2 crystal system.						
Crystal growth	Range σ	0.30-0.39		0.45-0.52		0.04-0.08	
	$\Delta C = C - C_e\left(\frac{mol}{m^3}\right)$	174-215		233-259		34-61	
	Average $C_e\left(\frac{mol}{m^3}\right)$	632.86		581.33		1053.16	
		(110)	(1-10)	(110)	(1-10)	(110)	(1-10)
	$R\left(\frac{\mu m}{sec}\right)$	0.09-1.13	0.11-1.05	0.02-0.15	0.01-0.35	0.02-0.37	0.03-0.34
	Growth mechanism	BCF	BCF	B&S	B&S	Diffusion controlled	Diffusion controlled
	Resistance mass transfer bulk	0.900 x 10^7	0.900 x 10^7	0.247 x 10^{12}	0.243 x 10^{12}	0.602 x 10^{11}	0.602 x 10^{11}
	Resistance mass transfer interface	0.195 x 10^{12}	0.208 x 10^{12}	0.153 x 10^{12}	0.133 x 10^3	0.305 x 10^{11}	0.274 x 10^{11}
	σ_{crit}	0.28	0.27	0.44	0.44	0.04	0.04
Conclusions	Growth is favoured in toluene solvent where similar range of growth rates were obtained for significantly lower levels of supersaturation. While growth in this case can occur at σ levels above 4%, σ levels above 27 and 44% are required for growth to proceed in n-dodecane and kerosene solvent respectively. The analysis of $G(\sigma)$ data revealed that growth is limited by transfer of growth units at the interface in n-dodecane solvent and within the bulk of the solution in kerosene and toluene solvents. Similarly, it suggested that integration of growth units to the crystal surface would proceed via a BCF and a B&S mechanism for growth from n-dodecane and kerosene solvents respectively. Integration of growth units for growth from toluene would be facilitated by the presence of sufficient kinks sites.						

9.2. Review of aims and objectives

Addressing objectives 1 and 4 of the thesis, suitable methodologies were developed to study the crystals´ morphology, nucleation and crystals growth kinetics of long chain molecules such as methyl esters and n-alkanes.

- The methodology to study the nucleation kinetics comprises: the detailed description of a novel kinetic model derivation, together with the development of a suitable experimental method for the collection of related polythermal data.

- Similarly, the methodology to study growth kinetics incorporates the derivation of a growth kinetics model, which includes the effect in series of the diffusional process within the bulk of the solution, and that at the crystal/solution interface.

- Given the lack of detailed structural information for these type of compounds, a useful method for the indexation of specific (hkl) faces was also developed.

Addressing objective 2 and 3, the solution state and nucleation kinetics of methyl palmitate and stearate were studied as a function of solution composition, employing as solvents five different representative compounds of diesel fuels and three representative unsaturated methyl esters. For each of the solutions analysed four different concentrations were used.

Addressing the first four objectives, a comprehensive assessment for methyl stearate crystallisation from three different solvents: n-dodecane, kerosene and toluene was also delivered. This included the analysis of the solution state, crystal morphology and nucleation and growth kinetics. The collection and analysis of these data was done through the application of the methodologies developed through the research.

Although relevant information on the thermodynamic, kinetic and chemical nature of crystallisation processes of methyl esters was presented, yet some work still to be done for the fulfilment of the objectives. This includes:

- Analysis of polythermal experimental data for representative n-alkanes in both diesel type and unsaturated esters solvents to examine the influence of solution environment on the solubility and nucleation kinetics of these systems.
- Collection and analysis of growth rates data for representative n-alkanes solutions.
- The development of a methodology for predicting the fractionation of practical fuel and biofuel systems.

9.3. Suggestions for future work

The projects on the crystallisation of fuels that have been carried out within the IPSE are the results of a long term partnership with Exxon mobile and later Infineum UK. This research has aimed to provide the fundamental science basis which will have direct utility in the formulation of mixed fuel systems & how these are impacted by the addition of cold-flow additives. The work presented in this thesis has made a contribution to this general goal by studying the solution state, nucleation kinetics, crystal´s morphology and growth kinetics of model methyl esters as a function of solution environment. However, within the framework of this general objective future work should be carried out to both fulfil the objectives of this work and to further extend the application of the methodologies here presented to more complex practical systems.

In line with this to fulfil the objectives of this thesis future work should address:

1. The automation of data collection and imaging analysis of the experimental methodology used to study crystals' growth kinetics and morphology. The way in which this analysis is currently carried out is time-consuming and thus does not allow the collection of experimental data for simultaneous

systems. This could be carried out by building a new microscopy platform using simultaneous measurements on eight growth cells units with the units being accurately displaced in two dimensions. A tool for the measurement of the growth of the (001) face of plate-like crystals should be also integrated to this systems. Given that the growth in the direction perpendicular to this face is very low this could be done through interferometry.

2. The development of a methodology to study fractionation in biodiesel and biodiesel/diesel fuel systems based on the solid-liquid equilibrium model given by equation (2.39). This work could be carried out in three stages:

   2.1. Improvement of a methodology previously developed within the group for the prediction of biodiesel fuels cooling fractionation [3].

   2.2. Develop of a methodology for the prediction of biodiesel/diesel fuel mixtures cooling fractionation. This could achieved via the following:

   - The definition of a suitable activity model for these kind of mixtures, which should include the calculation of solid phase activity coefficients for n-alkanes with carbon chain lengths ranging between ten and thirty four as well as for methyl palmitate and stearate.

   - The definition of a gas chromatography method that allows the analysis of the compositions of solutions containing both n-alkanes and methyl esters.

In the long term the research on this area could be integrated through an approach with specific inter-related work programs (WPs) as given in Fig. 9.1.

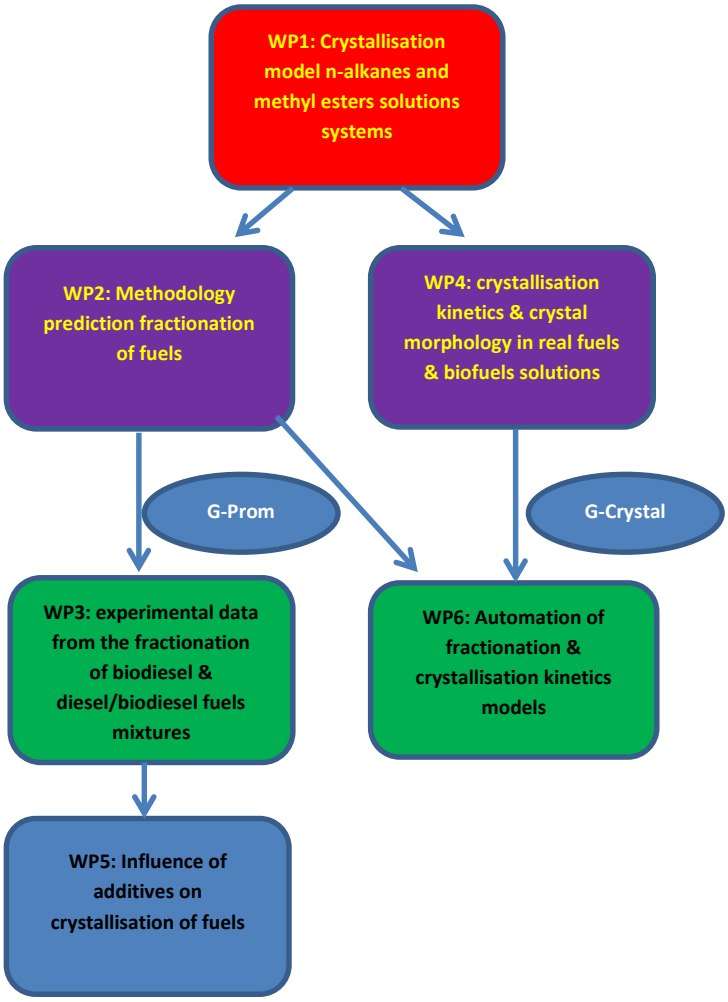

Figure 9.1 Flow chart for future work

WP1 would extend the collection of experimental data from model fuel systems to serve as the foundation for the development of the methodologies addressed in WPs 2 and 4. WP3 would involve the collection of experimental data for the validation of the fractionation model in WP2. WPs1, 2, 3 and 4 would provide the foundations for the experimental analysis in WP5 and the development of informatics tools addressed in WP6.

Work programme 1: n-alkanes and methyl esters crystallisation within representative compounds present in diesel mixtures and unsaturated methyl esters. Using the tools developed in this research, as a precursor to examining mixed diesel/biodiesel fuels mixtures, additional representative solutions systems of n-alkanes and methyl esters could be characterised with reference to its solubility, metastability, solution´s

ideality and nucleation and growth kinetics. The data obtained at this stage would serve as input for the development of a solubility model as specified in work program 2 as well as for the development of a methodology to assess nucleation and crystal growth kinetics in real fuels and biofuels solutions as specified in work program 4.

Work programme 2: Methodology for prediction of fractionation of fuels. In line with objectives 5 and 6 of this thesis a methodology could be developed for the characterisation of changes to the solution phase composition fuels during the crystallisation process. This would provide a valuable resource for solubility prediction in complex multi-component systems. The validation of the thermodynamic model could be done adapting an experimental methodology presented for the assessment of diesel fuels fractionation based on phase separation technologies and a calibrated Gas Chromatography (GC) analysis. The development of different GC methods will be needed for the analysis of biodiesel fuel and biodiesel/diesel fuel mixtures due to the differences in their molecular composition.

Work programme 3: Experimental data for the crystallisation of biodiesel fuel and diesel/biodiesel mixtures. On the basis of the underlying understanding developed above, the fractionation of biodiesel fuel and their mixture with diesel fuels could be examined. In the former case the three main types of biodiesel rapeseed methyl ester (RME), soya bean methyl ester (SOME) and palm methyl ester (PME) could be assessed. In the latter case the influence of the relative fraction of the two components (5/95 and 10/90 biodiesel/diesel ratios) could be analysed. This work would help to understand and quantify the molecular composition of the crystallised product and solution phases in relation to the feedstock.

Work program 4: Crystallisation kinetics and crystal morphology. The two previously developed methodologies for the assessment of nucleation and crystal growth kinetics of single solute solution´s systems could be further extend for the assessment of crystallisation in multicomponent systems. This work would aim understanding the inter-relationship between fuel composition, crystallisation kinetics and morphology of the solid phase formed.

Work programme 5: Influence of additives on crystallisation of fuels. Using the knowledge obtained previously, the crystallisation behaviour of biodiesel and diesel/biodiesel mixtures could be characterised benchmarking any changes to the crystallisation of the fuels following cold- flow improvers addition.

Work programme 6 (WP6): Automations of the prediction of fractionation behaviour and crystallisation kinetics. Drawing on the previous outcomes a G-prom based model could be developed for the dynamic prediction of the fractionation of fuels blends. This informatics tool would allow assessing the composition of the different phases after crystallisation as a function of temperature, for different initial ratios of bio-diesel/diesel fuel mixtures.

References

[1] D. Camacho, A. Borissova, R. Hammond, D. Kashchiev, K. Roberts, K. Lewtas, I. More, Nucleation mechanism and kinetics from the analysis of polythermal crystallisation data: methyl stearate from kerosene solutions, Crystengcomm, 16 (2014) 974-991.

[2] D.M. Camacho, K.J. Roberts, K. Lewtas, I. More, The crystal morphology and growth rates of triclinic n-docosane crystallising from n-dodecane solutions, Journal of Crystal Growth, 416 (2015) 47-56.

[3] Q. Hussain, Crystallisation of long chain methyl esters in relation to their cold flow behaviour, in: School of Process Environmental and Materials Engineering, University of Leeds, Leeds, 2012.

Appendix A

Additional and more detailed materials are provided as a supplement to Chapter 5. It includes:

1. Description of the Kashchiev-Borissova-Hammond-Roberts ($KBHR$) approach [1, 2] used for the analyses of solution crystallisation kinetics.
2. Sensitivity analysis of the experimental methodology for the collection of sufficient and reliable polythermal data.
3. Derivation of an expression allowing determination of a system nucleation mechanism from previous Nyvlt-type data analysis.

1. Detailed derivation of equations (5.9) and (5.20) in Chaper 5 from the Kolmogorov-Johnson-Mehl-Avrami ($KJMA$) expression

A detailed derivation of basic equations obtained within the framework of the Kashchiev-Borissova-Hammond-Roberts $KBHR$ approach [1, 2] is presented below. Using the classical nucleation theory and the $KJMA$ equation, expressions for the dependence of the critical undercooling on the cooling rate are derived for the cases of progressive nucleation (PN) and instantaneous nucleation (IN).

In solution crystallisation, the phase transformation kinetics can be described by the $KJMA$ equation [3]. The central idea of this equation is to focus on the increment in the fraction α of crystallised volume and to relate this increment to the current actual value of α. The fraction of crystallised volume is defined as

$$\alpha = \frac{V_c}{V} \tag{1}$$

where V_c is the total crystallised volume and V the solution volume.

Obtaining the dependence of αon time t from the $KJMA$ equation can be a complicated mathematical problem, especially when the solution supersaturation

and/or the crystal nucleation and/or growth rates vary with time. The $KJMA$ theory assumes that crystallisation occurs by nucleation of material points at a rate $J(t)$ which then only grow irreversibly in radial direction with growth rate $G(t)$ [3]. Under this assumption α can be easily expressed in terms of $J(t)$ and $G(t)$at the early stage of crystallisation when there are no contacts between the growing crystallites. The resulting $KJMA$ formula reveals how α is controlled by two basic kinetic parameters of the process of crystallisation, the crystallite nucleation and growth rates [1-3].

1.1. Progressive nucleation

In the case of PN, the $KJMA$ formula can be represented as [2, 3]

$$\alpha(t) = k_v \int_0^t J(t') \left[\int_0^{t-t'} G(t'')dt'' \right]^d dt' \quad for\ \alpha < 0.1 \tag{2}$$

where t' and t'' are time integration variables, $d = 1,2,3$ is the dimensionality of crystallite growth (e.g., 3 for spheres or cubes, 2 for disks or plates, 1 for needles), and k_v (m^{3-d}) is the crystallite growth shape factor, e.g. $\frac{4\pi}{3}$ for spheres, 8 for cubes, πH_0 for disks, $4H_0$ for square plates, $2A_0$ for needles (H_0 is the fixed disk or plate thickness, A_0 is the fixed needle cross-sectional area).

When steady cooling of the solution starts at $t = 0$ from the equilibrium temperature T_e, the relative undercooling u is defined as [2]

$$u = \frac{\Delta T}{T_e} = \frac{T - T_e}{T_e} \tag{3}$$

where T is the solution temperature, and ΔT is the undercooling.

From the classical theory of three dimensional $(3D)$ nucleation, the rate of crystallite nucleation can be expressed in terms of the relative undercooling as [2]

$$J(t) = k_J e^{\frac{-b}{(1-u)u^2}} \tag{4}$$

where k_J is the nucleation rate constant and the dimensionless thermodynamic parameter b is given by

$$b = \frac{k_n v_o^2 {\gamma_{eff}}^3}{kT_e\lambda^2} \tag{5}$$

Here k_n is the nucleus numerical shape factor e.g. $(16\pi/3$ for spherical nuclei and 32 for cubic nuclei), v_o is the volume occupied by a solute molecule in the crystal, γ_{eff} is the effective interfacial tension of the crystal nucleus, λ is the molecular latent heat of crystallisation, and k is the Boltzmann constant

The radial crystallite growth rate $G(t)$ can also be expressed in terms of undercooling [2]:

$$G(t) = m\left(\frac{T_e}{q}\right)^{m-1} k_G^m \left[1 - e^{\frac{-au}{(1-u)}}\right]^{nm} u^{m-1} \tag{6}$$

Here q is the cooling rate, k_G is the crystal growth rate constant, and n and $m > 0$ are the crystallite growth exponents ($n = 1$ for growth mediated by diffusion or interface transfer of solute, $n = 2$ for growth controlled by the presence of screw dislocations in the crystallite, and m ranges between ½ and 1 [2-4]. For instance, $m = 1/2$ for growth controlled by undisturbed diffusion of solute, and $m = 1$ for growth by diffusion of solute through a stagnant layer around the crystal and for normal or spiral growth limited by transfer of solute across the crystal/solution interface. At $m = 1$ the crystallite growth rate is time-independent [2-4]. As to a, it is the dimensionless molecular latent heat of crystallisation and is given by

$$a = \frac{\lambda}{kT_e} \tag{7}$$

Inserting equation (4) and (6) in equation (2) and defining $t' = \left(\frac{T_e}{q}\right)x$ and $t'' = \left(\frac{T_e}{q}\right)z$ allows expressing α in terms of undercooling [2]:

$$\alpha(u) = C_{m,d}\int_0^u e^{\frac{-b}{(1-x)x^2}}\left(\int_0^{u-x} z^{m-1}\left[1 - e^{\frac{-az}{(1-z)}}\right]^{nm} dz\right)^d dx \tag{8}$$

where the dimensionless parameter $C_{m,d}$ is given by

$$C_{m,d} = k_v m^d k_J k_G^{md}\left(\frac{T_e}{q}\right)^{md+1} \tag{9}$$

The integrals in equation (8) can be performed analytically [5] if the analysis is restricted to small enough values of u satisfying the inequalities

$$u < 0.1, au < 1 \tag{10}$$

then

$$1 - u \approx 1 \text{ and } 1 - e^{\frac{-au}{(1-u)}} \approx au \tag{11}$$

and equation (8) becomes [2]

$$\alpha(u) = C_{m,d}a^{nmd}\int_0^u e^{\frac{-b}{x^2}}\left[\int_0^{u-x} z^{(n+1)m-1}dz\right]^d dx \tag{12}$$

which, after performing the inner integral, takes the form [2]

$$\alpha(u) = C_{m,d}\left[\frac{a^{nm}}{(n+1)m}\right]^{d}\int_{0}^{u}(u-x)^{(n+1)md}e^{\frac{-b}{x^2}}dx \tag{13}$$

It has been shown [2, 5] that the integration in equation (13) can be carried out analytically for any u value only when $(n+1)md = 0,1,2,3\ldots$ .Then $\alpha(u)$ from equation (13) can be expressed exactly but n a rather complicated way by employing special mathematical functions [5]. However in the limit of sufficiently small u values satisfying the condition

$$u < \left(\frac{2b}{3}\right)^{1/2} \tag{14}$$

a series expansion of the special functions allows simplifying the exact complicated $\alpha(u)$ dependence and presenting it in the following approximate form [2]:

$$\alpha(u) = K_{m,d}\left(\frac{u^3}{2b}\right)^{(n+1)md+1}e^{\frac{-b}{u^2}} \tag{15}$$

Furthermore, it was found [2] that the accuracy of this $\alpha(u)$ dependence is higher when the exponential term in it is replaced by $e^{\frac{-b}{(1-u)u^2}}$. With this replacement, equation (15) yields the basic approximate $\alpha(u)$formula of the $KBHR$ theory [2]:

$$\alpha(u) = K_{m,d}\left(\frac{u^3}{2b}\right)^{(n+1)md+1}e^{\frac{-b}{(1-u)u^2}} \tag{16}$$

Here the dimensionless parameter $K_{m,d}$ is given by

$$K_{m,d} = \frac{\Gamma[(n+1)md+1]}{(n+1)^d}k_v a^{nmd}k_J k_G^{md}\left(\frac{T_e}{q}\right)^{md+1} \tag{17}$$

and Γ is the complete gamma function .

Upon replacing α by the number N of nucleated crystallites and setting $d = 0$, equation (16) leads to the approximate $N(u)$formula of the $KBHR$ theory [2]

$$N(u) = K_N \left(\frac{u^3}{2b}\right) e^{\left[\frac{-b}{(1-u)u^2}\right]} \tag{18}$$

where the factor K_N equals $K_{m,o}$ from equation (17) and, accordingly, is given by

$$K_N = \frac{V k_J T_e}{q} \tag{19}$$

Plotting the above $\alpha(u)$ and $N(u)$ dependence shows [2] that α and N are monotonically increasing functions of u, with a sharp rise at a certain u value that corresponds to the relative critical undercooling for crystallisation u_c defined as [2]

$$u_c = \frac{\Delta T_c}{T_e} \tag{20}$$

where

$$\Delta T_c = T_e - T_c \tag{21}$$

and T_c is the crystallisation temperature

For $u < u_c$ crystallites are so small and/or few that α and/or N cannot be detected, i.e. they are below the detection limit α_{det}, N_{det}, respectively . For $u > u_c$ the solution will contain sufficiently big and/or numerous crystallites so that α and/or N will be detected: $\alpha > \alpha_{det}$ and $N > N_{det}$. This means that u_c is the maximum relative undercooling that a solution can sustain without detectable crystallisation. In other words, u_c represents the solution metastability limit in terms of undercooling [1, 2]. This limit, however, depends on a number of parameters among which a

prominent one is the solution cooling rate q. With the help of equations (16) and (18),the $u_c(q)$ dependence can be determined.

Expressing equation (18) it in terms of u_c gives

$$N(u_c) = N_{det} = \frac{Vk_J T_e}{q}\left(\frac{{u_c}^3}{2b}\right) e^{\left[\frac{-b}{(1-u_c){u_c}^2}\right]} \tag{22}$$

Upon taking logarithms of both sides of equation (22) and rearranging, a model expression that relates the relative critical undercooling u_c with the cooling rate q is obtained [2]:

$$ln\ q = ln\ q_0 + a_1\ ln\ u_c - \frac{a_2}{(1-u_c){u_c}^2} \tag{23}$$

where the parameters q_0 , a_1 and a_2 are defined by

$$a_1 = 3 \tag{24}$$

$$a_2 = b \tag{25}$$

$$q_0 = \frac{Vk_J T_e}{N_{det}\ 2b} \tag{26}$$

Similarly when equation (23) is derived by means of α from equation (16), the parameters q_0, a_1 and a_2 are defined by [2]

$$a_1 = 3 + \frac{3nmd}{md+1} \tag{27}$$

$$a_2 = \frac{b}{md+1} \tag{28}$$

$$q_0 = T_e \left\{ \frac{\Gamma[(n+1)md+1] k_v a^{nmd} k_J k_G^{md}}{(n+1)^d \, (2b)^{(n+1)md+1} \alpha_{det}} \right\}^{\frac{1}{(md+1)}} \tag{29}$$

The parameters $\ln q_0$, a_1 and a_2 have a clear physical meaning: a_1 is related solely with the crystallites growth law as its values is determined by the growth dimensionality d and exponents n and m, a_2 is a fraction of or is equal to the thermodynamic nucleation parameter b and q_0 is controlled by parameters of both the nucleation and the growth of the crystallites.

It is important to bring attention to the fact that although equation (16) is only an approximation to equation (8), applicable for u values restricted by inequalities (10) and (14), it predicts u_c values quite close to those resulting from equation (8). As visualised in Fig. 1 presented below [2] the error in u_c determined from the approximate equation (16) for $\alpha(u)$ can be estimated by comparing the numerically obtained u_c from equation (8) and the calculated approximate u_c from equation (16) or, equivalently, from equation (23). From Fig. 1[2] we read that for $n = 1$ and 2, while the exact u_c values equal 0.084 and 0.094, the approximate u_c values equal 0.083 and 0.091, which corresponds to errors of 2% and 3% respectively. Thus, inequalities (10) and (14) are appropriate for ensuring sufficient accuracy of the u_c values from the approximate equation (23). Fig. 2 [2] illustrates the good accuracy of this equation in a range of q values.

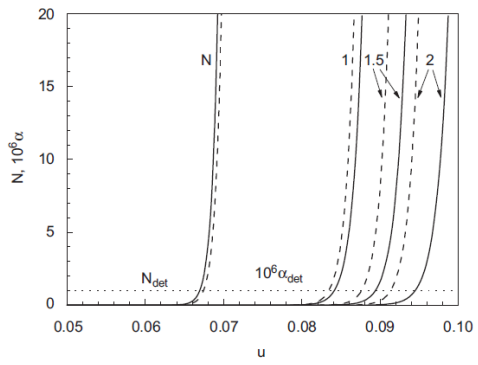

Figure 1. Dependence of total crystalline number *N* and volume fraction *α* on relative undercooling at a fixed cooling rate: solid lines numerically from eq. (8), dashed lines the approximate eq. (16) and (18). 1,

1.5 and 2 refer to the volume fraction at n =1, 1.5 and 2 respectively. "Reproduced by consent of the Journal of Crystal growth from D. Kashchiev, A. Borissova, R.B. Hammond, K.J. Roberts, Effect of cooling rate on the critical undercooling for crystallization, Journal of Crystal Growth, 312 (2010) 698-704"

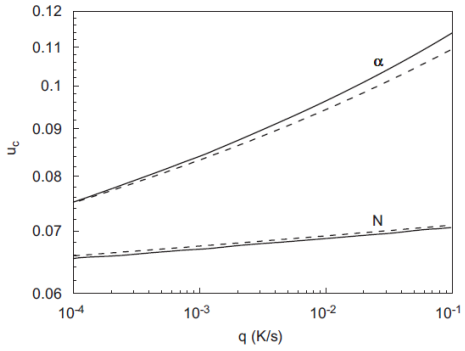

Figure 2. $log - log$ dependence of relative critical undercooling on cooling rate: solid lines –numerically from eq. (8) and, dashed lines the approximate eq.(23). "Reproduced by consent of the Journal of Crystal growth from D. Kashchiev, A. Borissova, R.B. Hammond, K.J. Roberts, Effect of cooling rate on the critical undercooling for crystallization, Journal of Crystal Growth, 312 (2010) 698-704"

1.2. Instantaneous nucleation

In the case of IN, a similar derivation was done [1] but by taking into account that now all crystal nuclei with a concentration C_o appear at once at the moment t_o and after that they only grow. An example of IN is heterogeneous nucleation (HEN) on strongly nucleation-active sites. These sites are not active during the period from $t = 0$ to $t = t_o$, because then the undercooling is not sufficient for HEN to take place on them. At $t = t_o$ all sites are suddenly occupied by the nucleated crystallites so that for $t > t_o$ further HEN on them is impossible despite that the solution is being further cooled down. Thus, quite often C_o can be merely equal to the concentration of nucleation-active sites in the system.

As in the IN case the $\alpha(u)$ dependence is controlled solely by the crystallite growth rate, it can be expressed as [1]

$$\alpha(t) = k_v C_o \left[\int_{t_0}^{t} G(t')\, dt'\right]^d \tag{30}$$

Using equation (6) and setting $t^{'} = \frac{T_e}{q}x$, an expression for α in terms of u can be found [1]

$$\alpha(u) = C_{m,d}\left(\int_{u_0}^{u} x^{m-1}\left[1 - e^{\frac{-ax}{(1-x)}}\right]^{nm} dx\right)^{d} \tag{31}$$

where the dimensionless parameter $C_{m,d}$ is given by

$$C_{m,d} = k_v m^d C_o \left(\frac{k_G T_e}{q}\right)^{md} \tag{32}$$

For small enough undercooling satisfying inequalities (10), the approximations (11) can be used to simplify and perform the integral in equation (31), the result being [1]

$$\alpha\,(u) = K_{m,d}\left[u^{(n+1)m} - u_o^{(n+1)m}\right]^{d} \tag{33}$$

In this expression u_o is the relative undercooling at the time t_o and is given by

$$u_o = \frac{\Delta T_o}{T_e} = \frac{q t_0}{T_e} \tag{34}$$

Here ΔT_o is defined by

$$\Delta T_0 = T_e - T_0 \tag{35}$$

where T_o is the solution temperature at the time t_o. As to the parameter $K_{m,d}$ in equation (33), it is given by

$$K_{m,d} = \frac{k_v C_o \left(\frac{a^n k_G T_e}{q}\right)^{md}}{(n+1)^d} \tag{36}$$

Equation (33) shows that, similar to the PN case, in IN-mediated crystallisation α is a monotonically increasing function of u ,with a sharp rise at a certain value that corresponds to the relative critical undercooling u_c (see Fig. 1 of Ref. [2]).

Upon using $\alpha(u_c) = \alpha_{det}$, taking logarithms of both sides of equation (33) and rearranging, an expression can be obtained for the dependence of the relative critical undercooling on the cooling rate [1]:

$$\ln q = \ln q_0 + \left(\frac{1}{m}\right) \ln\left[u_c^{(n+1)m} - u_0^{(n+1)m}\right] \tag{37}$$

In this expression $u_0 \geq 0$, $u_c > u_o$,and the parameter q_0 is given by

$$q_o = \left[\frac{k_v C_o}{(n+1)^d \alpha_{det}}\right]^{\frac{1}{md}} a^n k_G T_e \tag{38}$$

If the undercooling at which all nuclei spontaneously appear is small enough for the inequality

$$u_o^{(n+1)m} \ll u_c^{(n+1)m} \tag{39}$$

to be satisfied, equation (37) takes the simple form

$$\ln q = \ln q_o + (n+1) \ln u_c \tag{40}$$

It should be noted that comparison of equation (40) with the equation

$$ln\, q = ln\, q_0 + \left(3 + \frac{3nmd}{md+1}\right) ln\, u_c - \frac{a_2}{(1-u_c)u_c^2} \tag{41}$$

representing equation (23) for PN reveals how different the $u_c(q)$ function can be, depending on the mechanism by which the crystallite nucleation takes place. Whereas in the case of PN, this function contains parameters characterising both the nucleation and the growth of the crystallites, in the IN case the parameters in it are only related to the crystallite growth.

1.3. The crystallite growth shape factors

The crystallite growth shape factor k_v refers to the factor that relates the volume (V_n) and the effective radius (R') of an individual crystallite: $V_n = k_v(R')^d$ [3].

From this definition, the shape factor k_v is derived below for one-dimensional growth of needles with constant cross-sectional area A_0, for two-dimensional growth of disks or square prisms with constant thickness H_0 and for $(3D)$ growth of spheres or cubes [3].

Sphere, $R' = R'$ where R' is the sphere radius:

$$V_{Sph} = \frac{4}{3}\pi R'^3 = k_v R'^3$$
$$k_v = \frac{4}{3}\pi$$

Cube, $R' = \frac{L}{2}$ where L is the cube side length:

$$V_{cube} = L^3 = k_v R'^3$$
$$(2R)^3 = k_v R'^3$$
$$k_v = 8$$

Needle, $R' = \frac{h}{2}$ where h is the needle height:

$$V_{need} = A_0 * h = k_v R'^1$$
$$A_0 2R' = k_v R'$$
$$k_v = 2A_0$$

Disk, $R' = R'$ where R' is the disk radius:

$$V_{disk} = A_{circumference} * H_0 = k_v R'^2$$
$$\pi R'^2 H_0 = k_v R'^2$$
$$k_v = \pi H_0$$

Square plate, $R' = \frac{L}{2}$ where L is the plate side length:

$$V_{Sq\ plate} = A_{square} * H_0 = k_v R'^2$$
$$L^2 H_0 = k_v R'^2$$
$$(2R')^2 H_0 = k_v R'^2$$
$$4R'^2 H_0 = k_v R'^2$$

2. Sensitivity analysis of the experimental methodology to collect reliable polythermal experimental data for the application of the $KBHR$ approach

A polythermal methodology to experimentally collect a large enough set of crystallisation temperatures T_c was presented in the paper. Due to the stochastic nature of nucleation, the use of eight different cooling rates q at each solution concentration and ten temperature cycles at each cooling rate was suggested, the latter with the aim of reducing the standard deviation SD of the crystallisation temperatures T_c. However, the collection of all these data was not an easy task, as it required running 320 temperature cycles, each of which can last an average of three hours. Thus a sensitivity analysis for the applied experimental methodology was carried out. Three additional scenarios were used with the aim of assessing the influence that reducing the number of cooling rates and/or temperature cycles will have on the parameters calculated obtained by applying the $KBHR$ approach. The results are presented in Table 1 below.

In all cases the slopes of the best linear fit to the data are higher than three, still confirming that methyl stearate crystallises from kerosene by the PN mechanism. However the values of the slopes obtained from the original methodology (fourth

scenario) can be up to 40% higher than those of the first scenario as in the case of 250 g/l solution concentration.

The higher correlation coefficients R^2 in all cases are obtained for the second scenario, in which the number of cooling rates was reduced by 50% in comparison to the original methodology (fourth scenario). On the other hand, for three of the concentrations analysed, the lowest correlation coefficients R^2 were obtained for those scenarios in which the number of crystallisation temperatures collected at each cooling rate was reduced from ten to three.

As to the errors in the parameters, in the case of the linear fitting, the lowest errors in the slopes are obtained for those scenarios where eight cooling rates were used (third and fourth scenario). In the case of the fitting according to equation (23), for the parameter $\ln q_0$ in general, the lowest errors are reported again for the third and fourth scenarios, while for the parameter $a_{2,}$ the lowest errors are for the second and fourth scenarios. It can be inferred therefore that the number of cooling rates has less influence in improving the fitting of the data by either of the two models than the number of repetitions for crystallisation temperatures at each cooling rate. On the other hand, the use of a greater number of cooling rates seems to lead to lower errors in the parameters of the models.

In general, the best results in terms of data fitting and parameters errors were obtained for the second and fourth scenarios. In the former case, however, the effort in the collection of experimental data would be significantly reduced. It is also observed that the values of effective interfacial tensions γ_{eff} increase with increasing the number of cooling rates and the number of collected crystallisation temperatures at each cooling rate. These values in the fourth scenario can be between 8% to 60% greater than those in the second scenario. However, this difference only represents an increase of up to 0.6 $\left(\frac{mJ}{m^2}\right)$ in the values of the interfacial tension. Thus, the second methodology is recommended.

Table 1. Slopes of the best linear fit of the experimental data points plotted in $ln\ q$ vs $ln\ u_c$ coordinates and corresponding correlation coefficients: values of the three free parameters $a_1, a_2\ and\ ln\ q_o$ obtained from the data fitting in $ln\ q$ vs u_c coordinates according to equation (23) and corresponding correlation coefficients. All values provided at four different concentrations 200, 250, 300 and 350 g/l and four different experimental methodologies scenarios

4 cooling rates 3 temperature cycles at each cooling rate

Concentration (g/l)	Slope best fit data straight line of $\ln u_c\ Vs \ln q$	R^2linear fitting	a_1	$a_2 = b$	$\ln q_0$	$q_0\left(\frac{K}{s}\right)$	$\gamma_{eff}\left(\frac{mJ}{m^2}\right)$	$R^2 fitting\ equation\ (23)$
200	4.49±1.28	0.86	3	0.000365±0.000302	8.80±0.83	6634.51	1.43	0.86
250	3.45±0.82	0.90	3	0.000091±0.000147	8.49±0.57	4880.47	0.90	0.90
300	3.77±0.36	0.98	3	0.000157±0.000037	8.62±0.14	5515.71	1.08	0.99
350	3.91±0.95	0.89	3	0.000259±000174	8.83±0.57	6828.34	1.28	0.93

4 cooling rates 5 temperature cycles at each cooling rate

Concentration (g/l)	Slope best fit data straight line of $\ln u_c\ Vs \ln q$	R^2linear fitting	a_1	$a_2 = b$	$\ln q_0$	$q_0\left(\frac{K}{s}\right)$	$\gamma_{eff}\left(\frac{mJ}{m^2}\right)$	$R^2 fitting\ equation\ (23)$
200	4.92±0.81	0.95	3	0.000521±0.000146	8.98±0.37	7966.99	1.61	0.97
250	3.65±0.66	0.94	3	0.000132±0.000110	8.64±0.42	5639.20	1.02	0.95
300	4.22±0.36	0.99	3	0.000262±0.000029	8.70±0.093	5998.64	1.28	0.99
350	3.93±0.66	0.95	3	0.000239±0.000103	8.67±0.33	5847.78	1.25	0.97

8 cooling rates 3 temperature cycles at each cooling rate

Concentration (g/l)	Slope best fit data straight line of $\ln u_c\ Vs \ln q$	R^2linear fitting	a_1	$a_2 = b$	$\ln q_0$	$q_0\left(\frac{K}{s}\right)$	$\gamma_{eff}\left(\frac{mJ}{m^2}\right)$	$R^2 fitting\ equation\ (23)$
200	4.94±0.66	0.90	3	0.000531±0.000180	8.92±0.33	7488.15	1.62	0.90
250	3.92±0.52	0.91	3	0.000212±0.000116	8.55±0.27	5153.05	1.20	0.91
300	4.53±0.33	0.97	3	0.000410±0.000073	8.65±0.14	5719.92	1.49	0.98
350	4.93±0.57	0.93	3	0.000649±0.000142	8.90±0.24	7337.73	1.74	0.95

8 cooling rates 10 temperature cycles at each cooling rate

Concentration (g/l)	Slope best fit data straight line of $\ln u_c\ Vs \ln q$	R^2linear fitting	a_1	$a_2 = b$	$\ln q_0$	$q_0\left(\frac{K}{s}\right)$	$\gamma_{eff}\left(\frac{mJ}{m^2}\right)$	$R^2 fitting\ equation\ (23)$
200	5.17±0.57	0.93	3	0.000653±0.000148	8.97±0.26	7834.01	1.74	0.94
250	4.82±0.59	0.92	3	0.000543±0.000147	8.81±0.26	6673.54	1.64	0.93
300	5.05±0.47	0.95	3	0.000629±0.000113	8.83±0.19	6811.22	1.72	0.97
350	5.06±0.51	0.94	3	0.000698±0.000126	8.82±0.20	6761.14	1.79	0.96

3. Analysis of experimental data using the Nyvlt approach and derivation of a correlation equation whereby the nucleation mechanism can be determined from previous Nyvlt-type data analysis

As already mentioned, Nyvlt [6] developed an original approach for the interpretation of $MSZW$ data obtained by the polythermal method. The approach is based on the well-known semi-empirical power law [6, 7]

$$J = k_j(\Delta C_{max})^{m_0} \tag{42}$$

where k_j is an empirical parameter , m_0 is the order of nucleation, $\Delta C_{max} = C_{max} - C_e$ is the maximum concentration difference, C_{max} is the solution concentration at the metastability limit, and C_e is the solution equilibrium concentration or solubility.

Nyvlt suggested that a plot of the cooling rate q vs the critical undercooling ΔT_c in *ln-ln* coordinates will deliver the value of the nucleation order m_0 according to

$$\log q = (m_0 - 1)\log\frac{dC_e}{dT} + \ln k_j + m_o \ln \Delta T_c \tag{43}$$

Here ΔC_{max} and ΔT_c are related by

$$\Delta C_{max} = \frac{dC_e}{dT}\Delta T_c \tag{44}$$

and ΔT_c is defined by

$$\Delta T_c = T_{diss} - T_c \tag{45}$$

where T_{diss} is the dissolution temperature and T_c is the crystallisation temperature.

Using Nyvlt approach, ΔT_c values were calculated from the experimental data as the difference between the average dissolution and crystallisation temperatures at each cooling rate (see Table 2 below).

Table 2. Average dissolution and crystallisation temperatures as a function of cooling rate for methyl stearate in kerosene at 200, 250, 300 and 350 g/l. Corresponding critical undercooling calculated as the difference between dissolution and crystallisation temperatures

q (℃ /min)	T_c (℃)	T_{diss} (℃)	ΔT_c (℃)
200 g/l			
0.25	12.56	17.69	5.13
1.00	11.99	18.66	6.67
3.20	10.26	21.92	11.66
5.00	8.77	24.07	15.30
7.00	8.10	27.29	19.20
9.00	7.68	30.16	22.48
11.00	8.53	30.85	22.32
13.00	8.09	33.46	25.38
250 g/l			
0.25	14.88	19.59	4.71
1.00	14.16	20.81	6.65
3.20	12.15	24.85	12.71
5.00	10.82	28.49	17.67
7.00	10.27	31.88	21.61
9.00	9.09	34.12	25.02
11.00	10.49	36.30	25.81
13.00	10.54	38.78	28.24
300 g/l			
0.25	16.54	21.03	4.49
1.00	15.29	22.46	7.17
3.20	13.96	26.87	12.91
5.00	12.95	29.88	16.93
7.00	11.53	33.68	22.14
9.00	10.82	35.88	25.06
11.00	11.66	37.30	25.65
13.00	11.80	40.03	28.23
350 g/l			
0.25	17.75	22.19	4.43
1.00	16.85	23.71	6.86
3.20	15.12	28.29	13.17
5.00	14.33	31.44	17.11
7.00	13.31	35.36	22.06
9.00	11.69	37.52	25.84
11.00	12.86	38.96	26.11
13.00	12.91	40.12	27.21

At each concentration, the obtained values for ΔT_c were plotted as a function of the cooling rate q in $ln - ln$ coordinates and fitted by a straight line. According to the Nyvlt-type equation (43), the slope of the line delivers the nucleation order m_0. Fig. 3 below exemplifies the plot for methyl stearate in kerosene at 200 g/l.

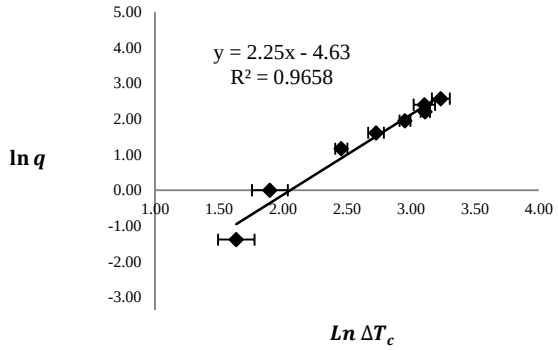

Figure 3. Plot of experimental data collected by means of the polythermal methodology in $ln\ q$ vs $ln\ \Delta T_c$ coordinates for methyl stearate in kerosene at a concentration of 200 g solute per litre of solvent. $\Delta T_c = T_{diss} - T_c$

The obtained nucleation order, correlation coefficient, parameter standard deviations and covariance at each concentration are given in Table 3 below.

Table 3. Nucleation order as a function of concentration and correlation coefficient of experimental data plotted in $ln\ q$ vs $ln\ \Delta T_c$ coordinates as well as standard deviation and covariance of the corresponding parameters of the linear fitting

$Concentration\ (g/l)$	$slope/Nucleation\ order\ (m_0)$	R^2	Slope Standard Deviation (SD)	Intercept Standard Deviation (SD)	Covariance Slope/Intercept
200	2.28±0.173	0.97	0.63	1.71	-1.06
250	1.95±0.127	0.98	0.56	1.57	-0.86
300	2.00±0.112	0.99	0.56	1.58	-0.87
350	1.96±0.103	0.98	0.56	1.55	-0.84

The slopes of the lines in all cases show that the nucleation order m_0 in equation (42) approximates two. As expected, the slopes of the best linear fit of the collected data using the Nyvlt approach [6, 7] are lower than those obtained from the best linear fit using the $KBHR$ approach. This is so because in the case of $KBHR$ approach, as derived analytically, the critical undercooling ΔT_c is defined as the difference between the solution equilibrium temperature T_e and the corresponding crystallisation temperature T_c .

On the other hand in the case, in the case of the Nyvlt approach, as derived from an empirical expression, the critical undercooling ΔT_c is defined as the difference

between the dissolution temperatures T_{diss} and the corresponding crystallisation temperature T_c. The equilibrium temperatures are always lower than the dissolution ones, because they are obtained by extrapolating to zero cooling rate the straight lines that fit best the $T_{diss}(q)$ data and because T_{diss} increases with q.

Nonetheless, it might be possible to analytically establish a relationship between the slopes obtained by applying the Nyvlt approach and those obtained by applying the $KBHR$ approach. In the case of the former approach, data are plotted on $Ln\ q\ vs\ ln\,\Delta T_c$ coordinates with $\Delta T_c = T_{diss} - T_c$. Then an approximation of the slope (s_1) of the best linear fit to the data could be obtained by choosing two experimental data pairs $(T_{c1}, T_{diss1})$and (T_{c2}, T_{diss2}) of the dissolution and crystallisation temperatures and using them in the following expression

$$s_1 = \frac{ln\,q_2 - ln\,q_1}{ln\,\Delta T_{c2} - ln\,\Delta T_{c1}} = \frac{ln\,q_2 - ln\,q_1}{ln(T_{diss2} - T_{c2}) - ln\,(T_{diss1} - T_{c1})} \tag{46}$$

This approximation could only holds if the bets linear fit to the experimental data according to the Nyvlt approach has a reasonable correlation coefficient R^2.

The same principle can be applied to obtain an approximation of the slope (s_2) of the best linear fit to data plotted in $ln\,q\ vs.\,ln\,u_c$ coordinates according to $KBHR$ approach with $u_c = \frac{\Delta T_c}{T_e} = \frac{T_e - T_c}{T_e}$, thus

$$s_2 = \frac{ln\,q_2 - ln\,q_1}{ln\,u_{c2} - ln\,u_{c1}} = \frac{ln\,q_2 - ln\,q_1}{ln\left(\frac{T_e - T_{c2}}{T_e}\right) - ln\left(\frac{T_e - T_{c1}}{T_e}\right)} = \frac{ln\,q_2 - ln\,q_1}{ln(T_e - T_{c2}) - ln(T_e - T_{c1})} \tag{47}$$

As T_e is greater than any of the experimentally collected dissolution temperatures T_{diss} by a known value Δ_T, equation (47) can be expressed as

$$s_2 = \frac{ln\, q_2 - ln\, q_1}{ln(T_{diss2} - T_{c2} - \Delta_{T2}) - ln(T_{diss1} - T_{c1} - \Delta_{T1})} \quad (48)$$

The numerators of expressions (46) and (48) are equal, therefore

$$s_1[ln(T_{diss2} - T_{c2}) - ln\,(T_{diss1} - T_{c1})] = s_2[ln(T_{diss2} - T_{c2} - \Delta_{T2}) - ln(T_{diss1} - T_{c1} - \Delta_{T1})]$$

From this equality the $KBHR$ slope s_2 could be estimated from the Nyvlt slope s_1 by means of the formula

$$s_2 = \frac{s_1[ln(T_{diss2} - T_{c2}) - ln\,(T_{diss1} - T_{c1})]}{[ln(T_{diss2} - T_{c2} - \Delta_{T2}) - ln(T_{diss1} - T_{c1} - \Delta_{T1})]} \quad (49)$$

Again the accuracy with which s_2 can be predicted from s_1 by using equation (49) will greatly depend on the expected correlation coefficient R^2 of the best linear fit to experimental data points by applying both the $KBHR$ and the Nyvlt approaches. In general, from analysis of previously obtained experimental data, the values of s_2 were observed to be between 1.5 to 2.5 higher than those of s_1. Using these approximations for the case of methyl stearate crystallising from kerosene, the $KBHR$ slope s_2 will be in the range from 3-5, because $m_0 = s_1 = 2$. This indicates that methyl stearate crystallises from kerosene by the PN mechanism, which is in agreement with the polythermal analysis presented in Chapter 5.

Appendix B

The complete set of planes delivered by the prediction of the BFDH morphology for triclinic n-docosane crystals is presented. These planes are organised in thirteen different groups defined by zone axis analysis.

Group 1/Zone axis [100]

hkl	Mult	d_{hkl}	Distance
{ 0 1 0}	2	4.59	21.81
{ 0 1 -1}	2	4.55	21.96
{ 0 1 1}	2	4.50	22.24
{ 0 1 -2}	2	4.41	22.68
{ 0 1 2}	2	4.30	23.23
{ 0 1 -3}	2	4.18	23.93
{ 0 1 3}	2	4.05	24.71
{ 0 2 -1}	2	2.29	43.62
{ 0 2 1}	2	2.28	43.90
{ 0 2 -3}	2	2.25	44.50
{ 0 2 3}	2	2.21	45.34
{ 0 3 -1}	2	1.53	65.37
{ 0 3 -2}	2	1.53	65.52
{ 0 3 1}	2	1.52	65.66
{ 0 3 2}	2	1.51	66.10

Group 2/Zone axis [010]

hkl	Mult	d_{hkl}	Distance
{ 1 0 2}	2	4.08	24.54
{ 1 0 3}	2	4.06	24.61
{ 1 0 1}	2	4.00	24.99
{ 1 0 0}	2	3.86	25.93
{ 1 0 -1}	2	3.66	27.32
{ 1 0 -2}	2	3.44	29.09
{ 1 0 -3}	2	3.21	31.17
{ 2 0 3}	2	2.02	49.40
{ 2 0 1}	2	1.97	50.80
{ 2 0 -1}	2	1.88	53.15
{ 2 0 -3}	2	1.78	56.32
{ 3 0 2}	2	1.32	75.75
{ 3 0 1}	2	1.30	76.70

Group 3/Zone axis [1-10]

hkl	Mult	d_{hkl}	Distance
{ 1 1 2}	2	3.66	27.33
{ 1 1 3}	2	3.63	27.51
{ 1 1 1}	2	3.62	27.62
{ 1 1 0}	2	3.52	28.37
{ 1 1 -1}	2	3.39	29.54
{ 1 1 -2}	2	3.22	31.08
{ 1 1 -3}	2	3.04	32.94
{ 2 2 3}	2	1.82	54.84
{ 2 2 1}	2	1.79	55.88
{ 2 2 -1}	2	1.73	57.81
{ 2 2 -3}	2	1.65	60.53

Group 4/Zone axis [2-10]

hkl	Mult	d_{hkl}	Distance
{ 1 2 2}	2	2.33	42.93
{ 1 2 1}	2	2.32	43.04
{ 1 2 3}	2	2.32	43.12
{ 1 2 0}	2	2.30	43.45
{ 1 2 -1}	2	2.26	44.15
{ 1 2 -2}	2	2.22	45.13
{ 1 2 -3}	2	2.16	46.36

Group 5/Zone axis [3-10]

hkl	Mult	d_{hkl}	Distance
{ 1 3 2}	2	1.60	62.37
{ 1 3 1}	2	1.60	62.40
{ 1 3 3}	2	1.60	62.55
{ 1 3 0}	2	1.60	62.63
{ 1 3 -1}	2	1.59	63.07
{ 1 3 -2}	2	1.57	63.71
{ 1 3 -3}	2	1.55	64.54

Group 6/Zone axis [110]

hkl	Mult	d_{hkl}	Distance
{ 1 -1 3}	2	2.67	37.49
{ 1 -1 2}	2	2.66	37.53
{ 1 -1 1}	2	2.64	37.90
{ 1 -1 0}	2	2.59	38.62
{ 1 -1 -1}	2	2.52	39.64
{ 1 -1 -2}	2	2.44	40.95
{ 1 -1 -3}	2	2.35	42.53
{ 2 -2 3}	2	1.33	75.35
{ 2 -2 1}	2	1.31	76.44

Group 7/Zone axis [210]

hkl	Mult	d_{hkl}	Distance
{ 1 -2 3}	2	1.78	56.18
{ 1 -2 2}	2	1.78	56.26
{ 1 -2 1}	2	1.77	56.57
{ 1 -2 0}	2	1.75	57.10
{ 1 -2 -1}	2	1.73	57.86
{ 1 -2 -2}	2	1.70	58.82
{ 1 -2 -3}	2	1.67	59.98

Group 8/Zone axis [310]

hkl	Mult	d_{hkl}	Distance
{ 1 -3 3}	2	1.31	76.54
{ 1 -3 2}	2	1.30	76.64
{ 1 -3 1}	2	1.30	76.91

Group 9/Zone axis [1-20]

hkl	Mult	d_{hkl}	Distance
{ 2 1 3}	2	2.11	47.41
{ 2 1 2}	2	2.09	47.95
{ 2 1 1}	2	2.05	48.75
{ 2 1 0}	2	2.01	49.79
{ 2 1 -1}	2	1.96	51.07
{ 2 1 -2}	2	1.90	52.55
{ 2 1 -3}	2	1.84	54.24

Group 10/Zone axis [3-20]

hkl	Mult	d_{hkl}	Distance
{ 2 3 3}	2	1.46	68.69
{ 2 3 2}	2	1.45	68.97
{ 2 3 1}	2	1.44	69.43
{ 2 3 0}	2	1.43	70.08
{ 2 3 -1}	2	1.41	70.90
{ 2 3 -2}	2	1.39	71.89
{ 2 3 -3}	2	1.37	73.05

Group 11/Zone axis [120]

hkl	Mult	d_{hkl}	Distance
{ 2 -1 3}	2	1.67	59.86
{ 2 -1 2}	2	1.66	60.39
{ 2 -1 1}	2	1.64	61.13
{ 2 -1 0}	2	1.61	62.06
{ 2 -1 -1}	2	1.58	63.19
{ 2 -1 -2}	2	1.55	64.50
{ 2 -1 -3}	2	1.52	65.97

Group 12/Zone axis [1-30]

hkl	Mult	d_{hkl}	Distance
{ 3 1 3}	2	1.40	71.31
{ 3 1 2}	2	1.39	72.09
{ 3 1 1}	2	1.37	73.04
{ 3 1 0}	2	1.35	74.15
{ 3 1 -1}	2	1.33	75.42
{ 3 1 -2}	2	1.30	76.83

Group 13/Zone axis [2-30]

hkl	Mult	d_{hkl}	Distance
{ 3 2 3}	2	1.35	74.17
{ 3 2 2}	2	1.34	74.88
{ 3 2 1}	2	1.32	75.75
{ 3 2 0}	2	1.30	76.78

Appendix C

- The complete set of planes delivered by the prediction of the BFDH morphology for orthorhombic *Pnab* methyl stearate crystals. These planes are organised in nine different groups defined by zone axis analysis.

Group 1/Zone axis [100]

hkl	Mult	d_{hkl}	Distance
{ 0 1 1}	4	7.33	13.64
{ 0 1 3}	4	7.16	13.96
{ 0 2 0}	2	3.68	27.20
{ 0 2 4}	4	3.63	27.52
{ 0 3 1}	4	2.45	40.81
{ 0 4 2}	4	1.84	54.43
{ 0 4 6}	4	1.83	54.76
{ 0 6 4}	4	1.22	81.70

Group 2/Zone axis [1-10]

hkl	Mult	d_{hkl}	Distance
{ 1 1 1}	8	4.46	22.44
{ 1 1 2}	8	4.44	22.51
{ 1 1 3}	8	4.42	22.63
{ 2 2 0}	4	2.23	44.82
{ 2 2 1}	8	2.23	44.84
{ 2 2 3}	8	2.23	44.94
{ 3 3 1}	8	1.49	67.24
{ 3 3 2}	8	1.49	67.27

Group 3/Zone axis [2-10]

hkl	Mult	d_{hkl}	Distance
{ 1 2 0}	4	3.08	32.51
{ 1 2 1}	8	3.07	32.53
{ 1 2 2}	8	3.07	32.58
{ 1 2 3}	8	3.06	32.66

Group 4/Zone axis [3-10]

hkl	Mult	d_{hkl}	Distance
{ 1 3 1}	8	2.25	44.53
{ 1 3 2}	8	2.24	44.56
{ 1 3 3}	8	2.24	44.63
{ 2 6 0}	4	1.12	89.03

Group 5/Zone axis [0-10]

hkl	Mult	d_{hkl}	Distance
{ 2 0 0}	2	2.81	35.63
{ 2 0 1}	4	2.81	35.65
{ 2 0 2}	4	2.80	35.69
{ 2 0 3}	4	2.80	35.77
{ 2 0 4}	4	2.79	35.88
{ 2 0 6}	4	2.76	36.19
{ 6 0 2}	4	0.94	106.92
{ 6 0 4}	4	0.93	106.98

Group 6/Zone axis [1-20]

hkl	Mult	d_{hkl}	Distance
{ 2 1 1}	8	2.62	38.15
{ 2 1 2}	8	2.62	38.20
{ 2 1 3}	8	2.61	38.27
{ 4 2 0}	4	1.31	76.28

Group 7/Zone axis [3-20]

hkl	Mult	d_{hkl}	Distance
{ 2 3 1}	8	1.85	54.17
{ 2 3 2}	8	1.84	54.21
{ 2 3 3}	8	1.84	54.26
{ 4 6 0}	4	0.92	108.33

Group 8/Zone axis [1-30]

hkl	Mult	d_{hkl}	Distance
{ 3 1 1}	8	1.81	55.16
{ 3 1 2}	8	1.81	55.19
{ 3 1 3}	8	1.81	55.24
{ 6 2 0}	4	0.91	110.30

Group 9/Zone axis [2-30]

hkl	Mult	d_{hkl}	Distance
{ 3 2 0}	4	1.67	59.97
{ 3 2 1}	8	1.67	59.98
{ 3 2 2}	8	1.67	60.01
{ 3 2 3}	8	1.67	60.05

- The complete set of planes delivered by the prediction of the BFDH morphology for monoclinic $A2/a$ methyl stearate crystals. These planes are organised in nine different groups defined by zone axis analysis.

Group 1/Zone axis [100]

hkl	Mult	d_{hkl}	Distance
{ 0 1 1}	4	7.31	13.68
{ 0 1 3}	4	7.14	14.00
{ 0 2 0}	2	3.67	27.29
{ 0 2 4}	4	3.62	27.61
{ 0 3 1}	4	2.44	40.94
{ 0 4 2}	4	1.83	54.61
{ 0 4 6}	4	1.82	54.93
{ 0 6 4}	4	1.22	81.96

Group 2/Zone axis [1-10]

hkl	Mult	d_{hkl}	Distance
{ 1 1 1}	4	4.07	24.59
{ 1 1 3}	4	3.92	25.52
{ 1 1 -1}	4	4.20	23.81
{ 1 1 -3}	4	4.31	23.20
{ 2 2 0}	4	2.07	48.37
{ 2 2 4}	4	2.00	50.08
{ 2 2 -4}	4	2.13	46.96
{ 3 3 1}	4	1.37	72.95
{ 3 3 -1}	4	1.39	72.16
{ 4 4 2}	4	1.03	97.53
{ 4 4 6}	4	1.01	99.25
{ 4 4 -2}	4	1.04	95.97
{ 4 4 -6}	4	1.06	94.57
{ 6 6 4}	4	0.68	146.71
{ 6 6 -4}	4	0.70	143.58

Group 3/Zone axis [2-10]

hkl	Mult	d_{hkl}	Distance
{ 1 2 0}	4	2.96	33.81
{ 1 2 2}	4	2.90	34.43
{ 1 2 -2}	4	3.00	33.31
{ 2 4 2}	4	1.47	68.21
{ 2 4 6}	4	1.44	69.56
{ 2 4 -2}	4	1.49	67.09
{ 2 4 -6}	4	1.51	66.22

Group 4/Zone axis [3-10]

hkl	Mult	d_{hkl}	Distance
{ 1 3 1}	4	2.19	45.76
{ 1 3 3}	4	2.16	46.26
{ 1 3 -1}	4	2.21	45.34

{ 1 3 -3}	4	2.22	45.02
{ 2 6 0}	4	1.10	91.08
{ 2 6 4}	4	1.09	92.00
{ 2 6 -4}	4	1.11	90.34

Group 5/Zone axis [0-10]

hkl	Mult	d_{hkl}	Distance
{ 2 0 0}	2	2.50	39.93
{ 2 0 2}	2	2.44	40.92
{ 2 0 4}	2	2.38	42.00
{ 2 0 6}	2	2.32	43.14
{ 2 0 -2}	2	2.56	39.03
{ 2 0 -4}	2	2.62	38.22
{ 2 0 -6}	2	2.67	37.52
{ 4 0 2}	2	1.24	80.84
{ 4 0 6}	2	1.21	82.90
{ 4 0 -2}	2	1.27	78.94
{ 4 0 -6}	2	1.29	77.23
{ 6 0 2}	2	0.83	120.76
{ 6 0 4}	2	0.82	121.75
{ 6 0 -2}	2	0.84	118.87
{ 6 0 -4}	2	0.85	117.97

Group 6/Zone axis [1-20]

hkl	Mult	d_{hkl}	Distance
{ 2 1 1}	4	2.34	42.66
{ 2 1 3}	4	2.29	43.64
{ 2 1 -1}	4	2.39	41.76
{ 2 1 -3}	4	2.44	40.96
{ 4 2 0}	4	1.18	84.40
{ 4 2 4}	4	1.16	86.28
{ 4 2 -4}	4	1.21	82.70

Group 7/Zone axis [3-20]

hkl	Mult	d_{hkl}	Distance
{ 2 3 1}	4	1.74	57.52
{ 2 3 3}	4	1.72	58.25
{ 2 3 -1}	4	1.76	56.86
{ 2 3 -3}	4	1.78	56.27
{ 4 6 0}	4	0.87	114.36
{ 4 6 4}	4	0.86	115.76
{ 4 6 -4}	4	0.88	113.11

Group 8/Zone axis [1-30]

hkl	Mult	d_{hkl}	Distance
{ 3 1 1}	4	1.62	61.90
{ 3 1 3}	4	1.59	62.88
{ 3 1 -1}	4	1.64	60.98
{ 3 1 -3}	4	1.66	60.12
{ 6 2 0}	4	0.81	122.87
{ 6 2 4}	4	0.80	124.77
{ 6 2 -4}	4	0.83	121.08

Group 9/Zone axis [2-30]

hkl	Mult	d_{hkl}	Distance
{ 3 2 0}	4	1.52	65.82
{ 3 2 2}	4	1.50	66.71
{ 3 2 -2}	4	1.54	64.99
{ 6 4 2}	4	0.75	132.52
{ 6 4 6}	4	0.74	134.35
{ 6 4 -2}	4	0.76	130.80
{ 6 4 -6}	4	0.77	129.19

- The complete set of planes delivered by the prediction of the BFDH morphology for monoclinic $C2$ methyl stearate crystals. These planes are organised in seventeen different groups defined by zone axis analysis.

Group 1/Zone axis [100]

hkl	Mult	d_{hkl}	Distance
{ 0 2 0}	1	3.70	27.03
{ 0 2 1}	2	3.69	27.13
{ 0 2 2}	2	3.65	27.43
{ 0 2 3}	2	3.58	27.92
{ 0 2 4}	2	3.50	28.60
{ 0 2 6}	2	3.28	30.44
{ 0 6 2}	2	1.23	81.22
{ 0 6 4}	2	1.23	81.62

Group 2/Zone axis [-100]

hkl	Mult	d_{hkl}	Distance
{ 0 -2 0}	1	3.70	27.03
{ 0 -2 1}	2	3.69	27.13
{ 0 -2 2}	2	3.65	27.43
{ 0 -2 3}	2	3.58	27.92

{ 0 -2 4}	2	3.50	28.60
{ 0 -2 6}	2	3.28	30.44
{ 0 -6 2}	2	1.23	81.22
{ 0 -6 4}	2	1.23	81.62

Group 3/Zone axis [1-10]

hkl	Mult	d_{hkl}	Distance
{ 1 1 -3}	2	4.45	22.48
{ 1 1 -2}	2	4.39	22.80
{ 1 1 -1}	2	4.28	23.36
{ 1 1 0}	2	4.14	24.13
{ 1 1 1}	2	3.98	25.10
{ 1 1 2}	2	3.81	26.24
{ 1 1 3}	2	3.63	27.53
{ 2 2 -3}	2	2.17	46.11
{ 2 2 -1}	2	2.11	47.44
{ 2 2 1}	2	2.03	49.18
{ 2 2 3}	2	1.95	51.29
{ 3 3 -2}	2	1.41	70.78
{ 3 3 -1}	2	1.40	71.56
{ 3 3 1}	2	1.36	73.30
{ 3 3 2}	2	1.35	74.27

Group 4/Zone axis [-1-10]

hkl	Mult	d_{hkl}	Distance
{ 1 -1 -3}	2	4.45	22.48
{ 1 -1 -2}	2	4.39	22.80
{ 1 -1 -1}	2	4.28	23.36
{ 1 -1 0}	2	4.14	24.13
{ 1 -1 1}	2	3.98	25.10
{ 1 -1 2}	2	3.81	26.24
{ 1 -1 3}	2	3.63	27.53
{ 2 -2 -3}	2	2.17	46.11
{ 2 -2 -1}	2	2.11	47.44
{ 2 -2 1}	2	2.03	49.18
{ 2 -2 3}	2	1.95	51.29
{ 3 -3 -2}	2	1.41	70.78
{ 3 -3 -1}	2	1.40	71.56
{ 3 -3 1}	2	1.36	73.30
{ 3 -3 2}	2	1.35	74.27

Group 5/Zone axis [3-10]

hkl	Mult	d_{hkl}	Distance
{ 1 3 -3}	2	2.26	44.34

{ 1 3 -2}	2	2.25	44.51
{ 1 3 -1}	2	2.23	44.80
{ 1 3 0}	2	2.21	45.20
{ 1 3 1}	2	2.19	45.73
{ 1 3 2}	2	2.16	46.36
{ 1 3 3}	2	2.12	47.10

Group 6/Zone axis [-3-10]

hkl	Mult	d_{hkl}	Distance
{ 1 -3 -3}	2	2.26	44.34
{ 1 -3 -2}	2	2.25	44.51
{ 1 -3 -1}	2	2.23	44.80
{ 1 -3 0}	2	2.21	45.20
{ 1 -3 1}	2	2.19	45.73
{ 1 -3 2}	2	2.16	46.36
{ 1 -3 3}	2	2.12	47.10

Group 7/Zone axis [0-10]

hkl	Mult	d_{hkl}	Distance
{ 2 0 -6}	2	2.78	35.92
{ 2 0 -4}	2	2.72	36.74
{ 2 0 -3}	2	2.68	37.36
{ 2 0 -2}	2	2.62	38.11
{ 2 0 -1}	2	2.56	38.99
{ 2 0 0}	2	2.50	39.99
{ 2 0 1}	2	2.43	41.09
{ 2 0 2}	2	2.36	42.30
{ 2 0 3}	2	2.29	43.59
{ 2 0 4}	2	2.22	44.98
{ 2 0 6}	2	2.09	47.96
{ 6 0 -4}	2	0.86	116.05
{ 6 0 -2}	2	0.85	117.93
{ 6 0 2}	2	0.82	122.14
{ 6 0 4}	2	0.80	124.45

Group 8/Zone axis [2-10]

hkl	Mult	d_{hkl}	Distance
{ 2 4 -6}	2	1.54	64.90
{ 2 4 -4}	2	1.53	65.36
{ 2 4 -2}	2	1.51	66.14
{ 2 4 0}	2	1.49	67.24
{ 2 4 2}	2	1.46	68.64
{ 2 4 4}	2	1.42	70.32
{ 2 4 6}	2	1.38	72.26

Group 9/Zone axis [-2-10]

hkl	Mult	d_{hkl}	Distance
{ 2 -4 -6}	2	1.54	64.90
{ 2 -4 -4}	2	1.53	65.36
{ 2 -4 -2}	2	1.51	66.14
{ 2 -4 0}	2	1.49	67.24
{ 2 -4 2}	2	1.46	68.64
{ 2 -4 4}	2	1.42	70.32
{ 2 -4 6}	2	1.38	72.26

Group 10/Zone axis [1-30]

hkl	Mult	d_{hkl}	Distance
{ 3 1 -3}	2	1.70	58.74
{ 3 1 -2}	2	1.68	59.58
{ 3 1 -1}	2	1.65	60.49
{ 3 1 0}	2	1.63	61.48
{ 3 1 1}	2	1.60	62.55
{ 3 1 2}	2	1.57	63.68
{ 3 1 3}	2	1.54	64.87

Group 11/Zone axis [-1-30]

hkl	Mult	d_{hkl}	Distance
{ 3 -1 -3}	2	1.70	58.74
{ 3 -1 -2}	2	1.68	59.58
{ 3 -1 -1}	2	1.65	60.49
{ 3 -1 0}	2	1.63	61.48
{ 3 -1 1}	2	1.60	62.55
{ 3 -1 2}	2	1.57	63.68
{ 3 -1 3}	2	1.54	64.87

Group 12/Zone axis [1-20]

hkl	Mult	d_{hkl}	Distance
{ 4 2 -6}	2	1.26	79.45
{ 4 2 -4}	2	1.24	80.87
{ 4 2 -2}	2	1.21	82.53
{ 4 2 0}	2	1.18	84.42
{ 4 2 2}	2	1.16	86.51
{ 4 2 4}	2	1.13	88.81
{ 4 2 6}	2	1.10	91.28

Group 13/Zone axis [-1-20]

hkl	Mult	d_{hkl}	Distance
{ 4 -2 -6}	2	1.26	79.45
{ 4 -2 -4}	2	1.24	80.87
{ 4 -2 -2}	2	1.21	82.53

{ 4 -2 0}	2	1.18	84.42
{ 4 -2 2}	2	1.16	86.51
{ 4 -2 4}	2	1.13	88.81
{ 4 -2 6}	2	1.10	91.28

Group 14/Zone axis [3-20]

hkl	Mult	d_{hkl}	Distance
{ 4 6 -6}	2	0.91	110.26
{ 4 6 -4}	2	0.90	111.28
{ 4 6 -2}	2	0.89	112.50
{ 4 6 0}	2	0.88	113.89
{ 4 6 2}	2	0.87	115.45
{ 4 6 4}	2	0.85	117.18
{ 4 6 6}	2	0.84	119.06

Group 15/Zone axis [-3-20]

hkl	Mult	d_{hkl}	Distance
{ 4 -6 -6}	2	0.91	110.26
{ 4 -6 -4}	2	0.90	111.28
{ 4 -6 -2}	2	0.89	112.50
{ 4 -6 0}	2	0.88	113.89
{ 4 -6 2}	2	0.87	115.45
{ 4 -6 4}	2	0.85	117.18
{ 4 -6 6}	2	0.84	119.06

Group 16/Zone axis [2-30]

hkl	Mult	d_{hkl}	Distance
{ 6 4 -6}	2	0.79	126.47
{ 6 4 -4}	2	0.78	128.02
{ 6 4 -2}	2	0.77	129.73
{ 6 4 0}	2	0.76	131.58
{ 6 4 2}	2	0.75	133.56
{ 6 4 4}	2	0.74	135.68
{ 6 4 6}	2	0.73	137.93

Group 17/Zone axis [-2-30]

hkl	Mult	d_{hkl}	Distance
{ 6 -4 -6}	2	0.79	126.47
{ 6 -4 -4}	2	0.78	128.02
{ 6 -4 -2}	2	0.77	129.73
{ 6 -4 0}	2	0.76	131.58
{ 6 -4 2}	2	0.75	133.56
{ 6 -4 4}	2	0.74	135.68
{ 6 -4 6}	2	0.73	137.93